Università degli Studi di Sassari
Doctoral course in
Life Science and Biotechnologies
Director Prof. Sechi L.A.
Cycle XXIX

Biomedical applications of different nanomaterials: Characterization and interaction with the immune system

Dr. Marco Orecchioni

Ph.D. Advisor Dr. Lucia Gemma Delogu

Academic year 2016/2017

Università degli Studi di Sassari
Doctoral course in
Life Science and Biotechnologies
Director Prof. Sechi L.A.
Cycle XXIX

La presente tesi è stata prodotta durante la frequenza del corso di dottorato in Life Sciences and Biotechnologies dell'Università degli Studi di Sassari, a.a. 2016/2017- XXIX ciclo, con il sostegno di una borsa di studio cofinanziata con le risorse del P.O.R. SARDEGNA F.S.E. 2007-2013 - Obiettivo competitività regionale e occupazione, Asse IV Capitale umano, Linea di Attività l.3.1 "Finanziamento di corsi di dottorato finalizzati alla formazione di capitale umano altamente specializzato, in particolare per i settori dell'ICT, delle nanotecnologie e delle biotecnologie, dell'energia e dello sviluppo sostenibile, dell'agroalimentare e dei materiali tradizionali".

La tesi è stata prodotta, altresì, grazie al contributo della Fondazione di Sardegna.

Alla mia famiglia…

Abstract

In the field of nanotechnology, research is nowadays deeply focusing on the translational application of nanomaterials in medicine. Whereas findings from physics, genetics and immunology have already changed the everyday clinical practice in different fields. Nanotechnology is expanding its legacy by implementing approaches aimed to delivering therapeutics and developing new diagnostic and imaging tools. One of the most fascinating frontiers of nanotechnology is the development of nanomaterials for diagnostic and therapeutic purposes possibly at the same time. However, before any effective application of in medicine, a critical step to be done is represented by the assessment of their impact on the immune system, independently of their specific purpose. Following parenteral administration (e.g. intravenous, intramuscular, subcutaneous, etc.), nanomaterials immediately enter in contact with peripheral immune cells either in the blood or in the peripheral tissues. In this context, during my thesis, I focused on the immunological impact of some of the main promising nanomaterials for biomedical applications: Carbon based materials such as carbon nanotubes (CNTs) and graphene, lipid nanocapsules (NCs) and super paramagnetic iron oxide nanoparticles (SPIONs), in order to study their potential to be applied in therapy and diagnostic applications taking advantage from their intrinsic properties. Initially, thanks to the evidences suggested by the literature and previous works of my advisor, the potential immunostimulatory properties of functionalized-CNTs to restore the dysregulation of immune functions found in absence of gravity was evaluated. Furtherly I focused my attention on graphene, particularly on its oxidized form [called graphene oxide (GO)] investigating the effects of several types of thoroughly characterized GO sheets, different in their lateral dimension and functionalization, on human primary lymphomonocytes from healthy donors. Wide range of assays looking at cell viability, cell activation, and molecular interaction were done. Moreover, to better dissect the immunological effects of these nanomaterials on individual cells, we applied single-cell mass cytometry to evaluate the effect of functionalized GOs on 15 cellular populations corresponding to 200 nodes of distinct but logically interconnected cell sub-populations. We used whole-transcriptomic analysis (Illumina BeadArray) for functional and molecular characterization of graphenes on human T-cells and monocytes. Following part of the findings got during the immune characterization of different graphenes, we were able to apply a new few-layer graphene (FLG) dispersions prepared by a mechano-chemical approach employing melamine as the exfoliating agent of graphite. We found, indeed, an intrinsic specific impact of FLG on

cells belonging to the monocytic lineage (CD14 positive) showing neither toxic nor activation effects on the other immune cells. Thanks to this intrinsic biological property, we further explored the possible therapeutic application of FLG on neoplastic monocytes *ex vivo*, from acute myeloid leukemia and chronic myelomonocytic leukemia patients. We also performed related experiment on other nanomaterials, such as NCs and SPIONs, looking at their impact on immune cells and exploiting the possible ultrasound contrast properties of SPIONs. The different studies presented in this thesis explicitly demonstrate that the interactions between nanomaterials and the immune cells depend on many factors correlated to their physicochemical characteristics. A positive impact of nanomaterials on the immune system, able to trigger both immune suppression and immune activation, is a concept helpful in the development of new nanoscale platforms in medicine. These analyzed platforms can be investigated as immunotherapy tools, vaccine carriers, adjuvants, and drug delivery systems to target pathology or inflammatory and inflammation-associated disorders.

Table of contents

Chapter 1

Introduction

The term "Nanotechnology" refers to the design, characterization and application of structures, devices and systems by controlling shape and size at atomic, molecular and supramolecular level [1]. Advances in nanotechnology have led to the development of new nanomaterials whose physico-chemical properties differ from those of their larger counterparts due to their higher surface-to-volume ratio. These novel properties make them excellent candidates for biomedical applications. Nanotechnology is a new discipline of science and engineering that has led to innovative approaches in many areas of medicine. Its applications in the screening, diagnosis, and treatment of diseases are collectively referred to as "nanomedicine", an emerging field that has the potential to revolutionize individual and population-based health of this century [2]. In contrast to conventional therapies, where the basic approach is to remove diseased cells faster than healthy cells, nanomedicine attempts to use sophisticated approaches to either kill specific cells or repair them, one cell at a time [3]. It is now possible to provide therapy at a molecular level with the help of different nanomaterials, treating diseases and adding light to our understanding of their pathogenesis. Nanomedicine can be considered a refinement of molecular medicine, integrating innovations in genomics and proteomics on the road to a more personalized medicine, so as to allow improved treatment efficacies for many diseases.

1.1 Nanomedicine

The advent of nanomaterials was forecast as long ago as 1959 by Richard P. Feynman, "the man who dared to think small" [1]. Feynman proposed using new materials to make smaller machine tools and so on until the atomic level [4]. Nowadays, nearly sixty years later, nanomedicine is playing a growing part in pharmaceutical research and development, primarily in the form of nanomaterials/nanoparticle-based delivery systems for drugs, genes and imaging agents, connecting a broad range of disciplines form biology to engineering. This field is characterized by continuous increasing interest given by the scientific community and the public in this domain [5]. Leading specialists suggest that nanomedicine will revolutionize almost all the branches of medicine, starting from basic medical check-ups and early diagnosis to personalized therapies [6].

1.2 Nanomaterials and the immune system

For any translational applications of nanomaterials into medical tools, a critical step is represented by the assessment of nanomaterial impact on the immune system, independently of their specific purpose [7].

It is well known that the immune system is the guardian of our body with the aim to protects it from any foreign element. It senses and reacts to external and internal aggressions, from pathogens to malignancies through different types of materials it may be in contact with. Immune reactions bring into play different types of cells and soluble factors that, together, will induce the most adapted response in order to try to eliminate intruders. They are classically divided in two arms called respectively innate and adaptive immunity. Innate immunity is the first line of defense and is rapidly set up upon any threat encounter. It mainly relies on the activation of the complement system, a complex system of plasma proteins, as well as of phagocytic cells (e.g. macrophages, neutrophils) present in tissues and body fluids. The final purpose of innate immune reactions is to eliminate the detected foreign element but it also helps triggering specific long-lasting mechanisms, namely adaptive immune reactions. Adaptive immunity takes more time to proceed but it leads to highly specific immune responses thanks to T and B lymphocytes, which express antigen-specific receptors. Antigen recognition together with co-stimulatory signals leads to lymphocyte activation and differentiation into effector cells. CD8+ T cells become cytotoxic (CTL) while CD4+ T cells become helper T cells, (Th) harbor varied cytokine secretion profiles allowing to define several subsets: some of them are pro-inflammatory (Th1 and Th17 subsets) while others are rather anti-inflammatory (Th2 subset). This system is also specialized in supporting B cell differentiation into antibody-secreting cells (called plasma cells). Although usually protective, immune reactions can also become harmful when they are directed towards self-components, leading to autoimmune disorders, or when they are over-stimulated by persistent intruders, leading to chronic inflammation for example [8]. Some researchers have shown that nanomaterials can stimulate and/or suppress the immune responses, and that their compatibility with the immune system is largely determined by their surface chemistry and dimension [9-11]. Indeed, modifications of the surface chemistry can significantly reduce the immunotoxicity and change the immune impact of nanomaterials making them useful platforms for many applications in biomedicine [12]. Following this statement, any type of nanomaterials could be designed modulating its physicochemical characteristics, to target or to avoid specific interactions with the immune

system. A contact between a nanoparticle and the immune system is considered desirable when it may lead to various beneficial medical applications, such as vaccines or therapeutics for inflammatory and autoimmune disorders [13]. However, the proper design of nanomaterials able to specifically modulate the immune system is still not well understood and needs to be clarified.

1.3 Nanomaterials for medical applications and interaction with the immune system

In this part of the thesis, examples are provided for some of the most interesting nanomaterials platforms exploited in the last years for therapeutic purpose i.e. Carbon Based Nanomaterials (CBMs), Nanoemulsions such as lipid nanocapsuels and Super paramagnetic Iron Oxide Nanoparticles, currently developed for several kind applications. A brief discussion is provided for each nanomaterial highlighting also the knowledge already present regarding their interaction with the immune system.

1.3.1 Carbon Based Materials

Carbon exists in nature in three different allotropic forms: amorphous carbon, graphite and diamond. With the discovery of fullerene (C60) in 1985, a large family of others carbon based materials have been discovered and these new carbon nanostructures obtained great interest in the field of nanotechnology and nanomedicine. The most investigated new forms of carbon that I will take in consideration for the following discussion are carbon nanotubes and graphene (**Figure 1**).

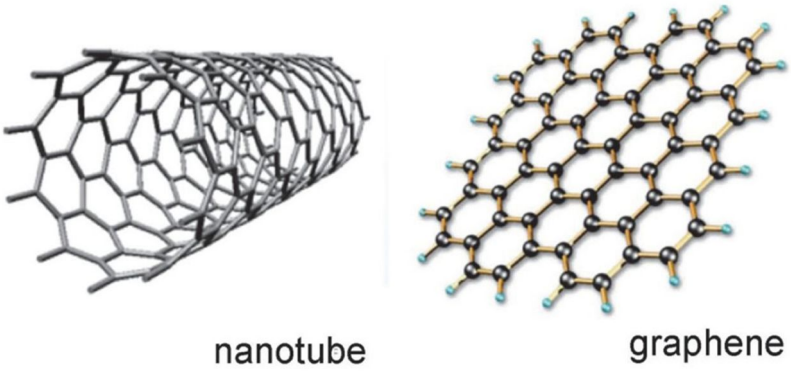

Figure 1: Nanostructured allotropic forms of carbon.

a) Carbon Nanotubes

Carbon nanotubes (CNTs) have been described for the first time at the atomic level in 1991 by Iijima, but the first evidence of their existence appeared already in the '50-'60, when they have been reported as carbon filament or carbon whiskers . CNTs are structures of 2D sheets of carbon (graphene) rolled up to form a 3D cylindrical structure with varying degrees of twist along their length, obtaining in this way a material with a variety of chiralities (**Figure 1**). The electronic properties of CNTs depend on the way to wrap the graphene layer. Depending to the number of wrap if they consist by a single shell of graphene or by multiple concentrical graphene sheets coaxially arranged around a central hollow core, CNTs can be classified in single-walled carbon nanotubes (SWCNTs) and multi-walled carbon nanotubes (MWCNTs). SWCNTs have a diameter from 0.7 to 3.0 nm and a length ranging between few nanometers to few micrometers. On the other hand, MWCNTs are larger and they can have a diameter up to 100 nm, with a length that could reach several millimetres.

CNTs, with their unique and extraordinary physicochemical properties, are currently being explored for biomedical and tissue engineering [14], imaging [9], biosensors [15] and drug delivery systems [16]. Interfacing CNTs with living systems has raised concerns about the toxicity of this material. This is an important issue that should render attentive the researchers when thinking about the potential use of CNTs in nanomedicine. It has been reported that pristine, (non-functionalized CNTs) are toxic. However, different *in vitro* and *in vivo* studies demonstrated that chemical functionalization of the surface of CNTs reduces their toxicity [7, 17, 18]. The effects of CNTs seem to depend on both the type of functionalization and the type of cells and/or organs analyzed [8, 19].

For example, Delogu LG et al discovered that functionalized water soluble CNTs increased the biocompatibility on primary cells isolated from human blood [20].

b) Graphene

Graphene is a single layer of carbon atoms arranged in a honeycomb lattice as shown in figure 1 It is the building block for other carbon-based materials where the rolling up graphene produces carbon nanotubes and buckyballs while stacking graphene produces graphite. The in-plane strength of the carbon bonds is much stronger than the c-axis bonds of graphite causing it to shear easily. It is this ability for graphite to cleave easily that lead to the first isolation of a single graphene by simply using adhesive tape in a technique known as mechanical exfoliation

[21]. Following the discovery of graphene in 2004 by Gaim and Novoselov at the University of Manchester came a huge wave of scientific research [21].

Graphene, is among other CBMs (fullerenes and CNTs) characterized by the most promising physicochemical properties [22]. The biological applications of graphene-based materials (GBMs) have significantly grown in the last years also in the field of medicine [23]. Graphene is a two-dimensional structure composed of carbon atoms with sp2 hybridization connected to form hexagons. It has impressive mechanical and physical properties such as over 100 times stronger than steel, and extremely high elasticity [24]. In addition, graphene presents high thermal durability and chemical resistance against water and organic solvents. Its extraordinary surface has the largest absorption capacity of chemical compounds including drugs, antibodies, proteins and nucleic acids. The last property is fundamental for medical applications ranging from drug delivery to biosensing. Its importance is given by the ability of graphene to be multifunctionalized, with drugs and also specific targeting molecules that can improve the specific delivery to the desired site [25].

1.3.2 Nanoemulsion the example of Lipid Nanocapsules

Nowadays, different colloidal systems such as nanoparticles and nanocapsules have been reported as potential carriers for drug delivery and also for different biomedical applications [26, 27]. Structured nanocapsules are generally described as colloidal systems with a core-shell structure, where the core acts as a liquid reservoir for several molecules or drugs, and the shell as a protective membrane. These nanosystems present promising applications as carriers of drugs, proteins, DNA chains and small interference RNA or in diagnosis applications as contrast agents [28, 29]. In particular, lipid nanocapsules (NCs), consisting of an oil-filled core with a surrounding polymer shell have special use for encapsulating and delivering hydrophobic drugs. The versatility of these NC for an efficient encapsulation in their oily core of several anti-cancer drugs has been demonstrated by several repots [30, 31]. Moreover, their useful properties include biocompatibility, biodegradability, low toxicity, controlled release of drugs and the ability to target specific tissues [32]. Current used drugs in pharmacotherapy, due to their hydrophobic character must use solubilizer agents for their intravenous administration [33, 34]. These agents being foreign substance has to be added in the blood stream and can interact with the immune system. This is why NCs offer a promising system and an excellent alternative to emulsions or microemulsions for pharmaceutical application of hydrophobic drugs [35].

Thanks to the drug protection and their controlled release on cancer cells, these kinds of nanoparticles provide an ideal solution, leading to selective cytotoxicity, minimizing the serious and unpleasant side effects of cancer drugs and preventing damage to healthy tissues [36, 37]. The shell of NCs can be formed by a wide variety of polymers/surfactants with hydrophilic segments such as polyethylene glycol (PEG), polyethylene oxide, poloxamers, poloxamines, polysorbates, chitosan, Pluronic and so on. [38-40]. These types of polymers, together with the enhancing of the intrinsic colloidal stability of the system, may help to avoid their recognition by the mononuclear phagocyte system, a major drawback that often arises after intravenous injection of drug carriers, causing a decrease in circulating NCs as well as undesirable accumulation of these colloids in different organs such as liver or spleen [28]. Therefore, the nature of the polymeric shell is crucial to minimize this action by repelling plasma proteins and achieving the so-called Stealth nanosystems [41]. This would increase the *in vivo* long-term stability of the nanoparticles, and it would also facilitate their ability to cross certain biological barriers. For example, nanoparticles coated with polysorbates or poloxamers have been reported to successfully pass the blood-brain-barrier and other physiological barriers [42].

1.3.3 Super Paramagnetic Iron Oxide Nanoparticles

Magnetic nanoparticles have attracted increasing interest as advanced nanomaterials for several types of applications, as well as for drug and gene delivery and/or imaging agents [43, 44]. In this context superparamagnetic iron oxide nanoparticles (SPIONs) have been investigated for biomedical applications such as tissue repair, immunoassays, detoxification of biological fluids, hyperthermia, drug delivery, probes, *in vitro* cell separation and to produce antibiotic-resistant biofilms. They are, indeed important candidate materials for new perspectives in nanomedicine [45]. SPIONs belong to the class of inorganic based particles having an iron oxide core coated by either inorganic materials (silica, gold) and organic materials (phospholipids, fatty acids, polysaccharides, peptides or other surfactants and polymers) [46, 47]. In contrast to other nanoparticles, their magnetic properties, based on their inducible magnetization, allow them to be directed to a defined location or heated in the presence of an externally applied magnetic field. These characteristics makes them attractive for many applications, ranging from various separation techniques and contrast enhancing agents for MRI to drug delivery systems, magnetic hyperthermia (local heat source in the case of tumor therapy), and magnetically assisted transfection of cells [45]. Research with SPIONs has already demonstrated that these particles have the potential to become an important tool for enhancing magnetic resonance

contrast. SPIONs coated with organic molecules showing an overall median diameter of less than 50 - 160 nm were available on the market as MRI contrast agents for detecting liver tumors or to differentiate metastatic from inflammatory lymph nodes. SPION functionalized with targeting peptides exhibit an additional potential for providing important information for a number of diseases for example due to the increased expression of cellular markers. Furthermore, they could help physicians to identify dangerous arteriosclerotic plaques by MRI [48]. The ongoing research is directed towards monitoring events on the physiological and molecular level, so that inflammatory diseases or tumors can be detected via the accumulation of SPIONs or markers expressed on the cell surface [49].

1.4 Nanomaterials biocompatibility and impact on immune cells

1.4.1 Carbon nanotubes

Carbon nanotubes have been investigated with great expectation by several research groups in many contexts, ranging from electronics to medicine. Through the years, however, their cytotoxic effects and their interaction with the immune system raised major concerns regarding the real possibility to apply carbon nanotubes in medicine as diagnostic or therapeutic applications. Pristine nanotubes in fact tend to form agglomerate, induce cellular necrosis/apoptosis and oxidative stress when ingested by phagocytes. In mice, they determine formation of granulomas, resembling in part the effect of asbestos [50, 51]. Moreover, carbon nanotubes can directly bind some plasma protein as fibrinogen and apolipoproteins and trigger activation of complement cascade [52]. Concerning the cytotoxicity, in general, higher is the dose higher is the toxic effect. The functionalization of pristine nanotubes is also the key for improving their biocompatibility [53]. Several studies have demonstrated that some f-CNTs bear immunostimulatory properties in absence of cytotoxicity [10, 20]. Importantly, most of the studies have shown lack of relevant toxicity of f-CNTs at relatively high concentrations both *in vitro* and *in vivo* [53, 54]. Following these aspects, several parameters as the number of walls, the diameter, the length, and, importantly, the type of functionalization of CNTs can influence the uptake, biocompatibility and/or activation also on the immune cells.

An example of the interaction of CNTs with immune cells is given by Dutta et al. that investigated the importance of plasma protein adsorption by oxidized SWCNTs in murine macrophages [55]. Intriguingly, the authors noticed that the complex between SWCNTs and

albumin inhibited the induction of cox-2 and suggested that the proteins adsorbed onto nanotubes may alter their immune modulatory and toxicity properties. Furthermore, other modifications (e.g. non anionic surfactant coating) could reduce albumin adsorption and decrease their anti-inflammatory properties. In a similar way also the uptake could be affected, indeed, Pantarotto et al. [56] had shown that f-CNTs were able to cross the cell membrane and accumulate into the cytoplasm or reach the nucleus of living cell, similarly Porter et al. observed that SWCNT can cross the membrane of macrophage and localize mostly into the lysosomes. It should be mentioned that different nanomaterial coating and functionalization are finalized not only to reach a good biocompatibility but also to elude phagocytic-mediated clearance. In this context a good example is given by the work performed by the group of Tasciotti [57], in which the authors showed how nanoporous silicon particles coated with cellular membranes can avoid opsonization, delay uptake by mononuclear phagocytes and elude lysosomal pathway. However, the elicitation of phagocytic cells (Monocytes/Macrophage) functions is desirable when the purpose is to enhance the immunogenicity of a certain molecule. Thus, monocytes and their differentiated progeny (macrophages and dendritic cells) play an important role in both the innate and adaptive immunity, by exerting immune-regulatory proprieties to the production of several modulatory cytokines [58]. During a potential injection of nanomaterials for diagnostic or therapeutic purposes, these cells will be the responsible population for a possible innate and thanks to a cross talk with lymphocytes, adaptive response of the immune system. Meunier et al. for example assessed the effect of pristine double-walled CNTs on monocytes, the authors observed an induced IL-1β secretion linked to caspase-1 and to Nlrp3 inflammasome activation in human monocytes, while no induction of the corresponding mRNA was observed. The authors also showed that similar increase of IL-1β was observed using oxidized Double walled CNTs. However, the researchers did not assess whether the IL-1β release mediated by oxidized CNTs was dissociated from the induction of caspase- mediated apoptotic stimuli. In absence of functionalization, in fact, CNTs are highly cytotoxic and can mediate the induction of several inflammatory cytokines through the activation of pathways associated to oxidative stress and caspase cascade [50]. As stated above during a normal immune response, Innate and adaptive immune systems often work together to induce an efficient protection against foreign intrusions and only *ex vivo* on different immune subpopulations and *in vivo* experiments allow to consider the complex molecular and cellular network that link the different immune response. A large number of studies took advantage of the easiness of *in vitro* culturing cell lines. The clear advantages in using these cell models

(highly reproducible experiments, low cost and favorable culture conditions) are somehow in contrast with its neoplastic characteristics that may not always reflect the physiological condition of immune cell behavior. To avoid this concern, Delogu LG et al explored the impact of different functionalized MWCNTs on PBMCs from healthy donors [20]. MWCNTs oxidized and functionalized with ammonium group by 1,3-dipolar cycloaddition were found to not induce T cell expansion or activation (evaluated by CD25, and CD69 markers), while all of them were able to activate NK cells, which upregulated CD69, and CD161 activation markers following f-CNTs treatment. Moreover, f-MWCNTs induce the expression of the CD25 activation markers and release of IL-1β, IL-6, TNF, and IL-10 by mostly in human monocytes not accompanied by the activation of cytotoxic mechanisms [10, 20]. Following this aspect, through a genome-wide analysis on T cells and monocyte cells, Pescatori M et al showed that ammino-functionalized as well as oxidized MWCNTs with larger diameter provoke a profound modulation of immune-regulatory pathways not accompanied by the induction of apoptotic pathways. They demonstrated that these f-CNTs induce profound modulation of inflammatory molecules at the transcriptomic level. Molecular pathways activated by these nanotubes included toll-like receptor (TLR), IL-6, dendritic cell maturation, TNF, NFKB, and T helper 1 chemokine pathways (CXCR3 and CCR5 ligand pathways) [10]. Because of the critical role of these inflammatory pathways (especially the Th1 chemokine pathways) in controlling immune-mediated tumor rejection, their findings suggested the highly promising application of this type of f-CNTs as adjuvant molecules in the contest of cancer immunotherapy or other adjuvant applications [59]. These intrinsic CNT immunostimulatory properties, if well-controlled, could be exploited for vaccination or any therapeutic protocol that requires activation of the immune system. Following this way undesirable effects might become desirable.

1.4.2 Graphene

Graphene based materials seem to retrace the same road of scientific expectation of CNTs. Even for this materials a careful assessment of toxicity *in vitro* and *in vivo* in appropriate models is necessary before starting its testing in clinical trials [60]. The precise structure of graphene has been the subject of debate over the years since it varies greatly with the preparation methods and extent of oxidation [61]. Nevertheless, graphene can be rich in functional groups such as carboxylic and hydroxyl groups which facilitate its surface modifications increasing its biocompatibility. Very recently, graphene and graphene oxide (GO) have been investigated in a growing number of medical applications, such as drug delivery, diagnostics, tissue

engineering and gene transfection all with the final aim to use it as a therapy material [62, 63]. However, one of the main concerns of using graphene in nanomedicine is its biocompatibility. Similarly, to many other nanomaterials, it is necessary to carefully address its biodegradability in aqueous solutions. In addition, the dimensions of the flakes of graphene could be responsible of different impacts on cell viability [11]. On the other hand, specific toxic effects of graphene on cancer cells could represent a positive point. Indeed, many reports have shown that this function of graphene could be useful in possible future therapeutic applications [64, 65], for example as an inhibitor of cancer cell metastasis [66].

Risk to benefit ratio needs to be accurately evaluated before any medical application i.e. as delivery tool, immunotheraphy and for biomarker detection.

As discussed above graphene and its derivatives have been proposed for several attractive biomedical applications. Most of these applications demand intravenous injection of graphene, and hence the evaluation of its immune impact is an essential prerequisite. The majority of papers since now for immune interaction are performed with GO [25]. This is explained by the better immune compatibility of the oxidized form compared to pristine graphene. As shown by Sasidharan *et al.* the oxidation of graphene significantly reduces the toxicity in a macrophage cell line compared to pristine form with no reactive oxygen species (ROS)-mediated apoptosis [67]. Similarly Zhou *et al.* confirmed the effect of pristine graphene on macrophages, highlighting also that sub-cytotoxic concentrations of pristine graphene on both primary murine macrophages and immortalized macrophages significantly stimulates the secretion of Th1/Th2 cytokines including IL-1α, IL-6, IL-10, TNF-α and GM-CSF as well as chemokines such as MCP-1, MIP-1α, MIP-1β and RANTES, evidencing a clear activation of macrophages [68]. Also the different size dimensions of GO are still under discussion in the context of the immune impact. Recent studies have shown that a lateral dimensions lower than 1 μm seems to trigger a higher activation of immune cells instead the higher lateral dimensions do not affect the immune activation or biocompatibility [11]. However, in other studies in macrophage cell lines GOs with an average dimension between 1 and 2 μm led to a Toll-like receptor 4 (TLR4)-dependent necrosis [69]. These contrasting findings highlight the need of new studies about the correlation of dimension and molecular immune interaction of graphene. In a similar way the chemical modifications of graphene can significantly affect their impact on the immune system. Indeed**,** is already illustrated by many reports how the functionalization can reduce the toxicity changing the ability of graphene to modulate the immune response. In this sense, the functionalization of graphene with biocompatible polymers such as polyethylene glycol (PEG)

was found to increase its stability in physiological conditions, minimizing the interactions with other biomolecules and reducing the risk of immunological response [70]. Feito *et al.* demonstrated a reduced activation of T- and B-lymphocytes and macrophages in the presence of GO-PEG in a dose-dependent manner. Moreover, no significant changes in cytokine secretion were found after treatment with different GO-PEGs [70]. On the other hand, alternative functionalizations of GO could improve the immune activation. Wu *et al.* for example demonstrated that both carboxylated and PEGylated GO was able to reduce the IgE production but at the same time modulate the humoral immunity and antigen-specific T-cell responses with no systemic toxicity [72]. With another functionalization strategy for the development of highly effective GO-based vaccine nano-adjuvants, Xu *et al.* proved the ability of GO functionalized with PEG and various types of polyethylenimine (PEI) to act as a positive modulator of the immune response promoting the maturation of dendritic cells (DCs) and enhancing their cytokine secretion through activation of multiple toll-like receptor (TLR) pathways while showing low toxicity [73]. The effects of different physicochemical parameters of graphene on immune cells are an open chapter and need to be fully understood. To date, understand how to control the different physicochemical parameters of graphene based on its biological action is mandatory to reduce possible immune toxicity effects and to take advantage of the intrinsic immune properties of this nanomaterial for possible biological applications.

1.4.3 Lipid nanocapsules

The appropriate carrier design and functionalization, particularly the composition and the surface properties, are essential to ensure high biocompatibility and to protect molecules of interest from degradation and premature elimination [41]. Biodegradable polymers and molecules have been extensively studied as loading molecules for NCs to improve their hydrophilicity in biological media, for new possible treatments of many diseases.

However, increasing the long term stability of NCs i.e. into the blood stream, could lead to augmented interactions with the immune system. It is already well known that emulsions and nanoemulsion are used in vaccines development. It has been reported that the nanoscale-sized emulsions such as NCs are able to permeate the nasal mucosa and carry the antigen to the antigen-presenting cells more efficiently than larger-sized emulsions. Nanoscale emulsion-based intranasal vaccines have been investigated for hepatitis B, HIV, influenza, and anthrax [13].

However, before any pre-clinical application in drug delivery, it is of fundamental importance to choose the most suitable coating for NCs able to avoid or to boost the interaction with the immune system. Indeed, the NCs immunocompatibility assessment is critical for any translation into clinical practice. As a matter of fact, the possible interactions between NCs with different coatings and the immune system, could result into an immunostimulation or an immunosuppression, which might either be applied in immunotherapy or may promote treatment in anti-inflammatory/autoimmune disorders [12, 13].

1.4.4 Super Paramagnetic Iron Oxide Nanoparticles

Regarding the SPION interaction with the immune cells there are still many question to be addressed to understand the mechanisms of their immune recognition. The composition of SPION comprise multiple magnetite-maghemite (Fe3O4 and -Fe2O3) crystals. The surface of the crystals is anionic. Biopolymer coating (dextran, carboxydextran, chitosan, etc.) is necessary to impart water solubility and colloidal stability to the particles. The main translational disadvantages of these nanoparticles are immune-related adverse effects and high nonspecific uptake by following injection. SPIONs show rapid clearance and uptake by liver and spleen macrophages [74] and leukocytes [75]. Several dextran-coated SPION formulations showed severe anaphylactic-like reactions in patients (this is the example of Feridex and Combidex recently withdrawn from the market). Indeed, the SPION structure made by iron oxide crystal lattice exhibits a molecular pattern of periodical anionic charges, whereas dextran is the biopolymer composed of periodic sugar groups. Dextran maintains aqueous solubility of nanoparticles, but it does not cover the crystal surface and the anionic crystals are significantly exposed and can come in contact with the immune cells giving undesirable reactions [76].
This unsuccessful use of SPIONs can be further addressed to improve knowledge about mechanisms of interactions between these nanoparticles and the immune system, increasing and exploiting also new types of functionalizations that could overcame the undesired effect found with dextran-coated SPIONs.

1.5 References

[1] T. Appenzeller, Science, 254 (1991) 1300.

[2] V. Dusastre, Nature, 451 (2008) 770-771.

[3] K.K. Wong, X.L. Liu, Pediatr Surg Int, 28 (2012) 943-951.

[4] R.P. Feynman, Engineering and Science, 23 (1960) 22-36.

[5] G. Sechi, D. Bedognetti, F. Sgarrella, L. Van Eperen, F.M. Marincola, A. Bianco, L.G. Delogu, Nanomedicine (Lond), 9 (2014) 1475-1486.

[6] A. Tarangelo, S.J. Dixon, Nat Nanotechnol, 11 (2016) 921-922.

[7] M. Orecchioni, D. Bedognetti, F. Sgarrella, F.M. Marincola, A. Bianco, L.G. Delogu, J Transl Med, 12 (2014) 138.

[8] H. Dumortier, Adv Drug Deliv Rev, 65 (2013) 2120-2126.

[9] L.G. Delogu, G. Vidili, E. Venturelli, C. Menard-Moyon, M.A. Zoroddu, G. Pilo, P. Nicolussi, C. Ligios, D. Bedognetti, F. Sgarrella, R. Manetti, A. Bianco, Proc Natl Acad Sci U S A, 109 (2012) 16612-16617.

[10] M. Pescatori, D. Bedognetti, E. Venturelli, C. Menard-Moyon, C. Bernardini, E. Muresu, A. Piana, G. Maida, R. Manetti, F. Sgarrella, A. Bianco, L.G. Delogu, Biomaterials, 34 (2013) 4395-4403.

[11] J. Russier, E. Treossi, A. Scarsi, F. Perrozzi, H. Dumortier, L. Ottaviano, M. Meneghetti, V. Palermo, A. Bianco, Nanoscale, 5 (2013) 11234-11247.

[12] M.A. Dobrovolskaia, S.E. McNeil, Nat Nanotechnol, 2 (2007) 469-478.

[13] B.S. Zolnik, A. Gonzalez-Fernandez, N. Sadrieh, M.A. Dobrovolskaia, Endocrinology, 151 (2010) 458-465.

[14] S. Bosi, L. Ballerini, M. Prato, Top Curr Chem, 348 (2014) 181-204.

[15] R.J. Chen, S. Bangsaruntip, K.A. Drouvalakis, N.W. Kam, M. Shim, Y. Li, W. Kim, P.J. Utz, H. Dai, Proc Natl Acad Sci U S A, 100 (2003) 4984-4989.

[16] A. Bianco, K. Kostarelos, M. Prato, Curr Opin Chem Biol, 9 (2005) 674-679.

[17] L.G. Delogu, S.M. Stanford, E. Santelli, A. Magrini, A. Bergamaschi, K. Motamedchaboki, N. Rosato, T. Mustelin, N. Bottini, M. Bottini, J Nanosci Nanotechnol, 10 (2010) 5293-5301.

[18] C. Bussy, K. Kostarelos, Adv Drug Deliv Rev, 65 (2013) 2061-2062.

[19] H. Ali-Boucetta, K. Kostarelos, Adv Drug Deliv Rev, 65 (2013) 1897-1898.

[20] L.G. Delogu, E. Venturelli, R. Manetti, G.A. Pinna, C. Carru, R. Madeddu, L. Murgia, F. Sgarrella, H. Dumortier, A. Bianco, Nanomedicine (Lond), 7 (2012) 231-243.
[21] K.S. Novoselov, A.K. Geim, S.V. Morozov, D. Jiang, Y. Zhang, S.V. Dubonos, I.V. Grigorieva, A.A. Firsov, Science, 306 (2004) 666-669.
[22] A.K. Geim, K.S. Novoselov, Nat Mater, 6 (2007) 183-191.
[23] M. Orecchioni, R. Cabizza, A. Bianco, L.G. Delogu, Theranostics, 5 (2015) 710-723.
[24] Nat Mater, 6 (2007) 169.
[25] M. Orecchioni, C. Menard-Moyon, L.G. Delogu, A. Bianco, Adv Drug Deliv Rev, 105 (2016) 163-175.
[26] Y. Malam, M. Loizidou, A.M. Seifalian, Trends Pharmacol Sci, 30 (2009) 592-599.
[27] D. Peer, J.M. Karp, S. Hong, O.C. Farokhzad, R. Margalit, R. Langer, Nat Nanotechnol, 2 (2007) 751-760.
[28] N.T. Huynh, C. Passirani, P. Saulnier, J.P. Benoit, Int J Pharm, 379 (2009) 201-209.
[29] P. Sanchez-Moreno, J.L. Ortega-Vinuesa, A. Martin-Rodriguez, H. Boulaiz, J.A. Marchal-Corrales, J.M. Peula-Garcia, Int J Mol Sci, 13 (2012) 2405-2424.
[30] A. Beduneau, P. Saulnier, J.P. Benoit, Biomaterials, 28 (2007) 4947-4967.
[31] F. Lacoeuille, E. Garcion, J.P. Benoit, A. Lamprecht, J Nanosci Nanotechnol, 7 (2007) 4612-4617.
[32] M. Nasr, S. Abdel-Hamid, Curr Pharm Biotechnol, 16 (2015) 322-332.
[33] K. Deepa, S. Singha, T. Panda, J Nanosci Nanotechnol, 14 (2014) 892-904.
[34] M.N. Khalid, P. Simard, D. Hoarau, A. Dragomir, J.C. Leroux, Pharm Res, 23 (2006) 752-758.
[35] G. Gaucher, R.H. Marchessault, J.C. Leroux, J Control Release, 143 (2010) 2-12.
[36] R. Karim, C. Palazzo, B. Evrard, G. Piel, J Control Release, 227 (2016) 23-37.
[37] B. Haley, E. Frenkel, Urol Oncol, 26 (2008) 57-64.
[38] N. Skandrani, A. Barras, D. Legrand, T. Gharbi, H. Boulahdour, R. Boukherroub, Nanoscale, 6 (2014) 7379-7390.
[39] J. Nicolas, S. Mura, D. Brambilla, N. Mackiewicz, P. Couvreur, Chem Soc Rev, 42 (2013) 1147-1235.
[40] P. Sanchez-Moreno, P. Buzon, H. Boulaiz, J.M. Peula-Garcia, J.L. Ortega-Vinuesa, I. Luque, A. Salvati, J.A. Marchal, Biomaterials, 61 (2015) 266-278.
[41] S. Tan, X. Li, Y. Guo, Z. Zhang, Nanoscale, 5 (2013) 860-872.

[42] A. Ambruosi, S. Gelperina, A. Khalansky, S. Tanski, A. Theisen, J. Kreuter, J Microencapsul, 23 (2006) 582-592.
[43] P. Pang, C. Wu, M. Shen, F. Gong, K. Zhu, Z. Jiang, S. Guan, H. Shan, X. Shuai, PLoS One, 8 (2013) e76612.
[44] C. Wu, F. Gong, P. Pang, M. Shen, K. Zhu, D. Cheng, Z. Liu, H. Shan, PLoS One, 8 (2013) e66416.
[45] A.K. Gupta, M. Gupta, Biomaterials, 26 (2005) 3995-4021.
[46] A.K. Gupta, A.S. Curtis, Biomaterials, 25 (2004) 3029-3040.
[47] M. Babic, D. Horak, M. Trchova, P. Jendelova, K. Glogarova, P. Lesny, V. Herynek, M. Hajek, E. Sykova, Bioconjug Chem, 19 (2008) 740-750.
[48] C. von Zur Muhlen, D. von Elverfeldt, N. Bassler, I. Neudorfer, B. Steitz, A. Petri-Fink, H. Hofmann, C. Bode, K. Peter, Atherosclerosis, 193 (2007) 102-111.
[49] D.L. Thorek, A.K. Chen, J. Czupryna, A. Tsourkas, Ann Biomed Eng, 34 (2006) 23-38.
[50] C.C. Chou, H.Y. Hsiao, Q.S. Hong, C.H. Chen, Y.W. Peng, H.W. Chen, P.C. Yang, Nano Lett, 8 (2008) 437-445.
[51] C.A. Poland, R. Duffin, I. Kinloch, A. Maynard, W.A. Wallace, A. Seaton, V. Stone, S. Brown, W. Macnee, K. Donaldson, Nat Nanotechnol, 3 (2008) 423-428.
[52] C. Salvador-Morales, E. Flahaut, E. Sim, J. Sloan, M.L. Green, R.B. Sim, Mol Immunol, 43 (2006) 193-201.
[53] H. Ali-Boucetta, A. Nunes, R. Sainz, M.A. Herrero, B. Tian, M. Prato, A. Bianco, K. Kostarelos, Angew Chem Int Ed Engl, 52 (2013) 2274-2278.
[54] T. Chen, J. Zang, H. Wang, H. Nie, X. Wang, Z. Shen, S. Tang, J. Yang, G. Jia, J Nanosci Nanotechnol, 12 (2012) 8008-8016.
[55] D. Dutta, S.K. Sundaram, J.G. Teeguarden, B.J. Riley, L.S. Fifield, J.M. Jacobs, S.R. Addleman, G.A. Kaysen, B.M. Moudgil, T.J. Weber, Toxicol Sci, 100 (2007) 303-315.
[56] D. Pantarotto, J.P. Briand, M. Prato, A. Bianco, Chem Commun (Camb), (2004) 16-17.
[57] A. Parodi, N. Quattrocchi, A.L. van de Ven, C. Chiappini, M. Evangelopoulos, J.O. Martinez, B.S. Brown, S.Z. Khaled, I.K. Yazdi, M.V. Enzo, L. Isenhart, M. Ferrari, E. Tasciotti, Nat Nanotechnol, 8 (2013) 61-68.
[58] D.C. Dale, L. Boxer, W.C. Liles, Blood, 112 (2008) 935-945.
[59] J. Galon, H.K. Angell, D. Bedognetti, F.M. Marincola, Immunity, 39 (2013) 11-26.
[60] A. Bianco, Angew Chem Int Ed Engl, 52 (2013) 4986-4997.

[61] K.V. Krishna, C. Menard-Moyon, S. Verma, A. Bianco, Nanomedicine (Lond), 8 (2013) 1669-1688.
[62] L. Zhang, J. Xia, Q. Zhao, L. Liu, Z. Zhang, Small, 6 (2010) 537-544.
[63] S. Dinescu, M. Ionita, A.M. Pandele, B. Galateanu, H. Iovu, A. Ardelean, M. Costache, A. Hermenean, Biomed Mater Eng, 24 (2014) 2249-2256.
[64] S. Jaworski, E. Sawosz, M. Grodzik, A. Winnicka, M. Prasek, M. Wierzbicki, A. Chwalibog, Int J Nanomedicine, 8 (2013) 413-420.
[65] S. Gurunathan, J. Han, J.H. Park, J.H. Kim, Int J Nanomedicine, 9 (2014) 1783-1797.
[66] H. Zhou, B. Zhang, J. Zheng, M. Yu, T. Zhou, K. Zhao, Y. Jia, X. Gao, C. Chen, T. Wei, Biomaterials, 35 (2014) 1597-1607.
[67] A. Sasidharan, L.S. Panchakarla, A.R. Sadanandan, A. Ashokan, P. Chandran, C.M. Girish, D. Menon, S.V. Nair, C.N. Rao, M. Koyakutty, Small, 8 (2012) 1251-1263.
[68] H. Zhou, K. Zhao, W. Li, N. Yang, Y. Liu, C. Chen, T. Wei, Biomaterials, 33 (2012) 6933-6942.
[69] G. Qu, S. Liu, S. Zhang, L. Wang, X. Wang, B. Sun, N. Yin, X. Gao, T. Xia, J.J. Chen, G.B. Jiang, ACS nano, 7 (2013) 5732-5745.
[70] M.J. Feito, M. Vila, M.C. Matesanz, J. Linares, G. Goncalves, P.A. Marques, M. Vallet-Regi, J.M. Rojo, M.T. Portoles, J Colloid Interface Sci, 432 (2014) 221-228.
[71] C.M. Girish, A. Sasidharan, G.S. Gowd, S. Nair, M. Koyakutty, Advanced healthcare materials, 2 (2013) 1489-1500.
[72] H.Y. Wu, K.J. Lin, P.Y. Wang, C.W. Lin, H.W. Yang, C.C. Ma, Y.J. Lu, T.R. Jan, International journal of nanomedicine, 9 (2014) 4257-4266.
[73] L. Xu, J. Xiang, Y. Liu, J. Xu, Y. Luo, L. Feng, Z. Liu, R. Peng, Nanoscale, 8 (2016) 3785-3795.
[74] D. Simberg, J.H. Park, P.P. Karmali, W.M. Zhang, S. Merkulov, K. McCrae, S.N. Bhatia, M. Sailor, E. Ruoslahti, Biomaterials, 30 (2009) 3926-3933.
[75] S. Inturi, G. Wang, F. Chen, N.K. Banda, V.M. Holers, L. Wu, S.M. Moghimi, D. Simberg, ACS Nano, 9 (2015) 10758-10768.
[76] D. Simberg, Nanomedicine (Lond), 11 (2016) 741-743.

Chapter 2

2.1 Aim of the thesis

Despite the everyday progresses of medicine solutions for human health, the development of new technologies to cure and prevent diseases such as cancer is still one of the biggest challenges for humanity. As presented in the introduction section nanotechnology is one of the best promises to develop new therapies in medicine. In the recent years, numerous nanomaterials have been explored for potential medical applications thanks to their properties. Compared to traditional diagnostic agents or drugs, nanomaterials can be engineered to improve and integrate multiple functions in a single system also to give the control of drugs release, being of hope for the building of a next generation therapy and imaging tools. However, still limited amounts of results are available on the biological responses and the possible toxic effects of nanomaterials. Moreover, independently from any specific purpose, a critical step for any translational application in medicine is represented by the assessment of nanomaterials safety and impact on the immune system. Following any type of exposures, nanomaterials immediately contact the organism immune cells. Hence the investigation of the immune cell reactions induced by nanomaterials is a milestone for the safe exploitation of these materials for therapeutic and diagnostic applications.

The present thesis (as summarized in **Scheme 1**) aim to provide new insights on the safety and immune impact of several types of nanomaterials, such as carbon based materials (carbon nanotubes and graphene), lipid nanocapsules and super paramagnetic iron oxide nanoparticles, analyzing their molecular impact into the heterogeneity of the immune cells exploiting also their possible biological applications in cancer therapy and imaging.

The summarized main objectives are:

1. The assessment of the immuno-activity of the above mentioned nanomaterials on several immune cell subpopulations such as: T and B Lymphocytes, Natural Killer cells, Monocytes and Dendritic Cells.

2. The classification of nanomaterials by the immune cell response with their physico-chemical correlation using also OMICS technology, to characterize by high-throughput methods the immunological impact of the different nanomaterials analyzed.

3. The assessment of new therapy and diagnostic applications of characterized nanomaterials, applying their intrinsic immune modulatory properties.

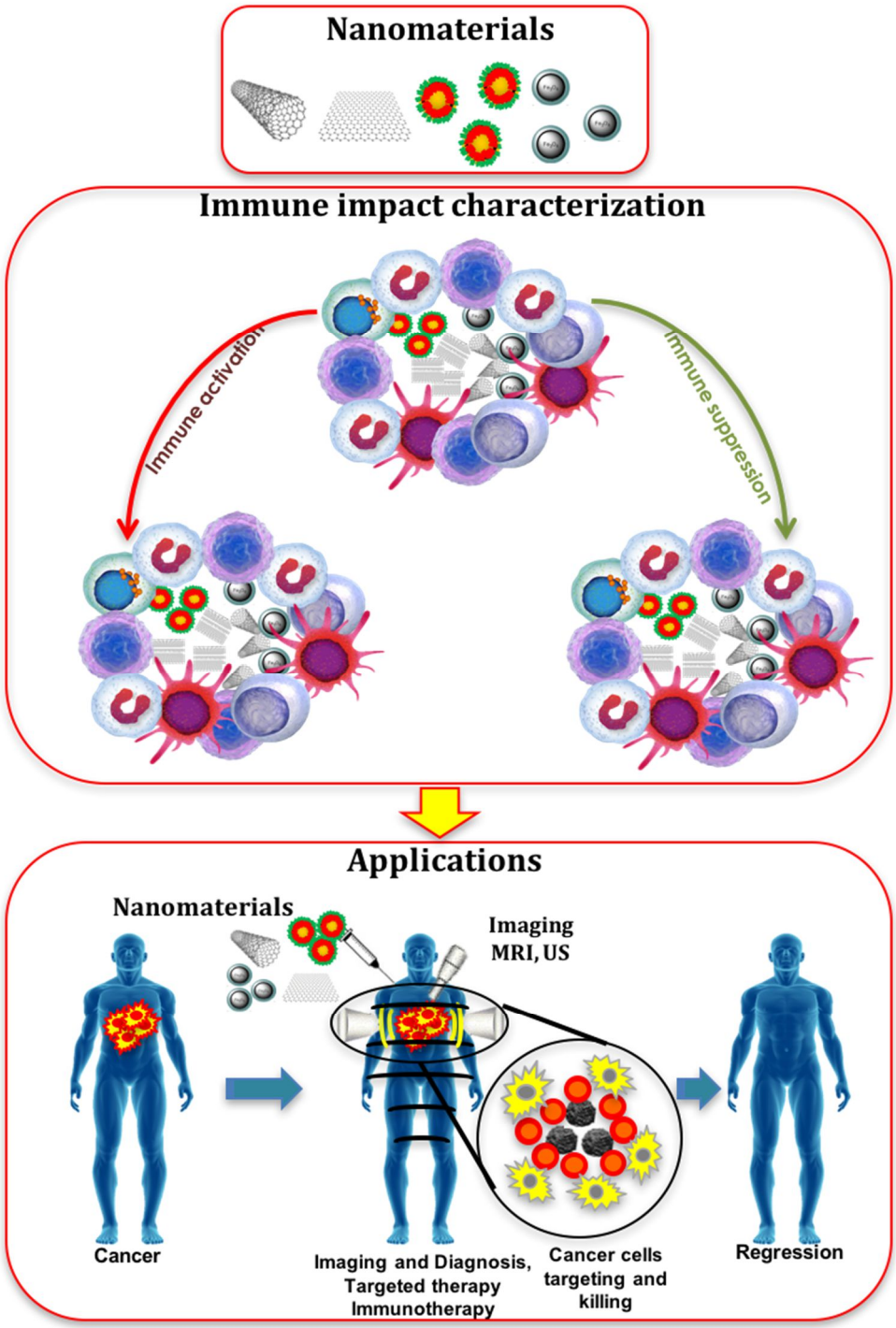

Scheme 1. Summary of thesis main objectives

Chapter 3

Brief summary of the presented results

In this thesis, the results are presented in six different papers according to the different nanomaterials used. A brief summary of the main results for each paper is presented below.

Paper I: In space, living organisms are confronted with two important factors: microgravity and cosmic radiation. A microgravity environment imparts to an object a lower acceleration compared to that produced by the Earth on its surface. It is well known that the constant influence of microgravity leads to several modifications of many physiological cellular processes, such as proliferation, differentiation, growth, signal transduction, cytoskeletal architecture, motility and gene expression. Moreover, immune cells are severely affected by microgravity, T lymphocyte functions were found altered in more than 50% of crewmembers in space. In a previous work my Ph.D. advisor and colleagues reported that functionalized multi-walled carbon nanotubes (f-MWCNTs) lead to an up-regulation of CD25 and CD69 marker expression in human primary immune cells, in particular in monocytes. In this study we wanted to evaluate the possibility of taking advantage of f-CNT immunostimulatory properties against spaceflight dysregulation of immune functions. Oxidation and functionalization of the nanotubes were performed with the ammonium groups and a fluorescent probe (FITC). First of all, we have seen with Transmission Electron Microscopy (TEM) that microgravity not affected the functionalization and the structure of f-CNTs. Moreover, flow cytometry and confocal microscopy analysis show a dose-dependent uptake of f-CNTs after 24h. Interestingly, we did not detect significant difference in the internalization under microgravity (0 x g). To evaluate the activating ability of f-CNTs to counteract spaceflight immune suppression, Peripheral Blood Mononuclear Cells (PBMC) were left untreated for 24 h or incubated with 50 µg/ml of f-CNTs in static controls and under microgravity conditions using a Random Positioning Machine (RPM). Lipopolysaccharides (LPS) and concanavalin A (ConA), due to their well-known activation properties, were used as positive controls for monocytes (CD14+) and T cells (CD3+) respectively. f-CNTs led to an increase expression of the activation marker CD25 on monocytes, both in static controls and under microgravity conditions. Instead, in microgravity we noticed a down-regulation of CD25 also in ConA treated samples due to the immune suppression as already reported. Interestingly, our results demonstrate that f-CNT together with

ConA counteract the down-regulation of CD25 due to the microgravity condition. We have seen indeed that nanotubes have a clear synergic effect with ConA both in static controls that in simulated microgravity. Cytokine analysis also confirm these data. Our experiments show that the effect of nanotubes appears to be particularly linked to an up-stimulation of the molecular effectors involved in the IL2 pathway. We assume that f-CNTs could promote the patching and capping of the ConA receptor. This action, together with IL2 pathway stimulation, can explain the synergic effect between f- CNTs and ConA in 0 x g. These preliminary findings open new perspectives on the capability of carbon nanotubes to act as immunomodulators proving this property by fighting immune function dysregulation under microgravity conditions, especially for T lymphocytes. We aim at reinforcing the concept that functionalized carbon based materials such as carbon nanotubes are able to stimulate immune cells having very interesting broad future applications in immunotherapy as vaccine adjuvants and, with data shown, as possible fighters to contrast spaceflight immune cell dysregulation.

Paper II: In the last few years, there has been enormous interest in graphene oxide (GO) for its promises in medicine fated to change the known medical practice in many healthcare applications. To improve the knowledge about the immune impact of GO, this work look at the molecular effects of two types of thin graphene oxide sheets (GOs), different only in their lateral dimension, on primary human immune cell populations using a wide range of assays, including high throughput screenings. GOs were thoroughly characterized by TEM, AFM, Raman spectroscopy and several other techniques to determine the specific lateral dimensions, number of graphene layers, and surface properties of each GO used. PBMCs from healthy donors were used, being a pool of immune cells that provide a closer insight to real *in vivo* conditions in humans, better than isolated sub-populations. The extent of early and late apoptosis, necrosis, cell activation, cytokine release were determined following exposure to the GO materials. Moreover, the impact on 84 genes related to innate and adaptive immune responses were analyzed. Lastly, whole genome analysis was conducted on T lymphocytes (Jurkat cells) and monocytes (THP1 cells). Both GOs used at increasing concentration form 25 to 75μg ml^{-1} generally did not show significant reduction in cell viability. However, exposure to small GO sheets (100-500 nm) was found to have a more significant impact on immune cells compared to the large sized GO (1- 10μm). The pilot expression analysis of 84 gene evidenced the higher genes induction of small GO compared to the large GO, confirmed in the secretion of many cytokine such as: IL1β, IL1α, TNFα, and IL6. Microarray data confirmed the small GO impact on immune cells. Particularly the activation was underlined by the up regulation of genes such as CCL5 and the induction of the chemokine pathways such as CXCL10 ligand pathway and

CXCR3 receptor, that are commonly associated with inflammation, immune-mediated tumor rejection and pathogen clearance. Furthermore, also a significant switch on energy-dependent pathways was found. In this work we demonstrated that the distinct shape dimensions could regulate the nature of GO interactions with immune cells. These findings represent the first step of a comprehensive molecular-characterization of different sized GOs on immune cells impact giving crucial information for the design of graphene for the control of its biocompatibility; paving the foundations for future preclinical studies with well-designed GOs as i.e. immunotherapy tools or safety drug delivery platform.

Paper III: The rationale of this work was driven by the common hope of a nanotechnology translation into the everyday clinical practice. However, such dream has to face something that can make the difference for almost any successful bio-application: the potential impact on the complex system of blood immune cells. The understanding of the interactions between nanoparticles and immune cells is hindered by the scant implementation of high throughput technologies in nanotechnology. Recently, a novel tool for flow cytometry analysis has been developed, gaining leverage with the precision of mass spectrometry. The use of the technique termed single-cell mass cytometry provides the measurement of more than 40 simultaneous cellular parameters at a single-cell resolution. We propose, for the first time in the context of nanotechnology, a new analytical strategy able to dissect the immunological impact of nanomaterials, at the single-cell level. The analytical pipeline here reported encompass the immunological characterization of the most studied nanomaterial in the last years: graphene. Mass cytometry enables us to describe the immune cell interactions of thin graphene oxide (GO) flakes and GO functionalized by amino groups ($GONH_2$) on 15 cellular populations corresponding to 200 nodes of distinct but logically interconnected cell sub-populations. Together we performed whole-transcriptomic analysis (Illumina BeadArray) for functional and molecular characterization on human T-cells and monocytes as a representative for the adaptive and innate response. Our results emphasize the importance of the functionalization on enhancing the biocompatibility of GO-based nanomaterials. Notably, only the functionalized $GONH_2$ was able to induce a specific monocytoid dendritic cell and monocyte activation skewed toward a T helper 1/M1 response. The positive impact of $GONH_2$ on specific immune cells could serve as a starting point for the development of new nanoscale platforms in medicine as novel immunotherapy, vaccine carrier, or nanoadjuvant tools.

Paper IV: Nanotechnology and specifically nanomedicine could provide new tools for an effective treatment of several diseases such as cancer, not only by taking advantage of the ability to functionalize and target the nanomaterials but also of their possible intrinsic biological properties. In this work, we developed a new few-layer graphene (FLG) dispersions prepared

by a mechano-chemical approach employing melamine as the exfoliating agent of graphite. The biological impact of new FLG on multiple human immune primary cell population (T, B and Natural Killer lymphocyte, monocytes, macrophages and dendritic cells) looking at cell viability and cell activation using a wide range of analysis were explored. We found an intrinsic specific impact of FLG on cells belonging to the monocytic lineage (CD14 positive) showing neither toxic nor activation effects on the other immune cells. Thanks to this intrinsic biological property, we further explored the possible therapeutic application of FLG on neoplastic monocytes *ex vivo*, from acute myeloid leukemia and chronic myelomonocytic leukemia patients. Intriguingly we demonstrated the FLG unique ability to target and successfully boost the necrosis of monocytic cancer cells. Moreover, the comparison between FLG and a common chemotherapeutic drug (i.e. Etoposide) confirmed the specificity and higher toxicity of FLG on cancer cells, evidencing the absence of toxicity of other immune cell populations. The functionality in terms of viability and activation of the other immune cell populations was also not affected, suggesting the ability of our graphene to preserve the normal function of the immune system. We here showed, for the first time, the great intrinsic biological properties of graphene obtained by exfoliation from graphite and applied them in oncology research versus an aggressive form of blood cancer. As a further step, in the near future, we can imagine not only to use the specific effect of FLG to improve the cancer cell toxicity but also, thanks to its high surface area, to take advantage of the conjugation with other drugs to enhance cancer therapy.

Paper V: Following the necessity to understand the immunological fate of different nanomaterials. In this manuscript we wanted to deeply investigate the action of three differently coated lipid nanocapsules (NCs) on human PBMCs. Considering the wide variety of NC applications in biomedicine a possible immune response to this type of nanomaterials is a crucial issue to be addressed. To the best of our knowledge this is the first comprehensive study on bio and immune-compatibility comparison analysis of differently functionalized NCs with chitosan, pluronic and PEG, fully characterized. We analyzed the impact of three different functionalizations of NCs looking first at the hemolytic impact. We then focused on human PBMCs and subpopulations (T, B, NK cells and monocytes) from healthy donors. Uptake assays were performed to assess whether a specific coating could be more suitable for the cell internalization. We explored the possible necrosis, apoptosis and proliferation of PBMCs and subpopulations of T cells and monocytes, as representative of the adaptive and innate immune response after NC treatment. The functionality effect was tested looking at the cell diameter modification, at the expression of the most critical activation markers (CD25 and CD69) and at the production of a wide variety of cytokines. In this work we demonstrated that the NCs impact on the immune cells response is strictly dependent on their coating. All three coated NCs were

well internalized inside all immune cell populations studied. Intriguingly, Pluro-NCs were able to induce immunomodulation of innate immunity through a clear induction of monocyte activations. Chito-NCs instead, mediated the activation of monocytes and T helper response that give the whole enhancement of the immune response after treatment. All these actions are exclusive for Chito-NCs that in our screening resulted as good starting material for further studies in the context of vaccine delivery, immunotherapy and immunomodulation activities. On the contrary, PEG-NCs were completely inert for the population of immune cells analyzed opening their perspectives as inert drug carriers.

Paper VI: In this manuscript we deeply investigate the immune impact of novel cystine functionalized SPIONs (Cy-SPIONs) exploring also their potential as ultrasound contrast agents. SPIONs are deeply investigated for many biomedical applications such as imaging for diagnostic and therapeutic purposes. A good functionalization that can combine the imaging goals together with a good biocompatibility remains one of the challenge for particles translation into medical practice. In this work, we focused on a novel functionalization of SPION with cystine (Cy-SPIONs); cystine, indeed, is able to make SPION stable and dispersible in culture cell media being an aminoacid easily biosynthesized in humans. To prove their potential as biomedical tools, we first gave new insights into the biological and immune effects of Cy-SPIONs with a wide variety of standard and molecular assays to evaluate cytotoxicity, cell activation, cytokine release and the expression of 84 genes related to the immune response. A good immune biocompatibility of Cy-SPIONs on *ex vivo* primary immune cells as well as *in vitro* cell lines was found. Moreover, an interesting potential of Cy-SPIONs for *in vivo* studies was pointed out where the preferential route of administration is by intravenous injections, thus in contact with immune cells. Currently, many studies focus on the use of SPION on Magnetic Resonance Imaging (MRI), instead our study focused on ultrasonography, which is a safer, less expensive and common imaging technology. The good echogenic properties of Cy-SPIONs in water and in whole blood were shown both in a phantom vein and in a microfluidic device for bloodstream simulations. Moreover, we report no cell toxicity under Cy-SPION treatment together with ultrasound irradiation, giving new insight on the use of Cy-SPIONs as new ultrasound contrast agents.

Chapter 4: Results

Paper I: *Immunomodulatory properties of carbon nanotubes are able to compensate immune function dysregulation caused by microgravity conditions*

Claudia Crescio[a], Marco Orecchioni[b], Cécilia Ménard-Moyon[c], Francesco Sgarrella[b], Proto Pippia[a], Roberto Manetti[d], Alberto Bianco[c*] and Lucia Gemma Delogu[b*]

[a]Dipartimento di Scienze Biomediche, Università degli studi di Sassari, 07100 Sassari, Italy.
[b]Dipartimento di Chimica e Farmacia, Università degli Studi di Sassari, 07100 Sassari, Italy.
[c]CNRS, Institut de Biologie Moléculaire et Cellulaire, Laboratoire d'Immunopathologie et Chimie Thérapeutique, 67000 Strasbourg, France.
[d]Dipartimento di Medicina Clinica, Sperimentale e Oncologica Università degli Studi di Sassari, 07100 Sassari, Italy.

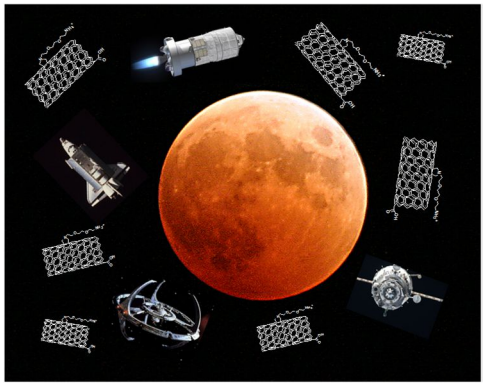

Published in:

Nanoscale

Nanoscale, 2014, 6, 9599

Abstract

Spaceflights lead to dysregulation of the immune cell functionality affecting the expression of activation markers and cytokine production. Short oxidized multi-walled carbon nanotubes functionalized by 1,3-dipolar cycloaddition have been reported to activate immune cells. In this Communication we have performed surface marker assays and multiplex ELISA on primary monocytes and T cells under microgravity. We have discovered that carbon nanotubes, through their immunostimulatory properties, are able to fight spaceflight immune system dysregulations.

Manuscript

Gravity is the force of attraction by which terrestrial bodies tend to fall toward the Earth. In space, living organisms are confronted with two important factors: microgravity and cosmic radiation. A microgravity environment imparts to an object a lower acceleration compared to that produced by Earth at its surface. Experiments conducted by American, Russian, and European investigators, in dedicated space missions as well as in simulations on Earth, have shown that mammalian cells are sensitive to gravitational changes.[1-8] It is well known that the constant influence of weightlessness leads to several modifications of many physiological cellular processes, such as proliferation, differentiation, growth, signal transduction, cytoskeletal architecture, motility and gene expression.[1-4] Moreover, immune cells are severely affected by microgravity.[5] T lymphocyte functions were found altered in more than 50% of crew members in space.[6] A severe inhibition of T cell activation in real and simulated microgravity conditions has been extensively demonstrated. Hashemi *et al.* reported a down regulation of CD25 and CD69 cell membrane activation markers in T cells after 24 hours of microgravity condition.[7] These findings were recently confirmed on US Astronauts onboard the Space Shuttle.[8] CD25 and CD69 are important markers in the T Cells mediate immune response. CD25 (alpha chain of the IL-2 receptor) is a late activation antigen. Activation mediated by the T-cell receptor (TCR) and costimulatory molecules induce an up-regulation of CD25 in T cells making them highly sensitive to IL-2. Whereas, CD69, member of the C-type lectin superfamily (Leu-23), is one of the earliest cell surface antigens expressed by T cells following activation.

We reported that functionalized multi-walled carbon nanotubes (*f*-MWCNTs) lead to an up-regulation of CD25 and CD69 markers expression in human primary immune cells, in particular in monocytes.[9] Very recently, through a whole genome wide study we proposed functionalized CNTs (*f*-CNTs) as immunomodulator systems showing their potential as immune activators [10]. We would like to highlight that in contrast to other types of CNTs, different in functionalization and shape investigated in immune cells,[9-12] we found that oxidized MWCNTs, further functionalized by 1,3-dipolar cycloaddition, can act as immunomodulators.[9] No data are present in literature regarding the interaction of CNTs and immune cells under microgravity conditions. Encouraged by our recent results, we wanted to evaluate the possibility of taking advantage of *f*-CNT immunostimulatory properties against spaceflight dysregulation of immune functions.

The high cost of experiments on board of spacecraft and space station facilities and the limited number of doubling experiments do not allow scientists to give continuity to the studies in real microgravity outside Earth. Currently, thanks to different and advanced facilities, it is possible to carry out studies in microgravity simulating in part the spaceflight conditions. In this work, a tridimensional clinostat or Random Positioning Machine (RPM) was used to simulate microgravity (M; 0xg) to evaluate if *f*-CNTs are able to compensate immune microgravity induced dysregulation. Static control cell cultures were installed in the basement of the RPM.

We first assessed the possible impact of microgravity on the functionalization of CNTs by transmission electron microscopy (TEM) and Kaiser test. To assess whether microgravity affect CNT uptake on primary human T cells and monocytes, we studied their internalization in microgravity by flow cytometry and confocal microscopy. Taking into consideration the results reported on activation markers by Hashemi *et al.*,[7] we then focused on CD25 expression on monocytes and T cells through peripheral blood mononuclear cells (PBMCs) analysis and CD69, both on T cells present on PBMCs and isolated T lymphocytes, T-helper cells (CD4+) and cytotoxic T cells (CD8+). To gain a larger picture about CNT effect on immune microgravity dysregulation, we also performed a multiplex cytokine assay on PBMCs (TNFα, IL6, IL10, IL13, IFNγ, IL2) and on isolated T lymphocytes (IFNγ, IL2).

By screening a series of functionalized carbon nanotubes, we previously obtained the major effect on immune activation treating human primary cells with oxidized MWCNTs subsequently functionalized by 1,3-dipolar cycloaddition of azomethine ylides.[9, 10] The present study was carried out with the same type of nanotubes in terms of functionalization and shape (**Fig. S1**). Characterization and functionalization methods of the MWCNTs has been previously

described by our group.[13] Kawanami *et al.* focused on the effect of microgravity on CNT synthesis,[14] but no data are reported in the literature about the possible impact of microgravity on *f*-CNTs. We first assessed by TEM and Kaiser test that MWCNTs (OX-MWCNT-NH_3^+) were not affected in their functionalization in microgravity. TEM images do not display differences in the morphology of the tubes under the microgravity (**Fig. 1**), while Kaiser test gave approximately the same values (within the uncertainty of this type of measurement) in term of amount of ammonium groups before (~40 µmol/g) and after (~50 µmol/g) treatment under microgravity. We previously showed a clear uptake on monocytes and T cells by the same type of nanotubes.[9]

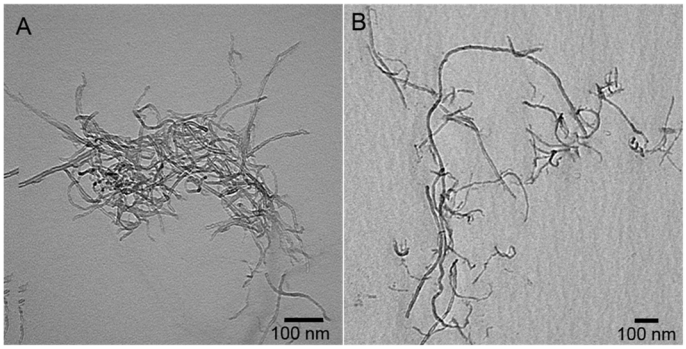

Figure 1. TEM images of OX-MWCNT-NH_3^+ before (A) and after microgravity treatment (B).

To make sure that the equivalent internalization can be possible under microgravity conditions, we used the same fluorescently labeled nanotubes (**Fig. S2**). As expected, data from flow cytometry showed a dose-dependent uptake of *f*-CNTs after 24 h. Interestingly, we did not detect significant difference in the internalization at 0xg (**Fig. S3A**). We confirmed our data at 100 µg/ml concentration for both the samples treated in static control or in microgravity by confocal microscopy (**Fig. S3B**). The absence of difference in cell uptake prompted us to go ahead in understanding the potential of carbon nanotubes to modulate the immune spaceflight effects. Cellular uptake results led us to choose a working concentration of 100 µg/ml of *f*-CNTs. We fixed the time of incubation at 24 h, the best time point to assess a possible immune response on primary human cells as used in the space mission and microgravity experiment on activation markers.[7]

To evaluate the ability of activator MWCNTs to counteract spaceflight immune suppression,[9] PBMCs were left untreated for 24 h or incubated with 100 µg/ml of OX-MWCNT-NH_3^+ in static controls and under microgravity conditions. Lipopolysaccharides (LPS) and concanavalin A (ConA), due to their well-known activation properties, were used as positive controls for

monocytes (CD14+) and T cells (CD3+) respectively (**Fig. 2**). In addition to our previous data obtained in static conditions,[9] we here tested a possible synergic action of *f*-CNTs in the presence of traditional activators (LPS or ConA + OX-MWCNT-NH_3^+ samples). We first performed a functionality assay on CD14+ monocytes focusing on CD25 marker (**Fig. 2A**). *f*-CNTs led to an increase of CD25 expression on monocytes, both in static controls and under microgravity conditions (M).

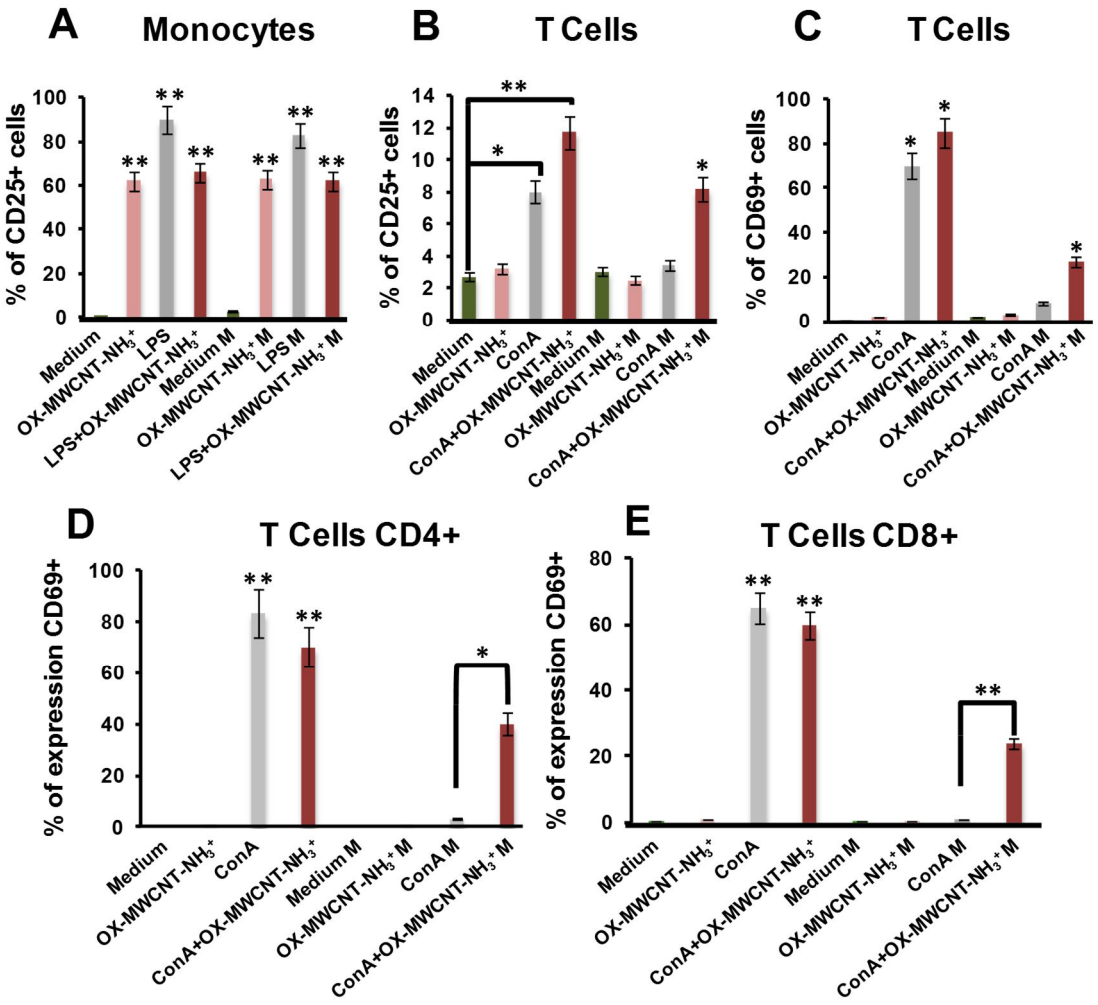

Figure 2. Activation marker assay. Microgravity (M) was compared with static controls. Peripheral blood mononuclear cells and isolated human T lymphocytes were left untreated (medium) for 24 h or incubated with 100 µg/ml OX-MWCNT-NH_3^+ alone or in the presence of cell activators (LPS or ConA). (A) Monocytes: CD25 expression was assessed by flow cytometry on CD14+ monocytes present on PBMCs. LPS (2 µg/ml) was used as positive control. (B and C) T cells: CD25 (B) and CD69 (C) expression was assessed by flow cytometry on CD3+ T cells present on PBMCs. ConA (10 µg/ml) was used as positive control. (D and E) Isolated T lymphocytes from PBMCs: staining for CD4+ (D) was performed to identify T-helper cell on isolated T lymphocytes; staining of CD8+ (E) was performed to identify cytotoxic T cells. Difference in statistical significance (Student's t-test) is indicated by * = $p < 0.05$ and ** = $p<0.01$. Bars indicate the compared samples under the different conditions; No-asterisk marked samples are compared to controls (medium).

This finding suggests that the ability of OX-MWCNT-NH_3^+ to act as monocyte activators [9, 10] is not affected by microgravity conditions. We then evaluated CD25 expression on CD3+ T lymphocytes (**Fig. 2B**). *f*-CNTs showed a synergic effect with ConA on CD25 expression in static controls. In microgravity we noticed a down-regulation of CD25 on ConA activated samples due the immune suppression as already reported.[7] Interestingly, in microgravity, samples treated with *f*-CNTs together with ConA did not show the down-regulation of CD25. Since it was also previously shown a down-regulation of CD69 early activation marker during clinorotation in spaceflight,[7] we decided to evaluate CD69 expression on T lymphocytes (**Fig. 2C**). Our results demonstrate again that *f*-CNTs have a clear synergic effect with ConA in static controls. The nanotubes counteract the down-regulation of CD69 due to the microgravity conditions. These findings show that the functional effect on T cells of *f*-CNTs in presence of ConA is not deeply affected by microgravity in comparison to the treatment with only this activator. It is well known that the activation of T cells by ConA is inhibited in 0xg condition. [17] Action of ConA on T cells is mediated by G protein that induce phospholipase C and then trigger the activation cascade of IL2. Patching and capping of ConA receptor are slightly retarded in microgravity. This action dramatically reduce the IL2 secretion therefore the T cell activation. [17]

To thoroughly evaluate CNT effect on CD69 expression in T cell in absence of other cells present in PBMCs, T lymphocytes were isolated and incubated for 24 h with 100 μg/ml of *f*-MWCNTs alone or in the presence of ConA, and compared to untreated control cells, CD4+ and CD8+ subpopulations were analyzed by flow cytometry (**Fig. 2D and 2E**). We confirmed that *f*-CNTs with ConA in both subpopulations are able to contrast the effect of microgravity. Moreover, these results clearly show that *f*-CNTs can act on T lymphocytes even in the absence of monocyte interactions.

The altered immune cell functionalities have been reported in different studies looking also to the cytokine production.[8, 15-19] Crucian *et al.* showed on Space Shuttle crew members that post-flight monocytes significantly reduced their production of IL-6, TNFα, and IL-10.[15] This reduction may impact overall immunocompetence. More recently, during the flight it has been shown a down-regulation of IFNγ, TNFα, IL10, IL4 and IL6 on whole blood sample of crew members after phorbol 12-myristate 13-acetate and ionomycin treatment.[8] The authors showed that a mitogenic stimulation led to a lower production of IFNγ and IL10, and to an up-regulation of TNFα and IL2.[8] Moreover, the strongly reduced T lymphocyte activation under spaceflight

conditions has been reported not only for CD25 marker but also for the production of IL2 after ConA stimulation.[17] To further confirm the ability of *f*-CNTs to act as immunomodulator systems and better investigate their interaction with immune cells under microgravity, we performed an assay on a wide range of cytokines. The samples were activated with ConA or left untreated in the presence of *f*-CNTs or without them. **Figure 3A** illustrates the cytokine production by multiplex ELISA on PBMCs supernatants. We confirmed the activator action of *f*-MWCNTs for the classical innate cytokines, TNFα and IL6, as previously reported,[9, 20] and we found the synergic effect of *f*-CNTs with ConA in static controls and under microgravity. Interestingly, in microgravity, also *f*-CNTs alone are able to up-regulate the IL6 production as they do in static controls. For the other investigated cytokines (IL10, IL13, IFNγ and IL2) we found that *f*-CNTs alone did not boost their production but they seem to act in concert with ConA potentiating its stimulation both in static controls and in 0xg conditions. To better understand the interaction of *f*-MWCNTs with T lymphocytes, the major population affected by microgravity, we assessed the release of two classical adaptive cytokines, IFNγ and IL2, on T isolated cell population (**Fig. 3B**).

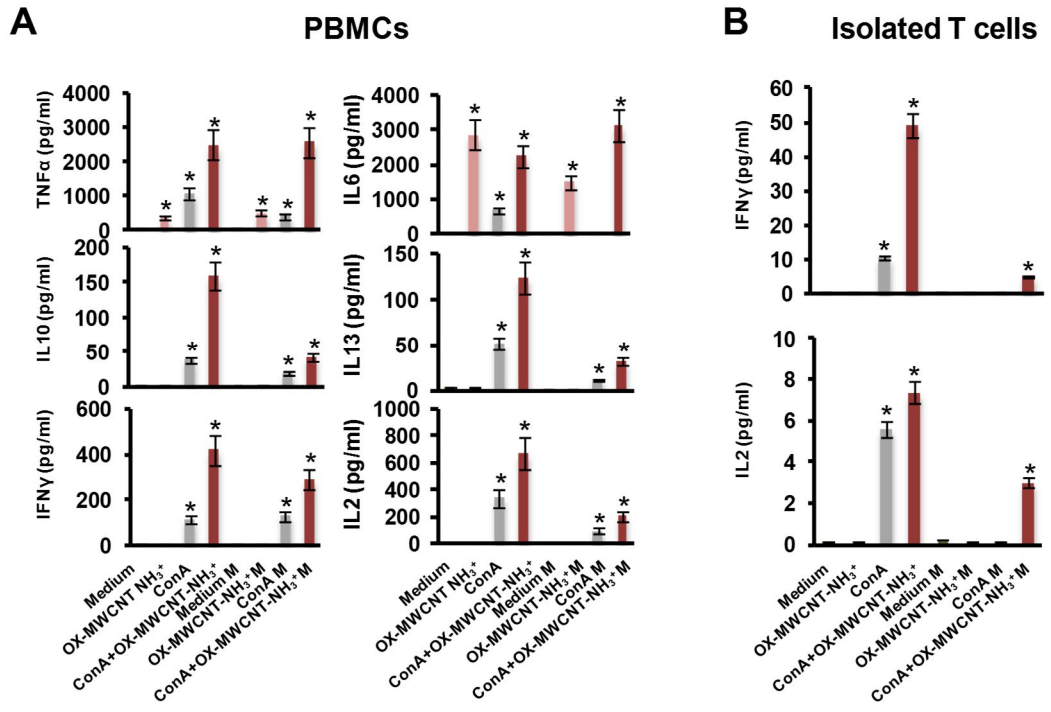

Figure 3. Cytokines secretion assay. Cytokine production was assessed by multiplex ELISA on PBMCs (A) and on isolated human T lymphocytes (B). Microgravity (M) were compared with static controls. Peripheral blood mononuclear cells and isolated T cells were left untreated (medium) for 24 h or incubated with 100 μg/ml MWCNTs, alone or in addition with 10 μg/ml ConA. Values are expressed in pg/ml. The statistical significance of differences between the samples versus medium controls was calculated by Student's t-test (*, $p<0.05$).

Cell functionality was inhibited by microgravity even in the presence of ConA stimulation. In static samples treated with ConA and nanotubes we found instead a statistically significant production of IFNγ and IL2 versus medium. Our experiments show that the effect of nanotubes appears to be particularly linked to an up-stimulation of the molecular effectors involved in IL2 pathway. We assume that *f*-CNTs could promote the patching and capping of ConA receptor; this action, together with IL2 pathway stimulation, can explain the synergic effect between *f*-CNTs and ConA in 0xg.

These findings, together with the surface marker data, open new perspectives on the capability of carbon nanotubes to act as immunomodulators proving this property by fighting immune function dysregulation in microgravity conditions, especially for T lymphocytes.

In conclusion, carbon nanotubes had attracted in the last years a huge interest from the scientific communities in a wide variety of biomedical applications.[21] Among other purposes, we and others focused on their possible relevance in biomedicine as drug carriers or contrast agents.[12, 13, 22, 23] Encouraged by our recent studies on functionalized carbon nanotubes we wanted to confirm the potential of specific functionalized carbon nanotubes as immunomodulators.[9, 10] NASA is working to achieve the goal of returning humans to Moon by 2020 and put footprints on Mars by 2024 (www.nasa.gov.html last access 12/12/2013). Even if this is a dreaming scenario for humanity, the immune system suppression related to spaceflight should be considered more thoroughly before taking in consideration long space voyages. In this context nanotechnology may bring additional help for the future of humans on space missions.[24] Based on the results of this study together with further future possible investigations, we can envision an immune system pretreatment of space crew members with functionalized CNTs intravenous administration. We aim at reinforcing the concept that functionalized carbon nanotubes are able to stimulate immune cells having very interesting broad future applications in immunotherapy, as vaccine adjuvants and, with data here shown, as possible fighter to contrast spaceflight immune cells dysregulation.

Acknowledgments

This work was partly supported by the Fondazione Banco di Sardegna (grant N° 186/2011.0484, 2013.1308 to L.G.D.), the University of Sassari (Italy), the Sardinia Region (grant N° CRP-59720 to L.G.D.), the "Gianfranco del Prete, doctor and scientist. The future: medicine, biology and nanotechnology Award" to L.G.D. A.B. wishes to thank the Centre National de la Recherche Scientifique, and the European Union Seventh Framework Programme FP7 (HEALTH-2007-201587, ANTICARB) program. L.G.D. wishes to thank Sardinia Region for supporting an Invited Professorship to A.B.

References

1. A. Guignandon, M. H. Lafage-Proust, Y. Usson, N. Laroche, A. Caillot-Augusseau, C. Alexandre and L. Vico, *FASEB J.*, 2001, 15, 2036-2038.

2. L. A. Cubano and M. L. Lewis, *J. Leukoc. Biol.*, 2001, 69, 755-761.

3. T. G. Hammond, F. C. Lewis, T. J. Goodwin, R. M. Linnehan, D. A. Wolf, K. P. Hire, W. C. Campbell, E. Benes, K. C. O'Reilly, R. K. Globus and J. H. Kaysen, *Nat. Med.*, 1999, 5, 359.

4. D. Ingber, *FASEB J*, 1999, 13 Suppl, S3-15.

5. N. Gueguinou, C. Huin-Schohn, M. Bascove, J. L. Bueb, E. Tschirhart, C. Legrand-Frossi and J. P. Frippiat, *J. Leukoc. Biol.*, 2009, 86, 1027-1038.

6. I. Walther, A. Cogoli, P. Pippia, M. A. Meloni, G. Cossu, M. Cogoli, M. Schwarzenberg, F. Turrini and F. Mannu, *Eur. J. Med. Res.*, 1999, 4, 361-363.

7. B. B. Hashemi, J. E. Penkala, C. Vens, H. Huls, M. Cubbage and C. F. Sams, *FASEB J.*, 1999, 13, 2071-2082.

8. B. Crucian, R. Stowe, S. Mehta, P. Uchakin, H. Quiriarte, D. Pierson and C. Sams, *J. Clin. Immunol.*, 2013, 33, 456-465.

9. L. G. Delogu, E. Venturelli, R. Manetti, G. A. Pinna, C. Carru, R. Madeddu, L. Murgia, F. Sgarrella, H. Dumortier and A. Bianco, *Nanomedicine (Lond)*, 2012, 7, 231-243.

10. M. Pescatori, D. Bedognetti, E. Venturelli, C. Menard-Moyon, C. Bernardini, E. Muresu, A. Piana, G. Maida, R. Manetti, F. Sgarrella, A. Bianco and L. G. Delogu, *Biomaterials*, 2013, 34, 4395-4403.

11. L. G. Delogu, S. M. Stanford, E. Santelli, A. Magrini, A. Bergamaschi, K. Motamedchaboki, N. Rosato, T. Mustelin, N. Bottini and M. Bottini, *J. Nanosci. Nanotechnol.*, 2010, 10, 5293-5301.

12. L. G. Delogu, A. Magrini, A. Bergamaschi, N. Rosato, M. I. Dawson, N. Bottini and M. Bottini, *Bioconjug. Chem.*, 2009, 20, 427-431.

13. L. G. Delogu, G. Vidili, E. Venturelli, C. Menard-Moyon, M. A. Zoroddu, G. Pilo, P. Nicolussi, C. Ligios, D. Bedognetti, F. Sgarrella, R. Manetti and A. Bianco, *Proc. Natl. Acad. Sci. USA*, 2012, 109, 16612-16617.

14. O. Kawanami and N. Sano, *Ann. N. Y. Acad. Sci.*, 2009, 1161, 494-499.

15. B. Crucian, R. Stowe, H. Quiriarte, D. Pierson and C. Sams, *Aviat. Space Environ. Med.*, 2011, 82, 857-862.

16. B. E. Crucian, R. P. Stowe, D. L. Pierson and C. F. Sams, *Aviat. Space Environ. Med.*, 2008, 79, 835-843.

17. I. Walther, P. Pippia, M. A. Meloni, F. Turrini, F. Mannu and A. Cogoli, *FEBS Lett.*, 1998, 436, 115-118.

18. S. K. Chapes, D. R. Morrison, J. A. Guikema, M. L. Lewis and B. S. Spooner, *Adv. Space Res.*, 1994, 14, 5-9.

19. G. Sonnenfeld, *Acta Astronaut.*, 1994, 33, 143-147.

20. H. Dumortier, S. Lacotte, G. Pastorin, R. Marega, W. Wu, D. Bonifazi, J. P. Briand, M. Prato, S. Muller and A. Bianco, *Nano Lett.*, 2006, 6, 1522-1528.

21. K. Kostarelos, A. Bianco and M. Prato, *Nat. Nanotechnol.*, 2009, 4, 627-633.

22. L. Meng, X. Zhang, Q. Lu, Z. Fei and P. J. Dyson, *Biomaterials*, 2012, 33, 1689-1698.

23. W. Wu, S. Wieckowski, G. Pastorin, M. Benincasa, C. Klumpp, J. P. Briand, R. Gennaro, M. Prato and A. Bianco, *Angew. Chem. Int. Ed.*, 2005, 44, 6358-6362.

24. A. Grattoni, E. Tasciotti, D. Fine, J. S. Fernandez-Moure, J. Sakamoto, Y. Hu, B. Weiner, M. Ferrari and S. Parazynski, *Aviat. Space Environ. Med.*, 2012, 83, 1025-1036.

Supporting Information

Material and Methods

Carbon nanotubes, TEM analysis and Kaiser test

Carbon nanotubes were obtained as purified material from Nanocyl (Sambreville, Belgium; Thin MWCNTs 95+% C purity, Nanocyl 3100®, batch n° 071119). The average diameter and length were 9.5 nm and 1.5 μm, respectively. Oxidation and functionalization of the nanotubes with the ammonium groups and a fluorescent probe (FITC) were performed as previously described.[1-3] The amount of ammonium groups per gram of nanotubes was assessed using Kaiser test as described in reference 1. CNTs were homogeneously dispersed at 1 mg/ml in sterile ultrapure water, then they were sonicated 45 min with a Branson 3200 water bath sonicator and vortexed for a few seconds. An additional sonication was performed for 15 min before each cell experiment.

Simulated microgravity conditions

Random Positioning Machine (RPM) is able to simulate microgravity very close to real spaceflight conditions (experiments carried out in space are from 1×10^{-6} to 1×10^{-4}xg, whereas the simulations with RPM are in the order of 1×10^{-3}xg). This apparatus has two rotating frames, driven by two separate motors. It rotates in such a way as to simulate weightlessness by removing the effects of gravity in any specific direction. As the rotation is autonomous and with random speeds and directions, it is termed Random Positioning Machine.

The Random Positioning Machine used in this work was developed by Fokker Space (Leiden, The Netherlands). It was located in a 37°C room and it was under the control of a computer with a dedicated program (RPM Control Software 14A, developed by Fokker Space, Leiden, The Netherlands). The rotation velocity of the frames was $60°xs^{-1}$. PBMCs and T lymphocytes were incubated under microgravity conditions for 24 h in 2.5 ml cryotubes (1×10^{6} cells/ml). Control cell cultures were installed in the basement of the RPM.

Cell cultures and isolation of human primary T lymphocytes

Experiments were performed using both PBMCs and isolated T lymphocytes. In both cases cells were obtained from informed healthy male donors (25-45 years old). At least three different donors were enrolled for each experiment. Cell separation was performed immediately

after blood withdrawing. PBMCs were isolated from fresh heparinized blood by FicollePaque PLUS (GE Healthcare) density gradient centrifugation. For each experiment, cells were suspended at the concentration of $1x10^6$/ml in fresh medium. Cell viability was evaluated through a Trypan Blue exclusion test and cells were maintained in RPMI 1640 and supplemented with 10% (v/v) heat-inactivated FBS, 20 mM HEPES, 10 ml/L penicillin/streptomycin at 37°C.

T lymphocytes were purified from PBMCs using high affinity CD3+ T-cell enrichment columns (R&D Systems, Minneapolis; MN). Columns allow purification of human T cells via high affinity negative selection. Total CD3+ cell recovery ranges between 37% and 54% and the purity of recovered cells ranges between 87% and 95%. Cell suspensions were stored for at least 12 h at 37°C to allow recovery from stress due to isolation procedure. Cells were suspended at the concentration of $1x10^6$/ml in fresh RPMI medium.

Uptake experiments

PBMCs were incubated in 2.5 ml cryotubes (1×10^6 cells/ml) with increasing amounts of OX-MWCNT-FITC (1, 10 and 100 μg/ml) for 24 h in microgravity or static conditions. Cells were then washed in phosphate buffered saline (PBS), centrifuged and stained with fluorochrome-conjugated monoclonal antibodies to identify major immune cell populations according to the expression of specific cell surface markers (clusters of differentiation [CD]). Phycoerythrin (PE)-, peridinin chlorophyll protein (PerCP)-, or allophycocyanin (APC)-conjugated anti-CD3 (SK7 clone), anti-CD14 (Mf9 clone), anti-CD25 (2A3 clone) were purchased from BD Biosciences (Mountain View, CA, USA). Flow cytometry measurements were performed using a FACSCalibur® (BD Biosciences). Ten-thousand and fifty-thousand events were collected.

Activation marker assays

Human primary cells were cultured in the presence or in the absence of *f*-MWCNTs, concanavalin A (ConA; 10 μg/ml) or bacterial endotoxin lipopolysaccharides (LPS; 1 μg/ml). ConA and LPS were purchased from Sigma-Aldrich. After 24 h incubation, cells were centrifuged and stained to identify immune cell populations of monocytes and T lymphocyte subpopulations and to analyze activation marker expression. Fluorescein isothiocyanate (FITC)-, phycoerythrin (PE)-, peridinin chlorophyll protein (PerCP)-, or allophycocyanin (APC)- conjugated anti-CD3 (SK7 clone), anti-CD14 (Mf9 clone), anti-CD69 (L78 clone), anti-

CD25 (2A3 clone), anti-CD4 (SK3 clone) and anti-CD8 (SK1 clone) were purchased from BD Biosciences (Mountain View, CA, USA). Staining was performed in the dark for 20 min. After washing, cells were then analyzed by flow cytometry.

Multiplex cytokine analysis

Cell culture supernatants from PBMCs and isolated T lymphocytes were used to quantify the production of cytokines using a MILLIPLEX MAP 5-plex Cytokine Kit (HCYTOMAG-60K - 05, Millipore, Billerica, MA), according to manufacturer's protocol. The following human cytokines were measured: TNFα, IL6, IL10, IL13, IFNγ and IL2. Briefly, supernatants were centrifuged for 10 min to remove debris and 25 ml were added to 25 ml of assay buffer. Then 25 ml of magnetic beads coated with specific antibodies were added to this solution and incubated for 2 h under shaking. At the end of the incubation, the plate was washed twice in buffer and incubated for 1 h with 25 ml of a secondary biotinylated antibody at room temperature. Then, the plate was incubated for 30 min with Streptavidine Phycoerythrin, washed twice, and incubated with 150 ml of sheath fluid for 5 min. The plate was observed immediately on a Luminex_ 100_/200_platform (Luminex Corporation) with xPONENT 3.1 software. Standard curves for each cytokine were generated (in duplicate) by using the supplied reference cytokine concentrations. Cytokine/chemokine concentrations in the samples were determined with a 5-parameter logistic curve. Final concentrations were calculated from the mean fluorescence intensity and expressed in pg/ml. The assay was performed in a 96-well plate, using all the assay components provided in the kit. All incubation steps were performed at room temperature and in the dark.

Statistical analysis

Statistical analyses were performed using Student's t-test. Data indicated with * and ** were considered statistically significant (p value *< 0.05; **<0.01). Data are presented as mean ± SD (n = 3). Incubations were performed in triplicate and experiments were carried out separately in cells from at least 3 different donors.

References

1. C. S. Samorì, R.; Ménard-Moyon, C.; Toma, F. M.; Venturelli, E.; Singh, P.; Ballestri, M.; Prato, M.; Bianco, A., *Carbon* 2011, 48, 2447-2454.

2. E. Venturelli, C. Fabbro, O. Chaloin, C. Menard-Moyon, C. R. Smulski, T. Da Ros, K. Kostarelos, M. Prato and A. Bianco, *Small*, 2011, 7, 2179-2187.

3. G. Pastorin, W. Wu, S. Wieckowski, J. P. Briand, K. Kostarelos, M. Prato and A. Bianco, *Chem. Commun. (Camb)*, 2006, 1182-1184.

Supporting figures

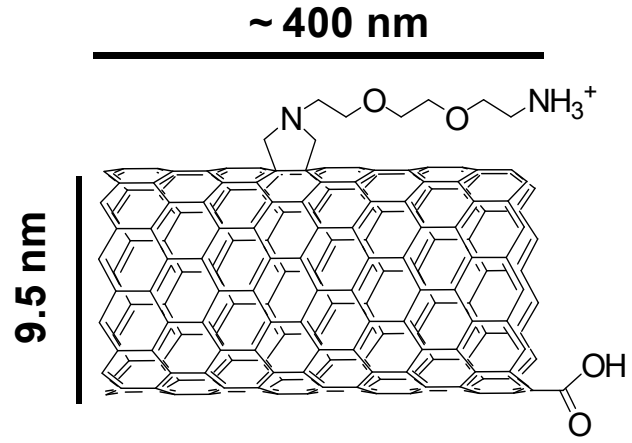

Figure S1. Structure of multi-walled carbon nanotubes functionalized by oxidation and 1,3-dipolar cycloaddition (OX-MWCNT-NH_3^+).

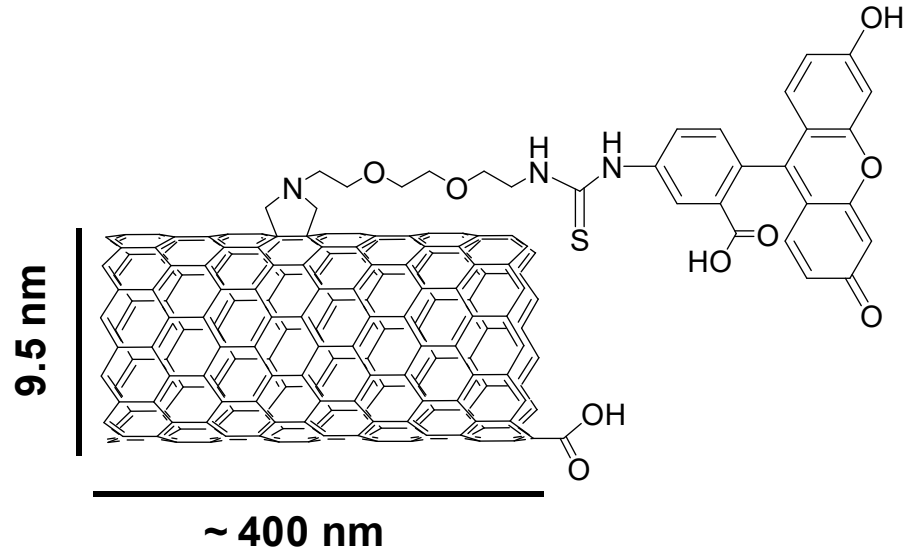

Figure S2. Structure of multi-walled carbon nanotubes functionalized with fluorescein isothiocyanate (OX-MWCNT-FITC).

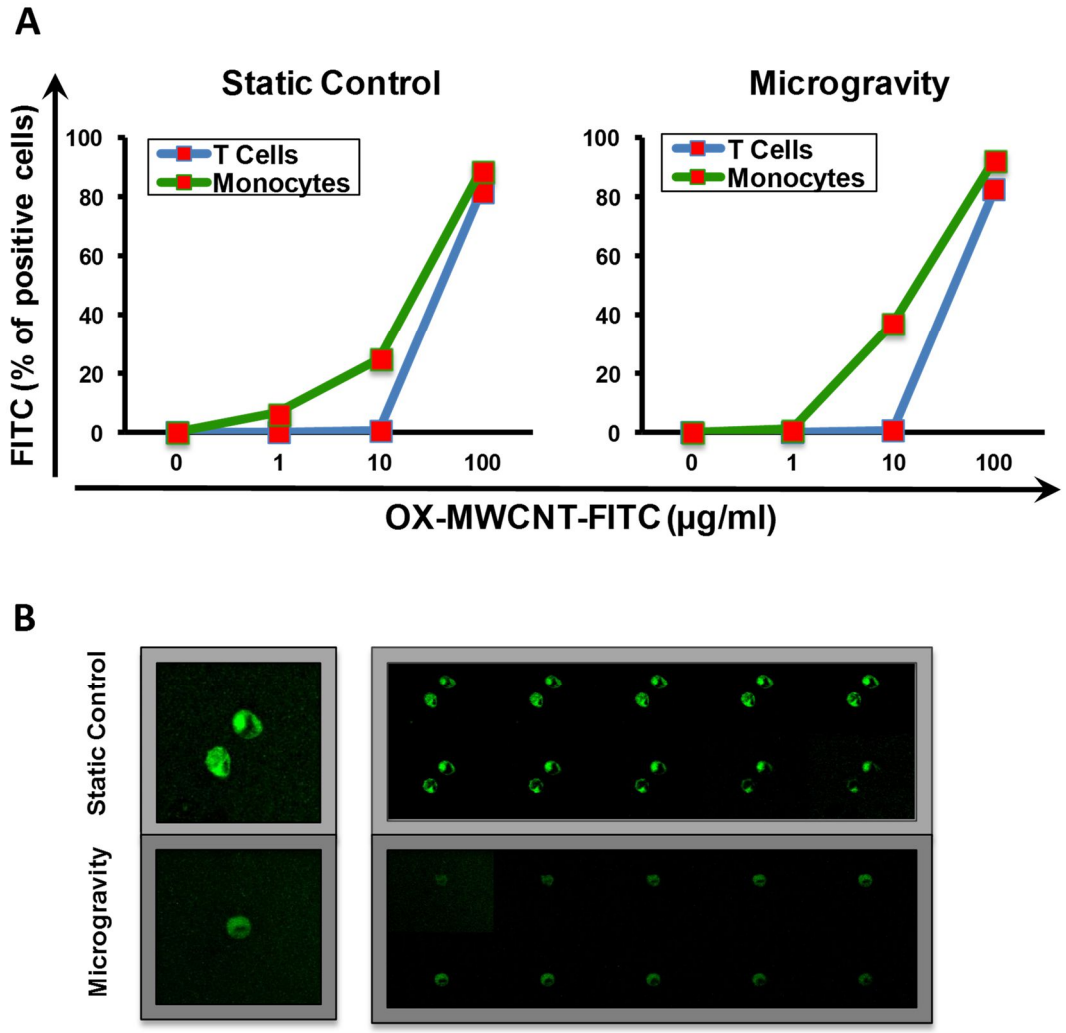

Figure S3. Uptake of OX-MWCNT-FITC by human primary immune cells. A) Peripheral blood mononuclear cells (PBMCs) were either left untreated or incubated for 24 h with 1, 10 and 100 µg/ml of OX-MWCNT-FITC. Uptake of increasing doses of fluorescent CNTs was investigated into T cells (CD3+) and monocytes (CD14+) after 24 h incubation in static controls on the left or in microgravity on the right. The highest uptake was detected at 100 µg/ml concentration in both cell types and conditions. B) *f*-CNT uptake was also assessed by confocal microscopy. PBMCs were incubated with 100 µg/ml of *f*-CNTs for 24 h and visualized by a Microradiance Nikon Eclipsa from Biorad (40 X). Microgravity conditions (bottom) were compared with static controls (top). Cells on left image are reported on the right as consecutive plans from the top to the bottom showing the presence of *f*-CNTs into the cytoplasm. Experiments were repeated three times with similar results.

Paper II: *Molecular and genomic impact of large and small lateral dimension graphene oxide sheets on human immune cells from healthy donors.*

Marco Orecchioni [1], Dhifaf Jasim [2], Mario Pescatori [1,3], Roberto Manetti [4], Claudio Fozza [5], Francesco Sgarrella [1], Davide Bedognetti [6], Alberto Bianco[7], Kostas Kostarelos[2] and Lucia Gemma Delogu [1*]*

[1] Department of Chemistry and Pharmacy University of Sassari, 07100 Sassari, Italy
[2] Nanomedicine Lab, Faculty of Medical & Human Sciences, The University of Manchester, Manchester M13 9PT, UK
[3] Heath-E-Solutions, Rotterdam, 3016 DL The Netherlands
[4] Department of Clinical Medicine and Experimental Oncology, University of Sassari, 07100 Sassari, Italy
[5] Department of Biomedical Science, University of Sassari, 07100 Sassari, Italy
[6] Research Branch, Sidra Medical & Research Centre, Doha, Qatar
[7] CNRS, Institut de Biologie Moléculaire et Cellulaire, Laboratoire d'Immunologie et Chimie Thérapeutiques, 67000 Strasbourg, France

Keywords: nanomedicine, immunotherapy, immunotoxicity, microarray, carbon nanomaterials

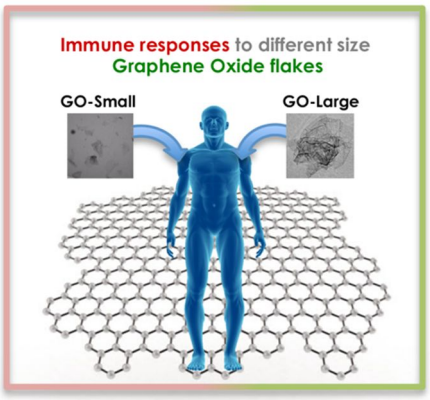

Published in:

ADVANCED HEALTHCARE MATERIALS

Adv. Healthcare Mater. 2016, 5, 276–287

Abstract

Graphene oxide (GO) is attracting great interest in biomedical sciences. The impact of GO on immune cells is one fundamental area of study that is often overlooked, but critical in terms of clinical translation. This work investigates the effects of two types of thoroughly characterized GO sheets, different in their lateral dimension, on human peripheral immune cells provided from healthy donors using a wide range of assays. After evaluation of cell viability, the gene expression was analyzed, following GO exposure on 84 genes relat- ed to innate and adaptive immune responses. Exposure to GO small sheets was found to have a more significant impact on immune cells compared to GO large sheets, reflected in the upregulation of critical genes implicated

in immune responses and the release of cytokines IL1β and TNFα. These findings were further confirmed by whole-genome microarray analysis of the impact of small GO sheets on T cells and monocytes. Activation in both cell types was underlined by the overexpression of genes such as CXCL10 and receptor CXCR3. Significant energy-dependent pathway modulation was identified. These findings can potentially pave the foundations for further design of graphene that can be used for immune modulation applications, for example in cancer immunotherapy.

Manuscript

Introduction

In the last few years, thanks to their remarkable characteristics and unique properties, there has been enormous interest in nanomaterials, including graphene [1], among the scientific community and the public [2]. Pristine graphene and graphene oxide (GO) have been used in a growing number of biomedical applications for therapy and diagnosis such as drug delivery and photodynamic therapy [3, 4]. Most studies have focused on GO [5], thanks to its ability to be well dispersible in aqueous media [6], but more systematic studies are needed urgently to fully explore graphene in medicine [7]. Most studies to date using intravenous administration (i.v.) have indicated accumulation of graphene-based materials (GBM) in organs of the reticuloendothelial system (RES), mainly liver, spleen and lungs [8, 9]. Immune cells will be the initial biological components that will interact with the GBM [10]. A recent study on GO *in vivo* biocompatibility indicated an inflammatory response typical of a foreign body reaction [11]. Wang K et al. i.e studied the toxicity of GO after injection on mice and found that GO at low (0.1 mg) and middle dose (0.25 mg) did not exhibit clear toxic effects to mice, while at high dose (0.4 mg) the authors evidenced chronic toxicity. In this contribution, the authors underlined the importance of further work on the possible mechanism of interaction between GO and immune cells in human body or mice [9].

Therefore, immunotoxicological evaluation is critical for most future clinical developments.

The interactions and potential modulation of the immune system by GBM exposure may also offer interesting possibilities for the development of immunotherapeutics or novel vaccination strategies [12, 13]. The impact exerted by GBM exposure is still controversial. Different studies report good biocompatibility and no cellular damage after exposure to GBM [14, 15], while others have evidenced cell toxicity, manifested as enhanced apoptosis and necrosis [16, 17]. Such reported discrepancies can be due to differences in the characteristics of GBM in terms of dimension, functionalization and purification.

The impact of well-characterized GO of different dimensions on human monocyte-derived macrophages (hMDM) has been reported [18]. However, in order to offer further understanding of the differential impact between large and small graphene flakes on the immune system, cell populations, other than macrophages, present in the systemic blood

compartment still need to be intensively investigated. Sasidharan et al. have considered the immune cell functionality besides biocompatibility, focusing on a few classic response parameters such as activation markers and cytokine production [19]. Although these approaches can elucidate the effect of GO flakes on the expression of some specific proteins, they are limited in their ability to provide a reliable insight into a global genomic effect that better reflects overall impact of exposure on the immune system. Our group previously described the effect of functionalized carbon nanotubes (*f*-CNTs) on immune cell activation [20, 21]. Moreover we and others underlined the importance of looking at the genomic level by using large genome expression analysis and high-throughput technologies to better understand the overall impact into immune cells [22, 23]. Recently, Chatterjee *et al.* used microarray analysis to investigate the effects on human liver cells of GO and reduced GO [24], but, to our knowledge, no report has used large genomic data approaches to investigate the impact of GO materials on immune cells.

In this work, we employed two types of thin GO flakes (between 1-2 graphene layers) thoroughly characterized by transmission electron microscopy (TEM), atomic force microscopy (AFM), Raman spectroscopy and several other techniques to determine lateral dimensions, number of graphene layers, and surface properties. Human peripheral blood mononuclear cells (PBMCs) from healthy donors were used. This pool of immune cell populations was able to provide closer relevance and insight to clinical conditions, rather than cell lines or specific sub-populations. The extent of early and late apoptosis, necrosis, cell activation, cytokine release were determined following exposure to the GO materials. The impact on 84 genes related to the immune response was then analyzed. Lastly, whole genome analysis was conducted on T lymphocytes (Jurkat cells) and monocytes (THP1 cells) as representative populations of the adaptive and innate immune responses.

Materials and Methods

Synthesis and characterization of graphene oxide

Graphene oxide (GO) was prepared by the modified Hummers' method in Ali-Boucetta et al. [7] with slight modifications. Briefly 0.2 g of graphite flakes (Barnwell, UK) was mixed with 0.1 g of NaNO3 (Sigma-Aldrich, UK) and 4.6 ml of 96% H2SO4 (Fisher Scientific, UK). After obtaining a homogenous mixture, 0.6 g KMnO4 (Sigma-Aldrich, UK) was then added slowly. Temperature was monitored carefully during the reaction and was kept between 98−100°C. The mixture was further diluted with 25 ml of deionized H2O and 3% H2O2 (Sigma-Aldrich, UK) was added gradually for the reduction of the residual KMnO4, MnO2 and Mn2O7. The resulting graphitic oxide suspension was exfoliated and purified by several centrifugation steps until the pH of the supernatant was around 7 and a viscous orange/brown layer of pure GO appeared on top of the oxidation by-products and thick graphitic pieces. This layer was seperated carefully and diluted in deionized water. TEM was performed using a BioTwin electron microscope (Philips/FEI), Tecnai 12 instrument operated at 120 kV accelerating voltage. A drop of sample was placed on a formvar / carbon coated copper grid. Excess material was removed by filter paper. Lateral size distributions were carried out using ImageJ software, after counting the lateral dimension of more than 100 individual GO sheets, from several TEM images. A multimode AFM was used on the tapping-mode with an E-type scanner, Nanoscope VI controller, Nanoscope v614r1 control software (Veeco, Cambridge, UK) and a silicon tapping tip (NSG01, NTI-Europe, Apeldoorn, The Netherlands) of 10 nm curvature radius, mounted on a tapping mode silicon cantilever with a typical resonance frequency 150 kHz and a force 14 constant of 5.5 N/m. Images were captured in air, by depositing 20µl of the GO dispersion on a freshly cleaved mica surface (Agar Scientific, Essex, UK) and allowed to adsorb for 30 seconds. Excess unbound material was removed by washing with filtered distilled water, and then allowed to dry in air. Thickness distributions were carried out using ImageJ software, after counting the height of approximately 100 individual GO sheets, from several AFM images. Fourier Transform Infrared Spectroscopy (FT-IR) at the mid-infrared range was carried out on dry samples using a PerkinElmer Spectrum 100 spectrophotometer and the transmittance results were analysed with the built-in spectrum software. Thermogravimetric analysis (TGA) we used a Pyris 6; Perkin-Elmer Ltd was used from 25 to 800◦ C at 10◦ C/ min. Samples (1-2 mg) were weighed into a ceramic crucible. Nitrogen (20 mL/min) was used as a purge gas. Electrophoretic mobility (µ) was measured by Malvern Zetasizer Nano ZS (UK) after dilution

of samples with water in disposable Zetasizer cuvettes (Malvern Instruments). Default instrument settings and automatic analysis were used for measurements, μ was converted automatically by the equipment software to zeta potential (ζ) values which is directly related to zeta potential by Henry's equation [25]. All values for samples prepared are triplicate measurements, values were mean ± SD. For Raman spectroscopy all samples were recorded after preparing the aqueous dispersions and drop casting them on glass slides and evaporating the solvent. Measurements were carried out using a 50x objective at 633 nm laser excitation using a Renishaw micro-Raman spectrometer. An average of at least three different locations within each sample was measured. Absorbance spectroscopy of samples was measured by a Varian Cary winUV 50 Bio-spectrophotometer, USA. Samples were diluted 100 times in water before measurement in a 1ml glass cuvette with 1 cm path length. Dual beam mode and baseline correction were used throughout the measurements to scan the peak wavelength and maximum absorbance between 200 and 800 nm.

Cell culture, viability and activation

Jurkat cells (T cell line), THP1 (Monocyte cell line) and peripheral blood mononuclear cells (PBMCs) were cultured as previously reported [22]. PBMCs were obtained from EDTA-venous blood samples from informed healthy male donors (25-50 years old) using a standard Ficoll-Paque (GE Healtcare) separation. Informed signed consent was obtained from all the donors. The cytotoxicity was evaluated by Flow cytometry (FACS Canto, BD Biosciences, Mountain View, CA, USA). PBMCs were incubated for 24 h. with increasing doses of GO-S and GO-L (25, 50 and 75 μg ml^{-1}). Ethanol was used as a positive control, while samples incubated with cell medium alone was used as negative control. All staining kits were purchased from Invitrogen, CA, USA: Annexin-V FITC (apoptosis), LIVE/DEAD FITC (late apoptosis and necrosis), propidium iodide (necrosis). PBMCs were treated with GO at the intermediate concentration of 50 μg ml^{-1} and stained to identify immune cell populations and activation markers, CD25 and CD69 (APC-conjugated anti-CD25, 2A3 clone, PE-conjugated anti-CD69, L78 clone, BD-Bioscience Mountain View, CA, USA). Concanavalin A (ConA, 4 μg/ml) and lipopolysaccharides (LPS, 2 μg/ml) were used as positive controls (Sigma-Aldrich, St. Louis, Missouri, USA). Staining with fluorochrome-conjugated monoclonal antibodies was performed in the dark for 20 min. Cells were analyzed by flow cytometry.

Immune gene array, cytokine assay, microarrays.

Total RNA was extracted and RNA purification was performed with TriZol Reagent (TriZol, Invitrogen, Carlsbad, CA, USA). After extraction, cDNA synthesis was performed using a SuperScript III reverse transcriptase (Invitrogen, Carlsbad, CA, USA). The expression of 84 immune response genes were performed with a RT2 Profiler PCR Array (PAHS-052ZD, Superarray Bioscience Corporation, Frederick, MD), (instrument CFX96 Bio-Rad). Cell culture supernatants from PBMCs were used to quantify the secretion of cytokines using a MILLIPLEX MAP 10-plex Cytokine Kit (HCYTOMAG-60K -10, Millipore, Billerica, MA) (IL1α, IL1β, IL2, TNFα, IFNγ, IL6, IL8, IL10, IL4, Rantes). Experiments and statistical analysis were performed as previously showed [22]. Total RNA was extracted and purified using the RNAeasy mini kit (Qiagen, Valencia, CA, USA). RNA purity was assessed by spectrophotometric analysis and integrity by microfluidic molecular sizing using the Bioanalyzer 2100 (Agilent). Samples with RIN (RNA Integrity Number) less than 8 were discarded. RNA (1 μg) was converted in cRNA and labeled (Illumina totalPrep RNA amplification kit, Ambion). Biotinylated cRNA was hybridized onto the Illumina HumanHT-12 v4 (Illumina, Inc., San Diego, CA, U.S.A.). The Illumina HumanHT-12 v4 interrogates the expression of 47.000 gene probes derived from the National Center for Biotechnology Information (NCBI) Reference Sequence RefSeq Release 38 (November 7, 2009) and other sources. Probe intensity and gene expression data were generated using the Illumina GenomeStudio software V2011.1 (Gene Expression Module V1.9.0).

Statistical analysis.

Statistical analyses for Raman ID/IG and D band width were performed using Student's t-test (two-side p value < 0.05). Data for Raman analysis and zeta potential are presented as mean ± SD. Data analysis for flow cytometry was performed using FACSDiva software (BD-Bioscience Mountain View, CA, USA). All the experiments were performed at least in triplicate. Statistical analyses for multiple cytokine assays were performed using Student's t-test. Data indicated with a star were considered statistically significant (two-side p value <0.05). Data are presented as mean ± SD. Multiplex ELISA tests on isolated human primary PMBCs were performed in samples from at least 3 different donors. Immune gene array data were analyzed by the comparative threshold cycle (CT) method. Relative quantification of gene expression using the $2^{-\Delta\Delta Ct}$ method correlated with the absolute gene quantification obtained

using a standard curve. Data were analyzed with RT2 profiler PCR array data analysis software (http://pcrdataanalysis.sabiosciences.com/pcr/arrayanalysis.php). Whole genome expression measurements were extracted and normalized using the Illumina Genome Studio software V2011.1 (Gene Expression Module V1.9.0). The same software was used for QC analysis of the Beadchips. Statistical analysis and visualization of gene expression data were performed using BRBArrayTools, developed by R. Simon and the BRBArrayTools Development Team (http://linus.nci.nih.gov/BRB-ArrayTools.html). We identified genes that were differentially expressed among the two classes by using a multivariate permutation test [26]. We used the multivariate permutation test to provide 80% confidence that the proportion of false discoveries did not exceed 5%. The test statistics used are random variance t-statistics for each gene [27]. Although t-statistics were used, the multivariate permutation test is non-parametric and does not require the assumption of Gaussian distributions.

We identified gene ontology (gene on.) groups of genes whose expression was differentially regulated among the classes. This analysis is different than annotating a gene list using gene on. categories. For each gene on. group we computed the number n of genes represented on the microarray in that group, and the statistical significance P value for each gene in the group. These P values reflect differential expression among classes and were computed based on random variance t-tests or F-tests. For a gene on. group, two statistics are computed that summarize the p values for genes in the group; the Fisher (LS) statistic and the Kolmogorov-Smirnov (KS) statistic as described in (Simon R and Lam A. BRB-ArrayTools User Guide, version 3.2. Biometric Research Branch, National Cancer Institute; http://linus.nci.nih.gov/brb). Samples of n genes are randomly selected from genes represented on the array and the summary statistic computed for those random samples. The significance level associated with the gene on. category is the proportion of the random samples giving as large a value of the summary statistic as in the actual n genes of the gene on. category. For each gene on. category, two significance levels are computed, corresponding to the two summary statistics. We considered a gen. on. category significantly differentially regulated if either significance level was less than 0.01. We considered all gene on. categories with between 5 and 100 genes represented on the array. Some of the categories were overlapping. We also uploaded the gene expression data to the “ingenuity Pathway analysis” (ipa) to visualize the expression levels of genes in relevant pathway charts.

Results

Graphene Oxide (GO) material characteristics

Structural characterization using TEM and AFM imaging techniques of small GO sheets (GO-S) and large GO (GO-L) is shown in **Fig.1A** and **Supporting Fig. S1A-D**. The lateral size distribution is shown in **Fig. 1B** for both GO-S (100-500nm) and GO-L (1-10µm) determined from analysis of several TEM images. AFM height images revealed that the sheets were 1 or 2 layers thick (1-2 nm). Thickness distribution for GO-S is shown in **S. Fig. 1E**, however for GO-L it were proven technically more challenging to obtain accurate thickness distributions due to folding and wrinkling that commonly distorted measurements. Despite that, in the few GO-L sheets accurately measured, thickness between 1-2nm was observed. FT-IR was used to identify the functional groups on the surface of GO (**Fig. 1E**). Both GO samples showed a broad band around 3100-3600 cm^{-1} due to the O-H stretching vibrations, and an intense peak at 1730 cm^{-1} for the C=O stretching vibrations. Aromatic and unsaturated bonds were apparent by the intense band at 1590 cm^{-1} and the broad band around 3000 – 3100 cm^{-1}. Several bands were detected around 1000-1070 cm^{-1} for the epoxy (C-O-C) symmetric stretching vibrations [28]. FT-IR spectra confirmed that the oxidation resulted in the formation of hydroxyl, carboxyl and oxide groups with the presence of aromatic regions, typical of GO materials [29], with very little differences between the two types of GO (the starting graphite material did not show any distinct peaks in the FT-IR spectrum).

Quantification of the functional groups was also correlated by thermogravimetry (TGA) (**Fig. 1F**)**.** TGA curves for the two GO materials and the starting graphite were obtained. Two main weight loss steps were observed after subtracting 10% due to evaporation of the water content up to 100ºC (**S. Tab. 1**). The first mass loss in the TGA curves between 100 and 260ºC was due to the decomposition of the labile oxygen groups (such as carboxylic and aldehyde groups) and the removal of any residual water. The second weight loss occurred between 260 and 460ºC and was due to the pyrolysis of the stable oxygen groups (mainly epoxides) [30]. No significant differences in the TGA melting curves were detected between GO-S and GO-L material. However, they were both significantly higher than graphite, which further confirmed their extensive surface oxidation. Raman spectra (**Fig. 1G**) indicated bond stretching of sp^2 hybridized carbon atoms resulted in the distinct Raman G band around 1590 cm^{-1} [31] in all samples. This band appeared wider and slightly blue shifted in both GO samples compared to

graphite. The D band at 1330 cm^{-1} due to disorder [32] created during oxidation was more distinct in the GO samples, while the 2D band near 2700 cm^{-1} disappeared, compared to the starting graphite. The D-to-G band intensity ratio (I_D/I_G), corresponding to a disorder metric [31] is also shown for each spectra (**Fig. 1G**). No statistical significance (using *Student's t-test*) was detected between the two GO samples (GO-S and GO-L) in both I_D/I_G ratio and also in the D band width, however both were significantly different than the starting graphite.

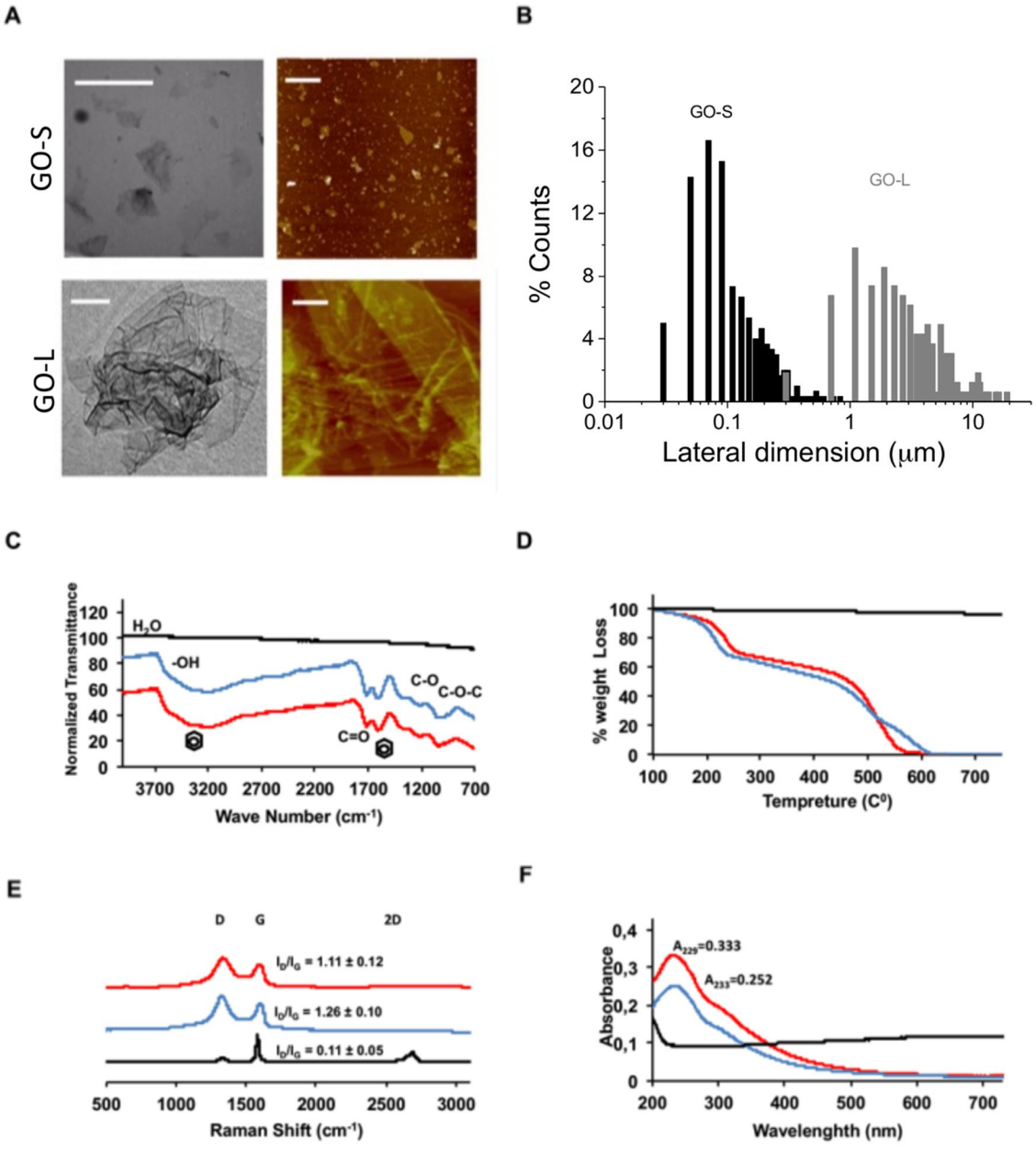

Figure 1. Physicochemical characterization of GO-S and GO-L. (A) Representative TEM images (left) and AFM images (right) of GO-S and GO-L (all scale bars are 1.5μm); (B) Size distribution detected by counting more than 100 GO sheets from several TEM images of GO-S and GO-L; (C-F) FT-IR spectra, TGA curves, Raman and UV-visible spectra respectively, for GO-S (red) and GO-L (blue) compared to the starting graphite (black).

In terms of surface charge, both GO samples were strongly negative, due to the multiple surface oxygen groups (S. **Fig. 1F**), but GO-L was of slightly higher negativity compared to GO-S. UV-Visible spectroscopy was then used to confirm the optical properties of the GO structures. Both GO samples showed a characteristic absorbance peak around 230 nm, with a shoulder around 300 nm with slight difference between the two samples, while graphite had featureless spectrum with high scattering due to the poor aqueous solubility (**Fig. 1H**). Such absorbance peaks have been described to arise from the delocalization of the π electrons due to the oxidation process, the 230nm peak due to C-C transitions, while that at 300nm due to C=O transitions [33].

Cell viability and activation markers

The first step in the interaction with immune cells was to study the impact in dose response of the two GO materials on cellular viability of PBMCs from healthy donors (**Fig.2**). Different staining for FACS were performed to detect: i) early apoptosis, ii) late apoptosis, iii) necrosis. AnnexinV staining showed the absence of a significant number of early apoptotic cells in treated samples at all tested GO concentrations (**Fig.2A**). An amine-reactive fluorescent staining was used to detect cells with compromised membranes (late apoptotic and necrotic cells) (**Fig.2B**).

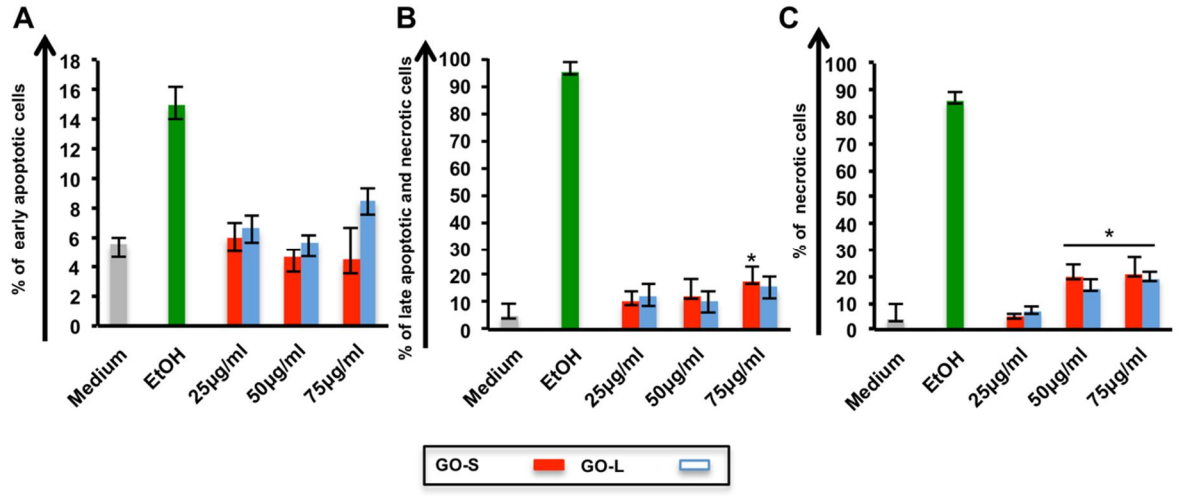

Figure 2. Viability of human primary immune cells. PBMCs were incubated for 24 hours with GO-S and GO-L at increasing doses of 25, 50, and 75 µg ml^{-1} or left untreated (medium), ethanol was used a positive control. (A) Early apoptosis was assessed by Annexin V staining. (B) Data from staining with an amine-fluorescent dye able react with amine free of compromised membranes of late apoptotic and necrotic cells. (C) To detect necrotic cells, propidium iodide staining was performed. Experiments were performed at least in triplicate and analyzed by flow cytometry; (* = P value <0,05).

The materials did not show significant cell toxicity. The only exception was a reduction in cell viability at high doses (75 μg ml^{-1}) for GO-S. The percentage of dead cells was then evaluated by propidium iodide staining (**Fig.2C**). Cell viability at exposures of 25 μg ml^{-1} GO was similar to controls, whereas at GO concentrations of 50 and 75 μg ml^{-1} PBMCs displayed mortality levels ranging between 15% and 20%, a statistically significant value when compared to the controls, but still very low in relation to the positive controls (**Fig. 2**). To investigate the functional impact of GO exposure on primary immune cells, considering their activation as a crucial endpoint, we measured the expression of CD69 and CD25 markers (**S. Fig. 2**). CD69, a member of the C-type lectin superfamily (Leu-23), is one of the earliest cell surface antigens expressed by immune cells following activation, while CD25 (alpha chain of the IL-2 receptor) is a late activation antigen. CD69 and CD25 expression in GO-exposed samples was comparable to the untreated negative controls (**S. Fig. 2**).

Immune gene expression array

To evaluate the possible effect on key pathways controlling innate and adaptive immune response, we performed a deep genomic analysis on the expression of a large number of highly selected immune genes (**Fig. 3**). The impact on GO-L or GO-S treated PBMCs was assessed by a 84 immune genes array. As a first step, the expression ratio between GO-L or GO-S and control samples for all 84 genes were clustered and displayed as heat map where individual elements of the plot are colored according to their standardized expression values (**Fig.3A**; red squares= up-regulated genes; green squares= down-regulated genes). The major impact on gene expression due to GO-S exposure was apparent when compared to the values obtained for GO-L (heat map values and gene names are reported in the **S. Fig. 3**). To better illustrate the different effects between GOs on the gene expression, the standardized expression values of modulated genes are also displayed as a heat-map detail in the **Fig. 3A** for the control, GO-S and GO-L samples, respectively (**Fig.3B**; red squares= high expression; green squares= low expression). The bright red strip marks indicate the enhanced effects of GO-S compared to GO-L. All genes reported in **Fig.3B** were up-regulated in GO-S, while GO-L samples displayed values similar to the untreated controls. By using a fold regulation cutoff (FR>4, both directions) we identified 16 up-regulated genes for GO-S and 5 up-regulated genes for GO-L (**Fig. 3C and 3D**).

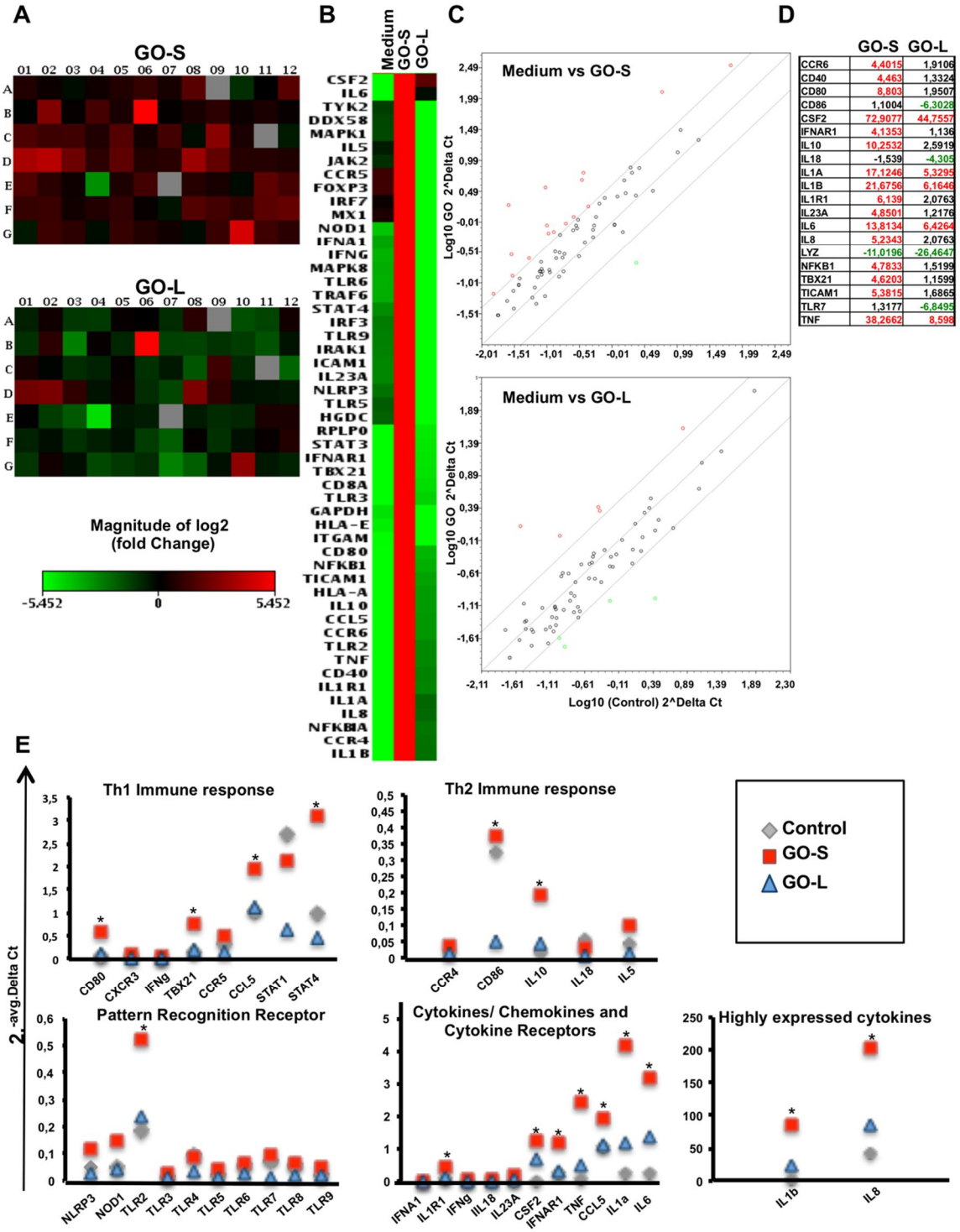

Figure 3. Immune gene expression array. A) Heatmap comparison of 84 genes after exposure to GO-S or GO-L. Genes were displayed for fold-change variations in respect to the controls and colored by their standardized expression value (Red= high expression, green= low expression). B) Heat map detail showing the immune transcript upregulated by GO-S in PBMCs; data are reported as mean of experiments carried out in triplicate. C) Scatter Plots chart. Genes upregulated with fold change greater than 4 are showed with red round, gene with fold change less than 4 are showed with green round; in black unmodulated genes. D) Table of modulate genes in GO-S e GO-L versus control. Red show genes with a fold change greater than 4, green show genes with a fold regulation less than 4. E) Analysis of representative GO-S and GO-L modulated genes, summarized into their own pathways expressed as 2 Δct values (* P value <0,05).

Moreover, we found that GO-L was able to induce down-regulation of 4 immune genes compared to only 1 of GO-S with a fold change minor than 4 (**Fig. 3C and 3D**). Most modulated genes were up-regulated compared to control samples, as it can also be more easily observed in the scatter-plot shown in **Fig.3C**. Some of the genes that offered a statistically significant difference in expression were: CSF2, TNF, IL6, IL10, CD80, IL1, IL1R1, TICAM1, IL8, IL23A, NFKB1, TBX21, CD40, CCR6 and IFNAR1. All of them were up-regulated at least 4-fold in GO-S treated samples. A list of all the modulated genes by GO-S and GO-L exposure, in terms of at least a 4-fold down or up regulated, is displayed in **Fig. 3D**. To better understand the involvement of specific pathways in the possible immune system modulation process triggered by GOs, we looked at the expression of specific groups of genes involved in controlling precise signaling aspects of the immune response (**Fig. 3E**). By looking at the RNA expression levels as $2^{-avg.\Delta Ct}$ values, we queried several pathways including Th1 and Th2 immune response, pattern recognition receptor (in particular toll-like receptors), cytokines/chemokines and cytokine receptors. We observed that following GO-S treatment, a marked up-regulation of genes involved in the Th1 immune response such as CD80 and TBX21 occurred (**Fig. 3E**). Regarding the toll-like receptor (TRL) pathways, TLR3, TLR5 and TLR9 showed a fold regulation greater than 2 (**S. Fig. 4**). The most regulated was TLR2 by GO-S (*p-value <0.05*) (**Fig. 3E**). Cytokines/Chemokines and cytokine receptors up regulated by GO-S (*p-value <0.05*) were: IL1R1, IFNAR1, CSF2, TNF, CCL5, IL6, IL1α, IL1β and IL8.

Cytokine secretion assay

To investigate the cytokine production, multiplex ELISA was used to measure IL1β, TNFα, IL10, IL6, IL8, IL2, IFNγ, IL4 and CCL5 (**Fig. 4**). Both types of GO were able to stimulate the release of some of the cytokines analyzed such as IL1β, IL1α, TNFα and IL10 (*p-value < 0.05*). The production of IL1β, TNFα, IL10 was significantly induced by GO-S exposure (**Fig.4A**). IL6 and IL8 increased equally following treatment with either types of GO (**Fig.4B**). On the other hand, IL2, IFNγ, IL4 and CCL5 production were not stimulated by either GOs (**Fig.4C**).

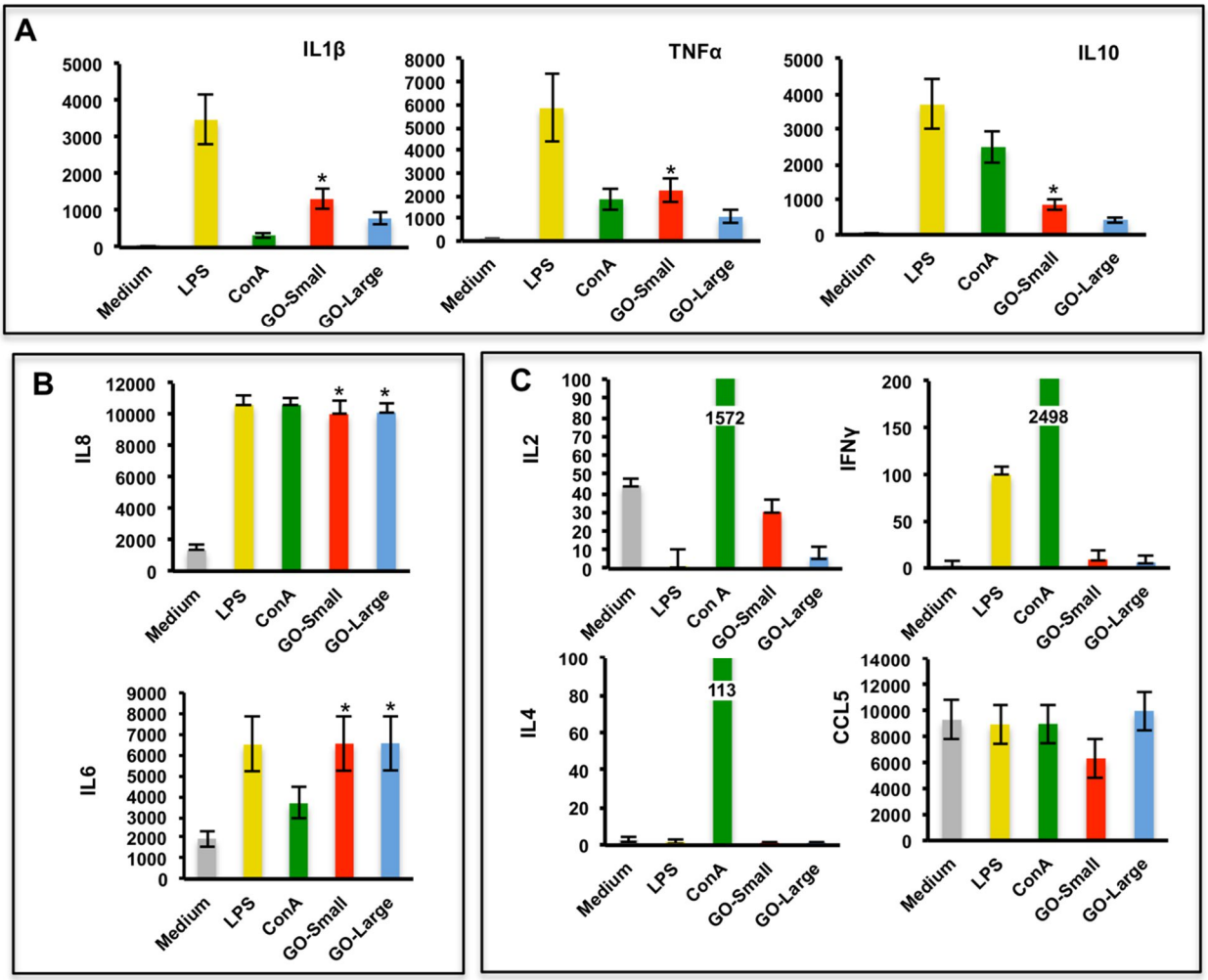

Figure 4. Cytokine secretion assay. Cytokine release was assessed by ELISA on PBMCs. Cells were incubated with GO-S and GO-L at 50 µg ml-1 . After 24h the supernatants were collected and analyzed for the secretion (expressed in pg/ml) of the following cytokines and chemokines: A) ILβ, TNFα, IL10; B) IL8, IL6; C) IL2, IL4, IFNγ, CCL5.

Whole genome expression analysis

Since a significant impact from GO-S exposure was revealed in terms of immune-related gene and protein up-regulation, we wanted to further investigate the effects on whole-genome expression at a higher definition. To achieve this goal we used the microarray approach (Illumina Beadchip technology) looking at more than 47000 genes on GO-S treated T lymphocyte cell line (Jurkat cells) and monocyte cell line (THP1 cells). Unsupervised Multi-Dimensional Scaling (MDS) identified four well-separated clusters identifying cell type and GO-S treatment as the parameters correlated to the first two components of variability (**Fig.5A**). To compute the probability of genes being differentially expressed, we used a random variance

t-test as implemented in BRB Array-Tools. To control the false discovery rate (FDR) in our list of genes, we used a permutation test to provide evidence that family-wise error rate was less than 5% within the 80% confidence interval (CI). Using this cutoff value (FDR<5%, CI 80%), we identified, for T cells, 738 genes up-regulated (FC >1) and 409 genes down-regulated (FC >1) out of 1147 genes differentially expressed (**S. Tab. 2**). In monocytes, 243 genes were up-regulated (FC >1) and 333 were down-regulated (FC >1) out of 576 total genes identified, compared to the control group (**S. Tab. 3**).

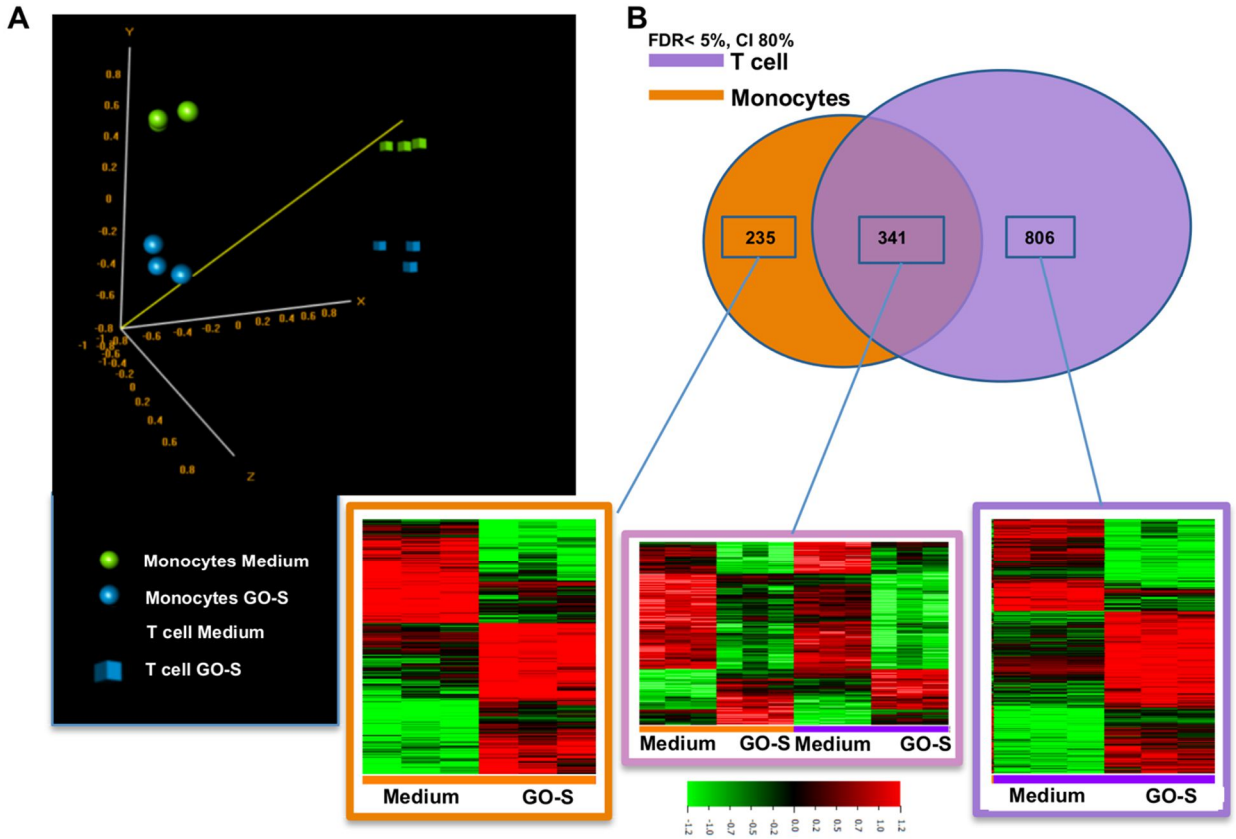

Figure 5. Gene expression analysis. A) 3D cluster graph identifies two different cell types treated and untreated with 50 µg ml^{-1} of GO-S. B) Heatmap and Venn diagrams show the number of probe-sets differently modulated by comparison of T cell and monocytes gene sets resulting after GO-S treatment, overlapping areas indicate the number of transcripts commonly modulated in both cell types. The heatmap indicate the change in expression in each subset (Red= high expression, green= low expression).

As can be observed in **Supporting Tables 2** and **3** all the genes passing the cut-off value were tabulated along with parametric p-value, fold change and links to major annotation sources. We clustered in a Venn diagram the genes differentially expressed in three groups (T cells, both T cells and monocytes, and monocytes) and displayed their standardized expression values as heat-maps (**Fig. 5B**). Only 341 significantly modulated genes were common in both cell lines,

and only one of these was differently regulated. We searched for evidence suggesting the consistency of our gene expression data with known features of the analyzed cell lines and with the results from our previous experiments in the immune gene arrays (**Fig. 3**).

The previous observations made using the immune array were confirmed since the analysis showed increased expression of genes such as: IL10, CCL5, CCR6, TYK2, IFNAR1, IRAK1, STAT6 in both cell types, CSF2, HLA-A, IL18, TLR9 and NFKB1 in T cells and DDX58, TLR3, TLR6, TLR7 and STAT3 in monocytes. To better understand at the mechanistic level the physiological significance of the changes in gene expression observed, we used the gene set comparison tool in BRB Array-Tools as a scoring tool to assign the functional category definitions according to the Gene Ontology Database. As a result, 559 and 532 gene sets were scored as significantly modulated in monocytes and T cells, respectively (**Supp.Tab.4 and 5**). The immune activation mediated by GO-S was confirmed by the over expression of some relevant pathways: T cell migration, regulation of T cell chemotaxis, macrophage activation, receptor signaling involved in phagocytosis and leukocyte chemotaxis pathways (**Fig. 6 A**). In particular, we found an up- regulation of genes closely related to inflammation such as CCL5 and the induction of the chemokine pathways such as CXCL10 ligand pathway and CXCR3 receptor (**Fig. 6 A, red box**). We confirmed this trend using the ingenuity pathways analysis (IPA) software. **Figure 6B** highlights the up-regulation of some genes that correlated with inflammation, illustrating the GO-S induced activation in T Cells. On monocytes, the IPA analysis did not reveal a significant activation on the same pathway.

This trend was confirmed also by the induction of IL10 pathway in T cells, displayed using IPA, by which we obtained a clear up-regulation pathway of IL10 and IL10R (**S. Fig. 5A**). Thus, IL10 overexpression is IL1-mediated by the induction of SP1 transcription factor (**S. Fig. 5A**). By contrast the absence of stimulation of IFNγ was also confirmed with the IFNγ pathway analysis. We have seen a marked down-regulation of STAT1 in T cells, the principal effector of IFNγ mediated cell activation (**S. Fig. 5B**).

Modification of cell metabolism was evident in both cell lines, characterized by the down-regulation of transcripts involved in the oxidative phosphorylation, mitochondrial ATP synthesis coupled proton transport and protein synthesis (large and small ribosomal subunit pathways) (**S. Fig. 6**), including cellular and mitochondrial ribosomal S and L proteins such as: RPS17, RPS26, RPS27, RPS27A, RPL4-RPL10, RPL39L (**S. Fig. 6**). Conversely, transcripts encoding glycolytic enzymes were up-regulated (**S. Fig 6**).

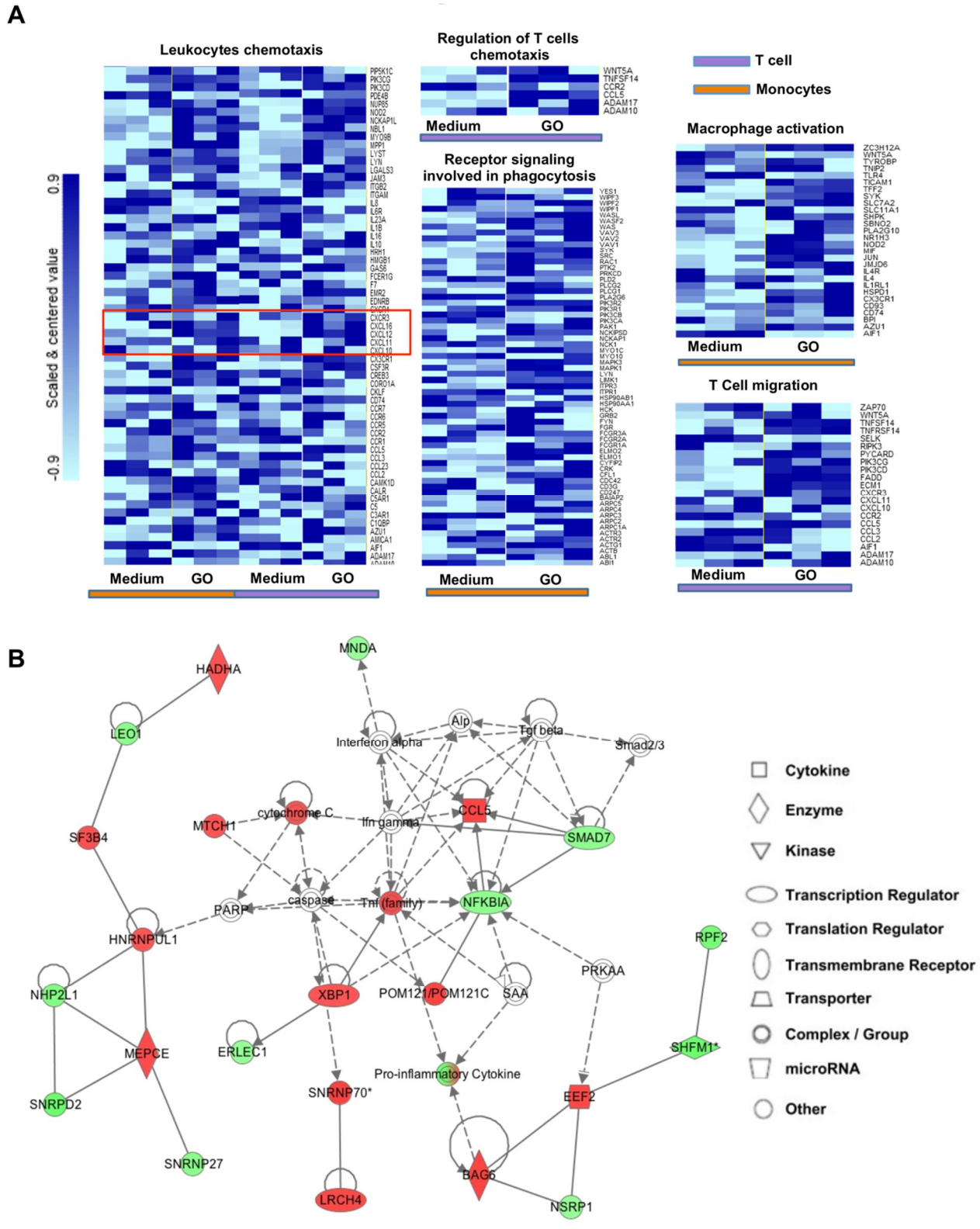

Figure 6. Gene expression of GO-S modulated pathways. A) Heatmap representation for relevant modulated pathways using Gene Ontology categories. **B)** Inflammation pathway in T cells after treatment with GO-S. The image was done with Ingenuity software. Bold lines indicate direct interaction, dotted lines indicate indirect interaction. Genes up-regulated by GO-S are highlighted in red, genes down-regulated are highlighted in green.

Discussion

There is a rapidly growing literature on the use of graphene-based materials, particular in its oxide form (GO), for biomedical uses [6, 34]. Compared to carbon nanotubes (CNTs) [20, 35] graphene has a larger available surface area [36] making it highly promising in the context of drug delivery and imaging [37]. As for any other nanomaterial designed to be a drug carrier, it is important to understand the possible adverse responses to GO and particularly its impact on the immune system [38]. Until today, there has been an inconclusive discussion whether GO should be considered immune-compromising or not [12]. As we previously reported for CNTs, the immune impact could be different between GOs with different lateral dimensions and functionalization [12]. Sasidharan et al. underlined that the toxicity effects of pristine graphene towards macrophage cells can be easily averted by surface functionalization [16, 19]. However, other studies are needed on the effect of different functionalized GOs on immune cells *ex vivo* and *in vivo* in order to assess the appropriate functionalization strategy.

The present study reports on the impact at the molecular level of well-characterized GOs on primary human immune populations. Previous works have studied only one or two cell population types, not in a complex human ex vivo cell pool [19, 39]. We carried out the present study on PBMCs from healthy donors that included different cell populations, T cells, B cells, monocytes, dendritic cells and natural killer cells to better reflect the effects on the pool of cell populations relevant to *in vivo* immune responses.

Regarding the graphene material characteristics, the question of whether the GO lateral dimensions can be a determinant factor of biological effects has been highlighted [4]. In this study GO of two different sizes (GO-S and GO-L) were prepared and characterized in terms of shape, structure, lateral size, thickness, functionalization, optical and surface properties. The two GO samples were only significantly different in lateral dimension as determined by TEM and AFM, while no significant differences were found in other properties. The second step was to characterize their possible cytotoxic effect and the impact of GO-S and GO-L on immune cell populations. We did not find significant differences in human PBMCs viability by the exposure to both GO types. Such findings were in agreement with previous studies on macrophages [18, 40]. Only few studies have been performed to date to understand the effect of graphene on the immune system [12], and in addition most previous work has focused only on the impact from graphene oxide exposure on traditional immunity markers, such as surface cluster of differentiation and cytokine release [15, 41].

The understanding of how the immune system is regulated and responds to nanomaterials cannot overlook the genomic level [22, 42]. Chatterjee et al. used an OMICS strategy to characterize the GO impact on hepatocytes (HepG2 cell line). They found a strong cytotoxic response induced by reduced GO mediated by a strong activation of ROS pathways [24]. Following these considerations, we used here for the first time an OMICS approach to point out the global function of exposure of small-sized sheets of GO (GO-S) on immune cells using bead array Illumina technology. To the best of our knowledge, no work used a genomic approach to point out the interaction of different GOs with immune cells today.

In this study we found a well-detectable difference in immune gene expression profiling between the two GO types. Our results suggest that the different sizes of GO flakes can impact PBMCs at the molecular level. This finding was also in agreement with Russier et al. [18], that focused only on macrophages to demonstrate that the small size of GO can have a higher impact compared to the large size GO. Based on this data, Bianco and colleagues have proposed "the mask effect of graphene" suggesting that the small size GO has the capacity for higher interactions with the cell membrane, a greater ability to enter into the cells and, therefore, inducing more biological effects compared to large-sized GO [18].
In our work the effect of GO-S particularly enhanced genes such as IL1, IL6, IL10, TNF, CD40, CD80 and CSF2 related to the innate response and also other genes such as TBX21, CD86 and CCL5 related with the adaptive immunity, not leading to apoptosis or necrosis. Moreover, the only 5 genes up-regulated by GO-L are also responsible for an innate immune cell response. Our results are in agreement with Zhi *et al.* who showed that the incubation with GO induced a specific activation of the innate immune system with a secretion of primary pro-inflammatory cytokines such as IL6, TNF and IL1β [43]. The data obtained in our study by immune array provided convincing evidence that the adaptive immune response is not directly but indirectly affected by GO-S, due to the major effect on antigen presenting cells in terms of activation. Indeed, genes implicated in direct T cell activation such as IL2 and IFNγ were not influenced. This was in perfect agreement with the absence of CD69 and CD25 expression, which is related to the IL2 secretion.

To confirm the indirect activation of T cells we showed a clear enhancement of CD80 and TBX21, essential genes for efficient cell-mediated recruitment of T cells [44]. These observations were further supported by whole genome array data that identified the immune activation of some relevant pathways correlated with T cell chemotaxis: T cell migration,

Dr. Marco Orecchioni. Titolo "Biomedical applications of different nanomaterials: Characterization and interaction with the immune system"
Tesi di dottorato in Life Sciences and Biotechnologies, Università degli Studi di Sassari.

regulation of T cell chemotaxis and leukocyte chemotaxis pathways. Intriguingly, we found in both T cell and monocytes the modulation of CXCL10 ligand pathway and CXCR3 receptor, commonly activated during acute inflammatory processes [45]. The main mechanism of action of immunotherapeutic agents (i.e. anti-CTLA4 mAbs) is represented by the induction of specific chemokines (such as CXCL10 and CXCR3). These chemokines, by binding to their corresponding receptors activated T helper 1 cells and NK cells which can mediate tumor rejection [46].

We previously showed that functionalized CNTs could act only as 'monocyte activating tools' [22], while here we found that GO-S could impact on both T cell and monocyte gene expression. Indeed a direct impact of GO-S on T cells was found, with 1148 genes differentially expressed (738 genes up-regulated, FC >1) (**Supp. Tab. 2**). We evidenced also the impact on TLR expression. Chen *et al.* found a GO-mediated TLR9 modulation inducing the expression of TNF receptor-associated factor 6 (TRAF6) that we have seen modulated also in our studies, thus suggesting a similar induction mechanism [47]. However, further experiments will be needed to assess a possible toll-like receptor mediated interaction i.e. with specific siRNAs. Moreover, the GO-S mediated secretion of IL1β and TNF cytokines is closely related to lymphocyte recruitment factors promoting the TLR mediated NF-kB and MAPK pathway activation, and is associated with the TRAF family. Speculatively, we consider that GO-S could elicit an innate but also an adaptive response providing strong recruitment of immune cells (in tumors for example), offering alternative strategies towards nano-immunotherapeutics as suggested by Goldberg for other nanomaterials [13].

Another interesting effect of GO-S was on cell metabolism with a strong modulation of energetic pathways by a down-regulation of oxidative phosphorylation (OX-PHOs) and mitochondrial ATP synthesis (**S. Fig. 6**) followed by a switch-on of glycolytic pathways in both cell types. Normally the metabolic switch occurs in cancer cells that change their metabolic phenotypes to adapt to microenvironmental modifications giving a selective advantage to cancer cells under an unfavorable environment [48]. Fantin et al. [49] confirmed the metabolic switch of cancer cells by a glycolysis suppression, through the use of inhibitors such as lactate dehydrogenase A (LDH-A). They found significant inhibition of tumor proliferation when glycolysis was suppressed. Intriguingly, our data indicated that GO-S was able to strongly down-regulate the oxidative phosphorylation pathways in the cell lines tested. This result was in agreement with the proteomic results of Zhou *et al.* [50] that showed a GO-induced inhibition

of breast cancer cell metastases by selective down-regulation of the protein PGC-1α, which accounts for the inhibition of OX-PHOs. Following these findings, a future perspective is the development of a nanosystem able to combine the action of our GO-S against the activation of oxidative phosphorylation pathway, with a targeted suppression of glycolysis through inhibitors such as LDH-A, may be effective in blocking cancer cell proliferation.

Conclusion

This work presented a wide-range approach to analyze the immunotoxicological impact of differently sized GOs on human PBMCs from healthy donors not previously reported. We demonstrated that different dimensions of 2D graphene materials could regulate the immune response and eventual biological responses of immune cells reflected in the differential immune gene and activation molecule expression patterns. We found that thin (few layer) GO sheets with small (100-500 nm) lateral dimensions had a more pronounced effect on immune cells. Moreover, the whole genome expression assay data obtained from cells in response to small GO sheet interactions suggested many interesting pathways implicated that could in the future allow the exploration of novel graphene-based immunotherapeutic tools.

Acknowledgments

This work was partly supported by the Fondazione Banco di Sardegna (grant N° 2013.1308, 2014.6035 to L.G.D.), the Sardinia Region (grant N° CRP-59720 to L.G.D.), the Gianfranco del Prete Association “The future: medicine, biology and nanotechnology Award” to L.G.D. The authors gratefully acknowledge financial support from EU FP7-ICT-2013-FET-F GRAPHENE Flagship project (no. 604391).

Declaration of Interest

Authors declare that no conflict of interest exists.

References

[1] A. K. Geim, K. S. Novoselov, Nature materials 2007, 6, 183.

[2] G. Sechi, D. Bedognetti, F. Sgarrella, L. Van Eperen, F. M. Marincola, A. Bianco, L. G. Delogu, Nanomedicine 2014, 9, 1475.

[3] a) D. Bitounis, H. Ali-Boucetta, B. H. Hong, D. H. Min, K. Kostarelos, Advanced materials 2013, 25, 2258; b) M. Orecchioni, A. Bianco, L.G. Delogu, Theranostics 2015, 5, 710; c) P. Huang, C. Xu, J. Lin, C. Wang, X. Wang, C. Zhang, X. Zhou, S. Guo, D. Cui, Theranostics 2011, 1, 240.

[4] K. Kostarelos, K. S. Novoselov, Science 2014, 344, 261.

[5] S. Park, R. S. Ruoff, Nature nanotechnology 2009, 4, 217.

[6] H. Ali-Boucetta, D. Bitounis, R. Raveendran-Nair, A. Servant, J. Van den Bossche, K. Kostarelos, Adv Healthc Mater 2013, 2, 433.

[7] a) A. Bianco, Angewandte Chemie 2013, 52, 4986; b) P. Wick, A. E. Louw-Gaume, M. Kucki, H. F. Krug, K. Kostarelos, B. Fadeel, K. A. Dawson, A. Salvati, E. Vazquez, L. Ballerini, M. Tretiach, F. Benfenati, E. Flahaut, L. Gauthier, M. Prato, A. Bianco, Angewandte Chemie 2014, 53, 7714.

[8] a) C. Bussy, D. Jasim, N. Lozano, D. Terry, K. Kostarelos, Nanoscale 2015, 7, 6432; b) D. A. M.-M. Jasim, C.; Begin, D.; Bianco, A.; Kostarelos, K, Chemical Science 2015, 6, 3952; c) B. Li, X. Y. Zhang, J. Z. Yang, Y. J. Zhang, W. X. Li, C. H. Fan, Q. Huang, International journal of nanomedicine 2014, 9, 4697; d) M. Nurunnabi, Z. Khatun, K. M. Huh, S. Y. Park, D. Y. Lee, K. J. Cho, Y. K. Lee, ACS nano 2013, 7, 6858.

[9] K. Wang, H. Song, J. Zhang, Y. Wo, S. Guo, D. Cui, Nanoscale Reseach Letters 2011, 6.

[10] X. Wang, R. Podila, J. H. Shannahan, A. M. Rao, J. M. Brown, International journal of nanomedicine 2013, 8, 1733.

[11] S. A. Sydlik, S. Jhunjhunwala, M. J. Webber, D. G. Anderson, R. Langer, ACS nano 2015, 9, 3866.

[12] M. Orecchioni, D. Bedognetti, F. Sgarrella, F. M. Marincola, A. Bianco, L. G. Delogu, Journal of translational medicine 2014, 12, 138.

[13] M. S. Goldberg, Cell 2015, 161, 201.

[14] a) M. Lv, Y. Zhang, L. Liang, M. Wei, W. Hu, X. Li, Q. Huang, Nanoscale 2012, 4, 3861; b) M. Wojtoniszak, X. Chen, R. J. Kalenczuk, A. Wajda, J. Lapczuk, M. Kurzewski, M. Drozdzik, P. K. Chu, E. Borowiak-Palen, Colloids and surfaces. B, Biointerfaces 2012, 89, 79; c) S. Shi, K. Yang, H. Hong, H. F. Valdovinos, T. R. Nayak, Y. Zhang, C. P. Theuer, T. E. Barnhart, Z. Liu, W. Cai, Biomaterials 2013, 34, 3002.

[15] H. Yue, W. Wei, Z. Yue, B. Wang, N. Luo, Y. Gao, D. Ma, G. Ma, Z. Su, Biomaterials 2012, 33, 4013.

[16] A. Sasidharan, L. S. Panchakarla, P. Chandran, D. Menon, S. Nair, C. N. Rao, M. Koyakutty, Nanoscale 2011, 3, 2461.

[17] a) N. V. Vallabani, S. Mittal, R. K. Shukla, A. K. Pandey, S. R. Dhakate, R. Pasricha, A. Dhawan, Journal of biomedical nanotechnology 2011, 7, 106; b) S. M. Kang, T. H. Kim, J. W. Choi, *Journal of nanoscience and nanotechnology* 2012, 12, 5185; W. Hu, C. Peng, W. Luo, M. Lv, X. Li, D. Li, Q. Huang, C. Fan, ACS nano 2010, 4, 4317.

[18] J. Russier, E. Treossi, A. Scarsi, F. Perrozzi, H. Dumortier, L. Ottaviano, M. Meneghetti, V. Palermo, A. Bianco, *Nanoscale* 2013, 5, 11234.

[19] A. Sasidharan, L. S. Panchakarla, A. R. Sadanandan, A. Ashokan, P. Chandran, C. M. Girish, D. Menon, S. V. Nair, C. N. Rao, M. Koyakutty, *Small* 2012, 8, 1251.

[20] L. G. Delogu, E. Venturelli, R. Manetti, G. A. Pinna, C. Carru, R. Madeddu, L. Murgia, F. Sgarrella, H. Dumortier, A. Bianco, *Nanomedicine* 2012, 7, 231.
[21] C. Crescio, M. Orecchioni, C. Menard-Moyon, F. Sgarrella, P. Pippia, R. Manetti, A. Bianco, L. G. Delogu, *Nanoscale* 2014, 6, 9599.
[22] M. Pescatori, D. Bedognetti, E. Venturelli, C. Menard-Moyon, C. Bernardini, E. Muresu, A. Piana, G. Maida, R. Manetti, F. Sgarrella, A. Bianco, L. G. Delogu, *Biomaterials* 2013, 34, 4395.
[23] E. Frohlich, C. Meindl, K. Wagner, G. Leitinger, E. Roblegg, *Toxicology and applied pharmacology* 2014, 280, 272.
[24] N. Chatterjee, H. J. Eom, J. Choi, *Biomaterials* 2014, 35, 1109.
[25] A. Adamson, *Physical Chemistry of Surfaces* Wiley Interscience New York, 1990.
[26] K. E. Simon R, L McShane , M. Radmacher , G. Wright, Y. Zhao, Springer-Verlag New York 2003.
[27] G. W. Wright, R. M. Simon, Bioinformatics 2003, 19, 2448.
[28] M. J. Willard HH, L. L., A. DJ, & Settle J, F. A. , *Instrumental methods of analysis*, Wadsworth, Inc, California, 1988.
[29] G. X. Wang, B. Wang, J. Park, J. Yang, X. P. Shen, J. Yao, *Carbon* 2009, 47, 68.
[30] G. M. Neelgund, A. Oki, Z. Luo, Journal of colloid and interface science 2014, 430, 257.
[31] A. C. Ferrari, Solid state communications 2007, 143, 47.
[32] A. C. Ferrari, J. C. Meyer, V. Scardaci, C. Casiraghi, M. Lazzeri, F. Mauri, S. Piscanec, D. Jiang, K. S. Novoselov, S. Roth, A. K. Geim, Physical review letters 2006, 97, 187401.
[33] S. C. Rattana, N. Witit-anun, N. Nuntawong, P. Chindaudom, S. Oaew, C. Kedkeaw, P. Limsuwan, Procedia Engineering 2012, 32, 759.
[34] K. V. Krishna, C. Menard-Moyon, S. Verma, A. Bianco, Nanomedicine 2013, 8, 1669; X. Zhou, F. Liang, Current medicinal chemistry 2014, 21, 855.
[35] a) V. Rastogi, P. Yadav, S. S. Bhattacharya, A. K. Mishra, N. Verma, A. Verma, J. K. Pandit, Journal of drug delivery 2014, 2014, 670815; b) L. G. Delogu, A. Magrini, A. Bergamaschi, N. Rosato, M. I. Dawson, N. Bottini, M. Bottini, Bioconjugate chemistry 2009, 20, 427; c) L. G. Delogu, S. M. Stanford, E. Santelli, A. Magrini, A. Bergamaschi, K. Motamedchaboki, N. Rosato, T. Mustelin, N. Bottini, M. Bottini, Journal of nanoscience and nanotechnology 2010, 10, 5293.
[36] L. Feng, Z. Liu, Nanomedicine 2011, 6, 317.
[37] a) L. G. Delogu, G. Vidili, E. Venturelli, C. Menard-Moyon, M. A. Zoroddu, G. Pilo, P. Nicolussi, C. Ligios, D. Bedognetti, F. Sgarrella, R. Manetti, A. Bianco, Proceedings of the National Academy of Sciences of the United States of America 2012, 109, 16612.
[38] M. A. Dobrovolskaia, S. E. McNeil, Nature nanotechnology 2007, 2, 469.
[39] a) H. Zhou, K. Zhao, W. Li, N. Yang, Y. Liu, C. Chen, T. Wei, Biomaterials 2012, 33, 6933; b) A. V. Tkach, N. Yanamala, S. Stanley, M. R. Shurin, G. V. Shurin, E. R. Kisin, A. R. Murray, S. Pareso, T. Khaliullin, G. P. Kotchey, V. Castranova, S. Mathur, B. Fadeel, A. Star, V. E. Kagan, A. A. Shvedova, Small 2013, 9, 1686.
[40] a) G. Qu, S. Liu, S. Zhang, L. Wang, X. Wang, B. Sun, N. Yin, X. Gao, T. Xia, J. J. Chen, G. B. Jiang, ACS nano 2013, 7, 5732; b) R. Feng, Y. Yu, C. Shen, Y. Jiao, C. Zhou, Journal of biomedical materials research. Part A 2014.
[41] Y. Li, Y. Liu, Y. Fu, T. Wei, L. Le Guyader, G. Gao, R. S. Liu, Y. Z. Chang, C. Chen, Biomaterials 2012, 33, 402.
[42] P. Ricciardi-Castagnoli, F. Granucci, Nature reviews. Immunology 2002, 2, 881.
[43] X. Zhi, H. Fang, C. Bao, G. Shen, J. Zhang, K. Wang, S. Guo, T. Wan, D. Cui, Biomaterials 2013, 34, 5254.

[44] a) K. N. Nielsen, M. A. Steffensen, J. P. Christensen, A. R. Thomsen, Journal of immunology 2014, 193, 1223; b) D. Zhang, X. Zhang, M. Ge, M. Xuan, H. Li, Y. Yang, R. Fu, F. Zhou, Y. Zheng, R. Yang, Human immunology 2014, 75, 129.
[45] L. M. Coussens, Z. Werb, Nature 2002, 420, 860.
[46] D. Bedognetti, E. Wang, M. R. Sertoli, F. M. Marincola, Expert review of vaccines 2010, 9, 555.
[47] G. Y. Chen, C. L. Chen, H. Y. Tuan, P. X. Yuan, K. C. Li, H. J. Yang, Y. C. Hu, Advanced healthcare materials 2014, 3, 1486.
[48] J. Zheng, Oncology letters 2012, 4, 1151.
[49] V. R. Fantin, J. St-Pierre, P. Leder, Cancer cell 2006, 9, 425.
[50] T. Zhou, B. Zhang, P. Wei, Y. Du, H. Zhou, M. Yu, L. Yan, W. Zhang, G. Nie, C. Chen, Y. Tu, T. Wei, Biomaterials 2014, 35, 9833.

Supporting Information

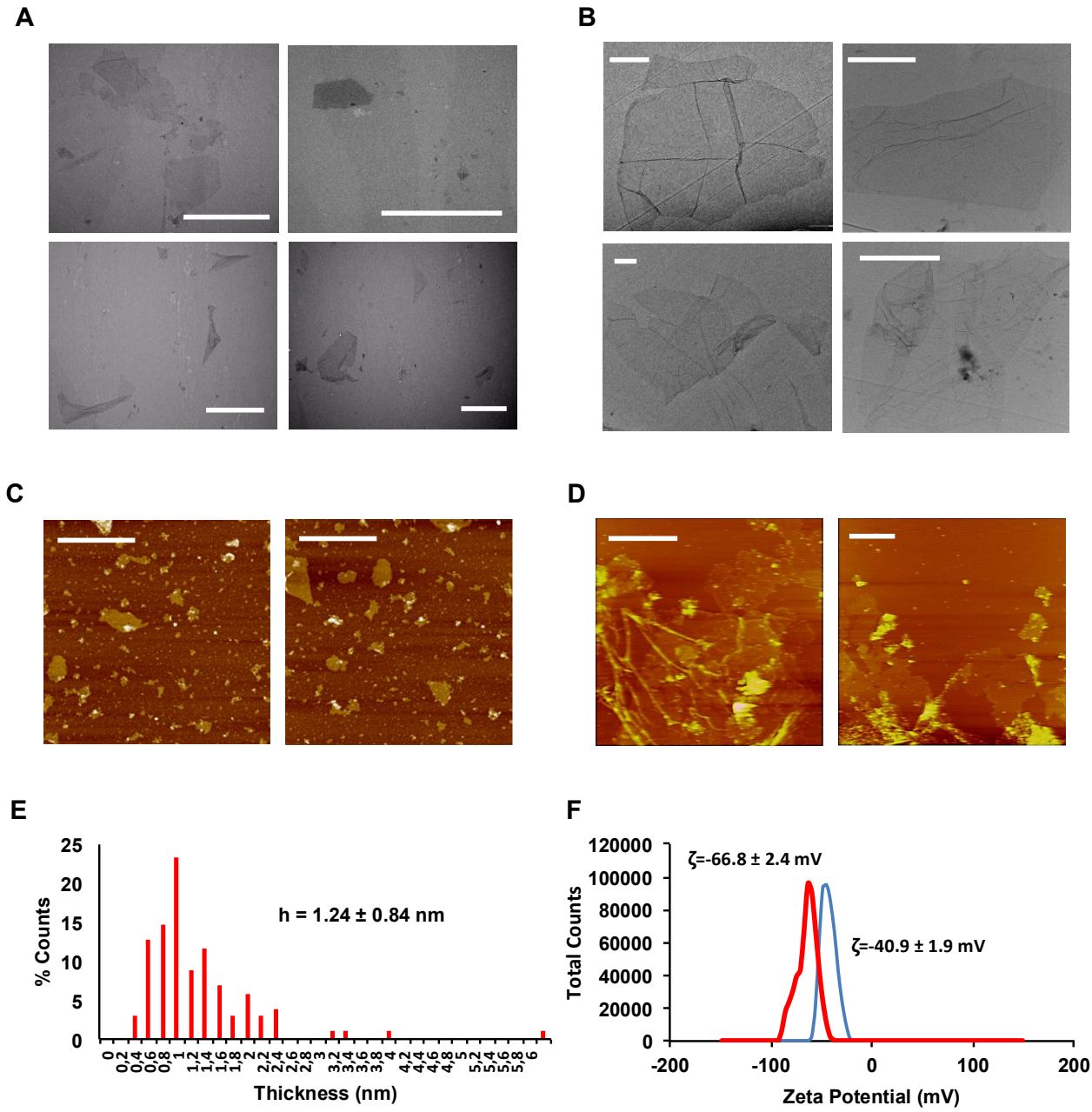

S. Fig. 1 Further Characterizations of GO-S and GO-L. (A) and (B) are TEM images of GO-S and GO-L respectively. (C) and (D) are AFM images of GO-S and GO-L respectively. All scale bars are 1μm. (E) Thickness of GO-S sheets determined by counting the height of more than 100 GO sheets from several AFM images. (F) Zeta potential graph of GO-S (red) and GO-L (blue).

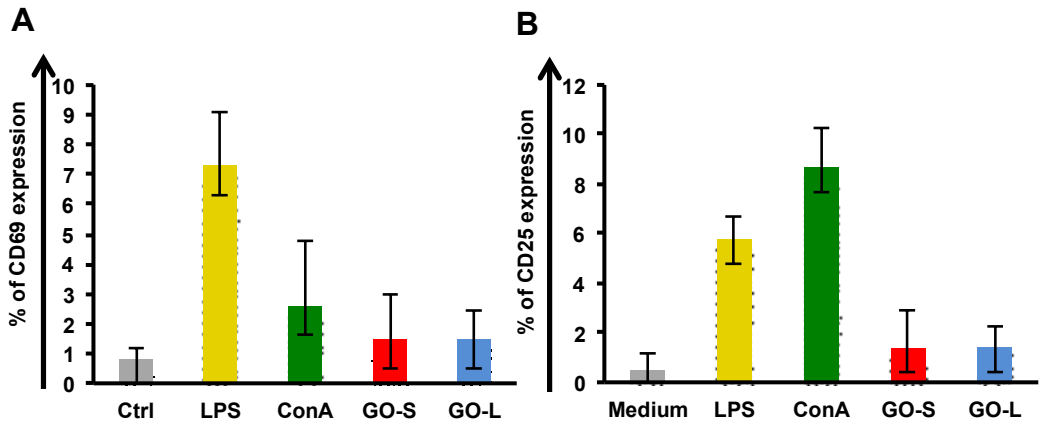

S. Fig. 2. Impact of GO-Small and GO-Large on human primary cell activation markers. PBMCs were incubate for 24h with 50µg/ml of graphenes or left untreated. Cell activation was assessed looking at the expression of CD25 and CD69. Concanavalin A (4 µg/ml) and lipopolysaccharides (2 µg/ml) were used as positive controls. Analysis was assessed by flow cytometry. Statistical significance compared to untreated cells (student's t test) is indicated by * = $p < 0.05$.

GO-Small

Layout	01	02	03	04	05	06	07	08	09	10	11	12
A	APCS 1.73	C3 1.24	CASP1 -1.20	CCL2 1.32	CCL5 1.80	CCR4 2.42	CCR5 1.43	CCR6 4.36	CCR8 2.15	CD14 -2.16	CD4 1.01	CD40 4.44
B	CD40LG -1.04	CD80 8.73	CD86 1.09	CD8A 3.08	CRP 1.56	CSF2 72.09	CXCL10 1.06	CXCR3 1.49	DDX58 2.12	FASLG 1.21	FOXP3 1.57	GATA3 1.13
C	HLA-A 3.61	HLA-E 2.74	ICAM1 2.81	IFNA1 1.69	IFNAR1 4.10	IFNB1 1.34	IFNG 3.01	IFNGR1 -1.23	IL10 10.14	IL13 1.53	IL17A 2.15	IL18 -1.55
D	IL1A 16.99	IL1B 21.58	IL1R1 6.11	IL2 2.10	IL23A 4.82	IL4 1.78	IL5 1.99	IL6 13.75	IL8 5.19	IRAK1 1.90	IRF3 1.82	IRF7 1.63
E	ITGAM 3.85	JAK2 2.02	LY96 1.28	LYZ -11.14	MAPK1 1.64	MAPK8 3.07	MBL2 2.15	MPO 1.88	MX1 1.50	MYD88 -1.16	NFKB1 4.75	NFKBIA 3.11
F	NLRP3 2.36	NOD1 2.66	NOD2 1.37	RAG1 1.74	RORC 2.29	SLC11A1 1.15	STAT1 -1.33	STAT3 3.94	STAT4 3.04	STAT6 2.14	TBX21 4.58	TICAM1 5.34
G	TLR1 -1.49	TLR2 2.71	TLR3 2.06	TLR4 -1.21	TLR5 2.49	TLR6 1.79	TLR7 1.31	TLR8 -1.18	TLR9 2.54	TNF 37.84	TRAF6 2.85	TYK2 2.00

GO-Large

Layout	01	02	03	04	05	06	07	08	09	10	11	12
A	APCS -1.59	C3 1.28	CASP1 -2.22	CCL2 -2.39	CCL5 1.11	CCR4 -1.01	CCR5 -1.92	CCR6 1.87	CCR8 -1.28	CD14 -3.15	CD4 -2.73	CD40 1.31
B	CD40LG -2.04	CD80 1.91	CD86 -6.42	CD8A 1.10	CRP -1.77	CSF2 43.77	CXCL10 -2.59	CXCR3 -2.67	DDX58 -2.13	FASLG -2.46	FOXP3 -3.36	GATA3 -1.31
C	HLA-A 1.42	HLA-E -1.06	ICAM1 -1.92	IFNA1 -1.63	IFNAR1 1.11	IFNB1 -2.05	IFNG -1.44	IFNGR1 -3.61	IL10 2.54	IL13 -1.79	IL17A -1.28	IL18 -4.38
D	IL1A 5.23	IL1B 6.07	IL1R1 2.04	IL2 -1.31	IL23A 1.20	IL4 -1.93	IL5 -2.82	IL6 6.33	IL8 2.04	IRAK1 -1.27	IRF3 -1.31	IRF7 -1.41
E	ITGAM -1.03	JAK2 -2.43	LY96 -3.65	LYZ -27.06	MAPK1 -1.40	MAPK8 -1.53	MBL2 -1.28	MPO -1.46	MX1 -1.86	MYD88 -1.78	NFKB1 1.49	NFKBIA 1.46
F	NLRP3 -1.68	NOD1 -1.24	NOD2 -2.01	RAG1 -1.58	RORC -1.28	SLC11A1 -2.41	STAT1 -4.08	STAT3 1.09	STAT4 -2.01	STAT6 -1.28	TBX21 1.14	TICAM1 1.66
G	TLR1 -2.13	TLR2 1.31	TLR3 -1.23	TLR4 -2.86	TLR5 -2.27	TLR6 -1.94	TLR7 -6.96	TLR8 -4.00	TLR9 -1.26	TNF 8.44	TRAF6 -1.43	TYK2 -1.64

S. Fig. 3 Heat Map description tab. Tables show the values of log 2 fold change for all genes taken into consideration in the expression analysis of Figure 3A.

Gene	GO-S	GO-L
CASP1	-1,1991	-2,1825
CCL2	1,3268	-2,3392
CCR4	2,4419	1,0028
CCR6	4,4015	1,9106
CD40	4,463	1,3324
CD40LG	-1,0295	-2,0083
CD80	8,803	1,9507
CD86	1,1004	-6,3028
CD8A	3,0908	1,1127
CSF2	72,9077	44,7557
CXCR3	1,4928	-2,6317
DDX58	2,1406	-2,0936
FASLG	1,2125	-2,4217
FOXP3	1,5779	-3,3081
HLA-A	3,6503	1,4479
HLA-E	2,7664	-1,0396
ICAM1	2,8442	-1,8738
IFNAR1	4,1353	1,136
IFNB1	1,3547	-2,0083
IFNG	3,0483	-1,4103
IFNGR1	-1,2159	-3,5455
IL10	10,2532	2,5919
IL18	-1,539	-4,305
IL1A	17,1246	5,3295
IL1B	21,6756	6,1646
IL1R1	6,139	2,0763
IL23A	4,8501	1,2176
IL5	1,9972	-2,7818
IL6	13,8134	6,4264
IL8	5,2343	2,0763
ITGAM	3,8852	-1,0042
JAK2	2,0392	-2,3883
LY96	1,2995	-3,5702
LYZ	-11,0196	-26,4647
MAPK8	3,0908	-1,5115
NFKB1	4,7833	1,5199
NFKBIA	3,134	1,4886
NLRP3	2,3916	-1,6426
NOD1	2,6907	-1,2193
SLC11A1	1,1551	-2,3718
STAT1	-1,3213	-3,9889
STAT3	3,9669	1,1127
STAT4	3,0695	-1,967
TBX21	4,6203	1,1599
TICAM1	5,3815	1,6865
TLR1	-1,4763	-2,0936
TLR2	2,7283	1,3324
TLR3	2,082	-1,2025
TLR4	-1,1991	-2,8011
TLR5	2,4932	-2,2284
TLR7	1,3177	-6,8495
TLR8	-1,1663	-3,934
TLR9	2,5633	-1,2363
TNF	38,2662	8,598
TRAF6	2,8839	-1,4006
TYK2	2,0111	-1,6088

S. Fig. 4. Modulate genes in GO-Small e GO-large versus control. Red show genes with a fold change greater than 2, green show genes with a fold change less than 2.

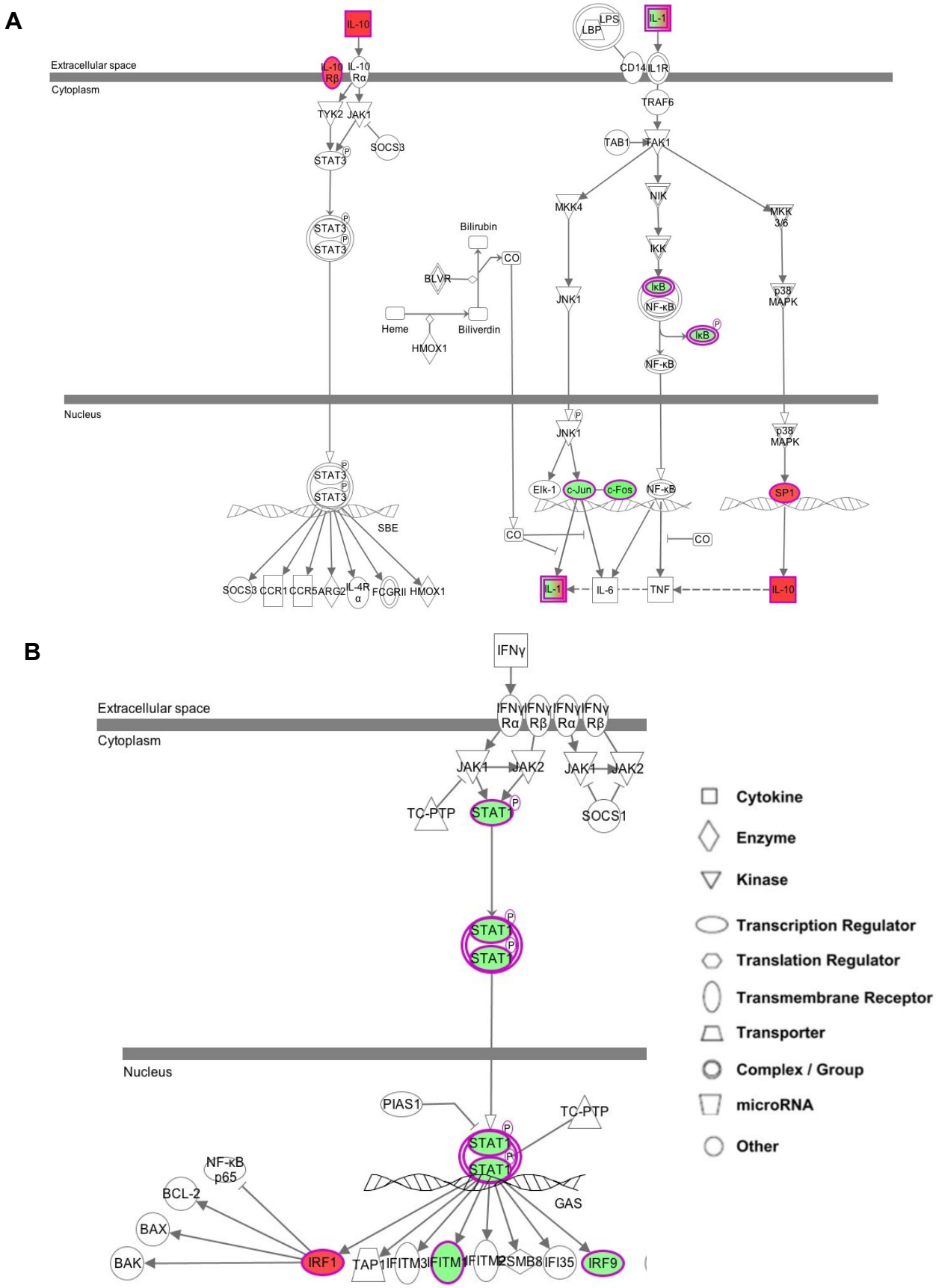
A
IL-10
LPS
LBP
IL-1
Extracellular space
Cytoplasm
IL-10 Rβ
IL-10 Rα
CD14
IL1R
TRAF6
TYK2
JAK1
TAB1
TAK1
SOCS3
STAT3
MKK4
NIK
MKK 3/6
Bilirubin
CO
IKK
BLVR
JNK1
IκB
NF-κB
p38 MAPK
Heme
Biliverdin
HMOX1
Nucleus
SBE
Elk-1
c-Jun
c-Fos
SP1
SOCS3
CCR1
CCR5
ARG2
IL-4R α
FCGRII
HMOX1
IL-6
TNF
B
IFNγ
IFNγ Rα
IFNγ Rβ
JAK1
JAK2
TC-PTP
STAT1
SOCS1
PIAS1
NF-κB p65
BCL-2
BAX
BAK
IRF1
TAP1
IFITM3
IFITM1
IFITM2
PSMB8
IFI35
IRF9
GAS
Cytokine
Enzyme
Kinase
Transcription Regulator
Translation Regulator
Transmembrane Receptor
Transporter
Complex / Group
microRNA
Other

S. Fig. 5. Signal transduction pathway of IL10 (A) and IFNγ (B), after treatment with GO-Small. Over-expressed genes are highlighted in red down-expressed are in green. Pathways were identified by ingenuty pathway analysis (IPA).

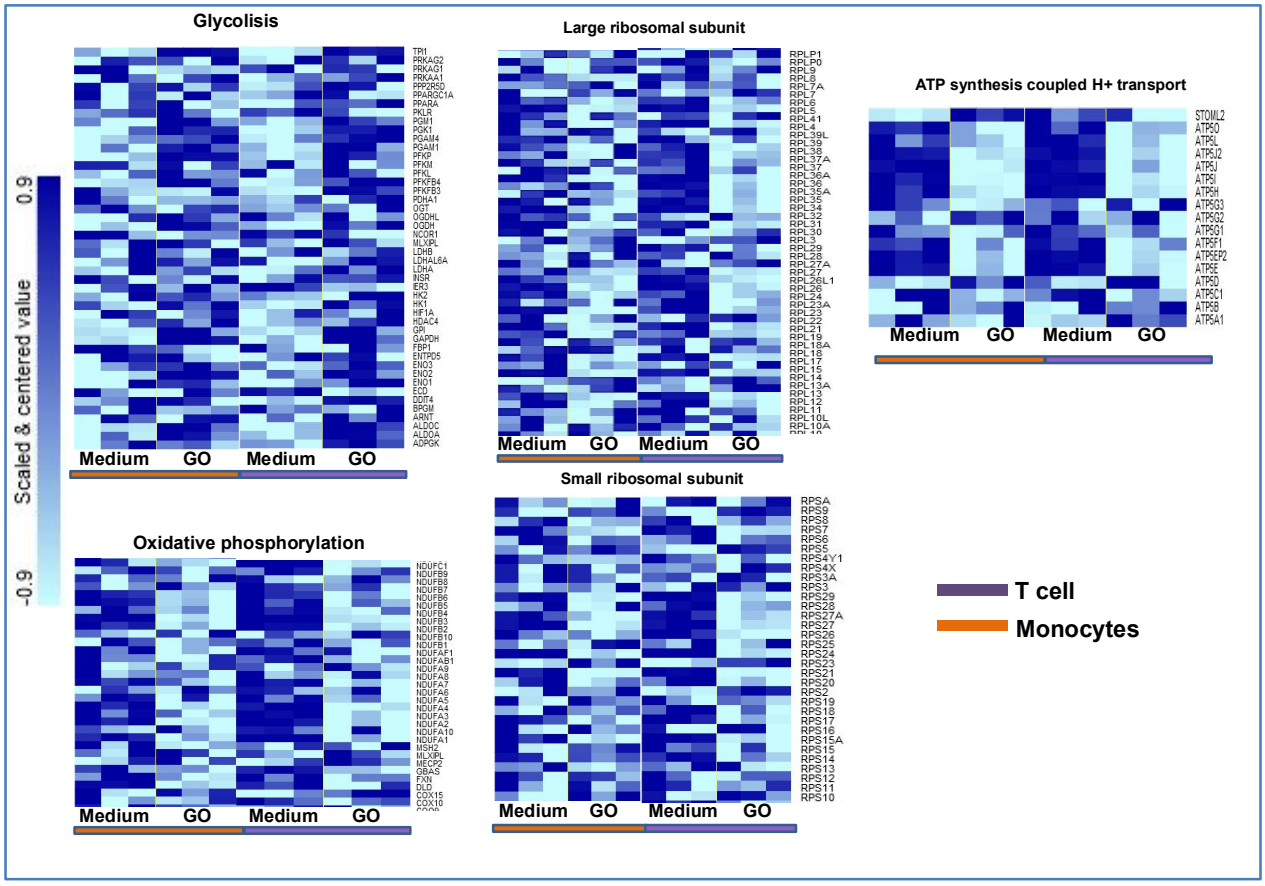

S. Fig. 6. Gene set enrichment with Gene Ontology. Identification of altered metabolism pathways after treatment with GO-Small. (Purple bar= T cells, Orange bar= Monocytes).

Sample	1st step		2nd step		Total % Weight Loss
	Tempreture (°C)	% Weight Loss	Tempreture (°C)	% Weight Loss	
GO-S	186,27	6,47	408,53	34,84	41,31
GO-L	165,97	5,59	389,35	41,41	47
Graphite	221,26	0,44	415,21	0,87	1,31

S. Tab. 1 Thermogravimetric analysis.

Paper III: *Single-cell mass cytometry reveals the impact of graphene nanomaterials with human primary immune cells*

Marco Orecchioni,[1] Davide Bedognetti,[2] Leon Newman,[3] Claudia Fuoco,[4] Filomena Spada,[4] Wouter Hendrickx,[2] Francesco M. Marincola,[5] Francesco Sgarrella,[1] Filipe A. Rodrigues,[3] Cécilia Ménard-Moyon,[6] Gianni Cesareni,[4] Kostas Kostarelos,[3] Alberto Bianco[6]* and Lucia Gemma Delogu[1,7]**

[1]*Department of Chemistry and Pharmacy University of Sassari, Sassari, Italy*
[2] *Immunology and Therapy Section, Division of Translational Medicine, Sidra Medical and Research Center, Doha, Qatar.*
[3] *Nanomedicine Laboratory, Faculty of Biology, Medicine, Health and National Graphene Institute University of Manchester, Manchester, United Kingdom.*
[4] *Department of Biology, University of Rome Tor Vergata, Rome, Italy*
[5]*Office of the Chief Research Officer, Sidra Medical and Research Center, Doha, Qatar.*
[6] *CNRS, Institut de Biologie Moléculaire et Cellulaire, Laboratoire d'Immunopathologie et Chimie Thérapeutique, Strasbourg, France*
[7] *Max Bergmann Center of Biomaterials and Institute for Materials Science, Dresden University of Technology , Dresden, Germany.*

Keywords:

Graphene, 2D materials, nanomedicine, nanotoxicology, single-cell mass cytometry.

Submitted

Abstract

Understanding the biomolecular interactions between graphene nanomaterials and human cells is a prerequisite for the utilization of graphene-based nanomaterials as a diagnostic or therapeutic tool. Currently, the impact of exposure to graphene and its derivate graphene oxide (GO) on the immune system remains elusive. To characterize the complex interactions between graphene nanomaterials and immune cells, we propose an integrative analytical pipeline encompassing the evaluation of molecular and cellular parameters. Single-cell mass cytometry was used to dissect the effect of GO flakes and GO functionalized with amino groups on 15 immune cell populations, interrogating 30 markers at the single-cell level. Next we integrated single-cell mass cytometry with genome-wide transcriptome analysis and we could conclude that the amino groups reduce the perturbations caused by GO on cell metabolism and increase biocompatibility. Moreover, $GONH_2$, but not GO, polarizes T-cell and monocyte activation toward a T helper-1/M1 immune response. These observations support the implementation of nanoscale platforms for immunotherapy, as vaccine carrier and nanoadjuvant. This study describes an innovative approach for the comprehensive analysis of nanomaterial interactions with distinct immune cells laying the foundation for the incorporation of single-cell mass cytometry for the characterization of nanomaterial immune cell interactions.

Manuscript

A the most promising frontier of nanotechnology is the development of nanomaterials for medical and diagnostic applications[1]. Graphene, a single layer of hexagonally arranged carbon atoms, and graphene oxide (GO), the oxidized form of graphene, are carbon nanomaterials characterized by extraordinary physicochemical properties and biocompatibility that enable their utilization in biomedical applications[2, 3, 4]. The impact exerted by GO on the immune system is still unclear[6, 7, 8, 9]. Differences among reports could be attributed to variability in the physicochemical characteristics of materials used in terms of lateral dimension, functionalization, and purity. Indeed, the role of lateral size and chemical functionalization on the immunological proprieties of GO is poorly characterized and deserves further investigation[14, 15, 16].

The understanding of the complex interactions between nanoparticles and immune cells is hindered by insufficient implementation of high throughput, deep phenotyping technologies in the field[10, 11, 12, 13]. The immune system is a sophisticated machine meant to protect the body against pathogens or tumors. Its dysfunction can induce pathologies such as autoimmunity diseases, allergies and cancer[17, 18]. Revealing the interactions of different GOs with this complex system remains a challenge. A comprehensive study of nanomaterial-immune system interactions should include tool that permit multiplex analysis of cell type, activation status, and release of soluble mediators with stimulatory and inhibitory properties[18, 19].

Flow cytometry has been primarily used to address single cell behavior through the measurement of multiple markers commonly associated with complex cellular systems such as the immune cells. Recently, a novel tool for flow cytometry analysis has been developed that leverages the precision of mass spectrometry. The combination of the two techniques, termed single-cell mass cytometry (CyTOF), allows the simultaneous measurement of more than 40 cellular parameters at single-cell resolution with over 100 available detection channels. The improvement of computational algorithms is expected to double these numbers within the next few years[20] therefore augmenting the ability to evaluate complex cellular systems and processes[21].

Compared to fluorescence-based cytometry, mass cytometry employs element-tagged probes that exploit the resolution of isotopes mass discrimination with minimal signal overlap. Furthermore, mass cytometry uses rare earth elemental tags that are not naturally found in cells, thereby avoiding the measurement of background cellular signal. All these attributes simplify

the large panel experimental design, thus uniquely enabling high-dimensional cytometry experiments not possible otherwise[20, 22, 23, 24]. For the first time in the context of nanotechnology, we demonstrate the use of single-cell mass cytometry to dissect the immunological effects of nanomaterials on individual cells. Thin GO flakes (single to few graphene layers) and GO conjugated to amino groups ($GONH_2$)[25] via epoxide ring opening were investigated (Materials and Methods). The physicochemical characterization of both GO and $GONH_2$ is reported in the Supporting Information (**Figure S1**). Briefly, the morphology was studied by both TEM and AFM (**Figure S1a-d**). These techniques indicate that the lateral dimensions of both GO and $GONH_2$ sheets ranged between approximately 50 nm and 1 μm, with a thickness corresponding to single to few (2-3) layers. The $GONH_2$ sheets were shown to be approximately 3 times thicker than the non-functionalized GO. The increased thickness of graphene-based materials following functionalization has been reported and is attributed to the presence of functional groups on the surface[26, 27]. Raman spectroscopy evidenced the presence of the characteristic D and G bands (1330 cm^{-1} and 1595 cm^{-1}, respectively) in both GO materials, confirming their *graphenaceous* structure. The I(D)/I(G) ratio, commonly used as a parameter of disorder[28], did not increase significantly, as expected, since the epoxy ring opening reaction conditions used for amination do not add further defects to the GO surface[29]. FT-IR measurements of the samples however, showed a clear difference between GO and $GONH_2$. Importantly, the presence of an extra band in the 1260-1330 cm^{-1} range in $GONH_2$ compared to the GO samples can be explained by the amine C-N stretching and C-H bending. Furthermore, the presence of a new band around 2900 cm^{-1}, indicative of the presence of the aliphatic C-H stretch, supports the successful amination of GO by epoxide ring opening due to the presence of the TEG chain. These results confirm the successful production of both GO and $GONH_2$ to be applied in our experiments[25, 30].

We used single-cell mass cytometry to analyze simultaneously 30 markers discriminating distinct subpopulations of peripheral blood mononuclear cells (PBMCs) to understand the response to nanomaterial exposure. CyTOF analysis allowed to check differential viability of 15 immune cell subpopulations exposed to GO and $GONH_2$ for 24 h. A concentration of 50 $\mu g \cdot mL^{-1}$ was chosen for these experiments as it was identified as an appropriate concentration for different GO-based biomedical applications[10, 15, 31]. One qualitative difference between flow cytometry and mass cytometry is the absence in the latter of the spectral overlap that

complicates the analysis of fluorescence data. Another advantage is the absence of cell-dependent background signals in the mass cytometry data[32].

Immune cell populations are identified according to the expression profile of "cluster of differentiations" (CDs) markers present on the cell surface. When immune cells go through different stages of maturation and differentiation the CD marker profiles change. Mass cytometry with its high dimensionality is an ideal approach to simultaneously characterize several cell markers. CyTOF could analyze the effect of GO and $GONH_2$ on a wide variety of immune cell populations determining also different maturation and activation stages. To reduce the dimensionality of the dataset we used SPADE (spanning-tree progression analysis of density-normalized events) clustering algorithm (**Figure 1a**), as reported by Bendall *et al*[32].

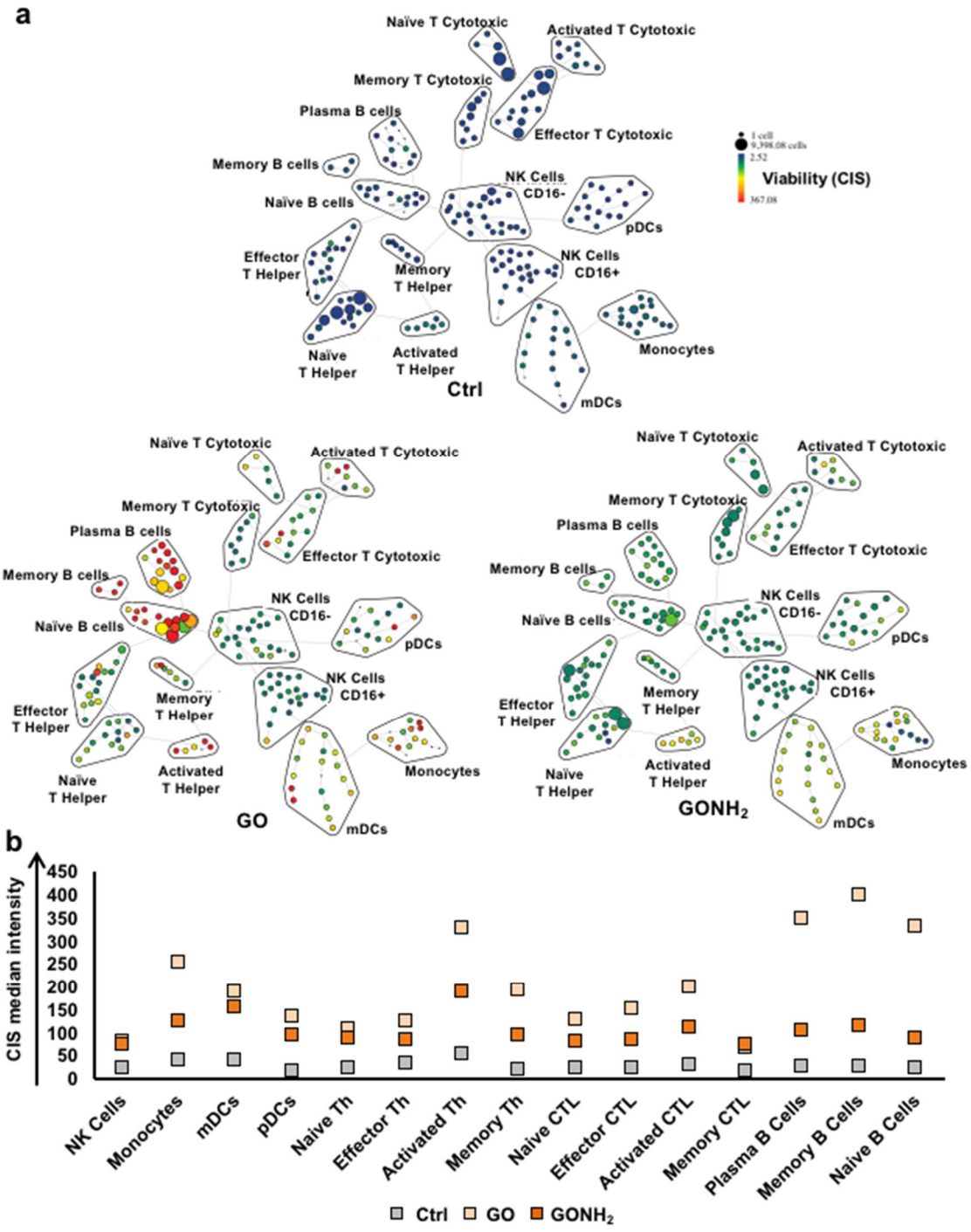

Figure 1. Cell viability analysis using CIS reagent with CyTOF. PBMCs were treated with GO and $GONH_2$, at the concentration of 50 $\mu g \cdot mL^{-1}$. **a**) The SPADE tree plots show the different gated immune cell subpopulations. The size of each cluster in the tree indicates relative frequency of cells that fall within the dimensional confines of the node boundaries. Node color is scaled to the median intensity of marker expression of the cells within each node, expressed as a percentage of the maximum value in the data set (CIS is shown). **b**) The graph reports the CIS median intensity in all subpopulations analyzed. The analysis is made out of three experiments. Th: T-helper; CTL: Cytotoxic T lymphocytes.

To construct the SPADE tree, we used 11 cell surface markers in treated and untreated healthy human PBMCs to identify the major immune cell populations. Sixteen additional markers were acquired. Among them, five extracellular markers were used to better define cell subpopulations. The remaining 11 intracellular makers were employed for the cytokine detection, and were excluded from the tree construction. Each node in the two dimensional representation describes a n-dimensional boundary encompassing a population of phenotypically similar cells. The size of each node in the tree is proportional to the number of cells within each population. Node color is scaled to the median intensity of marker expression. The approach uses a minimum-spanning tree algorithm, in which each node of cells is connected to its "most related" node as a means to convey the relationships between the cell clusters. As a result, the 15 manually assigned populations were segregated in 200 nodes of distinct but logically interconnected populations. These trees provide a convenient approach to map complex n-dimensional relationships into a representative 2D structure[32]. In this analysis, cisplatin (CIS) was used as marker for viability[33]. CIS is a molecule able to enter into the late apoptotic and necrotic cells that have lost membrane integrity. The SPADE tree clustering shows that GO induced cytotoxicity in all B cell subpopulations (**Figure 1a**). Monocytes and activated Th cells were also affected by the presence of GO. On the other end, the functionalized $GONH_2$ significantly reduced CIS signal in all subpopulations (**Figure 1b**, CIS median expression in distinct subpopulations). $GONH_2$ highlighted 3 times more biocompatibility in all B-cell populations than non-functionalized GO. This effect was also evident in activated cytotoxic T Lymphocytes (CTLs) and Th cells, where $GONH_2$ induced half of the GO toxicity. Overall, the functionalization of GO enhanced its biocompatibility towards the immune populations analyzed (**Figure 1a-b**) with the exception of natural killer (NK) cells and memory CTLs (see material and methods for gating strategy), in which both GO and $GONH_2$ induced minimal cytotoxicity. These results emphasize the importance of the amino group functionalization on enhancing the biocompatibility of GO-based nanomaterials. Interestingly, the same type of functionalization used to modify GO was previously found to improve the biocompatibility of other nanomaterials such as carbon nanotubes[11, 12] We further applied CyTOF to understand the functional impact of GO and $GONH_2$ on the immune subpopulations. The heatmap visualizes the median expression values of all intracellular markers used for each immune population (**Figure 2a**). GO caused a broad, non-cell-specific activation triggering the production of all cytokines analyzed in a variety of cell populations (**Figure 2a**), while $GONH_2$

Dr. Marco Orecchioni. Titolo "Biomedical applications of different nanomaterials: Characterization and interaction with the immune system"
Tesi di dottorato in Life Sciences and Biotechnologies, Università degli Studi di Sassari.

was more specific affecting, for instance, the production of only few cytokines in selected cell subpopulations. Among T-cells, GO induced the secretion of interleukin (IL) 2, 4 and 5 by Th and CTLs (**Figure 2b**).

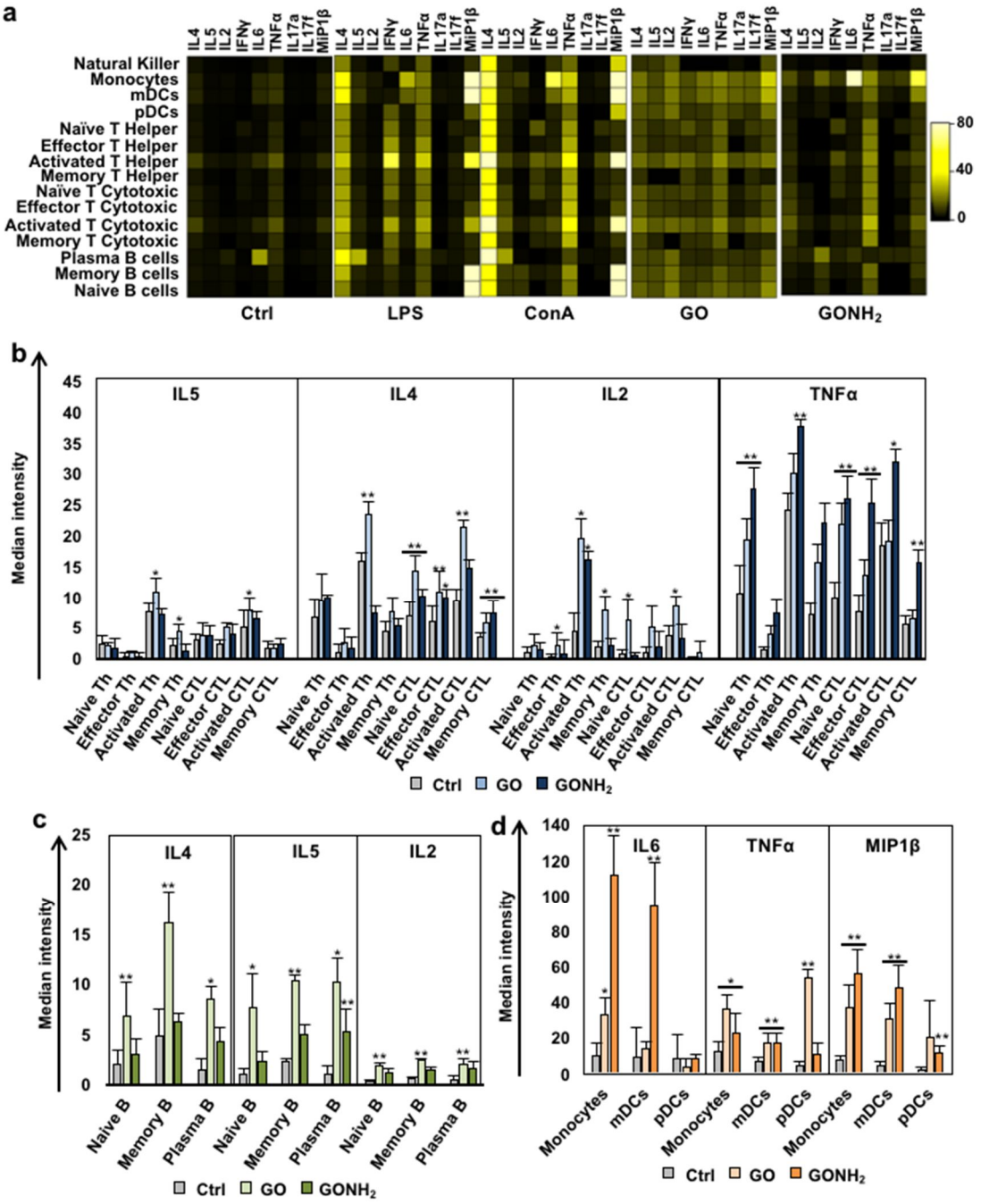

Figure 2. Analysis of the immune cell behavior using CyTOF. PBMCs were treated with GO and $GONH_2$ at the concentration of 50 $\mu g \cdot mL^{-1}$labeled with markers of immune cell lineages and cytokines, detected with CyTOF 2. **a**) Heat maps of median marker expression ratio for gated immune cell populations. Histograms of intracellular cytokine median expression. **b**) IL4, IL5, IL2 and TNFα in T-cell subpopulations. **c**) IL4, IL5 and IL2 median expression in B-cell subpopulations. **d**) IL6, TNFα and MIP1β median expression in monocytes and mDCs. The analysis is made out of three experiments (*= P value < 0.05, **= P value <0.01 Statistical analysis performed by One-Way ANOVA test between the median expression of each node into the boundaries compared with the control).

Functionalized $GONH_2$ instead selectively induced production of IL2 by activated T cells and a production of TNFα in several cells subpopulations. Moreover, $GONH_2$ did not affect production of IL5 by T-cells, and only modestly that of IL4 (**Figure 2b**). IL4/IL5 are markers of Th2 while TNFα/IL-2 of Th1 differentiation. Thus, it appears that $GONH_2$ elicits polarized Th1 immune response and a non-specific Th response. $GONH_2$ tropism for Th1 cytokines was mirrored in B-cells (**Figure 2c**). Moreover, $GONH_2$ was able to induce dendritic cell and monocyte activation skewed toward a M1 response, as demonstrated by increased production of classic M1 cytokines such as TNFα, IL6, and the CCR5 ligand CCL4 (MIP1β) (**Figure 2d**)[34, 35, 36]. Th2 responses are involved in asthmatic reactions and induction of allergy.[37] Moreover Th2 responses (sustained by M2 macrophages) favor cancer growth[38]. Conversely, Th1 responses (sustained by M1 macrophages) counteract cancer development[39, 40]. In fact, intratumoral Th1 (but not Th2) signatures have been invariably associated with favorable prognosis and responsiveness to immunotherapy [39, 41, 42, 43, 44, 45, 46, 47]. These data are of particular interest for further translational applications of amino-functionalized GOs in the immunotherapy of cancer or as a vaccine adjuvant. M1 cytokine production such as IL6, TNFα, and MIP1β after treatment with GO and $GONH_2$ is represented in **Figure 3**.

Negative controls are reported in **Figure S2**. We found increased expression of IL6 in monocytes, mDCs (monocytoid dendritic cells) and activated Th cells (red nodes) mediated mainly by $GONH_2$ (**Figure 3a**). As expected TNFα secretion was mediated by $GONH_2$ in monocytes, mDCs, activated CTLs, Th cells and in NK cells (**Figure 3b**). The expression of MIP1β was clearly observable in monocytes, mDCs and activated Th in response to both GOs. However, as previously mentioned the median intensity was higher in $GONH_2$ treated samples. GO, instead induced MIP1β expression also in B cell populations (**Figure 3c**). SPADE visualization could give further information on the impact played by GOs on single cells through heterogeneity analysis within nodes. Indeed, not all the cells into the same family display the same cytokine secretion intensity, underlining possible different maturation and/or activation stages. An example is given by TNFα secretion by CD16- NK cells treated with $GONH_2$ (**Figure 3b**) where half of the nodes included did not secrete TNFα. Overall the SPADE data suggest a cross-talk between monocytes/mDCs and CTLs/Th cells that could sustain a specific cell-mediated immunity, avoiding humoral response and possible hypersensitivity.

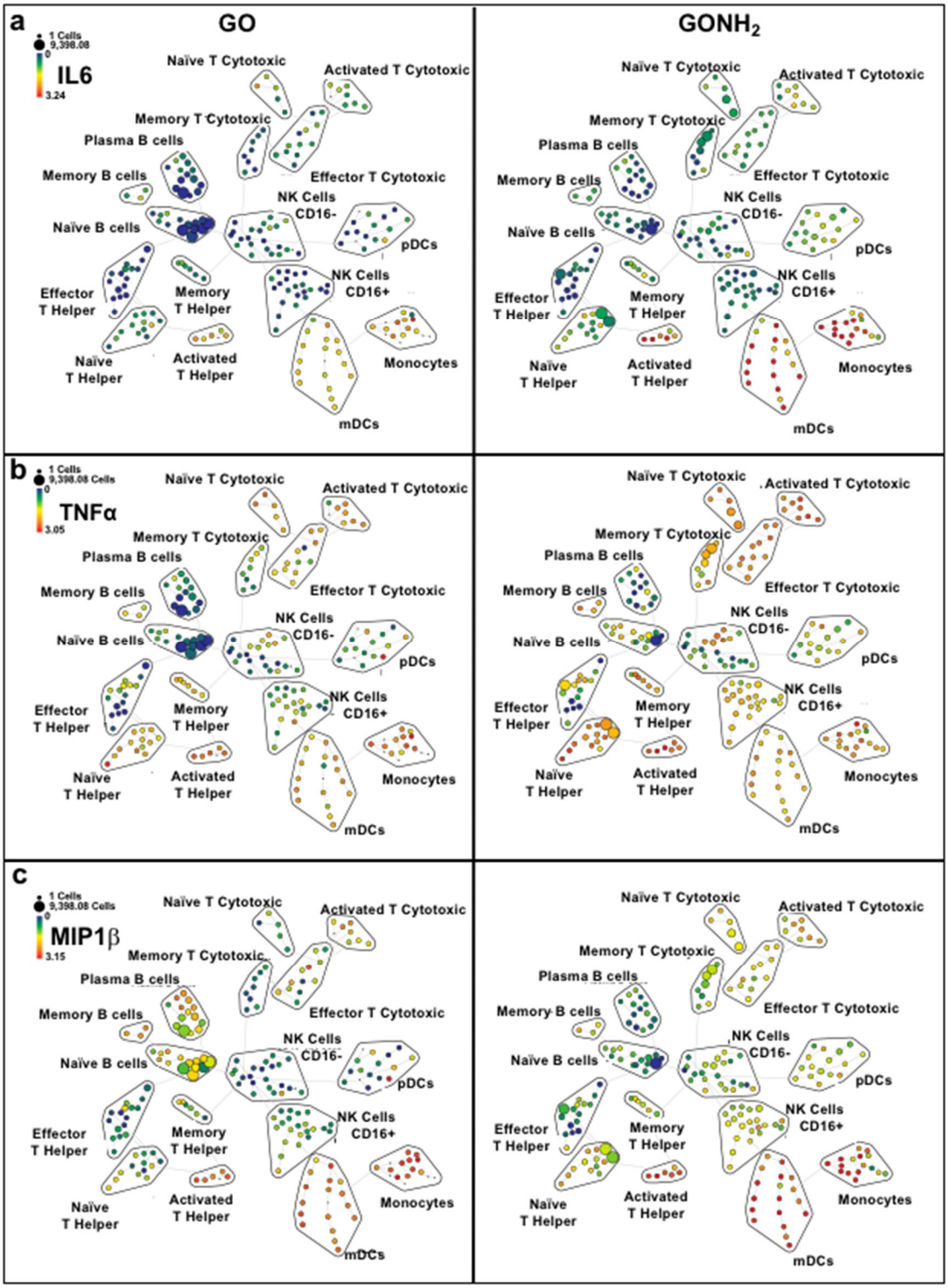

Figure 3. Summary of SPADE analysis of significantly secreted cytokines. The tree plots were constructed in the same way of Figure 1. Node color is scaled to the median intensity of marker expression of the cells within each node, expressed as a percentage of the maximum value in the data set. The spade trees show the median expression intensity of **a**) IL6; **b**) TNFα, and **c**) IL2 for GO and $GONH_2$-treated samples. The analysis is made out of three experiments.

Since this new single-cell mass cytometry technique was not previously applied to nanomaterials, we corroborated the analysis with several classical techniques to analyze cell apoptosis, necrosis, and activation and cytokine secretion. Analysis of human PBMCs using flow cytometry confirmed the trend observed with the CyTOF experiments. **Figure 4a** displays the histograms related to apoptosis and necrosis experiments [expression of Annexin V (apoptotic) and PI (necrotic) positive cells after treatment with GO and $GONH_2$] using the same conditions reported for the CyTOF analysis (P value <0.05). Data were also confirmed by a dose-response analysis (5, 25 and 50 $\mu g \cdot mL^{-1}$) using 7-amino actinomycin D (7AAD) to detect cells with compromised membranes (late apoptotic and necrotic cells). As expected, the functionalization improved the biocompatibility of GO with a reduction of necrotic events, from 42% to 24.7% (P value 0.045) (**Figure 4a**). Similar results are reported in **Figure 4b**. Indeed, at the highest concentration used, we found a reduction of necrotic events from 27.3% to 6.7% (P value 0.039) in $GONH_2$-treated samples. The improvement of biocompatibility mediated by $GONH_2$ was confirmed by hemolysis analysis in red blood cells (RBCs). Hemolysis is reported to be an undesirable effect mediated by GOs at high concentrations[48]. The release of hemoglobin from damaged RBCs after treatment with increasing doses (5, 25, 50 and 100 $\mu g \cdot mL^{-1}$) of GO and $GONH_2$ was analyzed (**Figure S3**). The highest concentration of GO was able to induce a significant release of hemoglobin, showing damage to RBCs. On the other hand, the functionalized $GONH_2$ did not damage RBCs at any of the tested concentrations (**Figure S3**). Further activation analyses were performed by flow cytometry, measuring CD69 and CD25, early and late activation markers, respectively (**Figure 4c**). Total PBMCs were treated with both GO and $GONH_2$ at the concentration of 50 $\mu g \cdot mL^{-1}$ for 24 h. $GONH_2$ induced higher (15.03%, P value 7.89E-05) expression of CD25 compared to GO (8.7%, P value 0.009) (**Figure 4c**). A similar trend was observed for CD69 expression with 8.4% (P value 0.001) and 5.8% (P value 0.012) of cells expressing the marker in $GONH_2$ and GO, respectively. Chances in cell diameter reflect the status of immune cell activation with larger size corresponding to an active status. The effect of GO and $GONH_2$ on cell size was analyzed using Scepter™ 2.0. PBMCs were treated with GO and $GONH_2$ at the concentration of 50 $\mu g \cdot mL^{-1}$ for 24 h. **Figure 4d** shows the cell diameter of lymphocytes, inactivated monocytes [**Figure 4d (i)**], and activated monocytes [**Figure 4d (ii)**]. $GONH_2$ induced higher changes in monocyte diameter compared to the untreated sample. In line with previous results on the action of $GONH_2$, we found 2.65×10^4 cells with a diameter larger than 11.75 μm,

compared to 9.78×10^3 cells for the control [**Figure 4d (iii)**]. The effect of $GONH_2$ was studied also by multiplex ELISA on the PBMC supernatants. The secretion of classical Th1/M1 cytokines such as CCL5, IL6, IL1β, and TNFα increased after stimulation with $GONH_2$ but not GO treatment (**Figure 4e**; P value < 0.05).

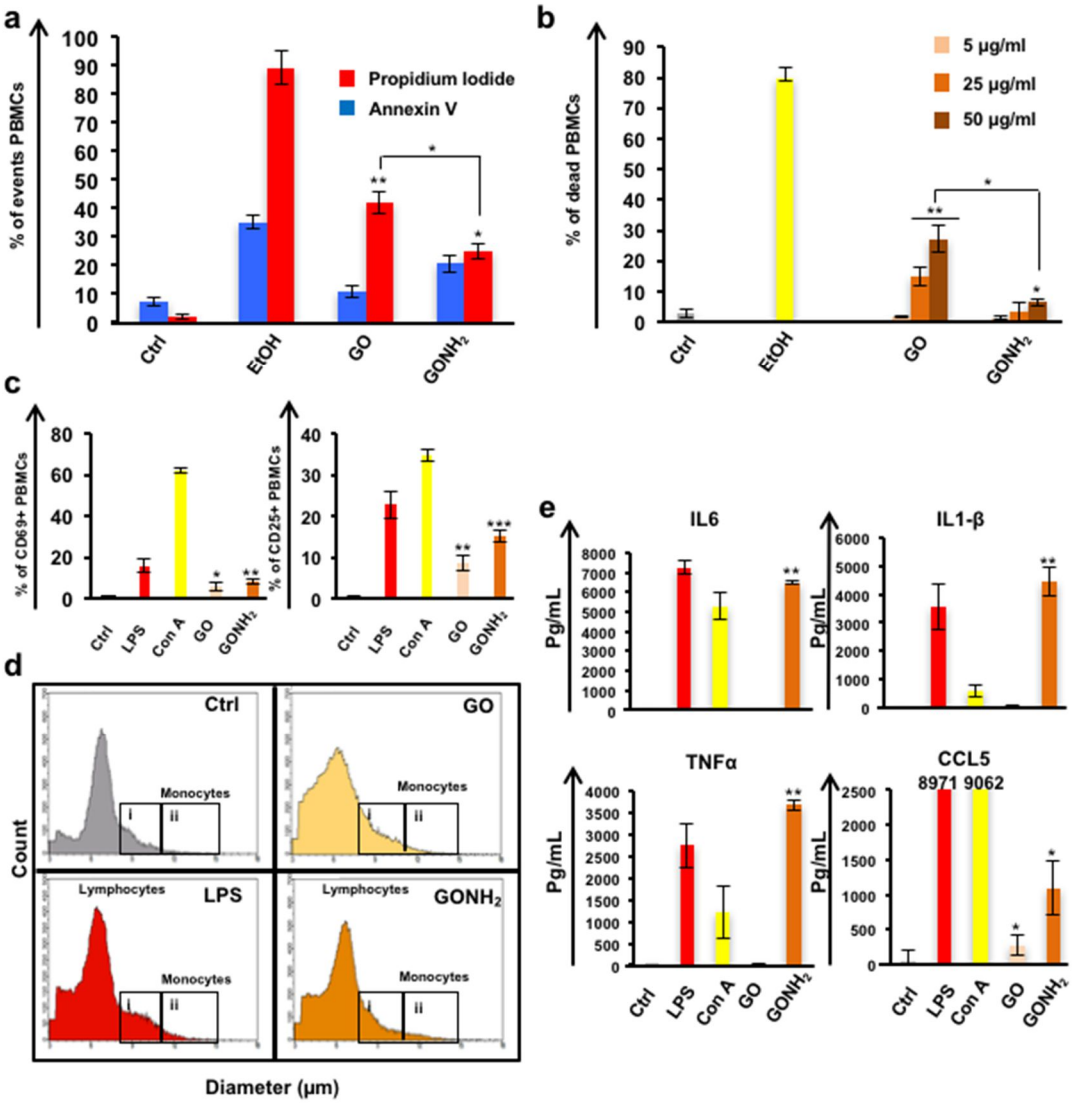

Figure 4. Standard cell viability and activation assays in ex vivo PBMCs. PBMCs were incubated with GO and $GONH_2$ at increasing doses (5, 25 and 50 $\mu g \cdot mL^{-1}$) and at a fixed dose (50 $\mu g \cdot mL^{-1}$) or left untreated (Ctrl). Data were analyzed using different stainings by flow cytometry. **a**) Necrosis and apoptosis were assessed treating the cells with 50 $\mu g \cdot mL^{-1}$using propidium iodide and Annexin V staining; ethanol was used a positive control. **b**) Percentage of late apoptotic and necrotic cells was assessed by staining with an amine-reactive dye (7AAD) after 24 h of incubation; ethanol was used as a positive control. Experiments were performed at least in triplicate (*= P value < 0.05 ** =<0.001, ***= P value 0.0001). **c**) Percentage of CD25 and CD69 cell surface activation marker expression in monocytes (50 $\mu g \cdot mL^{-1}$) (CD14 positive cells) analyzed by flow cytometry. **d**) Morphological analysis (count and diameter) of PBMCs using Scepter 2.0 highlighting the monocyte peaks (i), and activated monocytes (ii) with a diameter higher than 11.25 µm. The experiment is reported out of three; **e**) Cytokine release was assessed by multiplex ELISA on PBMCs and expressed as $pg \cdot mL^{-1}$. Surfactants of cells incubated with GO and $GONH_2$ ($\mu g \cdot mL^{-1}$) were harvested and analyzed by multiplex ELISA. Concanavalin A (ConA, 10 $\mu g \cdot mL^{-1}$) and lipopolysaccharides (LPS 2 $\mu g \cdot mL^{-1}$) were used as positive controls. All the experiments were performed at least in triplicate (*= P value < 0.05, **= P value <0.01 Statistical analysis performed by two tales student t test).

All data obtained through the use of classical techniques confirmed the CyTOF main findings, therefore supporting its use as a robust technique for comprehensive analyses of nanomaterial-immune cell interaction. To obtain a higher intensity portray of the interaction between nanomaterials and immune cells we used the Illumina Beadchip HumanHT-12 v4 genome wide technology analyzing about 47000 transcripts in GO and $GONH_2$-treated T lymphocyte (Jurkat cells) and monocyte (THP1) cell lines as representative of adaptive and innate immune responses respectively. These cell lines were incubated with GO and $GONH_2$ (50 $\mu g \cdot mL^{-1}$, 24 h) in the same conditions used for the previous CyTOF experiments. To compute the probability of genes being differentially expressed, we used a random variance *t*-test as implemented in BRB Array-Tools [see **Supporting Tables S1** and **S2.** Results were controlled for false discovery rate (FDR)]. We confirmed that the functionalization significantly reduced (P value <0.001 and FDR <0.05) the magnitude of the perturbations induced by GO (Venn diagram, **Figure 5a-c**). Overall, the number of transcripts modulated by $GONH_2$ was less than one third of the transcripts altered by GO. Following the treatment with functionalized $GONH_2$, 1163 transcripts were altered in T-cells and 977 in monocytes as compared with 4509 transcripts in T-cells and 3528 in monocytes in GO-treated samples (**Figure 5** and **Supporting Tables S1 and S2**). However, the effect of $GONH_2$ was clearly more specific. In fact 2845 transcripts were modulated in both T-cell and monocytes by GO. In contrast, only 390 transcripts were modulated in both treated cells by $GONH_2$ (**Figure 5a**). Venn diagrams in **Figures 5b** and **5c** describe the different modulation induced by GO and $GONH_2$ in the treated cells. To provide a functional interpretation of the transcriptional changes, we applied Ingenuity Pathways Analysis (IPA). The most differentially affected canonical pathways in GO- compared to $GONH_2$-treated T cells and monocytes are shown in **Figure 5d** while the 20 top canonical pathways are shown in **Figure S4**). While the perturbations induced by GO reflect the triggering of cytotoxic mechanisms, the changes induced by $GONH_2$ consist in selective immune activation of T-cells and monocytes. Indeed, the most significantly affected canonical pathway by GO are Eukaryotic Initiation Factor 2 (EIF2) signaling, oxidative phosphorylation and mTOR signaling, all related to cell metabolism and proliferative function. This effect is visible in both cell types (**Figure 5d**). More in detail, protein synthesis, as indicated by the negative Z-score of the EI2F pathway, was suppressed by GO treatment, in line with the induction of apoptotic mechanism showed by the CyTOF and flow cytometry analyses.

Conversely, the functionalized $GONH_2$ induced a coordinated induction of immune-activator pathways with limited impact on cell metabolism. Almost all the top 20 canonical pathways modulated by $GONH_2$ are related with immune functions (**Figure S4**).

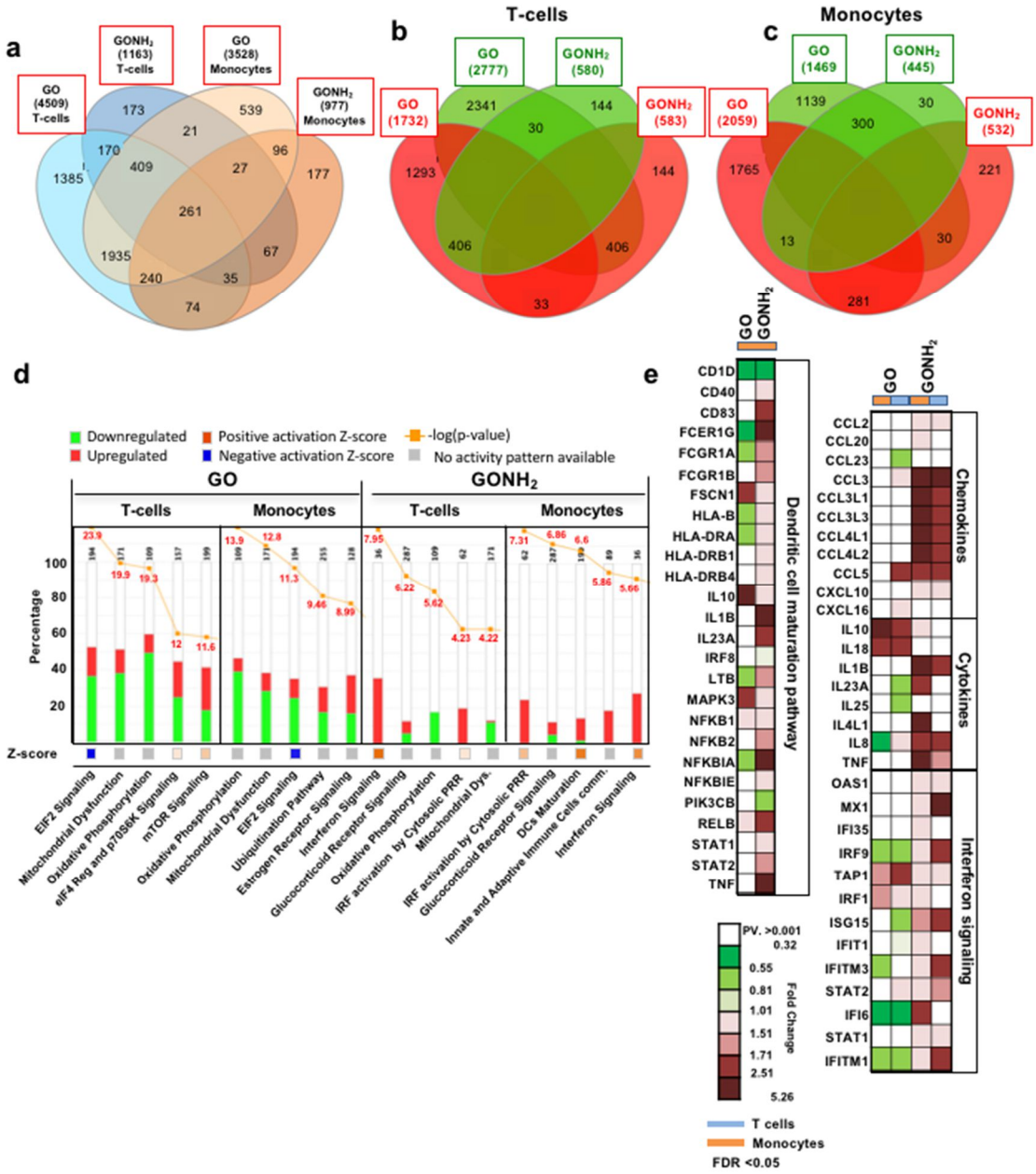

Figure 5. Gene expression impact of GO and $GONH_2$ on T- and monocyte cell lines. **a**) Venn diagrams for T-cells and monocytes reporting the number of transcripts modulated in response to graphene administration. Each Venn diagram is divided in four areas, one for each type of GO and $GONH_2$ in T-cells and monocytes. The total number of modulated genes in each areas are reported between the parentheses. **b**) Venn diagrams of differently expressed transcripts in T-cells and **c**) in monocytes. Overlapping areas indicate the number of transcripts commonly changed in their expression level between GO and $GONH_2$. Colored circles indicate the number of up-regulated (red), and down-regulated (green) transcripts with an absolute Fold Change > 1. **d**) Top 5 first canonical pathways ranking according to significance level [Fisher exact test es log (p-value) reported in red] modulated by the GO and $GONH_2$ in T-cells and monocytes identified using gene enrichment analysis. The Z-score of each pathway is expressed under each column; the –log(P value) is reported in red in top of each histogram. **e**) Expression heatmap of chemokines, cytokines, dendritc cell maturation, and interferon signaling pathway genes (as listed in IPA software) in $GONH_2$ and GO treated cells vs Controls; P-value <0.001 and FDR <0.05.

Such pathways include intracellular signaling implicated in the activation of T cells and in the maturation and activation of monocytes [e.g, interferon signaling, interferon regulatory factor (IRF) activation by pattern recognition receptor (PRR), antigen presenting and inflammasome pathways] **(Figure 5d** and **S4**). These differences for the two graphene oxides was confirmed using the gene set comparison tool in BRB Array-Tools as a scoring test to assign the functional category definitions according to the Gene Ontology database (GOd), with a P value <0.005 (see **Supporting Tables S3** and **S4**). The perturbation of the oxidative phosphorylation (OXPHOS) highlights IPA the impact on GO on cell metabolism (**Figure S5a** and **S5b**). The modulation of IFN-signaling in T-cells and DC-maturation pathway in monocytes induced by $GONH_2$ are represented in **Figure S6** and **S7**. Thus, GO compared to $GONH_2$ induces a stronger alteration of pathways related to cellular replication and metabolism (**Figure S4** and **Supporting Tables S3** and **S4**) with a downregulation of OXPHOS pathway (**Figures S5a** and **S5b**). In summary, $GONH_2$ was confirmed to upregulate immune-activation pathways without disrupting intracellular homeostasis. A list of immune-related genes modulated by $GONH_2$ in T cells and monocytes is reported in **Figure 5e**. These genes include Th1 chemokines[49] such as CXCL10 (CXCR3 ligand), CCL3, CCL3L3, CCL4L1, CCL4L2 and CCL5 (CCR5 ligands), pro-inflammatory cytokines such as TNFα and IL1ß (**Figure 5e**), and master regulators of the cross-talk between innate and innate immune response such as IRF1 and STAT1. To validate the Illumina Beadchip data, we performed real-time PCR with highly specific Taq-man probes. Again, IRF1, CCL3L3, IL1B, and CCL5 genes were consistently over-expressed only after $GONH_2$ treatment (**Figure S8a**). Further confirmation of the $GONH_2$ action at the protein level were given by ELISA through the assessment of the secretion of IL6, TNFα, and IL1β by monocytic cells (**Figure S8b**). Remarkably, these genes (i.e., CXCR3/CCR5 ligand genes, and the transcription factors STAT1 and IRF1) are central in the induction of immune-mediated tumor rejection[41, 44, 50] and their over-expression in resected tumors has been associated with favorable prognosis[43, 45, 46, 51]. Such transcripts are up-regulated in tumors from patients who are more likely to respond to immunotherapeutic approaches such as IL2[52], vaccine[53], adoptive therapies[42], and checkpoint inhibition[54, 55]. Moreover, the efficacy of cancer immunotherapy relies on the ability to trigger a Th-1/M1 anti-tumor response through the induction of the expression of the aforementioned transcripts[38, 41]. Recently, the use of different kinds of nanomaterials as immune modulators for vaccine adjuvant or immunotherapy applications have been described[56, 57, 58]. All the nano-adjuvants could greatly enhance the

immunogenicity of antigens, particularly in antigen presenting cells (APCs) such as DCs, thus helping the prevention or treatment of infectious diseases or cancer[59]. Recently, Xu *et al.* proposed the use of functionalized GO as vaccine adjuvant. GO functionalized with both polyethylene glycol and polyethyleneimine was found to promote the maturation of DCs, enhancing their cytokine secretion through the activation of multiple toll-like receptor (TLR) pathways while showing low toxicity[60]. In a similar and extensive way, the current morphological and genomic analysis suggest that $GONH_2$ might enable the initiation and induction of monocyte and DC activation possibly through TLR/PRR interactions. Moreover, our data suggests that amino-functionalized GO is likely to facilitate the differentiation of monocytes into monocyte-derived DCs (moDCs). MoDCs pulsed with certain tumor-associated antigens (and eventually prompted with functionalized GO) could expand tumor-specific T-cytotoxic cells and elicit anti-tumor immunity[61, 62, 63]

In conclusion we propose a new high-throughput strategy for the characterization of complex interactions between nanomaterials and the plethora of immune cell populations. The analysis of multicellular systems where cells carry out a diverse array of complex, and specialized functions is still a big challenge[23]. Regarding the immune system, a central issue has been the identification of the distinct subpopulation phenotypes of the specialized cells. This specialization occurs mostly through the expression of cell type-specific genes and proteins that generate the appropriate structures and molecular networks tracking their function during any different biological function and response. Single-cell mass cytometry enters successfully in this context with its unique capacity of simultaneously resolving a large amount of probes on a per-cell basis at high acquisition rates, thereby providing researchers with an unprecedented ability to phenotypically and functionally profile different cell subpopulations. This technology allows the sophisticated analysis of multiple immune cell interactions with nanomaterials, while overcoming the limitations of spectral overlap present in flow cytometry and, revealing all the possible modulations at the single-cell level.

We here focused on graphene oxide, one of the most recent biomedically promising nanomaterials. Thanks to this advanced technology, confirmed by classical flow cytometry methods, we report that amino-functionalization improves the biocompatibility of GO. Moreover, $GONH_2$ was found to induce a cell-specific activation of T cells, DCs and monocytes, which were polarized to sustain a M1/Th-1 immune response. The positive impact of nanomaterials on specific immune cells can serve as starting point for the development of

new nanoscale platforms in medicine as novel immunotherapy, vaccine carrier and nanoadjuvant tools [17]. Our pilot study paves the way for the future use of single-cell mass cytometry for a deep characterization of immune responses to any type of nanomaterials useful for biomedical applications.

Materials and Methods

Synthesis of GO

GO was prepared by a modified Hummers' method described in Ali-Boucetta *et al.*[64] with slight modifications. Briefly, 0.2 g of graphite flakes (Barnwell, UK) were mixed with 0.1 g of $NaNO_3$ (Sigma-Aldrich, UK) and 4.6 mL of 96% H_2SO_4 (Fisher Scientific, UK). After obtaining a homogenous mixture, 0.6 g of $KMnO_4$ (Sigma-Aldrich, UK) was slowly added. Temperature was carefully monitored during the reaction and was kept between 98 and 100 °C. The mixture was further diluted with 25 mL of deionized H_2O and 3% H_2O_2 (Sigma-Aldrich, UK) was added gradually for the reduction of the residual $KMnO_4$, MnO_2, and Mn_2O_7. The resulting graphitic oxide suspension was exfoliated and purified by several centrifugation steps until the pH of the supernatant was around 7 and a viscous orange/brown gel-like layer of pure GO appeared on top of the oxidation by-products and thick graphitic pieces. This layer was extracted and diluted in MilliQ water.

Synthesis of $GONH_2$

2,2'-(Ethylenedioxy)bis(ethylamine) (410 µL) was added to a 20 mL of a GO dispersion (1 $mg \cdot mL^{-1}$) in deionized water, and the mixture was stirred for two days at room temperature. The solution was then filtered using an Omnipore® polytetrafluoroethylene (PTFE) membrane (0.45 µm, Millipore). The solid was dispersed in methanol (100 mL), sonicated for 2 min and filtered again. This procedure was repeated with DMF and methanol. The solid was dispersed in deionized water and dialyzed against deionized water using a dialysis membrane of MWCO 12–14 000 Da.

Characterizations of the materials

For TEM characterization, 20 µL of sample (100 µg·mL^{-1}) were deposited on a carbon coated copper grid (Electron Microscopy Services, USA). Excess material was removed by filter paper. Imaging was performed using a FEI Tecnai 12 BioTWIN microscope (Techni, Netherlands) at an acceleration voltage of 100 kV. Images were taken with a Gatan Orius SC1000 CCD camera (GATAN, UK). Lateral size distributions were carried out using ImageJ software after counting the lateral dimension of more than 100 individual GO sheets from several TEM images. For AFM, freshly cleaved mica (Agar Scientific, UK) was used as a substrate. Pristine GO samples required a pre-coating step of the negatively charged mica surface with 20 µL of 0.01% poly-L-lysine (Sigma-Aldrich, UK). All samples were prepared by depositing 20 µL aliquots of the respective GO dispersions (100 µg·mL^{-1}) on the mica substrates and allowing them to adsorb for 2 min. Unbound structures were removed by gentle washing with 2 mL of MilliQ water and samples were left to dry at 37ºC. AFM images were acquired in air using a Multimode 8 atomic force microscope (Bruker, UK) in tapping mode, using an OTESPA tip (Bruker, UK) mounted on a tapping mode silicon cantilever with a typical resonant frequency of 300 kHz. Areas corresponding to 512x512 points were scanned at a rate of 1 Hz, using an integral gain of 1 and a proportional gain of 5; amplitude set point values were approximately constant across all measurements. The acquired height images were processed using the Nanoscope Analysis software (Version 1.4, Bruker, UK) in order to assess lateral dimensions and thickness of the GO samples. A drop of the original GO dispersions was placed onto a Tensor 27 FTIR spectrometer (Bruker, UK) equipped with a 3000 Series High Stability Temperature Controller with RS232 Control (Specac, UK) and a MKII Golden Gate Single Reflection ATR system (Specac, UK) for measurements in ATR mode. The drop was allowed to dry on the plate for 5 min at 60°C, until a dry powder remained. Transmittance spectra of GO were recorded by acquiring 32 scans between 700 and 4000 cm^{-1} with a resolution of 4 cm^{-1}. Data processing was completed using OriginPro 8.5.1 software (Origin Lab, USA). For Raman spectroscopy, the samples were prepared for analysis by drop casting 20 µL of sample (100 µg/mL) dispersion onto a glass slide. The samples were left to dry for at least 2 h at 37°C. The spectra were collected using a DXR micro-Raman spectrometer (Thermo Scientific, UK) using a λ = 633 nm laser. The spectra were considered between 500 and 3400 cm^{-1}, enabling visualization of the D and G bands. The spectra were collected at a laser power

of 0.4 mW at a magnification lens of 50× with 25 ms exposure time, and averaged over 5 different locations.

Cell culture, viability, proliferation and activation assays

Jurkat cells (T-cell line), THP1 (monocyte cell line) and PBMCs were cultured in RPMI-1640 medium added with FBS 10% and 1% of Penicillin/Streptomycin solution. PBMCs were obtained from ethylenediamine tetraacetic acid (EDTA)-venous blood samples from informed healthy male donors (25-50 years old) using a standard Ficoll-Paque (GE Healthcare) separation. Informed signed consent was obtained from all the donors. The study was reviewed and approved by the Ethics Committee of the University of Sassari. All the experiments were carried out in accordance with the approved guidelines.

The cytotoxicity was evaluated by flow cytometry (FACS Canto, BD Biosciences, Mountain View, CA, USA). PBMCs were incubated for 24 h with increasing doses of GO and $GONH_2$ (5, 25 and 50 $\mu g \cdot mL^{-1}$). Ethanol was used as a positive control, while samples incubated with cell medium alone were used as negative controls. All staining kits were purchased from Invitrogen, CA, USA: Annexin-V FITC (apoptosis), PI (necrosis), and 7AAD (late apoptosis and necrosis).

To perform the proliferation assay, the Click-iT® EdU Alexa Fluor® 488 Flow Cytometry Assay Kit (Life Technologies) was used. Experiments were performed according to the manufacturer's instructions. Cells were seeded at the concentration of $1x10^6$ cells$\cdot mL^{-1}$ in 96-multiwell rounded bottom plates. T-cell and monocyte cell lines were treated with GO and $GONH_2$ at the concentration of 50 $\mu g \cdot mL^{-1}$ and 20% of FBS or left untreated (10% FBS). 5-Ethynyl-2-deoxyuridine (EdU) were added in sterile conditions 16 h before analysis. After 48 h of incubation, cells were harvested, washed with PBS, fixed with 4% paraformaldehyde, washed in PBS plus 1% Bovine Serum Albumin (BSA), permeabilized with a saponin-based reagent and prepared for the Cu-assisted EdU-Azide Click-iT reaction. The reaction occured after adding 500 µL of Click-iT reaction cocktail (PBS, $CuSO_4$, fluorescent dye azide and reaction buffer additive) to each sample. Analyses were performed by flow cytometry (C6 Accuri using C6 software, BD Biosciences). A total of 50,000 events per sample were recorded. PBMCs were treated with GO and $GONH_2$ at the intermediate concentration of 50 $\mu g \cdot mL^{-1}$ and stained to identify immune cell populations and activation markers, CD25 and CD69 (APC-conjugated anti-CD25, 2A3 clone, PE-conjugated anti-CD69, L78 clone, BD-Bioscience

Mountain View, CA, USA). Concanavalin A (ConA, 4 $\mu g \cdot mL^{-1}$) and lipopolysaccharides (LPS, 2 $\mu g \cdot mL^{-1}$) were used as positive controls (Sigma-Aldrich, St. Louis, Missouri, USA). Staining with fluorochrome-conjugated monoclonal antibodies was performed in the dark for 20 min. Cells were analyzed by flow cytometry.

Single-cell mass cytometry

Single-cell mass cytometry analysis was completed using PBMCs purified form Buffy-Coat. The volume of the Buffy-Coat was reinstated 1 to 10 adding PBS, after that the PBMCs were purified using a standard Ficoll-Paque (GE Healthcare) separation. PBMCs were seeded at a concentrations of 3×10^6 cells per well (6 multi-well plates) and treated with GO and $GONH_2$ at a concentration of 50 $\mu g \cdot mL^{-1}$ for 24 h. After the incubation period, cells were harvested and washed with PBS. The further procedure was made following the Maxpar® Cytoplasmic/Secreted Antigen Staining protocol. Briefly, before the staining, the cells were suspended in Maxpar Cell Staining Buffer (Fluidigm, Cat# 201068) in a volume of 100 µL, into 15 mL polystyrene tubes for each sample to be stained. One hundred µL of the antibody cocktail was added to each tube. The final staining volume was 200 µL (100 µL of cell suspension plus 100 µL of antibody cocktail, in a final dilution of 1:100 for each antibody). Cells were stained using Maxpar® Human Peripheral Blood Phenotyping and Human Intracellular Cytokine I panel kits (Fluidigm® Cat# 201304 and 201308). Samples were gently vortexed and incubated for 30 min at room temperature (RT). After incubation, the samples were washed twice by adding 2 mL Maxpar Cell Staining Buffer to each tube, centrifuged for 5 min at 600 × *g* and the supernatant discarded. Cells were resuspended in residual volume by gently vortexing and incubated for 1h at RT in the intercalation solution, composed of Cell-ID Intercalator-Ir (Fluidigm, Cat# 201192A, 125 µM) into Maxpar Fix and Perm Buffer (Fluidigm, Cat# 201067) to a final concentration of 125 nM (a 1000× dilution of the 125 µM stock solution). Cells were washed twice by adding 2 mL of Maxpar Cell Staining Buffer and centrifuged for 5 min at 800 × *g*. Pellets obtained were resuspended with 2 mL of Milli-Q water (Millipore). Prior to mass cytometry data acquisition, the cell concentration was adjusted to 2.5–5 × 10^5/mL with Milli-Q water and the cell suspension was filtered into 5 mL round bottom polystyrene tubes with a 30 µm-cell strainer cap. Data was analyzed using mass cytometry platform, of DVS Sciences (CyTOF2), after stabilization and calibration of the instrument. To construct the

SPADE tree, we used 11 cell surface markers listed as follow: CD45, CD3, CD4, CD8a, CD20, CD19, CD14, CD16, CD11c, CD123 and HLADR.

Hemolysis analysis

Hemolysis test was conducted following previously used protocols as described by Li H *et al*.[65] Fresh human whole blood was taken from volunteer healthy donors stabilized with 0.2% EDTA. Serum was removed from blood samples by centrifugation at 200 g for 5 minutes. Resulting RBCs were washed five times with sterile isotonic PBS and then diluted 10 X with 0.2% EDTA. The hemolytic activity of GO and $GONH_2$ at different concentrations (5, 25, 50, 100 $\mu g \cdot mL^{-1}$) were determined by the incubation of graphenes with the RBC suspension (0.2 mL, 4×10^8 cells$\cdot mL^{-1}$) in a final volume of 1 mL, completed with PBS. After vortexing, the mixtures were left at room temperature for 2 h, NCs and intact RBCs were removed by centrifugation. A microplate reader (Sunrise, Tecan) measured the absorbance (A) of the hemoglobin in the supernatant at 570 nm, with the absorbance at 620 nm as a reference.

Cytokine assay and microarrays analysis

Total mRNA was extracted with TriZol Reagent (TriZol, Invitrogen, Carlsbad, CA, USA) and purified using the RNAeasy mini kit (Qiagen, Valencia, CA, USA). RNA purity was assessed by spectrophotometric analysis and integrity by microfluidic molecular sizing using the Bioanalyzer 2100 (Agilent). Samples with RIN (RNA Integrity Number) less than 8 were discarded. RNA (1 μg) was converted in cRNA and labeled (Illumina totalPrep RNA amplification kit, Ambion). Biotinylated cRNA was hybridized onto the Illumina HumanHT-12 v4 (Illumina, Inc., San Diego, CA, U.S.A.). The Illumina HumanHT-12 v4 interrogates the expression of 47,000 gene probes derived from the National Center for Biotechnology Information (NCBI) Reference Sequence RefSeq Release 38 (November 7, 2009) and other sources. Probe intensity and gene expression data were generated using the Illumina GenomeStudio software V2011.1 (Gene Expression Module V1.9.0). After extraction, cDNA synthesis was performed using a SuperScript III reverse transcriptase (Invitrogen, Carlsbad, CA, USA).

Cell culture supernatants from PBMCs were used to quantify the secretion of cytokines using a MILLIPLEX MAP plex Cytokine Kit (HCYTOMAG-60K, Millipore, Billerica, MA) [IL1β,

TNFα, IL6, Rantes (CCL5)]. Experiments and statistical analysis were performed as previously showed[10, 12].

Real-time PCR

Real-time PCR was performed as follows: 1 mg of total RNA was reverse transcribed using the superscript IV reverse transcription kit (Invitrogen) following standard protocols. The cDNA reaction (20 mL) was brought to a 100 mL volume with H_2O and 1 mL used for each PCR reaction. Real-time PCR was performed on an Applied Biosystems 7300 thermal cycler, using the Applied Biosystems real-time PCR master mix and the following premade Taqman gene expression assays: GAPDH Hs99999905_m1 and ACTB Hs99999903_m1 as housekeeping genes, IRF1 Hs00971966_g1, CCL3L3 Hs03407473_uh, CCL5 HS99999048_m1 and IL1B Hs01555410_m1. All experiments were performed in triplicate. Gene expression measurements were computed by the $2^{\Delta\Delta cT}$ method.

Statistical analysis

The statistical analysis of CyTOF data was performed as described by Bendal SC *et al.* [32]. Briefly, normalized, background-subtracted FCS files were imported into Cytobank for single cell and population gating. The gating strategy for the different subpopulations is reported in **Figure S9**. Cytobank was also used to create the heatmap comparing fluorescence and mass cytometry measurements using log2 ratio of the stimulated population with mean fluorescent intensity (MFI) versus the unstimulated control. For spanning tree visualization and comparison, singlet-gated FCS files were analyzed in Cytobank using the SPADE tool comparing the median fluorescence intensity.

Statistical analyses for flow cytometry were performed using FACS Diva software (BD-Bioscience Mountain View, CA, USA). All the experiments were performed at least in triplicate. Statistical analyses for multiple cytokine assays were performed using Student's t-test. Data indicated with a star were considered statistically significant (two-tales P value <0.05). Data are presented as mean ± SD. Multiplex ELISA tests on isolated human primary PMBCs were performed in samples from at least 3 different donors. Immune gene array data were analyzed by the comparative threshold cycle (CT) method. Relative quantification of gene expression using the $2^{\Delta\Delta Ct}$ method correlated with the absolute gene quantification obtained using a standard curve. Data were analyzed with RT2 profiler PCR array data analysis software

(http://pcrdataanalysis.sabiosciences.com/pcr/arrayanalysis.php). Whole genome expression measurements were extracted and normalized using the Illumina GenomeStudio software V2011.1 (Gene Expression Module V1.9.0). The same software was used for QC analysis of the Beadchips. Statistical analysis and visualization of gene expression data were performed using BRBArrayTools, developed by R. Simon and the BRBArrayTools Development Team (http://linus.nci.nih.gov/BRB-ArrayTools.html). We identified genes that were differentially expressed among the two classes by using a multivariate permutation test. We used the multivariate permutation test to provide 80% confidence that the proportion of false discoveries did not exceed 5%. The test statistics used are random variance t-statistics for each gene. Although t-statistics were used, the multivariate permutation test is non-parametric and does not require the assumption of Gaussian distributions. We identified gene ontology database (GOd) groups of genes whose expression was differentially regulated among the classes. This analysis is different than annotating a gene list using GOd categories. For each group, we computed the number of genes represented on the microarray in that group, and the statistical significance P value for each gene. These P values reflect differential expression among classes and were computed based on random variance T-tests or F-tests. For a GOd group, two statistics are computed that summarize the P values for genes in the group; the Fisher (LS) statistic and the Kolmogorov-Smirnov (KS) statistic as described in (Simon R and Lam A. BRB-ArrayTools User Guide, version 3.2. Biometric Research Branch, National Cancer Institute; http://linus.nci.nih.gov/brb). Samples of n genes are randomly selected from genes represented on the array and the summary statistic computed for those random samples. The significance level associated with the gene ontology database category is the proportion of the random samples giving as large a value of the summary statistic as in the actual n genes of the database category. For each GOd category, two significance levels are computed, corresponding to the two summary statistics. We considered a GOd category significantly differentially regulated if either significance level was less than 0.005. We considered all GOd categories with between 5 and 100 genes represented on the array. Some of the categories were overlapping. We also uploaded the gene expression data to the "Ingenuity Pathway analysis" (IPA) to visualize the expression levels of genes in relevant pathway charts.

Acknowledgments

This work was partly supported by the Fondazione Banco di Sardegna (grant no° 2015.0077 to L.G.D.), the Gianfranco del Prete Association "The future: medicine, biology and nanotechnology Award" to L.G.D., the Italian Association against Leukemia (AIL) (early career grant to L.G.D.). This work was partly supported by the Centre National de la Recherche Scientique (CNRS) by the Agence Nationale de la Recherche (ANR) through the LabEx project Chemistry of Complex Systems (ANR-10-LABX-0026_CSC) (to A.B.), and by the International Center for Frontier Research in Chemistry (icFRC). The authors gratefully acknowledge financial support from EU H2020-Adhoc-2014-20 GrapheneCore1 (no. 696656), and from ANR (ANR-15-GRFL-0001-05) and MIUR JTC Graphene 2015 (G-IMMUNOMICS project).

References

1. Xia Y. Nanomaterials at work in biomedical research. *Nat Mater* 2008, **7**(10)**:** 758-760.
2. Geim AK, Novoselov KS. The rise of graphene. *Nat Mater* 2007, **6**(3)**:** 183-191.
3. Ferrari AC, Bonaccorso F, Fal'ko V, Novoselov KS, Roche S, Boggild P*, et al.* Science and technology roadmap for graphene, related two-dimensional crystals, and hybrid systems. *Nanoscale* 2015, **7**(11)**:** 4598-4810.
4. Wang K, Ruan J, Song H, Zhang J, Wo Y, Guo S*, et al.* Biocompatibility of Graphene Oxide. *Nanoscale Res Lett* 2011, **6**(1)**:** 8.
5. Orecchioni M, Bedognetti D, Sgarrella F, Marincola FM, Bianco A, Delogu LG. Impact of carbon nanotubes and graphene on immune cells. *J Transl Med* 2014, **12:** 138.
6. Yang K, Wan J, Zhang S, Zhang Y, Lee ST, Liu Z. In vivo pharmacokinetics, long-term biodistribution, and toxicology of PEGylated graphene in mice. *ACS Nano* 2011, **5**(1)**:** 516-522.
7. Sasidharan A, Panchakarla LS, Sadanandan AR, Ashokan A, Chandran P, Girish CM*, et al.* Hemocompatibility and macrophage response of pristine and functionalized graphene. *Small* 2012, **8**(8)**:** 1251-1263.
8. Schinwald A, Murphy FA, Jones A, MacNee W, Donaldson K. Graphene-based nanoplatelets: a new risk to the respiratory system as a consequence of their unusual aerodynamic properties. *ACS Nano* 2012, **6**(1)**:** 736-746.
9. Li Y, Liu Y, Fu Y, Wei T, Le Guyader L, Gao G*, et al.* The triggering of apoptosis in macrophages by pristine graphene through the MAPK and TGF-beta signaling pathways. *Biomaterials* 2012, **33**(2)**:** 402-411.

10. Orecchioni M, Jasim DA, Pescatori M, Manetti R, Fozza C, Sgarrella F*, et al.* Molecular and Genomic Impact of Large and Small Lateral Dimension Graphene Oxide Sheets on Human Immune Cells from Healthy Donors. *Adv Healthc Mater* 2016, **5**(2)**:** 276-287.
11. Delogu LG, Venturelli E, Manetti R, Pinna GA, Carru C, Madeddu R*, et al.* Ex vivo impact of functionalized carbon nanotubes on human immune cells. *Nanomedicine (Lond)* 2012, **7**(2)**:** 231-243.
12. Pescatori M, Bedognetti D, Venturelli E, Menard-Moyon C, Bernardini C, Muresu E*, et al.* Functionalized carbon nanotubes as immunomodulator systems. *Biomaterials* 2013, **34**(18)**:** 4395-4403.
13. Delogu LG, Vidili G, Venturelli E, Menard-Moyon C, Zoroddu MA, Pilo G*, et al.* Functionalized multiwalled carbon nanotubes as ultrasound contrast agents. *Proc Natl Acad Sci U S A* 2012, **109**(41)**:** 16612-16617.
14. Orecchioni M, Menard-Moyon C, Delogu LG, Bianco A. Graphene and the immune system: Challenges and potentiality. *Adv Drug Deliv Rev* 2016.
15. Russier J, Treossi E, Scarsi A, Perrozzi F, Dumortier H, Ottaviano L*, et al.* Evidencing the mask effect of graphene oxide: a comparative study on primary human and murine phagocytic cells. *Nanoscale* 2013, **5**(22)**:** 11234-11247.
16. Bhattacharya K, Mukherjee SP, Gallud A, Burkert SC, Bistarelli S, Bellucci S*, et al.* Biological interactions of carbon-based nanomaterials: From coronation to degradation. *Nanomedicine* 2016, **12**(2)**:** 333-351.
17. Zolnik BS, Gonzalez-Fernandez A, Sadrieh N, Dobrovolskaia MA. Nanoparticles and the immune system. *Endocrinology* 2010, **151**(2)**:** 458-465.
18. Goldberg MS. Immunoengineering: how nanotechnology can enhance cancer immunotherapy. *Cell* 2015, **161**(2)**:** 201-204.
19. Fessenden M. The cell menagerie: human immune profiling. *Nature* 2015, **525**(7569)**:** 409-411.
20. Janes MR, Rommel C. Next-generation flow cytometry. *Nat Biotechnol* 2011, **29**(7)**:** 602-604.
21. Spitzer MH, Nolan GP. Mass Cytometry: Single Cells, Many Features. *Cell* 2016, **165**(4)**:** 780-791.

22. Bendall SC, Nolan GP. From single cells to deep phenotypes in cancer. *Nat Biotechnol* 2012, **30**(7)**:** 639-647.
23. Benoist C, Hacohen N. Immunology. Flow cytometry, amped up. *Science* 2011, **332**(6030)**:** 677-678.
24. Doerr A. A flow cytometry revolution. *Nat Methods* 2011, **8**(7)**:** 531.
25. Vacchi IA, Spinato C, Raya J, Bianco A, Menard-Moyon C. Chemical reactivity of graphene oxide towards amines elucidated by solid-state NMR. *Nanoscale* 2016, **8**(28)**:** 13714-13721.
26. Georgakilas V, Bourlinos AB, Zboril R, Steriotis TA, Dallas P, Stubos AK*, et al.* Organic functionalisation of graphenes. *Chem Commun (Camb)* 2010, **46**(10)**:** 1766-1768.
27. Wang B, Luo B, Liang M, Wang A, Wang J, Fang Y*, et al.* Chemical amination of graphene oxides and their extraordinary properties in the detection of lead ions. *Nanoscale* 2011, **3**(12)**:** 5059-5066.
28. Ferrari AC, Basko DM. Raman spectroscopy as a versatile tool for studying the properties of graphene. *Nat Nanotechnol* 2013, **8**(4)**:** 235-246.
29. Jasim DA M-MC, Begin D, Bianco A, Kostarelos K. Tissue distribution and urinary excretion of intravenously administered chemically functionalized graphene oxide sheets. *Chem Sci* 2015, **6:** 3952-3964.
30. Acik M, Mattevi C, Gong C, Lee G, Cho K, Chhowalla M*, et al.* The role of intercalated water in multilayered graphene oxide. *ACS Nano* 2010, **4**(10)**:** 5861-5868.
31. Bitounis D, Ali-Boucetta H, Hong BH, Min DH, Kostarelos K. Prospects and challenges of graphene in biomedical applications. *Adv Mater* 2013, **25**(16)**:** 2258-2268.
32. Bendall SC, Simonds EF, Qiu P, Amir el AD, Krutzik PO, Finck R*, et al.* Single-cell mass cytometry of differential immune and drug responses across a human hematopoietic continuum. *Science* 2011, **332**(6030)**:** 687-696.
33. Fienberg HG, Simonds EF, Fantl WJ, Nolan GP, Bodenmiller B. A platinum-based covalent viability reagent for single-cell mass cytometry. *Cytometry A* 2012, **81**(6)**:** 467-475.
34. Sica A, Mantovani A. Macrophage plasticity and polarization: in vivo veritas. *J Clin Invest* 2012, **122**(3)**:** 787-795.
35. Italiani P, Boraschi D. From Monocytes to M1/M2 Macrophages: Phenotypical vs. Functional Differentiation. *Front Immunol* 2014, **5:** 514.

36. Buttari B, Profumo E, Segoni L, D'Arcangelo D, Rossi S, Facchiano F*, et al.* Resveratrol counteracts inflammation in human M1 and M2 macrophages upon challenge with 7-oxo-cholesterol: potential therapeutic implications in atherosclerosis. *Oxid Med Cell Longev* 2014, **2014:** 257543.
37. Farace C, Sanchez-Moreno P, Orecchioni M, Manetti R, Sgarrella F, Asara Y*, et al.* Immune cell impact of three differently coated lipid nanocapsules: pluronic, chitosan and polyethylene glycol. *Sci Rep* 2016, **6:** 18423.
38. Mantovani A, Romero P, Palucka AK, Marincola FM. Tumour immunity: effector response to tumour and role of the microenvironment. *Lancet* 2008, **371**(9614)**:** 771-783.
39. Jin P, Zhao Y, Liu H, Chen J, Ren J, Jin J*, et al.* Interferon-gamma and Tumor Necrosis Factor-alpha Polarize Bone Marrow Stromal Cells Uniformly to a Th1 Phenotype. *Sci Rep* 2016, **6:** 26345.
40. Jin P, Civini S, Zhao Y, De Giorgi V, Ren J, Sabatino M*, et al.* Direct T cell-tumour interaction triggers TH1 phenotype activation through the modification of the mesenchymal stromal cells transcriptional programme. *Br J Cancer* 2014, **110**(12)**:** 2955-2964.
41. Galon J, Angell HK, Bedognetti D, Marincola FM. The continuum of cancer immunosurveillance: prognostic, predictive, and mechanistic signatures. *Immunity* 2013, **39**(1)**:** 11-26.
42. Bedognetti D, Spivey TL, Zhao Y, Uccellini L, Tomei S, Dudley ME*, et al.* CXCR3/CCR5 pathways in metastatic melanoma patients treated with adoptive therapy and interleukin-2. *Br J Cancer* 2013, **109**(9)**:** 2412-2423.
43. Miller LD, Chou JA, Black MA, Print C, Chifman J, Alistar A*, et al.* Immunogenic Subtypes of Breast Cancer Delineated by Gene Classifiers of Immune Responsiveness. *Cancer Immunol Res* 2016, **4**(7)**:** 600-610.
44. Wang E, Bedognetti D, Marincola FM. Prediction of response to anticancer immunotherapy using gene signatures. *J Clin Oncol* 2013, **31**(19)**:** 2369-2371.
45. Bedognetti D, Hendrickx W, Ceccarelli M, Miller LD, Seliger B. Disentangling the relationship between tumor genetic programs and immune responsiveness. *Curr Opin Immunol* 2016, **39:** 150-158.

46. Bedognetti D, Hendrickx W, Marincola FM, Miller LD. Prognostic and predictive immune gene signatures in breast cancer. *Curr Opin Oncol* 2015, **27**(6)**:** 433-444.
47. Tosolini M, Kirilovsky A, Mlecnik B, Fredriksen T, Mauger S, Bindea G*, et al.* Clinical impact of different classes of infiltrating T cytotoxic and helper cells (Th1, th2, treg, th17) in patients with colorectal cancer. *Cancer Res* 2011, **71**(4)**:** 1263-1271.
48. Liao KH, Lin YS, Macosko CW, Haynes CL. Cytotoxicity of graphene oxide and graphene in human erythrocytes and skin fibroblasts. *ACS Appl Mater Interfaces* 2011, **3**(7)**:** 2607-2615.
49. Weiss GR, Grosh WW, Chianese-Bullock KA, Zhao Y, Liu H, Slingluff CL, Jr.*, et al.* Molecular insights on the peripheral and intratumoral effects of systemic high-dose rIL-2 (aldesleukin) administration for the treatment of metastatic melanoma. *Clin Cancer Res* 2011, **17**(23)**:** 7440-7450.
50. Panelli MC, Stashower ME, Slade HB, Smith K, Norwood C, Abati A*, et al.* Sequential gene profiling of basal cell carcinomas treated with imiquimod in a placebo-controlled study defines the requirements for tissue rejection. *Genome Biol* 2007, **8**(1)**:** R8.
51. Murtas D, Maric D, De Giorgi V, Reinboth J, Worschech A, Fetsch P*, et al.* IRF-1 responsiveness to IFN-gamma predicts different cancer immune phenotypes. *Br J Cancer* 2013, **109**(1)**:** 76-82.
52. Bedognetti D, Wang E, Sertoli MR, Marincola FM. Gene-expression profiling in vaccine therapy and immunotherapy for cancer. *Expert Rev Vaccines* 2010, **9**(6)**:** 555-565.
53. Ulloa-Montoya F, Louahed J, Dizier B, Gruselle O, Spiessens B, Lehmann FF*, et al.* Predictive gene signature in MAGE-A3 antigen-specific cancer immunotherapy. *J Clin Oncol* 2013, **31**(19)**:** 2388-2395.
54. Ji RR, Chasalow SD, Wang L, Hamid O, Schmidt H, Cogswell J*, et al.* An immune-active tumor microenvironment favors clinical response to ipilimumab. *Cancer Immunol Immunother* 2012, **61**(7)**:** 1019-1031.
55. Ascierto ML, McMiller TL, Berger AE, Danilova L, Anders RA, Netto GJ*, et al.* The Intratumoral Balance between Metabolic and Immunologic Gene Expression Is Associated with Anti-PD-1 Response in Patients with Renal Cell Carcinoma. *Cancer Immunol Res* 2016, **4**(9)**:** 726-733.

56. Xu L, Liu Y, Chen Z, Li W, Liu Y, Wang L*, et al.* Surface-engineered gold nanorods: promising DNA vaccine adjuvant for HIV-1 treatment. *Nano Lett* 2012, **12**(4)**:** 2003-2012.

57. Xu L, Liu Y, Chen Z, Li W, Liu Y, Wang L*, et al.* Morphologically virus-like fullerenol nanoparticles act as the dual-functional nanoadjuvant for HIV-1 vaccine. *Adv Mater* 2013, **25**(41)**:** 5928-5936.

58. Moon JJ, Suh H, Bershteyn A, Stephan MT, Liu H, Huang B*, et al.* Interbilayer-crosslinked multilamellar vesicles as synthetic vaccines for potent humoral and cellular immune responses. *Nat Mater* 2011, **10**(3)**:** 243-251.

59. Palucka K, Banchereau J. Cancer immunotherapy via dendritic cells. *Nat Rev Cancer* 2012, **12**(4)**:** 265-277.

60. Xu L, Xiang J, Liu Y, Xu J, Luo Y, Feng L*, et al.* Functionalized graphene oxide serves as a novel vaccine nano-adjuvant for robust stimulation of cellular immunity. *Nanoscale* 2016, **8**(6)**:** 3785-3795.

61. Schuler-Thurner B, Dieckmann D, Keikavoussi P, Bender A, Maczek C, Jonuleit H*, et al.* Mage-3 and influenza-matrix peptide-specific cytotoxic T cells are inducible in terminal stage HLA-A2.1+ melanoma patients by mature monocyte-derived dendritic cells. *J Immunol* 2000, **165**(6)**:** 3492-3496.

62. Leon B, Ardavin C. Monocyte-derived dendritic cells in innate and adaptive immunity. *Immunol Cell Biol* 2008, **86**(4)**:** 320-324.

63. Steinman RM. Dendritic cells in vivo: a key target for a new vaccine science. *Immunity* 2008, **29**(3)**:** 319-324.

64. Ali-Boucetta H, Bitounis D, Raveendran-Nair R, Servant A, Van den Bossche J, Kostarelos K. Purified graphene oxide dispersions lack in vitro cytotoxicity and in vivo pathogenicity. *Adv Healthc Mater* 2013, **2**(3)**:** 433-441.

65. Li HC, Hsieh FJ, Chen CP, Chang MY, Hsieh PC, Chen CC*, et al.* The hemocompatibility of oxidized diamond nanocrystals for biomedical applications. *Sci Rep* 2013, **3:** 3044.

Supporting informations

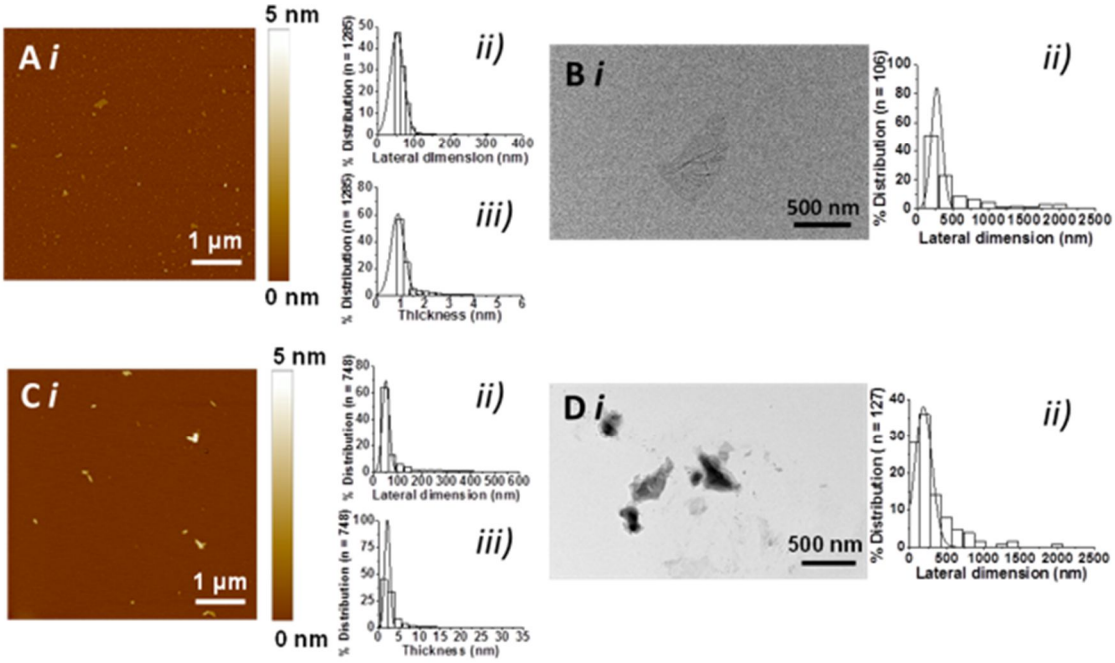

Parameter	Technique	GO	$GONH_2$
Lateral dimension	TEM	50 nm – 1 µm	50 nm –1µm
	AFM	50 nm – 300 nm	50 nm – 590 nm
Thickness	AFM	0.5 nm – 5.5 nm	0.4 nm – 10 nm
I(D)/I(G)	Raman	1.35 ± 0.01	1.42 ± 0.11

Figure S1. Physicochemical characterization of GO and $GONH_2$. GO structural characterization using **A**i) AFM, scrutinized for ii) lateral dimension and iii) thickness. **B**i) Representative TEM micrographs with ii) lateral dimension distribution. $GONH_2$ characterization using Ci) AFM, scrutinized for ii) lateral dimension and iii) thickness. **D**i) Representative TEM micrograph with ii) lateral dimension distribution. **E**) Raman spectra of GO (red) and $GONH_2$ (blue). **F**) FT-IR spectra of GO (red) and $GONH_2$ (blue). G) UV-Vis spectra of GO (red) and $GONH_2$ (blue). H) Summary of the characterization.

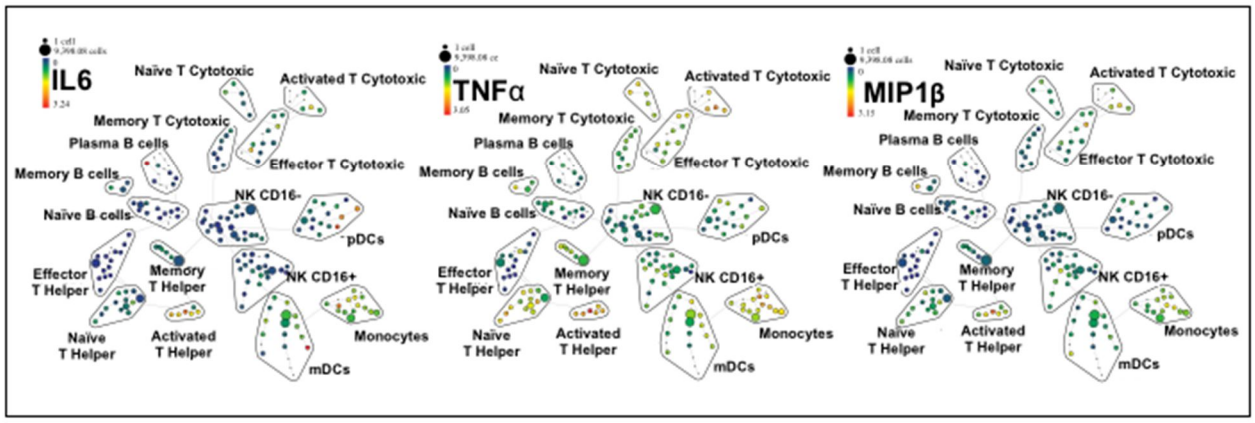

Figure S2. Summary of SPADE analysis. SPADE tree plots of untreated samples (CTRL) for significantly expressed cytokines (IL6, TNFα and MIP1β).

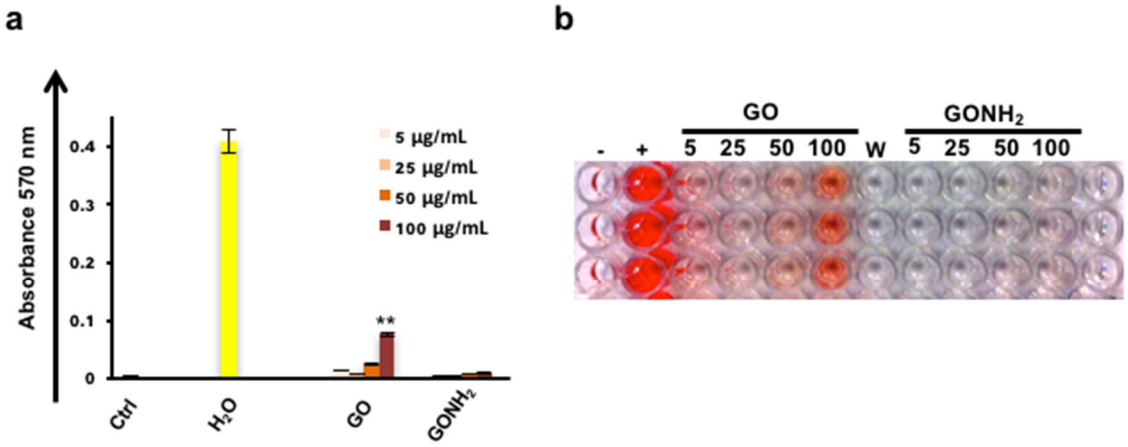

Figure S3. **Hemolysis analysis**. GO and $GONH_2$ were incubated (at increasing concentrations of 5, 25, 50, 100 $\mu g \cdot mL^{-1}$) with red blood cells (RBCs) at 25°C for 2 h. **a**) Sample absorbance measured at 570 nm. **b**) Pictures of human RBCs treated with the different GOs. The red color of the solution is due to the release of hemoglobin from the damaged RBCs. PBS mixed with RBCs (-) and ultrapure water mixed with RBCs (+) served as negative and positive control, respectively. PBS alone was used as additional control (W). The experiments were performed in triplicate (**= P value <0.01 Statistical analysis performed by two tales student t test).

Figure S4. Ingenuity pathways analysis. Top 20 canonical pathways and Z-score ranking according to significance level [Fisher exact test -log (p-value)] modulated by GO and $GONH_2$ in **a**) T-cells and **b**) monocytes identified using IPA software.

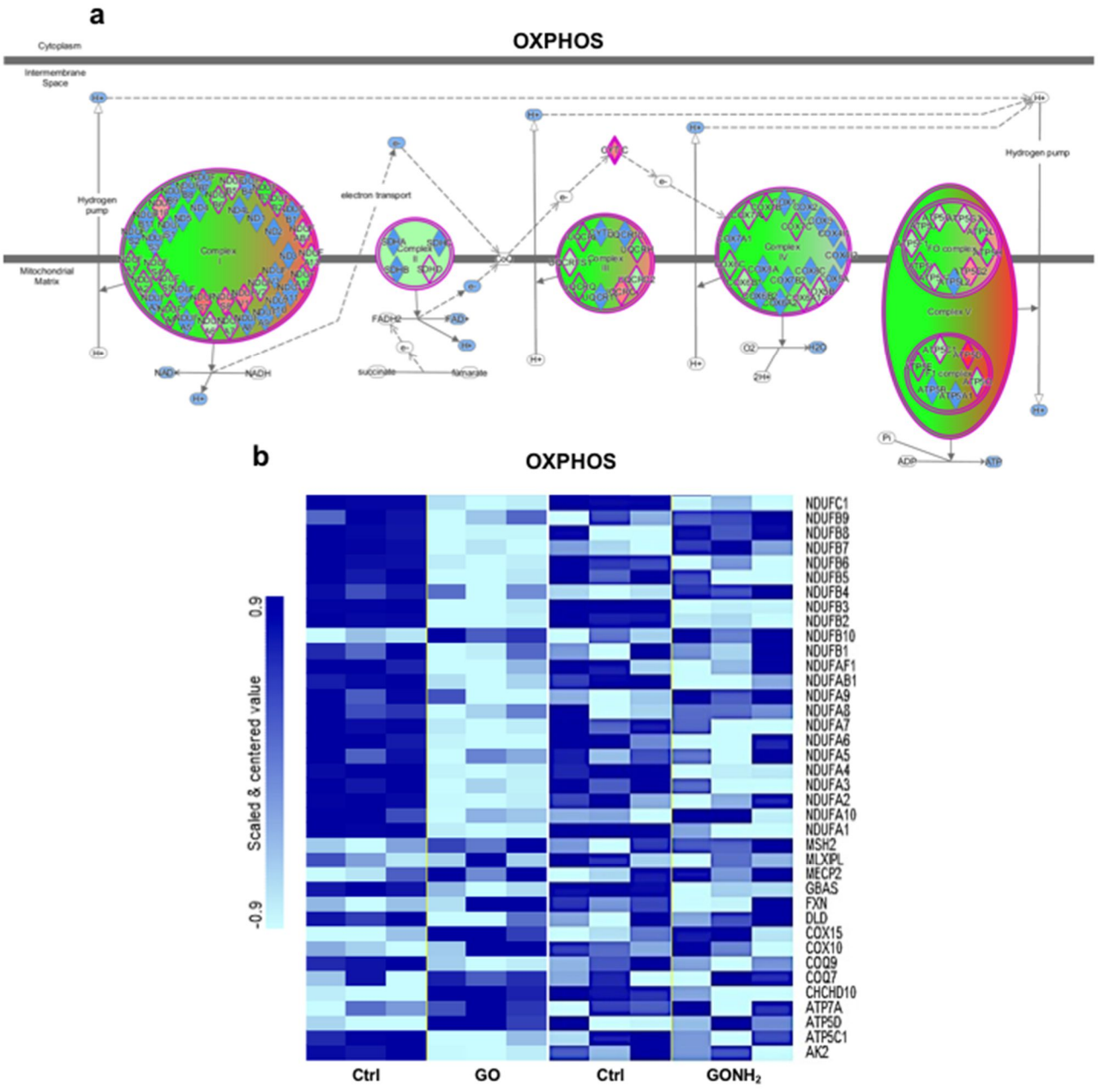

Figure S5. Gene set enrichment with Gene Ontology and IPA analysis. a)OXPHOS pathway found modulated in GO sample. **b)** Gene ontology visualizationheatmap of OXPHOS pathway after treatment with GO and GONH2 in T-cells.

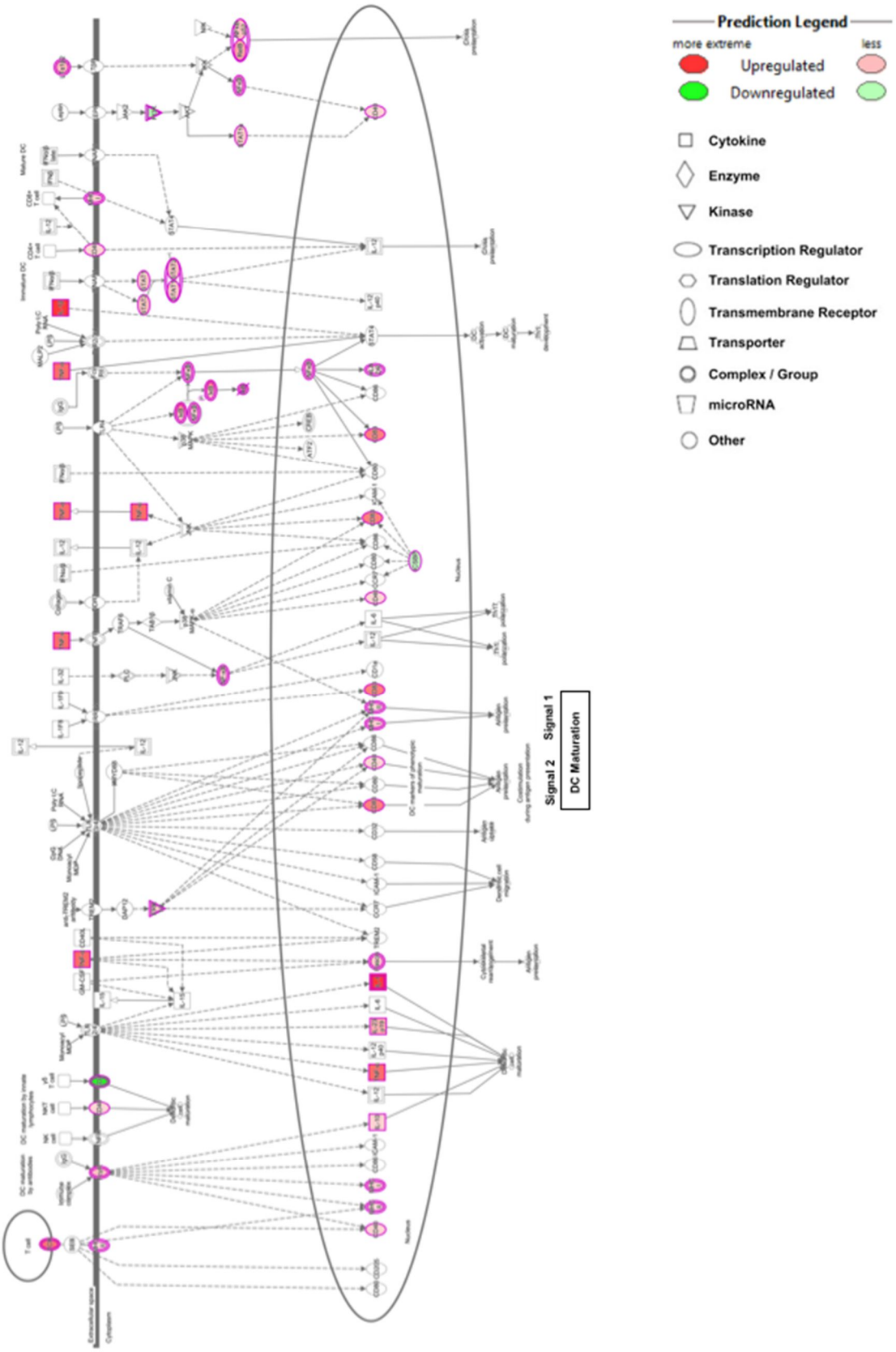

Figure S6. Significant canonical pathways. DC maturation pathway in monocytes after treatment with $GONH_2$.

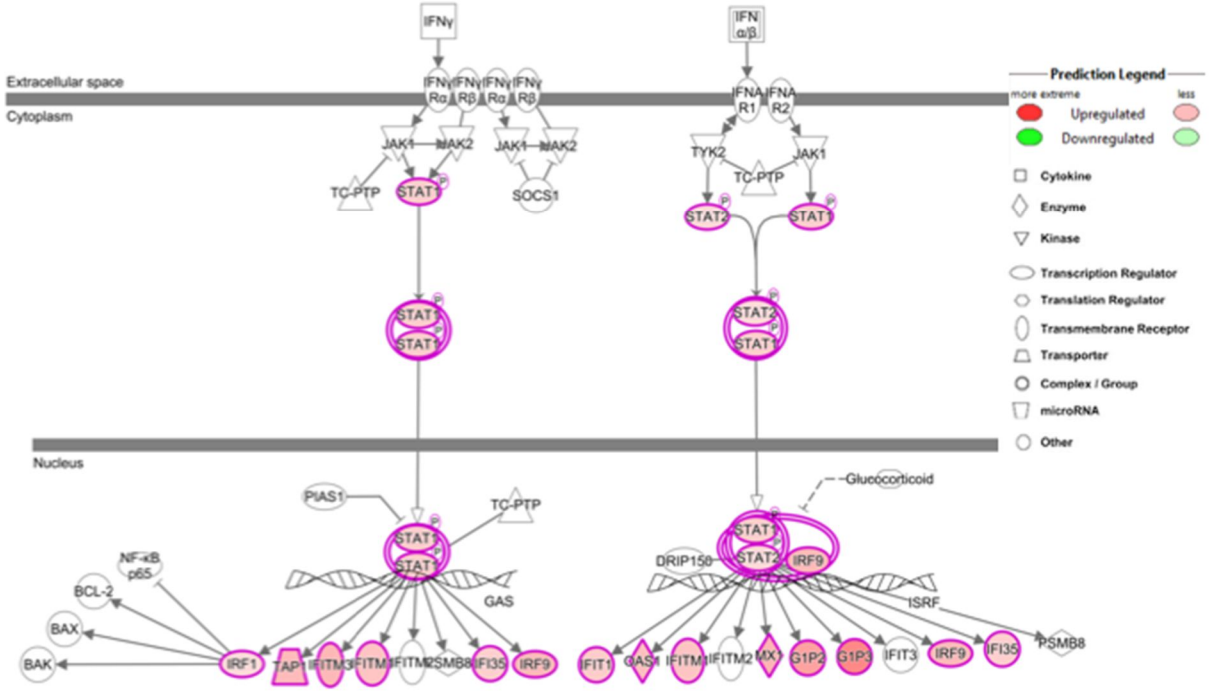

Figure S7. Significant canonical pathways. IFN signaling pathway in T-cells after treatment with $GONH_2$.

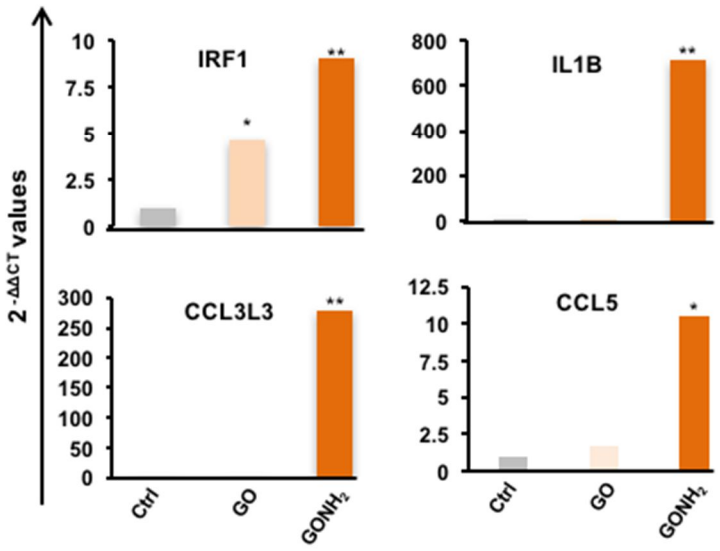

Figure S8. Microarray data validation in monocytes cell line. mRNA levels were measured in triplicate by quantitative real-time PCR. Histograms show residual mRNA level expressed as $2^{-\Delta\Delta ct}$ that gives the measure of fold changes between GO and $GONH_2$ and controls (always expressed as 1) (*= P value < 0.05, **= P value <0.01 Statistical analysis performed by two tales student t test).

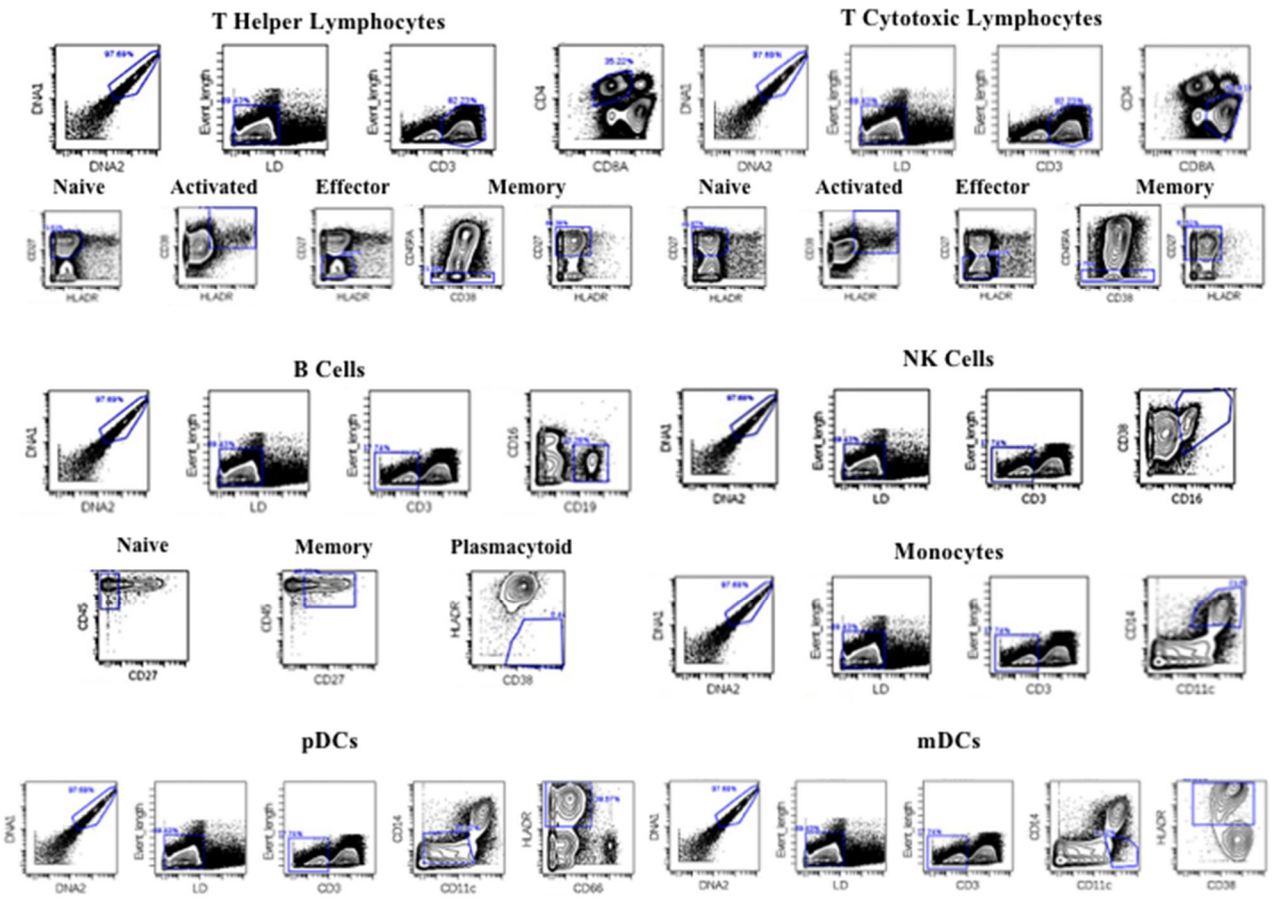

Figure S9 Gating strategy of different immune cell subpopulations. The used gating strategy for the identification of the different immune cell subpopulations in shown for the control sample as a contour dot plots. The gating was performed following the Fluidigm instruction of the Maxpar panel used. The cell events discrimination was performed first using Ir 191 Di(DNA1) and Ir 193 Di (DNA2), LD stands for CIS.

Paper IV: *Few-layer graphene kills selectively tumor cells from myelomonocytic leukemia patients.*

Julie Russier,[†] Véronica Léon,[§] Marco Orecchioni,[‡] Eri Hirata,[†,⊥] Patrizia Virdis,[//] Claudio Fozza,[//] Francesco Sgarrella,[‡] Gianaurelio Cuniberti,[#] Maurizio Prato, [¥,¶,π] Ester Vazquez, [§*] Alberto Bianco,[†*] Lucia G. Delogu[‡,#*]

[†]*CNRS, Institut de Biologie Moléculaire et Cellulaire, Laboratoire d'Immunopathologie et Chimie Thérapeutique, 67000 Strasbourg, France*
[§]*Departamento de Química Orgánica, Facultad de Ciencias y Tecnologías Químicas-IRICA, Universidad de Castilla-La Mancha, 13071 Ciudad Real, Spain*
[‡]*Department of Chemistry and Pharmacy, University of Sassari, 07100 Sassari, Italy*
[⊥]*Department of Oral Functional Science, Graduate School of Dental Medicine, Hokkaido University, 060-8586, Sapporo, JAPAN*
[//]*Department of Biomedical Science, University of Sassari, 07100 Sassari, Italy*
[#]*Max Bergmann Center of Biomaterials and Institute for Materials Science, Dresden University of Technology, 01069 Dresden, Germany*
[¥]*Dipartimento di Scienze Chimiche e Farmaceutiche, Università di Trieste 34127, Trieste, Italy*
[¶]*CIC BiomaGUNE, Parque Tecnológico de San Sebastián, Paseo Miramón, 182, 20009 San Sebastián (Guipúzcoa), Spain*
[π]*Basque Foundation for Science, Ikerbasque, Bilbao 48013, Spain*

Keywords: Graphene, nanomaterials, myelomonocytic leukemia, cancer therapy, immune system

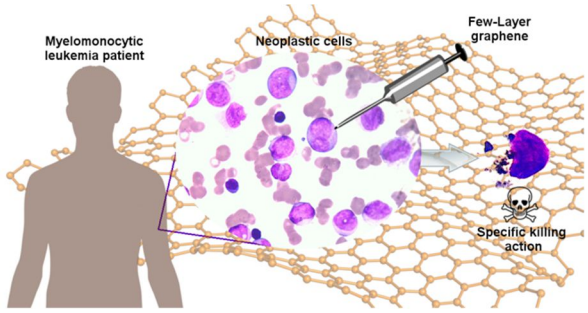

Published in:

Angew Chem Int Ed Engl. 2017 Feb 3 [Epub ahead of print]

Abstract

In the cure of cancer, a major cause of today's mortality, chemotherapy is the most common treatment, though serious frequent challenges are encountered by current anticancer drugs. We discovered that few-layer graphene (FLG) dispersions have a specific killer action on monocytes, showing neither toxic nor activation effects on other immune cells. We confirmed the therapeutic application of graphene on an aggressive type of cancer, i.e. myelomonocytic leukemia, where the monocytes are in their malignant form. We demonstrated that graphene has the unique ability to target and boost specifically the necrosis of monocytic cancer cells. Moreover, the comparison between FLG and a common chemotherapeutic drug, etoposide, confirmed the higher specificity and toxicity of FLG. Since current chemotherapy treatments of leukemia still cause serious problems, these findings open the way to new and safer therapeutic approaches.

Manuscript

The scientific and medical battle against cancer remains one of the biggest challenges of our times. Cancer is still one of the major causes of mortality.[1] The blood-related cancers, such as leukemia in its multiple variants, are among those ones with the highest incidence of mortality.[2] Acute myeloid leukemia (AML) and chronic myelomonocytic leukemia (CMML) represent two different subtypes of the so called myeloid neoplasms.[3] This type of cancer is usually dominated by the rapid growth of abnormal immature white blood cell precursors, that accumulate in bone marrow and peripheral blood interfering with the normal hematopoietic function.[4,5] Both AML and CMML are characterized by circulating monocytic neoplastic cells. The conventional treatment of these disorders is usually based on different chemotherapeutic regimens, which are often characterized by disappointing remission rates especially in elderly patients. Traditional therapies to counteract cancer in general, and also myelomonocytic leukemia, are limited by multiple problems, including nonspecific systemic distribution of antitumor agents, inadequate drug concentrations reaching the tumor site, intolerable cytotoxicity, limited ability to monitor the therapeutic responses, and development of multiple drug resistance.[6]

In this scenario, nanotechnology could be the hoped medical revolution allowing to treat cancer effectively, reducing undesired side effects.[7] The development of new nanomaterials endowed of unique properties could represent a strong enhancement in the cure of cancer. Graphene is one of the nanomaterials that has raised tremendous interest in the scientific community and the society.[8] Graphene is being explored for many potential applications due to its exceptional physicochemical characteristics.[9] Very recently, different types of graphene have been investigated in a growing number of medical applications, including drug delivery, diagnosis, tissue engineering and gene transfection.[10]

In this work, we studied FLG dispersions,[11] and discovered a highly specific toxicity on primary human monocytes. Based on this interesting result, we evaluated the killing activity of graphene in monocytic neoplastic cells from a cohort of AML and CMML patients.

The majority of the biomedical studies using graphene-based nanomaterials have focused on graphene oxide, while there are only a limited number of biological studies on graphene.[12] The reason for this is the difficulty of having graphene directly in water or in culture media. In this context, we have prepared few-layer graphene by exfoliation of graphite through interaction with melamine using a ball-milling process, in solvent-free conditions.[11] This methodology

allows to produce 3-4 layer graphene dispersions in water (0.1 mg mL^{-1}). Moreover, water can be easily replaced by filtration or lyophilisation with cell culture medium to form stable graphene dispersions.[13] **Figure 1** shows the relevant characterization data of the FLG material. Thermogravimetric analysis (TGA) was used to quantify the presence of functional groups in FLG (**Fig. 1A**).

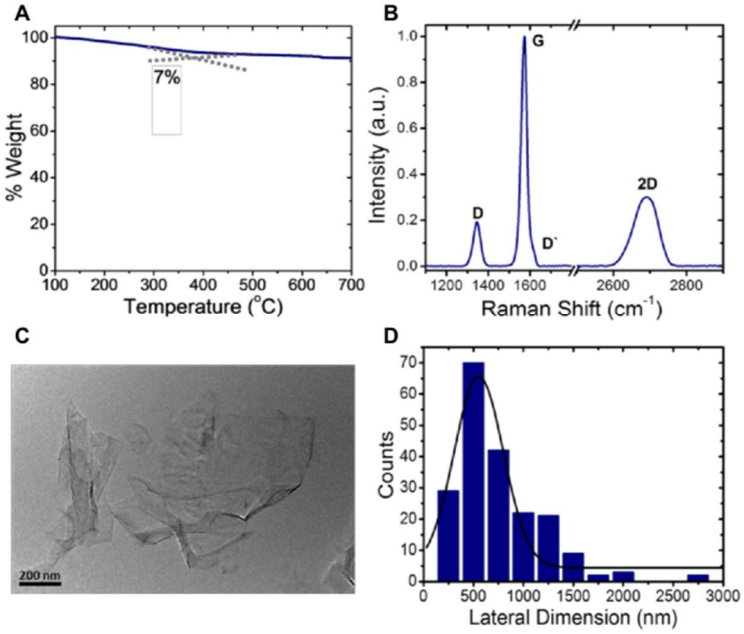

Figure 1. Characterization of FLG. A) Thermogravimetric analysis. B) Normalized Raman spectrum. C) TEM micrograph of FLG in cell culture medium and D) lateral dimension distribution.

The low weight loss observed in FLG (7%) confirms the low quantity of oxygen groups generated during the exfoliation process, which was also corroborated by elemental analysis (see Experimental Section in SI). Further proof of the non-oxidative milling process was confirmed by Raman spectroscopy (**Fig. 1B** and SI). Graphene exhibits G and 2D modes around 1573 and 2700 cm^{-1}, respectively. The D to G band intensity ratio, be used to quantify the defects, was calculated at different topographies, giving a significantly low value (0.2). A representative TEM image of FLG dispersions in cell culture medium is shown in **Figure 1C**, evidencing the typical wrinkled aspect of the graphene flakes. Statistical analysis of TEM images afforded a major population with lateral size around 500-750 nm, with a small fraction above 2000 nm (**Fig. 1D**). Additional XPS data are shown in **Fig. S1**.

FLG stable in cell culture media resulted immediately an interesting material to study its impact on primary human immune cells. The use of these cells is at the forefront in the study of the effects of new materials in a biomedical or toxicological context.[7c, 14] For this purpose,

we analyzed the impact of FLG on peripheral blood mononuclear cell (PBMC) populations looking at T, B, NK, dendritic cells and monocytes. The cells were treated with different doses of FLG from 0.5 μg mL^{-1} to 75 μg mL^{-1} for 24 h (**Fig. S2**), which we consider the optimal time for graphene cellular internalization, and were analyzed by flow cytometry.[14b, 15]

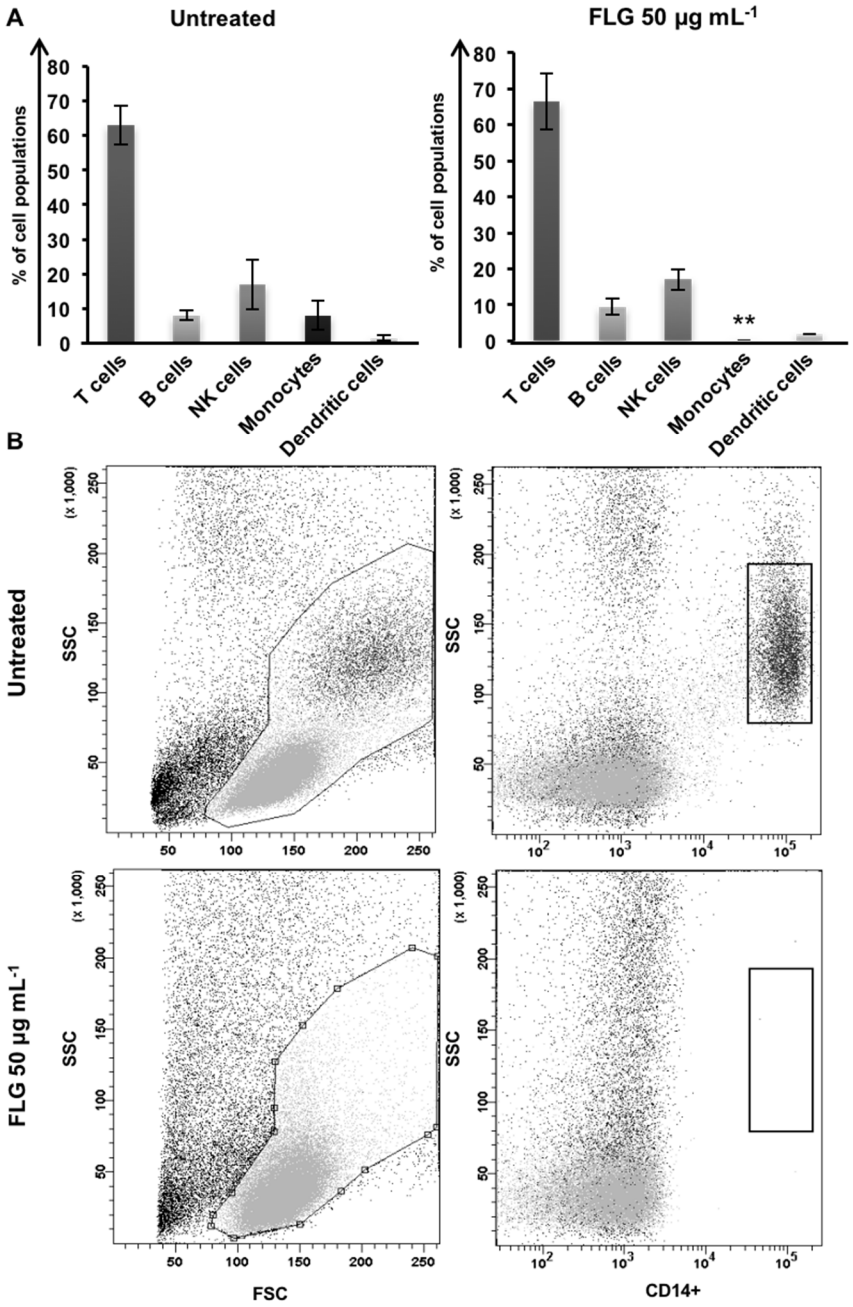

Figure 2. Impact of FLG on different immune cell populations. A) Relative percentage of the different immune cells either incubated for 24 h with 50 μg mL^{-1} FLG or left untreated. Statistical significance compared to untreated cells (student's t test) is indicated by ** = $p < 0.01$. B) Relative morphological dot plots out of at least three experiments of total PBMCs treated with FLG or left untreated. The gate on monocytes was done looking at the CD14 positive events (red dots). The other immune populations are left in green.

Very interestingly, we found a specific cytotoxic activity of FLG on monocytes ($CD14^+$ cells), while the percentage of events reported for T, B, NK and dendritic cells remained unchanged. This effect is appreciable also in the dot plots, where the positive events for the $CD14^+$ completely disappeared (**Fig. 2**), and it was not due to the presence of residual melamine (**Fig. S4**). The other immune cell populations remained unaffected in terms of cell viability (**Fig. S3)**. The highly specific effect of FLG was also confirmed by evidencing its non-cytotoxic impact on other types of cells (**Fig. S5**).

As we could not record any direct activation of monocytes (i.e. no significant increase of CD86 expression, **Fig. S6**), we decided to investigate whether an indirect activation of monocytes *via* the activation of T cells was occurring. Indeed, FLG-mediated activation of T cells could induce a strong stimulation of monocytes triggering their death.[16] We analyzed the expression of specific lymphocyte activation markers, namely CD25 and CD69. Their expression in FLG-exposed samples was comparable to the untreated negative controls (**Fig. S7)**. These data exclude any T cell activation mediated by FLG. The absence of activation of the T cells suggested a direct action of FLG on monocytes. The hypothesis of a selective activity of the FLG towards monocytes is consistent with the transmission electron microscopy (TEM) analysis on total PBMCs (**Fig. S7**). The fact that only monocytes are able to internalize FLG could explain our results on cellular activation and cytokine production. Other reports showed an effect of graphene, and in particular of GO, on macrophages or DCs.[17] However, none of them reported such strong specific killing on monocyte compared to other immune cell populations. In fact we evidenced that treatments of PBMCs with a commercial graphene oxide do not affect the monocyte population (**Fig S9**).[18]

We then investigated the cell death on monocytes isolated from PBMCs. Monocytes were treated with FLG at 50 $\mu g\ mL^{-1}$ and at different time points (1, 4, 12, and 24 h) to analyze the induced specific death processes (**Fig. 10A**). The morphological dot plots (**Fig. S10B**) show the progressive reduction of monocytes ($CD14^+$ cells). Even at early time points (1 and 4 h) of incubation a significant induction of dead cells was observed (**Fig. S10C**). The necrotic cells increased also significantly from 6.2% in the control sample to 29% after 1 h and 36.5% after 4 h (**Fig. S10A**). Mortality of monocytes reached 71.3% after 24 h of incubation with FLG (P-value<0.01). We also observed the absence of a significant number of apoptotic cells in all FLG treated samples (**Fig. S10A**) suggesting that graphene directly triggers necrosis on monocytes.

To investigate the mechanisms of FLG mediated cell death we first performed a whole-genome expression, looking at more than 41,000 transcripts on isolated monocytes from healthy patients. Venn diagram in **Figure S11A** shows the number of genes that passed the cutoff at the different time points. As expected the number of genes modulated by FLG increased from 773 after 30 min to 836 and 966 after 90 and 270 min, respectively. The genes up-regulated by FLG were mainly chemokines and cytokines (**Table S1**). They all account for the activation process played by FLG on monocytes that increased proportionally with incubation time. To understand the biological function of FLG we then performed a pathway analysis. **Figure S11B** displays the 10 most significantly modulated pathways corresponding to IL-10, IL-6 and TREM1 signaling. All these pathways confirmed again the activating action of FLG on monocytes. IL-10 signaling pathway is in general induced by the activation of toll-like receptors (TLR) 2 and 4 with the regulation of the inflammation through the inhibition of pro-inflammatory cytokines TNFα and IL-6.[19] It was previously evidenced how the internalization of graphene could be mediated by TLR2 and TLR4.[20] The toxicity of our FLG is likely induced by the activation of both TLR signaling via TNFα production.[19, 21] To investigate whether TLR2/TLR4 receptors were involved in the selective cytotoxic effect of FLG on monocytes, we analyzed *ex vivo* the monocytes treated with and without TLR2/TLR4 blocking antibodies. The experiments revealed that TLR4 seems not or only partially involved in the mechanism inducing selective cell death of monocyte by FLG (**Fig. S12A**). Instead, the inhibition of TLR2 blocked the expression of CD25 in treated monocytes (**Fig. S12B**). Moreover, the inhibition of TLR2 was able to restore the number of monocytes compared to the controls. Together with the gene expression analysis, these results suggest that the FLG toxicity on monocytes is mediated by the interaction of FLG with TLR2 and the subsequent expression of TNFα and TNFR family (see also SI).[22]

The high selective capacity of our FLG to kill human monocytes is promising for the treatment of myelomonocytic leukemia, which presents high percentages of circulating monocytic neoplastic cells. Therefore, we analyzed the effect of FLG as a new chemotherapeutic tool in myeloid malignancies. In particular, we evaluated the monocytoid $CD14^+$ cell viability in PBMCs obtained from a cohort of seven patients (6 male and 1 female) with a median age of 70, newly diagnosed with AML or CMML, before starting the therapeutic treatment (**Fig. 3**). The presence of FLG accumulated into the monoblasts (**Fig. S13A**) was observed into the peripheral blood smear of AML (**Fig. S13B**) and CMML (**Fig. S13C**) patients.

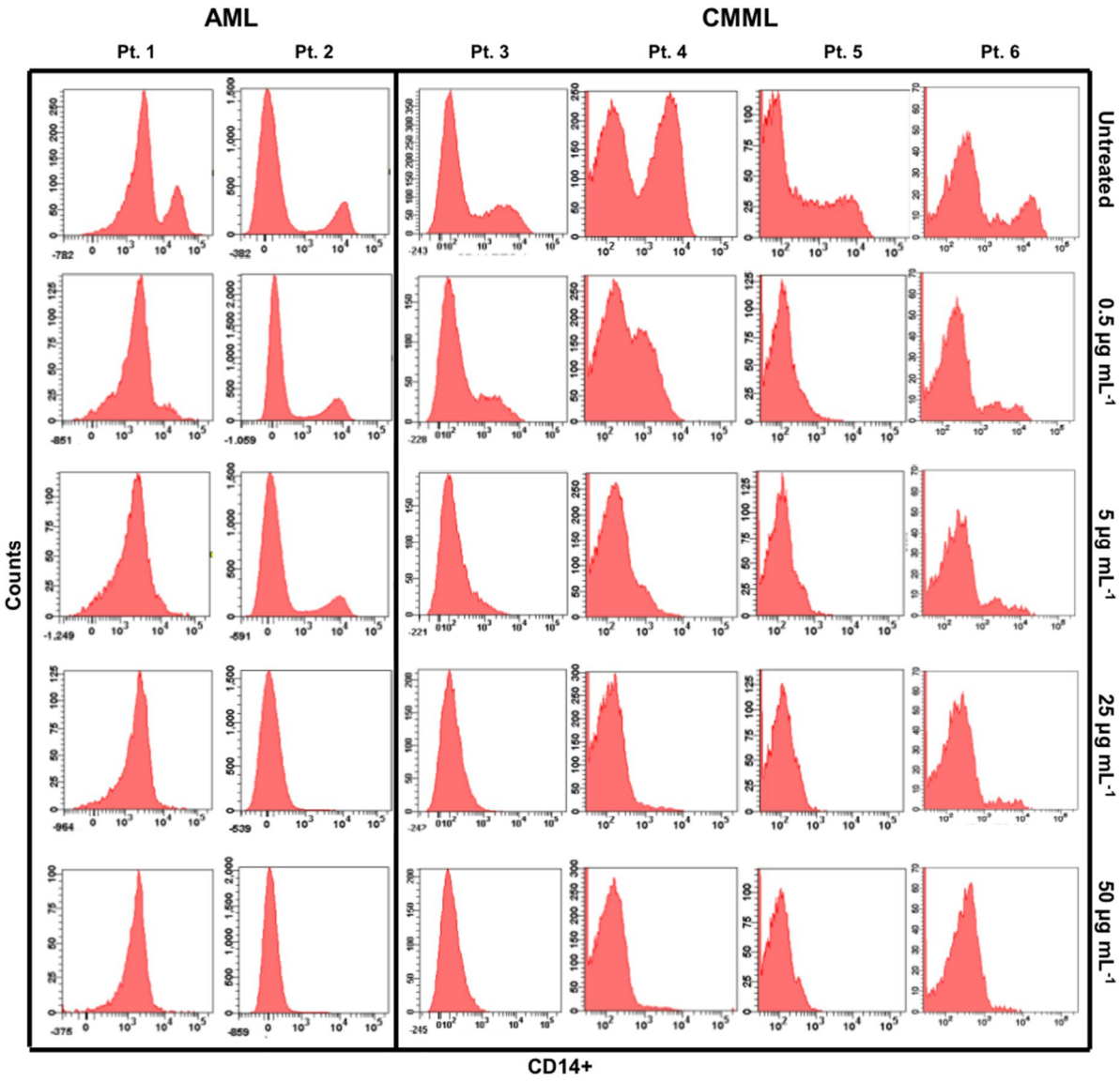

Figure 3. FLG impact on *ex vivo* PBMCs from AML and CMML patients. Monocytoid cells were highlighted by CD14 positivity (right peaks), the other populations were negative (left peaks).

PBMCs of the patients were then treated with increasing doses of FLG to assess the capacity of graphene to specifically kill the neoplastic monocytes. In the untreated samples of all patients (**Fig. 3**), two peaks of cells are well visible: the first on the left comprises all cells negative to the CD14 marker corresponding to non-neoplastic cells (i.e. T cells, B cells, NK and dendritic cells), while the peak on the right identifies $CD14^+$ monocytoid cancer cells. After the treatment with FLG, the cancer cell population was strongly reduced in all AML and CMML patients in an FLG concentration dependent manner with no effect on the other immune cells (**Fig. 3**). We would like to point out that in the 6 patients, the number of cancer cells was strongly reduced even at low concentrations (0.5 and 5 µg mL^{-1}) with two fold, and three fold average decrease,

respectively. Regarding the ablation obtained at 25 and 50 μg mL^{-1}, the percentage of cells was extremely reduced from an average of 24% to an average of 2.2% and 1.6%, respectively (**Fig. 3** and **Fig. S14**). In particular, patient 4 was characterized by a critical condition with an extremely high number of monocytoid cancer cells comparable to all other immune cells. The treatment with FLG even at the lower concentrations has shown 40% and 83% reduction of the neoplastic cell number, reaching the total ablation at 25 μg mL^{-1} (**Fig. 3**, Pt.4). The analysis of the cytokine secretion in CMML patients after the treatment with FLG did not evidence any induction of inflammatory processes in other immune cells. Thus, only monocyte-associated cytokines were found overexpressed under FLG treatment (**Fig. S15**).

Furthermore, we compared the specific effect of FLG with etoposide, a common chemotherapeutic agent clinically used in the treatment of both AML and CMML. Etoposide was specifically selected because of its ability to selectively induce monocytopenia, the deficiency of monocytes mandatory to prevent tumor expansion.[23] We tested concentration of etoposide between 50 and 200 μM, normally used to treat AML and CMML.[24] The comparison of the effect of FLG at 50 μg mL^{-1} with the different etoposide doses in PBMCs isolated from AML patients underlines the safety use of FLG with no toxic effect on the other immune cell populations (**Fig. 4A**). As expected, etoposide induced a significant T, B and NK cell toxicity at all concentrations (**Fig. 4A**). In B cells, we found a 49.6% of dead cells at the lowest concentration and a 68.3% at the highest. We further confirmed the strong specific effect of FLG on neoplastic $CD14^+$ cells compared to etoposide (**Fig. 4B**). These findings open the way to a possible application of FLG as a specifically targeted tool against neoplastic cells in AML and CMML. This new therapeutic strategy based on graphene might be extremely advantageous over the traditional treatments using conventional chemotherapeutic agents such as etoposide, cytarabine, anthracyclines or hydroxyurea,[4, 5] that are non specific and impair all immune cell subpopulations, causing possible infections and death. Moreover, some of these chemotherapies act by activating the apoptosis pathway in tumor cells. Paradoxically, the fact that anticancer agents are effective primarily because they activate apoptosis raises the concern that tumors intrinsically resistant to chemotherapy are unable to activate the apoptotic machinery and may be resistant to any chemotherapeutic drug.[25] The necrosis-mediated action of FLG could avoid the resistance of tumor cells.

Finally, given the complexity of the toxicology and pharmacokinetic issues with graphene-based materials, we characterized the systemic body reaction to FLG *in vivo*. All injected mice behaved normally and did not show signs of adverse reactions (see **Fig. S16**).

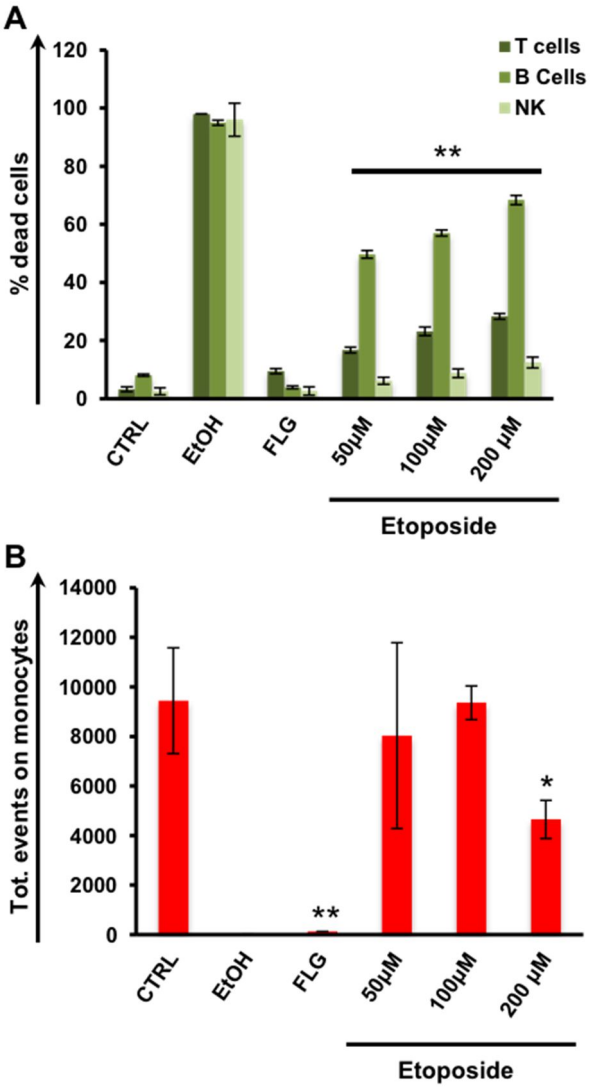

Figure 4. Comparison between etoposide and FLG on PBMCs from AML patients. PBMCs were incubated with 50 µg mL^{-1} FLG and etoposide at different concentrations. After 24 h the cells were harvested and stained with a viability marker dye (7AAD). A) Viability screening of different immune cell populations (i.e. T, B and NK cells). B) Count of monocytoid cells ($CD14^{+}$) treated with FLG (50 µg mL^{-1}) and etoposide or left untreated. Statistical significance compared to untreated cells (student's t test) is indicated by *= $p < 0.05$ and ** = $p < 0.01$.

In summary, in this work, we found a specific toxicity of FLG on primary human monocytes. In particular, we demonstrated a unique ability of graphene to target and successfully boost the necrosis of monocytoid cancer cells for acute myeloid leukemia and chronic myelomonocytic leukemia patients. Moreover, the comparison between FLG and a common chemotherapeutic

drug confirmed the specificity and higher toxicity of FLG on cancer cells, evidencing the absence of toxicity on other immune cell populations. Considering the FLG specific ability to target and kill cancer cells of an aggressive form of malignancy, extremely promising potentials as a new cancer tool can be envisaged for graphene.

Acknowledgments

This work was partly supported by the Italian Association against Leukemia (AIL), by the Centre National de la Recherche Scientique, by the Ministerio de Economia y competitividad CTU2014-53600-R and by the Japan Society for the Promotion of Science through a Research Fellowship for Young Scientists (grant no° 24006076). The authors gratefully acknowledge financial support from EU FP7-ICT-2013-FET-F GRAPHENE Flagship project (no. 604391) and from MIUR JTC Graphene 2015 (G-IMMUNOMICS project). E.V. thanks Emilio Pérez and Viviana Jehová González (IMDEA Nanociencia, Madrid) for the Raman measurements.

References

[1] M. Lopez-Gomez, E. Malmierca, M. de Gorgolas, E. Casado, *Crit. Rev. Oncol. Hematol.* **2013**, *88*, 117-122.

[2] N. Holler, R. Zaru, O. Micheau, M. Thome, A. Attinger, S. Valitutti, J. L. Bodmer, P. Schneider, B. Seed, J. Tschopp, *Nat. Immunol.* **2000**, *1*, 489-495.

[3] J. W. Vardiman, J. Thiele, D. A. Arber, R. D. Brunning, M. J. Borowitz, A. Porwit, N. L. Harris, M. M. Le Beau, E. Hellstrom-Lindberg, A. Tefferi, C. D. Bloomfield, *Blood* **2009**, *114*, 937-951.

[4] H. Dohner, D. J. Weisdorf, C. D. Bloomfield, *New Engl. J. Med.* **2015**, *373*, 1136-1152.

[5] C. B. Benton, A. Nazha, N. Pemmaraju, G. Garcia-Manero, *Crit. Rev. Oncol. Hematol.* **2015**, *95*, 222-242.

[6] a) R. Misra, S. Acharya, S. K. Sahoo, *Drug Discov. Today* **2010**, *15*, 842-850; b) G. Szakacs, J. K. Paterson, J. A. Ludwig, C. Booth-Genthe, M. M. Gottesman, *Nat. Rev. Drug Discov.* **2006**, *5*, 219-234.

[7] a) M. S. Goldberg, *Cell* **2015**, *161*, 201-204; b) M. Orecchioni, R. Cabizza, A. Bianco, L. G. Delogu, *Theranostics* **2015**, *5*, 710-723; c) M. Pescatori, D. Bedognetti, E. Venturelli, C. Menard-Moyon, C. Bernardini, E. Muresu, A. Piana, G. Maida, R. Manetti, F. Sgarrella, A. Bianco, L. G. Delogu, *Biomaterials* **2013**, *34*, 4395-4403.

[8] a) G. Sechi, D. Bedognetti, F. Sgarrella, L. Van Eperen, F. M. Marincola, A. Bianco, L. G. Delogu, *Nanomedicine (Lond)* **2014**, *9*, 1475-1486.

[9] A. K. Geim, K. S. Novoselov, *Nat. Mater.* **2007**, *6*, 183-191.

[10] a) L. Zhang, J. Xia, Q. Zhao, L. Liu, Z. Zhang, *Small* **2010**, *6*, 537-544; b) L. Feng, S. Zhang, Z. Liu, *Nanoscale* **2011**, *3*, 1252-1257; c) S. Dinescu, M. Ionita, A. M. Pandele, B. Galateanu, H. Iovu, A. Ardelean, M. Costache, A. Hermenean, *Biomed. Mater. Eng.*

2014, *24*, 2249-2256; d) S. Jaworski, E. Sawosz, M. Grodzik, A. Winnicka, M. Prasek, M. Wierzbicki, A. Chwalibog, *Int. J. Nanomed.* **2013**, *8*, 413-420.
[11] V. Leon, M. Quintana, M. A. Herrero, J. L. Fierro, A. de la Hoz, M. Prato, E. Vazquez, *Chem. Commun. (Camb)* **2011**, *47*, 10936-10938.
[12] M. Orecchioni, C. Menard-Moyon, L. G. Delogu, A. Bianco, *Adv. Drug Deliv. Rev.* **2016**, doi:10.1016/j.addr.2016.05.014
[13] V. Leon, J. M. Gonzalez-Dominguez, J. L. Fierro, M. Prato, E. Vazquez, *Nanoscale* **2016**, *8*, 14548-14555.
[14] a) J. Russier, E. Treossi, A. Scarsi, F. Perrozzi, H. Dumortier, L. Ottaviano, M. Meneghetti, V. Palermo, A. Bianco, *Nanoscale* **2013**, *5*, 11234-11247; b) M. Orecchioni, D. A. Jasim, M. Pescatori, R. Manetti, C. Fozza, F. Sgarrella, D. Bedognetti, A. Bianco, K. Kostarelos, L. G. Delogu, *Adv. Healthc. Mater.* **2016**, *5*, 276-287.
[15] Y. Li, H. Yuan, A. von dem Bussche, M. Creighton, R. H. Hurt, A. B. Kane, H. Gao, *Proc. Natl. Acad. Sci. U.S.A.* **2013**, *110*, 12295-12300.
[16] C. A. Roberts, A. K. Dickinson, L. S. Taams, *Front Immunol.* **2015**, *6*, 571.
[17] Y. Li, Y. Liu, Y. J. Fu, T. T. Wei, L. Le Guyader, G. Gao, R. S. Liu, Y. Z. Chang, C. Y. *Biomaterials* **2012**, *33*, 402-411.
[18] a) G. Qu, S. Liu, S. Zhang, L. Wang, X. Wang, B. Sun, N. Yin, X. Gao, T. Xia, J. J. Chen, G. B. Jiang, *ACS Nano* **2013**, *7*, 5732-5745; b) A. Sasidharan, L. S. Panchakarla, A. R. Sadanandan, A. Ashokan, P. Chandran, C. M. Girish, D. Menon, S. V. Nair, C. N. Rao, M. Koyakutty, *Small* **2012**, *8*, 1251-1263; c) A. V. Tkach, N. Yanamala, S. Stanley, M. R. Shurin, G. V. Shurin, E. R. Kisin, A. R. Murray, S. Pareso, T. Khaliullin, G. P. Kotchey, V. Castranova, S. Mathur, B. Fadeel, A. Star, V. E. Kagan, A. A. Shvedova, *Small* **2013**, *9*, 1686-1690.
[19] Y. Yanagawa, K. Onoé, *J. Immunol*. **2007**, *178*, 6173-6180.
[20] G. Qu, S. Liu, S. Zhang, L. Wang, X. Wang, B. Sun, N. Yin, X. Gao, T. Xia, J.-J. Chen, G.-B. Jiang, *ACS Nano* **2013**, *7*, 5732-5745.
[21] F. Marques-Fernandez, L. Planells-Ferrer, R. Gozzelino, K. M. Galenkamp, S. Reix, N. Llecha-Cano, J. Lopez-Soriano, V. J. Yuste, R. S. Moubarak, J. X. Comella, *Cell Death Dis.* **2013**, *4*, e493.
[22] A. O. Aliprantis, R.-B. Yang, D. S. Weiss, P. Godowski, A. Zychlinsky, *EMBO J.* **2000**, *19*, 3325-3336.
[23] J. W. van't Wout, I. Linde, P. C. Leijh, R. van Furth, *Inflammation* **1989**, *13*, 1-14.
[24] a) A. Montecucco, F. Zanetta, G. Biamonti, *EXCLI J* **2015**, *14*, 95-108; b) M. A. Papiez, W. Krzysciak, K. Szade, K. Bukowska-Strakova, M. Kozakowska, K. Hajduk, B. Bystrowska, J. Dulak, A. Jozkowicz, *Drug. Des. Devel. Ther.* **2016**, *10*, 557-570.
[25] Y. A. Hannun, *Blood* **1997**, *89*, 1845-1853.

Supporting informations

Experimental Section

FLG characterization

The thermogravimetric analysis was performed with a TGA Q50 (TA Instruments) at 10ºC/min in a nitrogen atmosphere. For Raman spectroscopy, the water dispersion was drop-cast onto a silicon surface (Si-Mat silicon wafers, CZ). Measurements were carried out using a 100x objective at 532 nm laser excitation using a SENTERRA Raman Microscope. X-Ray photoelectron spectra (XPS) were obtained with a VG Escalab 200R spectrometer equipped with a hemispherical electron analyser with a pass energy of 50 eV and a Mg K α (h ν = 1254.6 eV) X-ray source, powered at 120 W. Binding energies were calibrated relative to the C 1s peak at 284.8 eV. High-resolution spectra envelopes were obtained by curve fitting synthetic peak components using the software "XPS peak". Symmetric Gaussian–Lorentzian curves were used to approximate the line shapes of the fitting components. For TEM analysis, cell culture medium (RPMI-1640, ref. R8758) dispersion was dip-cast on a copper grid (3.00 mm, 200 mesh, coated with carbon film) and dried under vacuum, Sample was investigated by high-resolution transmission electron microscopy (HRTEM) JEOL 2100. Lateral dimension distribution was carried out using Fiji-win32. Elemental analysis (EA) afforded the following percentages: %C: 94.84±1.08, %H: 0.30±0.13, N: 0.29±0.02 and %O: 4.58±0.96. From these data 0.5% of melamine is present in the sample. EA was performed in a LECO CHNS-932 analyzer (Model No: 601-800-500). The control GO sample was obtained from NanoInnova (Spain) (Batch no° GOZ.10.2-12).

Cell culture and maintenance

Human peripheral blood mononuclear cells (PBMCs) were obtained from informed healthy male donors (25 to 50 years old) and a cohort of seven patients (6 male and 1 female) with a median age of 70, diagnosed with AML (3) or CMML (4) before the start of the classical therapeutic treatment. Informed signed consent was obtained from all the donors. The present research was evaluated and approved by the local ethic committee of the University of Sassari. Cell separation and experiments were performed immediately after blood drawing. PBMCs were isolated from the fresh heparinized blood by Ficoll-Paque PLUS (FLG Healthcare) density gradient centrifugation. Primary monocytes from purified PBMCs were isolated by Dynabeads Untouched Human Monocytes Kit (Invitrogen), following the manufacturer protocol. PBMCs

and isolated monocytes were cultured in RPMI 1640 medium (Gibco) containing 1% antibiotic-antimycotic mixture and 10% heat-inactivated fetal bovine serum (FBS) (Gibco).

TEM analysis of PBMCs

For the TEM observation, cells were exposed to FLG (25 μg mL^{-1}) during 24 h. As the monocyte population completely disappears at the highest concentration (50 μg mL^{-1}), we decided again to reduce the maximum concentration to 25 μg mL^{-1} in order to observe the interactions between FLG and PBMCs, including monocytes. At the end of incubation time, cells were precipitated by centrifugation (1200g during 5 min) and fixed overnight at 4 °C with 2.5% glutaraldehyde. On the following day, cells were again precipitated and the pellet was included in agarose (1.5%). The agarose pellet was collected, washed twice in distilled water and then submitted to a secondary fixation with 1% aqueous osmium tetroxide (30 min at room temperature). After rinsing cells three times with distilled water, dehydratation was performed through a series of baths: twice with 50% ethanol (10 min), once with 70% ethanol (20 min), once with ethanol 95% (10 min), twice with absolute ethanol (10 min) and finally twice with propylene oxide (for 10 min each). Infiltration with epoxy resin Epon was done using mixtures of propylene oxide and Epon resin in 2:1 (1 h) and 1:2 (1 h) ratio and finally with pure resin (1 h). On the last day, resin was replaced with fresh one and further incubated during three hours. Polymerized block with embedded cells were then prepared filling gelatine capsules with fresh resin and placing them upon the agarose inclusions in which the pellet of cells was previously included. As-prepared capsules were then placed into the oven to polymerize the resin at 60 °C for 48 h afterwards ultrathin sections (70 nm thick) were obtained using an ultramicrotome (Leica) with a diamond knife (DiATOME). The ultrathin sections were then collected on butvar-coated single-slot copper grids and examined by TEM (Hitachi H600).

Viability and activation analysis of PBMCs from healthy donors

Healthy PBMCs were incubated for 24 h with increasing concentrations of FLG (0.5, 5, 25, 50 and 75 μg mL^{-1}). After 24 h cells were stained with Live and Dead staining (Invitrogen). Ethanol (70%) treated samples were used as positive controls, while samples incubated with cell medium alone were used as negative controls. The viability screening of total PBMCs and different immune subpopulations was made by flow cytometry (FACS Canto, BD Biosciences). Major immune cell populations from PBMCs were identified by flow cytometry according to the expression of specific cell surface markers [clusters of differentiation (CD)] that were

Dr. Marco Orecchioni. Titolo "Biomedical applications of different nanomaterials: Characterization and interaction with the immune system"
Tesi di dottorato in Life Sciences and Biotechnologies, Università degli Studi di Sassari.

detected with fluorescently-labeled monoclonal antibodies. Specifically for the cell phenotyping we used anti-CD3, anti-CD14, anti-CD56, anti-CD20 and anti-CD123 antibodies purchased from BD Biosciences (Mountain View, CA, USA). Staining with fluorochrome-conjugated monoclonal antibodies was performed in the dark for 20 min. Cell typing was performed using the above mentioned antibodies to recognize the major population of PBMCs: $CD3^+$ for T cells, $CD20^+$ for B cells, $CD56^+$/CD3- for NK cells, $CD14^+$ for monocytes and $CD123^+$ for dendritic cells. To investigate the functional impact of FLG at the medium concentration of 50 μg mL^{-1} on PBMCs, considering activation of cells as a crucial endpoint, we choose CD25 and CD69 that are critical markers for the immune response. Concanavalin A (ConA, 10 μg mL^{-1}) and lipopolysaccharides (2 μg mL^{-1}) were used as positive controls. After 24 h of incubation, PBMCs were harvested, washed two times with PBS and stained to identify immune cell populations and analyze activation marker expression. The specific effect of FLG (50 μg mL^{-1}) on monocytes (CD14 positive population) was evaluated also with the effect comparison with melamine (0.5%) after 24 h incubation.

Cellular activation was explored through CD86 expression evaluation. Briefly, after FLG treatment, PBMCs were collected and stained with PE-Mouse anti-Human CD86 antibodies (Clone 2331(FUN-1), BD Pharmingen 555658), prior to flow cytometry acquisition. Lipopolysaccharide (LPS, 100 ng mL^{-1}) was used as cellular activation positive control. As the monocyte population completely disappears at the highest concentration (50 μg mL^{-1}), we decided to reduce the maximum concentration to 25 μg mL^{-1} in order to observe and analyze the effect of FLG on PBMCs including at least few monocytes. The CD86 associated fluorescence intensities were determined by acquiring at least 100,000 events using a Gallios Flow Cytrometer (Beckman Coulter) and analyzing the data with FlowJo software.

FLG viability on non-immune cell lines

MDA-MB-231 and PC3 cell lines cultured in Dulbecco modified eagle edium (DMEM), completed with 10% FCS and 1X penicillin streptomycin solution in incubator at 37°C and 5% CO_2, were exposed to different concentrations of FLG (5 to 50 μg mL^{-1}) for 24 h. Necrosis and apoptosis were assessed using 7AAD and Annexin V staining and analyzed by flow cytometry. Ethanol was used a positive control.

FLG gene expression analysis

Isolated monocytes from healthy donors were incubated at early time points (30, 90 and 270 min) with 50 μg mL^{-1} of FLG. After the incubation the total mRNA was extracted with TriZol Reagent (TriZol, Invitrogen, Carlsbad, CA, USA) and purified using the RNAeasy minikit (Qiagen, Valencia, CA, USA). RNA purity was assessed by spectrophotometric analysis and integrity by microfluidic molecular sizing using the Bioanalyzer 2100 (Agilent). Samples with RIN (RNA Integrity Number) less than 8 were discarded. RNA (1 μg) was converted in cRNA and labeled (Agilent One-Color Microarray-Based Gene Expression Analysis kit). Biotinylated cRNA was hybridized onto 072363 SurePrint G3 Human GE 8×60K array slide (60 000 probes, Agilent technologies). Slides were then hybridized (Agilent protocol), washed, and scanned on an Agilent C Scanner according to the manufacturer's instructions. Data were finally analyzed using the GeneSpring GXI (Agilent Technologies) and Ingenuity Pathways Analysis software (Qiagen, Valencia, CA, USA).

Viability of isolated monocytes from healthy donors

Isolated monocytes from healthy donors were incubated at different time points (1, 4, 12, and 24 h) with 50 μg mL^{-1} of FLG. Live and Dead staining (Invitrogen) and Annexin-V FITC, propidium iodide (PI) apoptosis and necrosis kit (Invitrogen) stainings were done. The screening was made by flow cytometry (FACS Canto, BD Biosciences).

FLG impact on cancer monocytes from myelomonocytic leukemia patients *ex vivo*

MML PBMCs were incubated for 24 h with FLG at increasing concentrations (0.5, 5, 25, 50 μg mL^{-1}). After the incubations cells were harvested and washed with PBS. Staining for flow cytometry was made with anti-CD14 antibody.

Etoposide and FLG impact comparison on PBMCs from MML patients

AML and CMML PBMCs were incubated for 24 h with FLG (50 μg mL^{-1}) and etoposide (50, 100 and 200 μM). After the incubations all cells were harvested and washed with PBS. The viability analysis was made with the 7AAD dye in flow cytometry (FACS Canto, BD Biosciences). Same staining and gating strategies for healthy PBMCs viability was made for the screening of different immune cell populations. The specific effect of graphene and etoposide on monocytes (CD14 positive cells) was made through the count of total events recorded in treated and untreated samples.

***In vivo* systemic toxicity**

Seven male C57BL/6 mice (weight 15-30 g) were divided into two groups: a treated group injected with FLG and a control group injected with fresh, sterile saline. Mice were intraocularly injected with FLG at the concentration of 50 μg mL^{-1} of blood (treatment group) or saline (control group). Mice were housed in groups of 3 and 4 animals per cage, fed with standard food and water *ad libitum* and monitored for any sign of adverse reaction or fatality for 7 days. After 7 days, mice were sacrificed and several organs and whole blood were harvested. Bone marrow cells were flushed from femur and tibia, spleen and lymph nodes were mechanical dissociated by gentle trituration and filtered through a cell strainer to create a single cell suspension. Collected cells were stained with anti-mouse CD3, CD19/Cd45R, Gr1, CD11b, F4/80 and CD14 antibodies to detect, T cells, B cells, granulocytes, DCs, macrophages and monocytes analyzed by LSR II flow cytometer (BD Biosciences). The blood count test was performed with heart harvested whole blood. The analysis was performed with a Coulter LH 780 analyzer (Beckman Coulter).

Animal study

The study was carried out in accordance with current Italian legislation [D.L. 116, 1992], and in strict accordance with European Council directives on the matter [n. 2007/526/CE]. All possible efforts were made to minimize animal pain and discomfort and to reduce the number of experimental subjects.

Statistical analysis

Data analysis for flow cytometry experiments was performed using FACSDiva software (BD-Bioscience Mountain View, CA, USA). All the experiments were performed at least in triplicate. Statistical analyses were performed using Student's t-test. Data indicated with star were considered statistically significant (two-side p value, *= P Value <0.05; **= P Value <0.01). Data are presented as mean SD. Multiplex ELISA tests and flow cytometry analysis on isolated human primary PBMCs from healthy donors were performed in samples from at least 3 different donors.

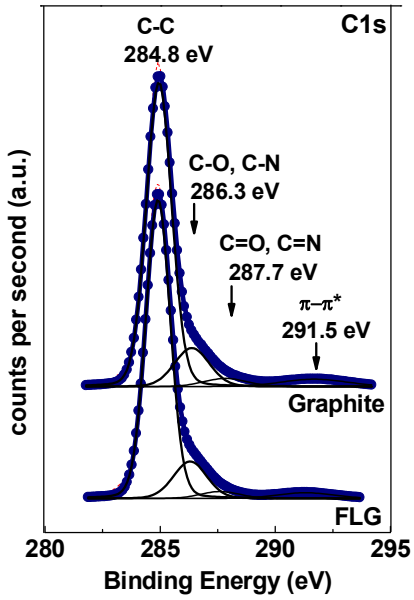

	C1s		N1s	
Graphite	284.93	**C-C**		
	286.31	**C-O**		
	287.78	**C=O**		
	291.48	**π–π***		
FLG	284.93	**C-C**	399.04	**N-H**
	286.29	**C-O**	400.16	**N=C**
	287.67	**C=O**		
	291.33	**π–π***		

Figure S1. Top: C 1s XPS spectra of graphite and FLG. Bottom: results of the XPS C 1s and N 1s curve fittings for graphite and FLG.

Additional Raman analysis

It is commonly accepted that the thickness of few-layer graphene nanosheets is reflected in the shapes of their 2D Raman bands (around 2700 cm^{-1}). Following the equations reported by Coleman and coworkers,[1] we calculated the number of layers of our FLG in water and in cell culture medium. The number of layers (N_G) is calculated considering also the Raman spectrum of the starting graphite material.

$$N_G = 10^{0.84M+0.45M^2}$$

Where M is equal to:

$$M = \frac{I_{G'ene}(\omega = \omega_{p,G'ite})/I_{G'ene}(\omega = \omega_{s,G'ite})}{I_{G'ite}(\omega = \omega_{p,G'ite})/I_{G'ite}(\omega = \omega_{s,G'ite})}$$

$I_{G'ene}$ and $I_{G'ite}$ correspond with the intensity of G' band for graphene and graphite, respectively. We have analyzed at least 50 individual Raman spectra of few-layer graphene dispersed in water and in culture media, obtaining the following average results. Raman results suggest that our few-layer graphene consists of flakes with a average thickness of 3-4 layers.[2, 3]

	Intensity 2723.35 cm^{-1} (I1)	Intensity 2683.40 cm^{-1} (I2)	Relation I1/I2	M	N_G
Graphite	0.41	0.20	2.03	1	
FLG in water	0.42	0.40	1.04	0.51	3.55
FLG in culture media	0.41	0.37	1.11	0.55	3.95

Table. Average values for the Intensity of the 2D band at the wavelength associated with the peak of graphite ($\omega_{p,G'ite}$) (I1) and at the wavelength associated with the low energy shoulder of the graphite 2D band ($\omega_{s,G'ite}$) (I2) for graphite and FLG dispersed in water and in culture media. Number of layers (N_G) for FLG dispersed in water and culture media.

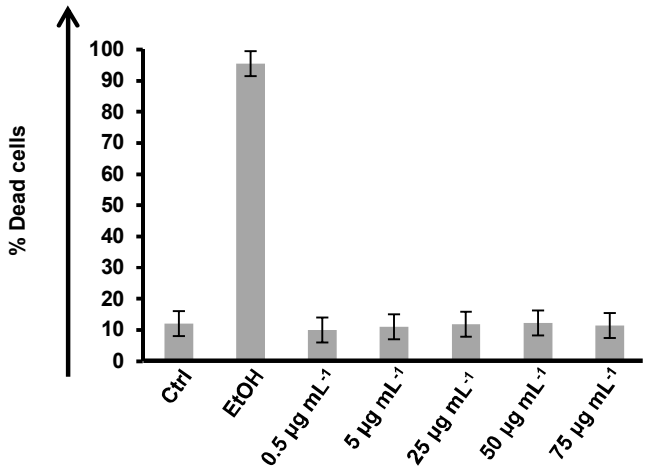

Figure S2. Viability of human primary immune cells. A) PBMCs were incubated for 24 h with FLG at increasing doses of 0.5, 5, 25, 50 and 75 µg mL^{-1} or left untreated, ethanol was used a positive control. Data obtained from staining with an amine-fluorescent dye able to react with the free amines of compromised membranes of late apoptotic and necrotic cells. Experiments were performed at least in triplicate and analyzed by flow cytometry (* = P value <0,05).

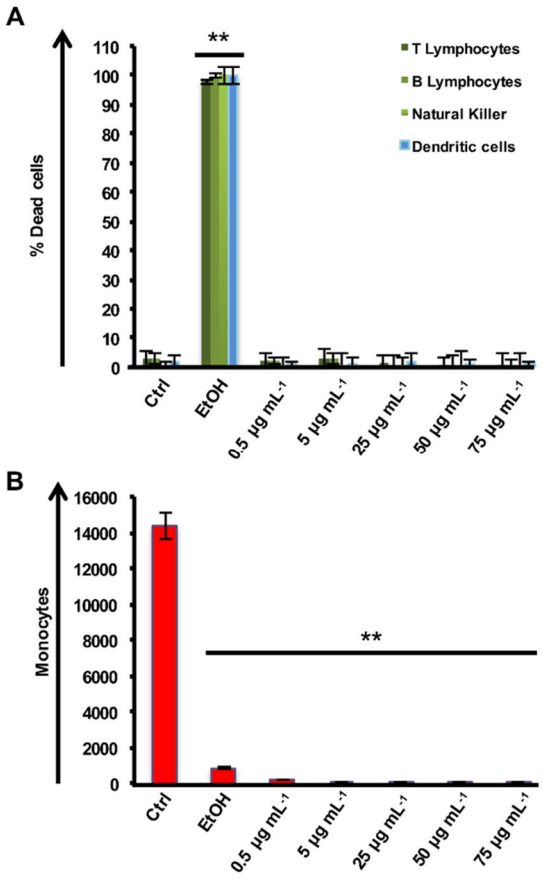

Figure S3. Viability screening of FLG on the different immune cell populations. A) Percentage of T cells, B cells, NK cells and dendritic cells dead events after treatment with increasing doses of FLG (0.5, 5, 25, 50 and 75 µg mL^{-1}). B) Count of monocyte events before and after treatment with FLG at different concentrations. All analyses were performed by flow cytometry. Statistical significance compared to untreated cells (student's t test) is indicated by *= $p < 0.05$ and ** = $p < 0.01$.

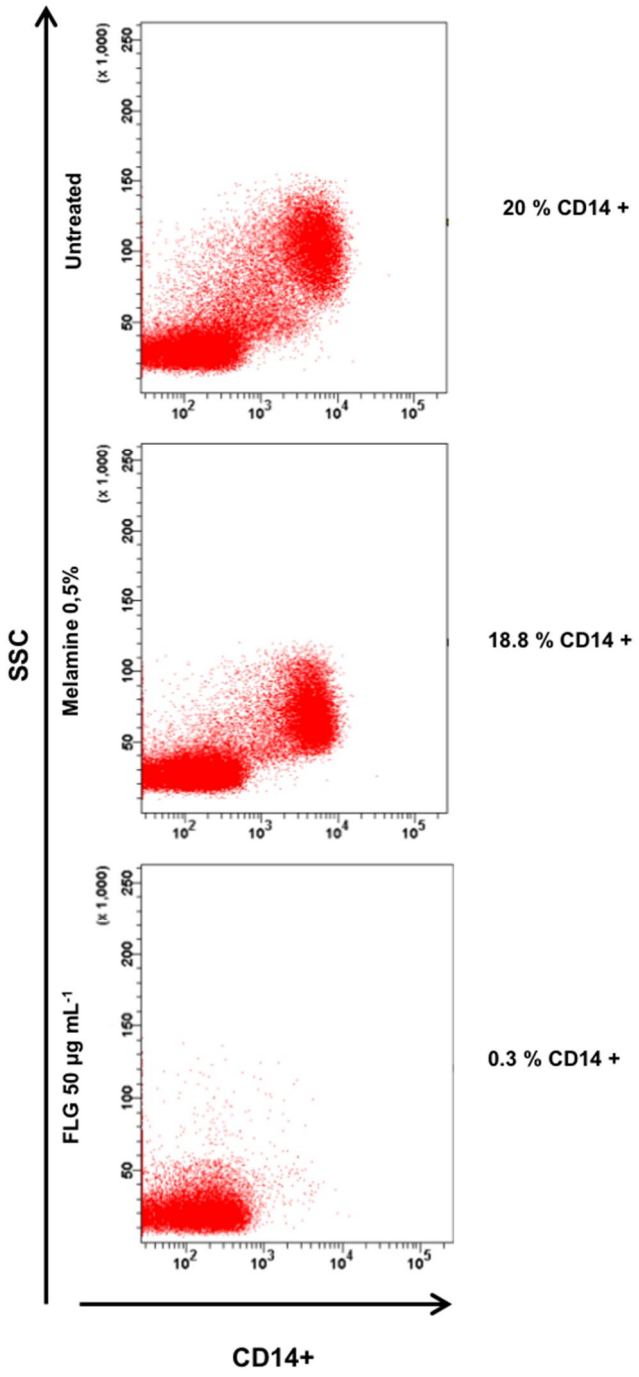

Figure S4. Immune cell impact of melamine. PBMCs were incubated for 24 h with 50 µg mL^{-1} of FLG, 0.5% of melamine or left untreated. Morphological dot plots were measured with side scatter (SSC) and CD14 antibody by flow cytometry. Dot plots were derived from one representative experiment out of three.

In order to exclude that the specific effect of FLG on monocytes was due to the presence of residual melamine in the FLG dispersions,[4] we performed a comparative analysis looking at the effect of this molecule on the viability of monocytes. The number of monocytes remained

similar to the control with 20% of CD14 positive events after the treatment with melamine at 0.5% (w/v) concentration, which corresponds to the amount of molecule that remained complexed to FLG after the exfoliation process.

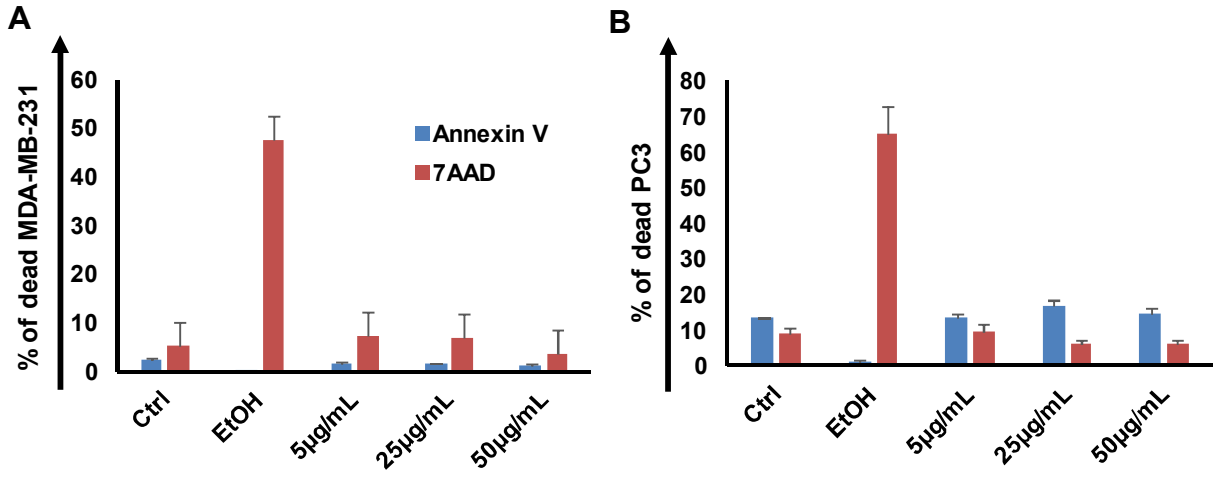

Figure S5. Flow cytometry analysis of cellular viability of breast cancer and prostate cancer cells. A) MDA-MB-231 and B) PC3 cell lines were exposed to different concentrations of FLG (5 to 50 µg mL^{-1}). Necrosis and apoptosis were assessed treating the cells using 7AAD and Annexin V staining, respsctively. Ethanol was used as positive control. Two tails student T test was performed to determine the statistical differences versus control cells. The experiments, performed in triplicate, showed no significant differences (P value >0.05) in all cells treated at the different concentrations.

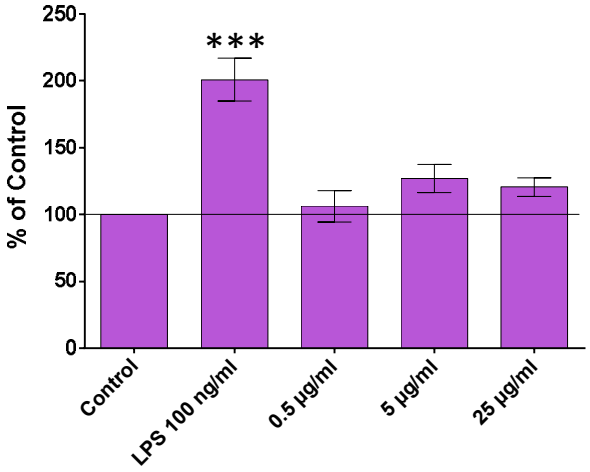

Figure S6. Cellular activation in PBMCs. Flow cytometry analysis of CD86 expression in PBMCs exposed to different concentrations of FLG. One-Way ANOVA followed by Dunnett's post-test was performed to determine the statistical differences versus control cells (*p<0.05; **p<0.01; ***p<0.001).
As the monocyte subpopulation completely disappears at the highest concentration (50 µg mL^{-1}), we decided to reduce the maximum concentration to 25 µg mL^{-1} in order to observe and analyze the effect of FLG on PBMCs including at least few monocytes. Our data revealed that the activation state of PBMCs (CD86 expression) was not influenced by the incubation with FLG up to 25 µg mL^{-1} even if a very little increase could be registered at the highest concentrations.

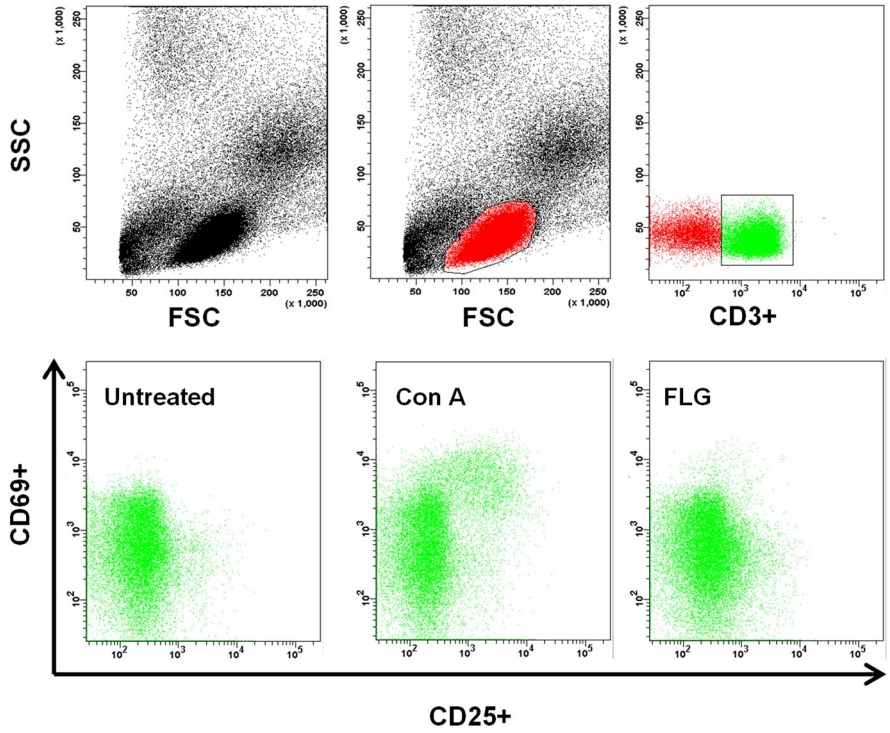

Figure S7. Activation analysis of FLG on human immune cells. PBMCs were incubated for 24 h with 50 µg mL^{-1} of FLG or left untreated. A specific gate using forward light scatter (FSC) and side light scatter (SSC) on total lymphocyte populations (red) was assessed to better visualize the T cell population (CD3 positive events in green). Activation test was performed looking at the expression of CD69 and CD25 in T cells. Concanavalin A (10 µg mL^{-1}) was used as a positive control. Dot plots of CD69 and CD25 expression on T cells was assessed by flow cytometry. Data were derived from one representative experiment out of five.

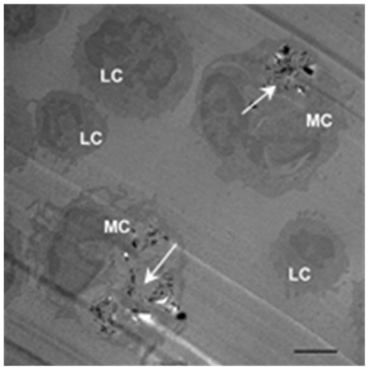

Figure S8. FLG cell uptake by human primary immune cells. TEM caption of PBMCs incubated with FLG (25 µg mL^{-1}) for 24 h. Arrows are indicating FLG sheets inside the cells. MC: Monocytes; LC: Lymphocytes. Scale bar = 2 µm.

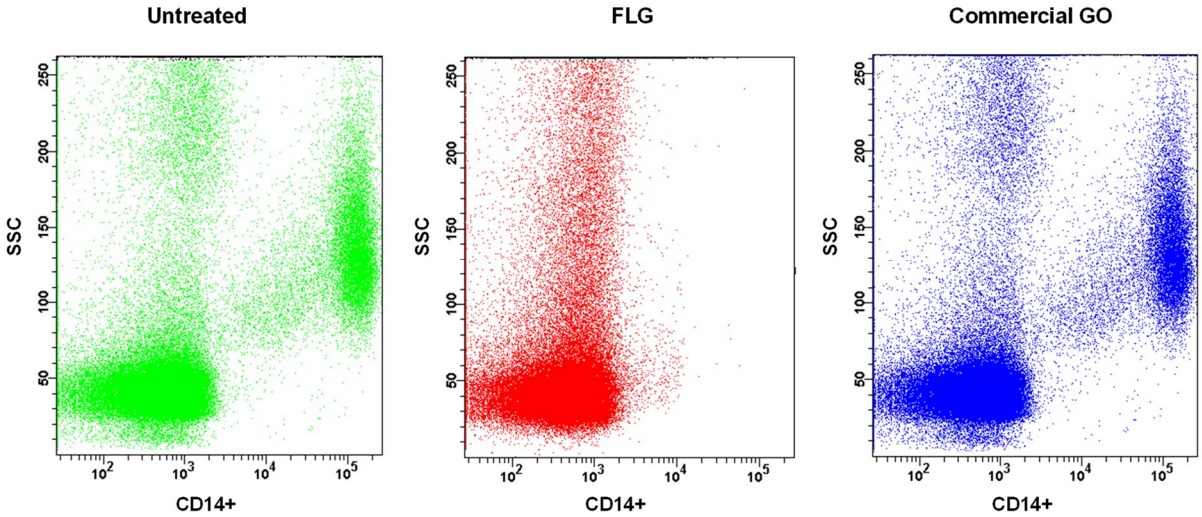

Figure S9. Comparison of the effect of FLG with a commercial GO. PBMCs from healthy donors were incubated with FLG and commercial GO at the concentration of 50 µg mL-1 for 24 h or left untreated. Morphological dot plots were performed using side light scatter (SSC) and CD14 by flow cytometry. Dot plots were derived from one representative experiment out of three.

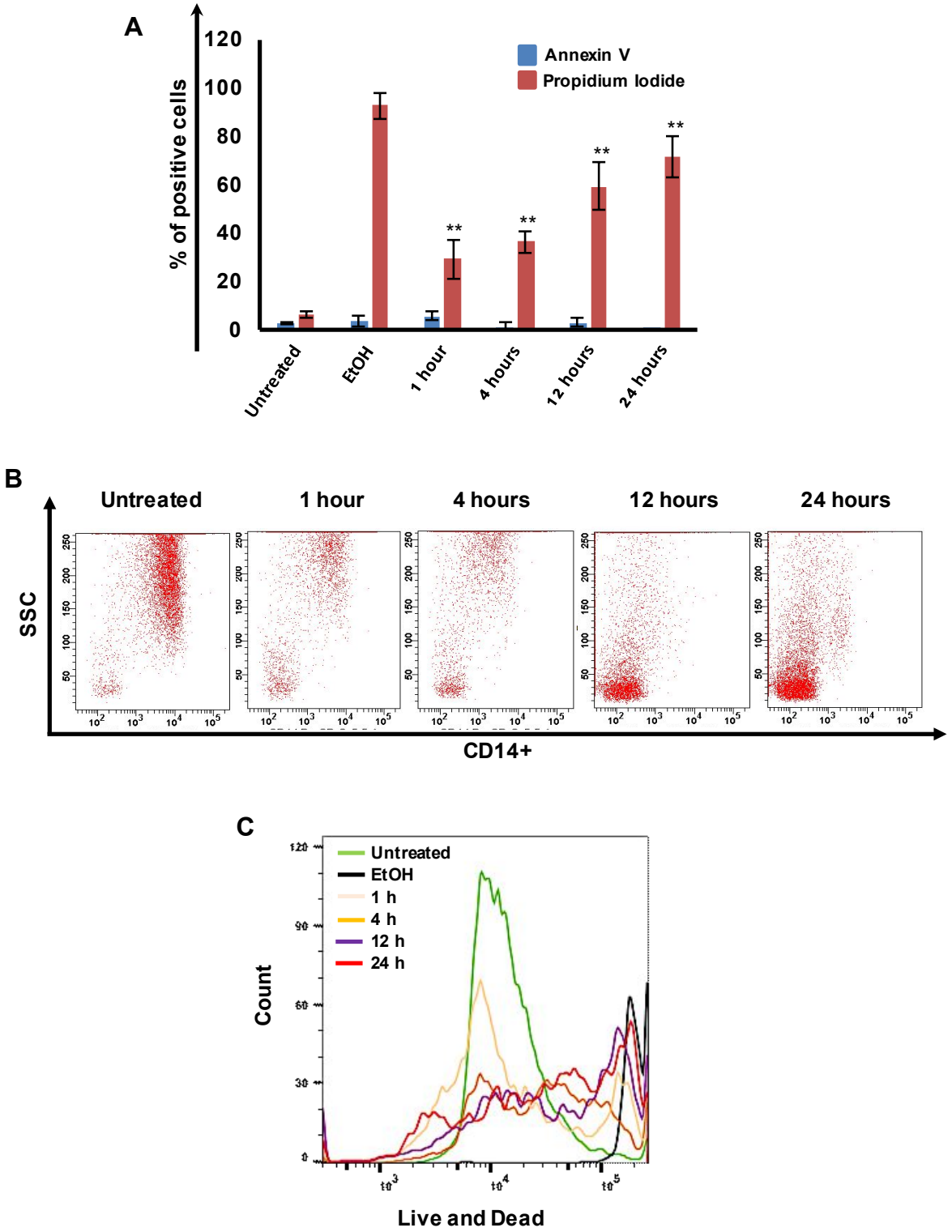

Figure S10. Viability of isolated monocytes after treatment with 50 μg mL^{-1} FLG. A) Annexin V and PI staining indentify necrotic and apoptotic cells, respectively. Statistical significance compared to untreated cells (student's t test) is indicated by ** = $p < 0.01$. B) Morphological analysis was conducted with side light scatter (SSC), and CD14. C) Viability assay was also performed using Live and Dead staining. Dot plots in the panel B were derived from one representative experiment out of three.

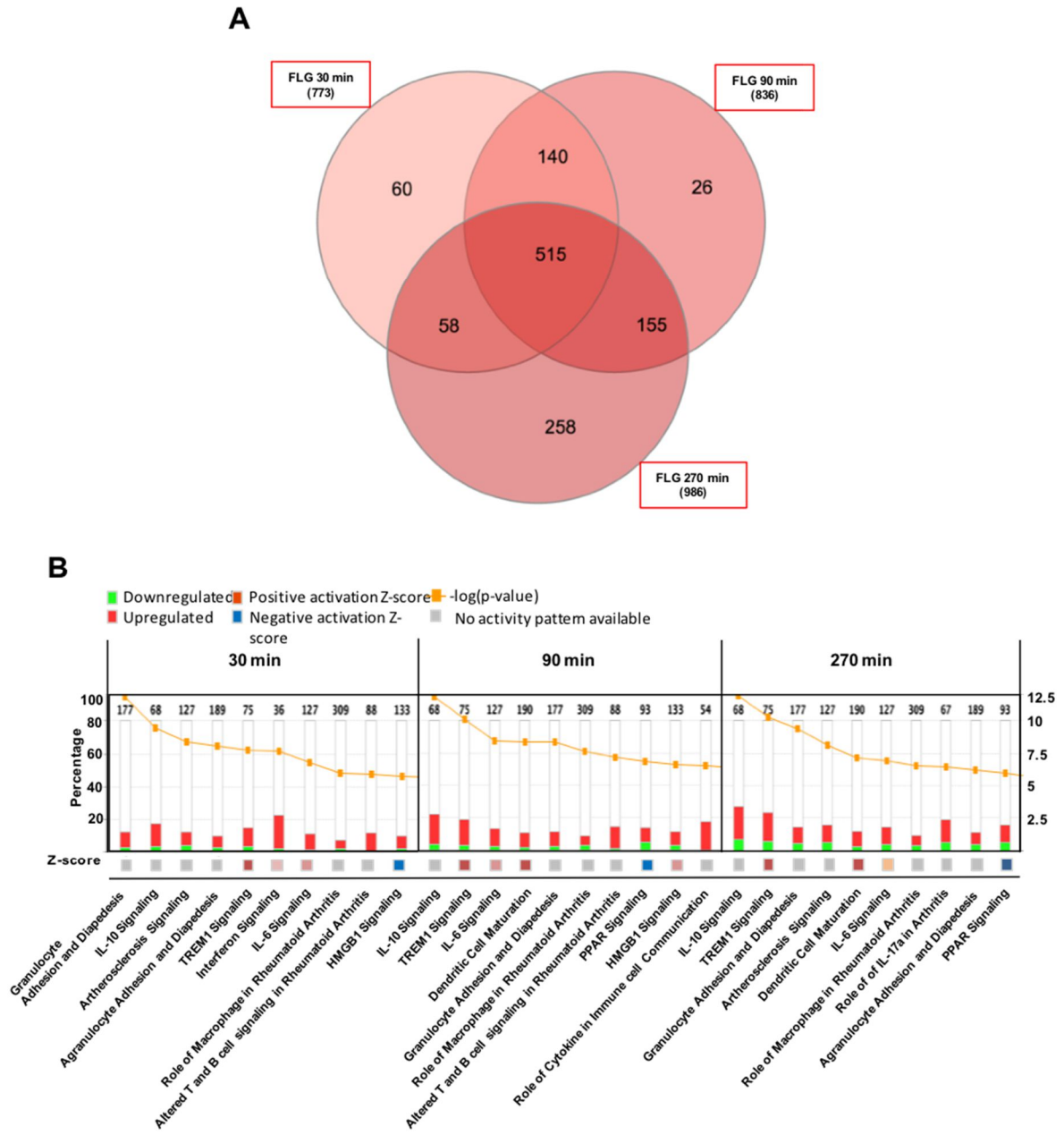

Figure S11. Gene expression impact of FLG at early time points in human isolated monocytes. A) Venn diagrams reporting the number of probe-sets modulated in response to FLG incubations for 30, 90 and 270 min. The Venn diagram is divided in three areas, one for each time points used. The total number of modulated genes in each areas are reported between the parenthesis. B) Top 10 first canonical pathways ranking according to significance level [Fisher exact test es log (p-value) reported in red] modulated by FLG identified using gene enrichment analysis. The Z-score of each pathway is expressed under each column.

The mechanisms of FLG mediated cell death was studied looking at whole-genome expression at early time points using the microarray technology. To achieve this goal, we used the microarray approach (Agilent technology) looking at more than 41000 transcripts on isolated

monocytes from healthy patients. The cells were incubated with 50 µg ml^{-1} of FLG at very early time points (30, 90 and 270 min) or left untreated. To compute the probability of genes being differentially expressed between the treated samples and controls, we used a random variance ANOVA test as implemented in Gene Spring GX Software (Agilent Technology). All genes that passed the cutoff p-value of 0.001 with a false discovery rate (FDR) lower than 5% are shown in Table S1. Venn Diagram is displayed in Figure S11A. To understand the biological function of FLG we then used Ingenuity Pathway Analysis (IPA). In Figure S11B are shown the 10 most significantly modulated pathways according to -log(P-Value) and the Z score.

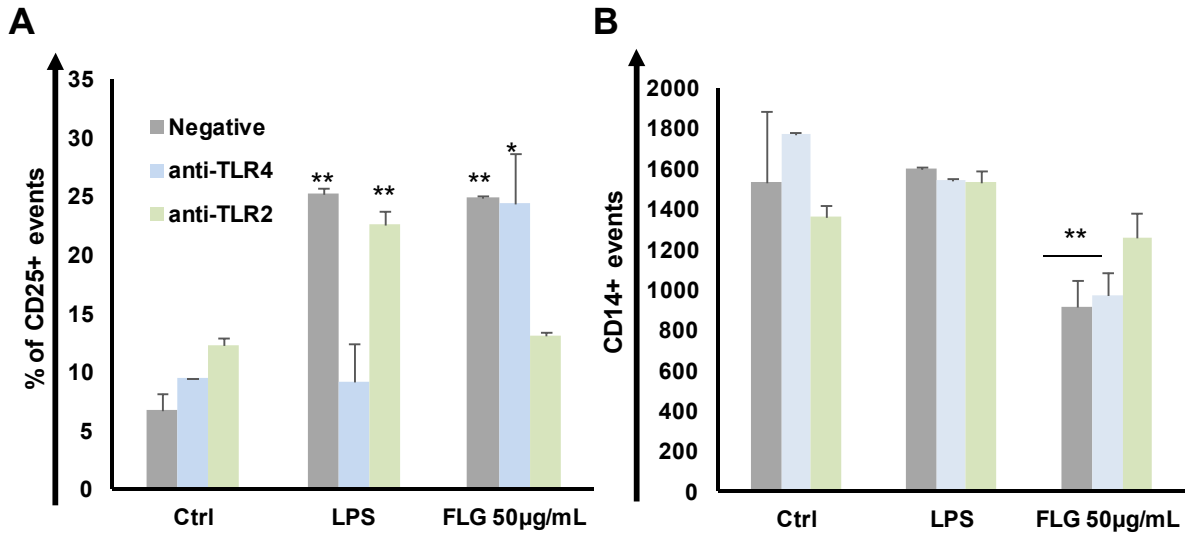

Figure S12. Role of TLR2 and TLR4 receptor in the FLG effect in isolated monocytes. Flow cytometry analysis of cellular viability of *ex vivo* monocytes exposed to FLG at the concentration of 50 µg mL^{-1} without or with anti-hTLR2 and anti-hTLR4-IgG blocking antibodies (1 µg mL^{-1}; Invivogen mabg-htlr2; mabg-htlr4) after 90 min of incubation. A) Count of monocytoid cells (CD14+). B) Activation marker expression (CD25) by monocytes. Two tail student T test was performed to determine the statistical differences versus control cells under non-blocking and blocking conditions (*$p<0.05$; **$p<0.01$).

The experiments aimed to assess the role of TLRs in the absence or in the presence of specific blocking antibodies were performed after 90 min of incubation as found by the microarray analysis to be the optimal time point to understand the early effect of FLG on monocytes. We performed several experiments looking at the cell activation and viability of monocytes using CD25 as a marker and the cell event evaluation (**Fig. S12**). As anticipated in the main text, the induced expression of TNFα could activate apoptosis and necrosis processes through the

contact with specific receptors (the so-called Death Receptors).[5] Our hypothesis is also confirmed by the up-regulation of TNFRSF6B found in FLG treated samples. This gene, also called FAS receptor, is part of the Death Receptors and after the contact with FAS ligands is able to activate the death effector domain leading to cell death.[6] Our data highlight an inflammatory induced toxicity played by FLG demonstrating that TLR2 signaling pathway has a central role in initiating the acute inflammatory response leading to necrosis induced by FLG administration.

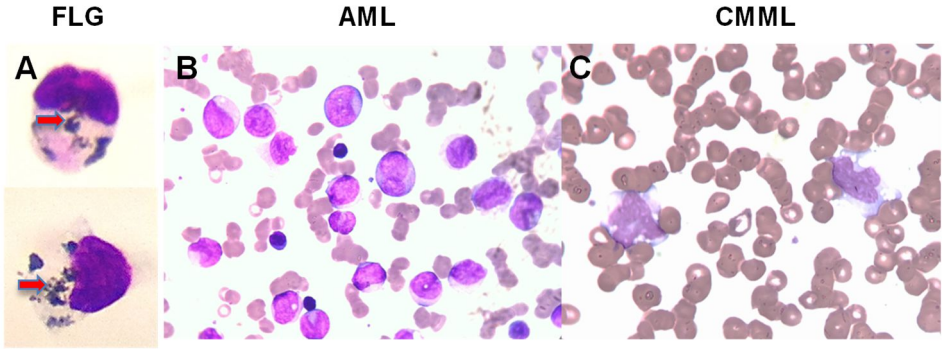

Figure S13. Intracellual presence of FLG on *ex vivo* PBMCs from AML and CMML patients. PBMCs from AML and CMML patients were incubated for 24 h with different FLG concentrations (0.5, 5, 25 and 50 μg mL^{-1}) or left untreated. (A) Visualization of FLG into AML monocytoid cancer cells highlighted by red arrows. Pictures of AML (B) and CMML (C) patients' blood, stained with May-Grunwald/Giemsa.

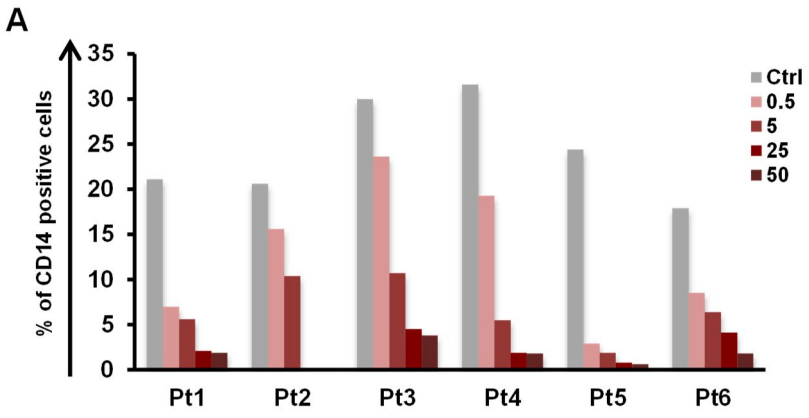

Figure S14. Histograms of myeloid CD14 positive cell ablation in PBMCs from AML and CMML patients incubated for 24 h with different FLG concentrations (0.5, 5, 25 and 50 μg mL^{-1}) or left untreated. All analyses were performed by flow cytometry.

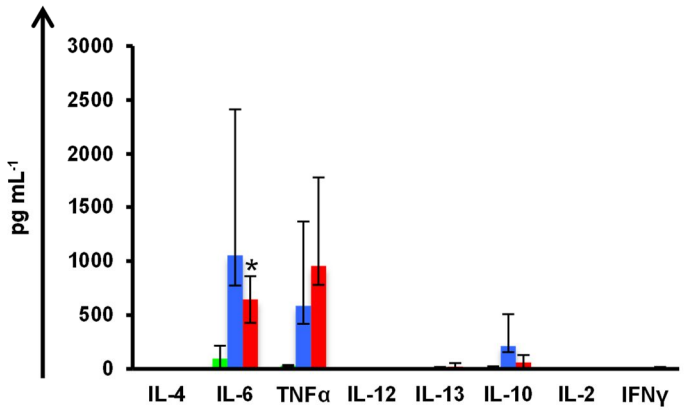

Figure S15. Cytokine secretion assay. Multiple cytokine secretion assay (ELISA) on total PBMCs from CMML patients. All analyses were performed by flow cytometry. Statistical significance compared to untreated cells (student's t test) is indicated by * = $p < 0.05$ and ** = $p < 0.01$.

A

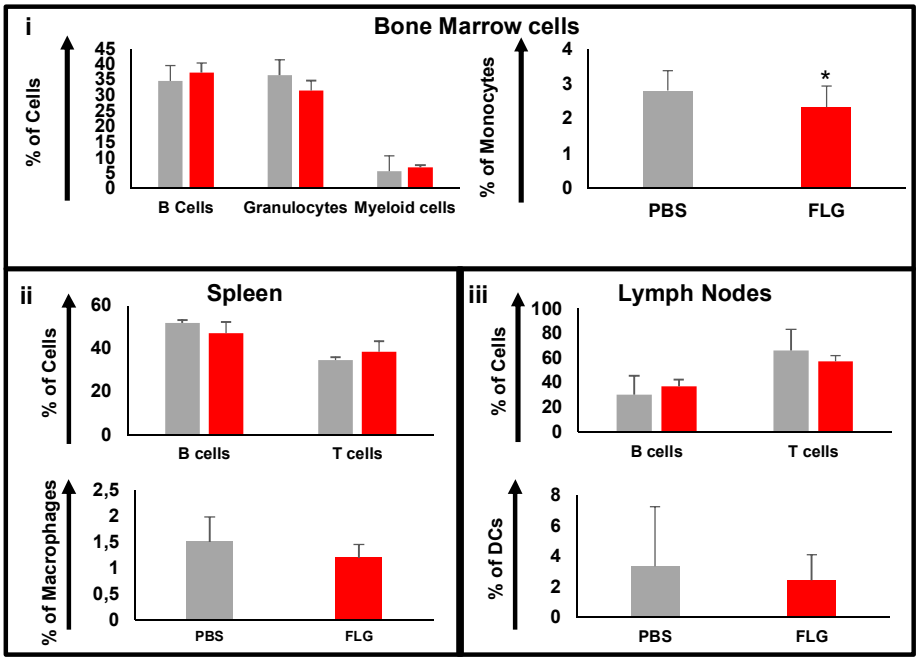

B

Blood Count	Ctrl Avg +/- Sd	FLG Avg +/- Sd	P value	Units
WBC	2.28 +/- 1.57	4.125 ± 1.52	0.18	10^9/L
RBC	4.24 +/- 0.93	4.46 ±0.86	0.76	10^{12}/L
HGB	3.9 +/- 0.82	4.1 ±0.81	0.76	mmol/L
HCT	0.22 +/- 0.05	0.23 ±0.04	0.91	Ratio
MCV	52 +/- 1.68	50.55 ±0.47	0.15	fL
MCH	0.92 +/- 0.009	0.92 ±0.007	0.79	fmol
MCHC	286 +/- 0.72	18.175 ±0.15	0.28	mmol/L
PLT	286 +/- 82.29	434.25 ±162.41	0.22	10^9/L
MPV	7.87 +/- 0.35	7.48 ±0.21	0.12	fL
PDW	8.1 +/- 0.82	7.38 ±0.21	0.14	fL
PCT	0.22 +/- 0.06	0.33 ±0.12	0.22	%

Figure S16. *In vivo* inflammation and toxicology analysis of FLG. The effects of FLG were evaluated on *in vivo* mice model. After one week from injection with 50µg mL^{-1} of blood (100 µg injected per mouse), mice were sacrificed and several organs and whole blood were harvested. (A) **i)** Bone marrow cells were flushed from femur and tibia; **ii)** spleen, and **iii)** lymph nodes were mechanical dissociated by gentle trituration and filtered through a cell strainer to create a single cell suspension. Collected cells were analyzed by flow cytometry. B) Blood count table on harvested whole blood. Two tails student T test was performed to determine the statistical differences versus control cells.

FLG at the concentration of about 50 µg mL^{-1} of blood were intravenously injected by intraocular route in C57BL/6. The effect were compared to negative control mice injected only with saline. Inflammatory reaction analysis was assessed. Bone marrow cells, spleen and lymph nodes were analyzed (**Fig. S16A**). We found no significant changes (P value >0.05) on immune cell populations in analyzed organs (**Fig. S16Ai, ii, iii**). As expected only $CD14^+$ bone marrow monocytes were significantly reduced in percentage (P value <0.05) compared to controls (**Fig.**

S16Ai). The FLG impact on whole blood exhibit no modulation in blood cell counts (**Fig. S16B**).

References

[1] K. R. Paton, E. Varrla, C. Backes, R. J. Smith, U. Khan, A. O'Neill, C. Boland, M. Lotya, O. M. Istrate, P. King, T. Higgins, S. Barwich, P. May, P. Puczkarski, I. Ahmed, M. Moebius, H. Pettersson, E. Long, J. Coelho, S. E. O'Brien, E. K. McGuire, B. Mendoza Sanchez, G. S. Duesberg, N. McEvoy, T. J. Pennycook, C. Downing, A. Crossley, V. Nicolosi, J. N. Coleman, *Nature Mater.* **2014**, *13*, 624-630.

[2] V. León, M. Quintana, M. A. Herrero, J. L. G. Fierro, A. de la Hoz, M. Prato, E. Vázquez, *Chem. Commun.* **2011**, *47*, 10936-10938.

[3] V. León, A. M. Rodriguez, P. Prieto, M. Prato, E. Vázquez, *ACS Nano* **2014**, *8*, 563-571.

[4] H. D. Heck, R. W. *Regul. Toxicol. Pharmacol.* **1985**, *5*, 294-313.

[5] F. Marques-Fernandez, L. Planells-Ferrer, R. Gozzelino, K. M. Galenkamp, S. Reix, N. Llecha-Cano, J. Lopez-Soriano, V. J. Yuste, R. S. Moubarak, J. X. Comella, *Cell Death Dis.* **2013**, *4*, e493.

[6] H. Matsumura, Y. Shimizu, Y. Ohsawa, A. Kawahara, Y. Uchiyama, S. Nagata, *J. Cell Biol.* **2000**, *151*, 1247-1256.

Paper V: *Immune cell impact of three differently coated lipid nanocapsules: pluronic, chitosan and polyethylene glycol*

Cristiano Farace[1,‡], Paola Sánchez-Moreno[2,‡], Marco Orecchioni[3], Roberto Manetti[3], Francesco Sgarrella[3], Yolande Asara[1], José M. Peula-García[5,6], Juan A. Marchal[7,8,9], Roberto Madeddu[1,10] and Lucia G. Delogu[2]*.*

[1] Department of Biomedical Science, University of Sassari, 07100 Sassari, Italy.
[2] Biocolloid and Fluid Physics Group, Department of Applied Physics, University of Granada, 18071 Granada, Spain.
[3] Department of Chemistry and Pharmacy University of Sassari, 07100 Sassari, Italy
[4] Department of Clinical Medicine and Experimental Oncology, University of Sassari, 07100 Sassari, Italy.
[5] Biocolloid and Fluid Physics Group, Department of Applied Physics, University of Granada, 18071 Granada, Spain.
[6] Department of Applied Physics II, University of Málaga, 29071 Málaga, Spain
[7] Biopathology and Medicine Regenerative Institute (IBIMER), University of Granada, 18100 Granada, Spain.
[8] Biosanitary Institute of Granada (ibs.GRANADA), University Hospitals of Granada-Univesity of Granada, 18071Granada, Spain.
[9] Department of Human Anatomy and Embryology, University of Granada, 18012 Granada, Spain.
[10] National Institute of Biostructures and Biosystem (INBB), Rome, Italy.

Keywords: Nanocapsules, nanomedicine, immune system, toxicity, biomedicine

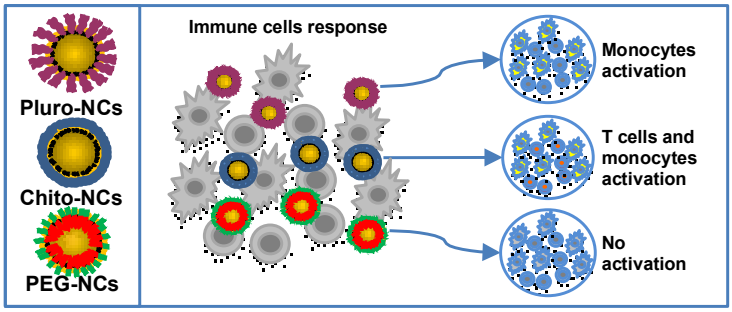

Published in:

SCIENTIFIC REPORTS

Sci Rep. 2016 Jan 5;6:18423

Abstract

Lipid nanocapsules (NCs) represent promising tools in clinical practice for diagnosis and therapy applications. However, the NC appropriate functionalization is essential to guarantee high biocompatibility and molecule loading ability. In any medical application, the immune system-impact of differently functionalized NCs still remains to be fully understood. A comprehensive study on the action exerted on human peripheral blood mononuclear cells (PBMCs) and major immune subpopulations by three different NC coatings: pluronic, chitosan and polyethylene glycol-polylactic acid (PEG) is reported. After a deep particle characterization, the uptake was assessed by flow-cytometry and confocal microscopy, focusing then on apoptosis, necrosis and proliferation impact in T cells and monocytes. Cell functionality by cell diameter variations, different activation marker analysis and cytokine assays were performed. We demonstrated that the NCs impact on the immune cell response is strongly correlated to their coating. Pluronic-NCs were able to induce immunomodulation of innate immunity inducing monocyte activations. Immunomodulation was observed in monocytes and T lymphocytes treated with Chitosan-NCs. Conversely, PEG-NCs were completely inert. These findings are of particular value towards a pre-selection of specific NCs coatings depending on biomedical purposes for pre-clinical investigations; *i.e.* the immune-specific action of particular NC coating can be excellent for immunotherapy applications.

Manuscript

Introduction

Nanomedicine has reached the interest not only of the scientific community but also of the public, becoming one of the most promising approaches for developing new tools in clinical practice [1,2]. Among other nanomaterials, biodegradable lipid nanocapsules (NCs) present incredible characteristics as drug carriers or in diagnosis applications as contrast agents [3,4]. Their useful properties include biocompatibility and biodegradability [5], the ability to perform a controlled release of drugs [6,7] and to target specific tissues [8]. Specifically, NCs consisting of an oil-filled core with a surrounding polymer shell can be used to encapsulate and deliver hydrophobic drugs [9,10]. The appropriate carrier design and functionalization, particularly the composition and surface properties, are essential to ensure high biocompatibility and to protect molecules of interest from degradation and premature elimination [11]. Biodegradable polymers and molecules have been extensively studied as loading molecules for NCs to improve their hydrophilicity in biological media, for new possible treatments of many diseases. Well before any pre-clinical application, it is of fundamental importance to choose the most suitable coating for the NCs. Moreover, for any medical application which requires intravenous injection, the first type of cells that will interact with the NCs are the blood immune cells making the NCs immunocompatibility assessment of critical importance for any translation into clinical practice. Aiming at providing an extensive overview on the immune impact of differently functionalized NCs, we report for the first time a comprehensive analysis on immune cell interaction with three different NCs coatings: pluronic F68 (Pluro), chitosan (Chito) and polyethylene glycol-polylactic acid (PEG-PLA, indicated in the text as PEG). Pluro, Chito and PEG coatings have been successfully used for NC functionalization for many applications [12,13]. PEG has been significantly employed to functionalize several nanomaterials to better deliver different genes and drugs such as camptothecin for the cancer treatment [14-17]. Controversial studies have been published in literature on the ability of PEG coating to be internalized into cells. Some studies have already reported the capability of PEG coating to be internalized into macrophages and other cells such as hepatocytes [18,19]. However, very recently Yang Q and colleagues have shown a reduced uptake of PEG coated nanoparticles by macrophages, but these interactions with phagocytic cells are critically dependent on the conformation of individual PEG chains and on the brush conformation onto the particles. Furthermore, very few

results were reported about internalization of PEG coating into other immune cells subpopulations [20]. NCs loaded with chitosan have been extensively studied to enhance the therapeutic use of siRNAs [12,21]. Moreover, chitosan is commonly used as a transacylation polymer evidencing its non-toxicity [12,21,22]. In order to improve the NC drug delivery abilities, the NC shell can be also functionalized with pluronic, a nonionic triblock copolymer. Thus its amphiphilic structure can be used to increase the water solubility of many substances. For this reason, pluronic coated NCs have been evaluated for various drug delivery applications, *i.e.* in cancer cells [13]. Moreover, these nanocarriers have been shown to inhibit multiple drug resistant proteins (MDR) and other drug efflux transporters on the surface of cancer cells; MDR proteins are responsible for drug efflux from cells and hence decrease the susceptibility of cancer cells to chemotherapeutic agents such as doxorubicin [23]. All these substances have been successfully used to improve the ability of NCs to deliver drugs and genes for the treatment of cancer and other diseases.

Biocompatibility analyses of NCs have been previously conducted, focusing on different organs and evidencing low toxicity [24]. However, to the best of our knowledge no studies reported a comprehensive immune-compatibility comparison analysis of differently functionalized NCs on immune cells, specifically *ex vivo* from healthy donors. For any translational application of nanomaterials in medicine, a key step is represented by the assessment of their possible interactions with the immune system, independently of their specific purpose [25-28]. In this context, the lack of information in literature created an urgent need to better understand different NC-coating effects on the immune system.

Hence, here the impact of three differently functionalized NCs was analyzed, namely Pluronic, Chitosan, and PEG, on human primary immune cells populations, in particular on red blood cells (RBCs) hemolysis and peripheral blood mononuclear cells (PBMCs) from healthy donors. First, we deeply analyzed the possible differences in NC internalization on PBMCs and subpopulations, such as T, B, NK cells and monocytes, to assess whether a certain coating could be more suitable for the cell uptake. We explored the possibility of necrosis, apoptosis and proliferation of PBMCs and subpopulations of T cells and monocytes, as representative of the adaptive and innate immune response. The functionality effect was tested observing: (i) the cell diameter modification; (ii) the expression of the most critical activation marker, namely CD25 and CD69; (iii) the production of a wide variety of cytokines.

Results

Nanocapsules synthesis and characterization

Two nanocapsule systems, indicated as EPI and CS in Sánchez-Moreno *et al.*[8], were previously obtained and characterized with an anionic (Pluro NCs) and a cationic surface (Chito NCs); instead, a new nanocapsule system (PEG NCs) was prepared by a solvent-displacement technique following the procedure of Prego *et al.* [29] by mixing an organic and an aqueous phase. **Figure 1A** shows a scheme of the nanocapsule composition.

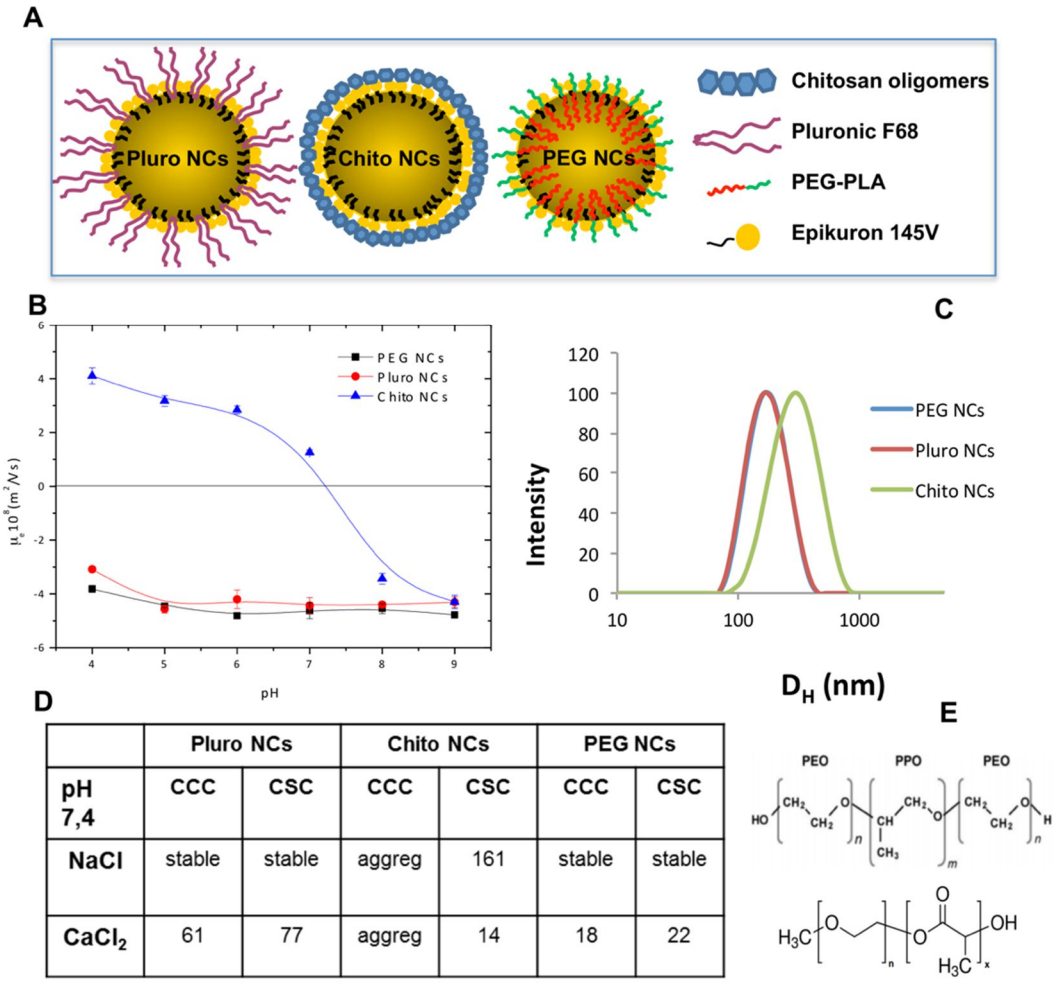

	Pluro NCs		Chito NCs		PEG NCs	
pH 7,4	CCC	CSC	CCC	CSC	CCC	CSC
NaCl	stable	stable	aggreg	161	stable	stable
$CaCl_2$	61	77	aggreg	14	18	22

Figure 1 Nanocapsule characterization: (A) Schematic details of the nanocapsule composition. (B) Electrophoretic mobility vs. pH of nanocapsules. (C) Intensity-weighted size distribution of NCs obtained from a DLS measurement. (D) Critical coagulation concentration (CCC) and critical stabilization concentration (CSC) data (mM), at pH 7.4, using NaCl and CaCl2 as aggregating salts. (E) Chemical structure of Pluronic F68 (average MW 8400 g/mol) with a central hydrophobic fragment of polyoxypropylene (PPO) and identical hydrophilic chains of polyoxyethylene (PEO) at both sides. n = 75 PEO units and m = 30 PPO units (upper image). Chemical structure of PEG-PLA. PEG average MW 350 g/mol (n = 8 EO) units.) PLA average MW 1000 g/mol (lower image).

All nanosystems were formed by olive oil in their hydrophobic core and epikuron on their shell; depending on the composition of the aqueous phases (pluronic F68, chitosan or PEG-PLA), the final samples showed different shell composition and thus, different interface properties. The nanocapsule size and electrophoretic mobility were characterized by dynamic light scattering (DLS) while the colloidal stability was spectrophotometrically studied working at physiological pH in simple saline media (NaCl and $CaCl_2$) by analyzing the change of particles diameter as a function of time.

The hydrodynamic size of all nanocapsule systems showed a narrow distribution (PDI < 0.15), as it is illustrated by the representative intensity weighted size distribution of different NCs reported in **Figure 1C**. In the present study, the synthesis procedure yielded to spherical nanocapsules with an average diameter in the nanometric scale that is potentially useful for biological applications; in fact, a mean diameter under 200-300 nm is advised in specialised literature. The size of PEG NCs was 167 ± 14 nm, while the size of Pluro NCs and Chito NCs were 170 ± 20 nm and 340 ± 30 nm, respectively, as previously reported [8]. The electrophoretic mobility data of PEG NCs, gathered from low-ionic-strength media, are also shown in **Figure 1E**. The μ_e results agree with the nature of the shell and they confirm the presence of the different molecules used in their synthesis. Pluro and PEG NCs showed a typical behaviour of colloids with weak acid groups, which come exclusively from the epikuron molecules with phosphatidyl-choline as the major component, giving lower μ_e values at acidic pH values than those found at neutral and basic pH [30,31]. PLA chains absorb onto hydrophobic interfaces, while PEG hydrophilic chains remain extended in the hydrophilic phase. Since PEG is a non-ionic surfactant it does not alter the electrical state of the surface. A similar pattern was observed for Pluro NCs, in which the non-ionic polyethylene oxide chains from pluronic did not influence the electric surface behaviour. On the other hand, the μ_e behavior of Chito NCs radically changed as a consequence of the presence of chitosan chains with glucosamine groups, presenting with a weak basic character and driving mobility from positive values at acidic pH to negative values at basic pH [32]. The analysis of coagulation kinetics enabled us to calculate the stability factor W, which provides information on the coagulation probability (W = 1 indicates a completely unstable system, while W = ∞ means total stability); at the same time, nanoparticle critical coagulation concentration (CCC) and critical stabilization concentration (CSC) were obtained, which are considered fundamental parameters in colloidal-stability studies. A thorough explanation of the respective significances of these values and on the

Dr. Marco Orecchioni. Titolo "Biomedical applications of different nanomaterials: Characterization and interaction with the immune system"
Tesi di dottorato in Life Sciences and Biotechnologies, Università degli Studi di Sassari.

method applied to obtain CCC and CSC values from coagulation kinetics data, is given in the supplementary section of reference [33]. The CCC value is related to destabilization processes and it indirectly gives information on the surface-charge density of the particles; thus, a low CCC means low stability caused by a low surface-charge density. Instead, the CSC value – defined as the minimum salt concentration at which the system begins to re-stabilize when salinity is increased– is associated with the surface hydrophilicity. This kind of restabilization phenomenon at high salt concentrations is well known in hydrophilic colloidal systems and it is governed by hydration forces [34]. **Figure 1D** shows the CCC and CSC values of different NC systems. With respect to the stability of the PEG system in NaCl, no aggregation of the particles was detected even at concentrations up to 4M because the CCC and CSC concentrations overlapped, inducing completely stable systems. An analysis of the colloidal stability in $CaCl_2$ indicated that Chito NCs were the least stable of the systems [8] since they coagulated as soon as the nanocapsules were immersed in the buffer at pH 7.4. In a high-salinity solution this system was stable due to the action of the repulsive hydration forces due to the fact that chitosan in an hydrophilic material. PEG NCs presented lower CCC value (22mM) compared to Pluro NCs (61mM), since the number of polyethylene oxide (PEO) fragments in the pluronic (75 units) was higher compared to the number of ethylene oxide (EO) in the PEG (8 units) as shown in **figure 1B**; in conclusion, these molecules contribute to the stabilization of the systems by means of a steric mechanism and increase the surface hydrophilicity [32,35]. The CSC data corresponding to $CaCl_2$ confirm the presence of pluronic (in Pluro NCs) and PEG (in PEG NCs) molecules on the surface, showing a restabilization process typical of surfaces with hydrophilic character. Nanoemulsion behaviour in several fluids (water, PBS and DMEM with 10%FBS) was also evaluated, revealing high stability in all tested solutions (data not shown).

Functionalized nanocapsule biocompatibility in red blood cells and immune cells.

The release of hemoglobin from damaged RBCs was observed and any NC-related damage on red blood cells was excluded (**S. Figure 1**). To assess the immune cell internalization ability of NCs, they were encapsulated with Courmarin 6 as a fluorophor in the hydrophobic cores of Pluro, Chito and PEG NCs. A dose-response analysis of the nanoparticle uptake at $1x10^{10}$NCs mL^{-1}, $1x10^{11}$NCs mL^{-1} and $1x10^{12}$ NCs mL^{-1} was performed (**S. Figure 2A**). The ability of differently functionalized NCs to enter inside the cells was described through an accurate analysis by flow cytometry [33] and confocal microscopy. Moreover, it has been previously

determined that after few hours of exposure, the amount of adhering particles is in most cases minimal in comparison to the active uptake and the internalized load [36]. The performed time response showed no uptake difference in the three analyzed time points (at 6, 12 and 24 hours) (**S. Figure 2B**). Furthermore, the Trypan Blue washing was performed to quench the NC signal outside the cells, as we previously performed for other nanomaterials [17] (**S. Figure 2C**). The 24-hour incubation time was adopted for all the other investigation since this is a good time point to study the effect of any nanoparticle or nanomaterial on immune cells, as other research groups suggested [39,40].

Data shown at $1x10^{11}$NCs mL^{-1} and at $1x10^{12}$ NCs mL^{-1} after 24-hour incubation that almost 100% of cells internalized all three NCs (**S. Figure 2A**).

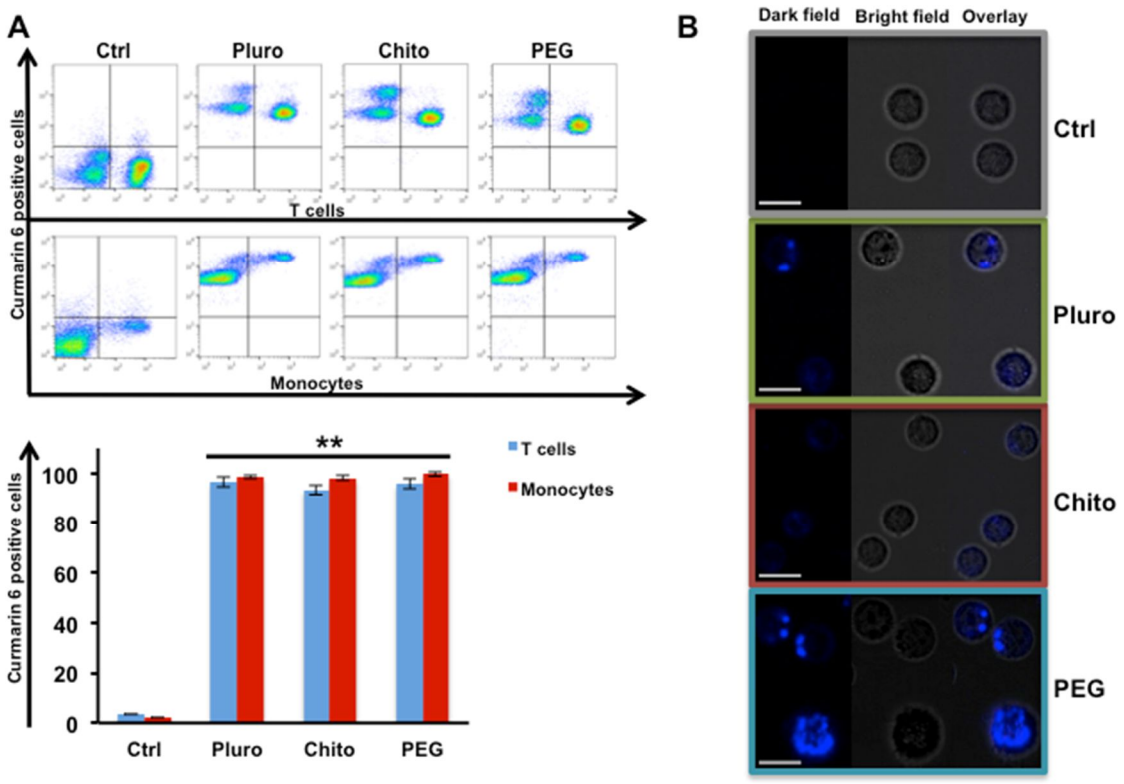

Figure 2 Uptake analysis of Nanocapsules. A) T cells (CD3+) and Monocytes (CD14+) uptake of Pluro, Chito, PEG nanocapsules loaded with Courmarin 6. Samples were analysed by FACS Calibur (BD Biosciences) and FlowJo software. On the upper pseuducolor Dot Plot are representative experiments out of 4 independent investigations. Down **= P value < 0,01. B) Confocal microscopy imaging of PBMCs incubated with Pluro, Chito and PEG NCs loaded with Courmarin 6 at the concentrations of 1x1011 mL-1. Dark field, bright field and overlay images were captured with Leica TCS SP5 confocal (Leica). Scale bar 25 µm.

Intriguingly, during the present study no inhibition was observed in NC internalization mediated by PEG (**Figure 2A and S. Figure 2 A and B**). The PEG mediated action on

internalization is still under discussion due to its well-known stealth property [20]. However, other recent studies evidenced how a specific PEG coating can enhance the nanoparticle uptake, such as in the case of cancer cells [37,38]. On the other hand, the chosen time point (24h) might be also responsible for the no PEG mediated uptake inhibition, as it was also reported in the study of Sheng Y *et al.* [41]. The concentration chosen for the further experiments was $1x10^{11}$NCs mL^{-1}; indeed, a high uptake for all NC coatings was found at this amount of particles, ensuring that any interaction into immune cells, upon internalization, was missed. Moreover this concentration was previously found to be optimal for drug delivery studies [42].

To confirm the preliminary uptake data, the cell internalization in the subpopulations of immune cells was detected. Cells were gated by specific membrane markers for the two major subpopulations of PBMCs, T cells and monocytes (**Figure 2A**). All types of NCs were able to target T cells and monocytes with a high frequency close to 100%, as showed by the FACS pseudocolor Dot Plot and by histograms. The uptake analysis was tested also on a wide variety of other subpopulations, such as lymphocytes T helper, lymphocytes T cytotoxic, natural killer cells and B cells gated by different surface marker staining by flow cytometry (**S. Figure 3**); again, NCs were able to enter into all studied cell types with a passive targeting of immune cells. Moreover, the internalization of Pluro, Chito and PEG NCs was confirmed by confocal microscopy. PBMCs were treated with NCs at the concentration of $1x10^{11}$NCs mL^{-1} for 24 hours and then visualized. All pictures confirmed the internalization of Pluro, Chito, PEG NCs into cells (**Figure 2B**). This data gives further proof of the great potential of NCs to perform intracellular drug delivery [3,6,33,43-45]. The impact of the differently functionalized NCs on cell viability was studied performing a live/dead staining. PBMCs were either incubated for 24 hours with the NCs or left untreated; positive control was set up by ethanol incubation. Upon exposure to the three types of NCs, no significant necrotic cell levels were noticed (**Figure 3A**). The early apoptotic cells with Annexin V staining on T lymphocytes and monocytes were then observed. Flow cytometry analysis showed a different impact on cells NC-coating dependent (**Figure 3B**). The Annexin-V staining evidenced that the NC functionalization could influence the viability on different cell types. Similar results for both Pluro and PEG NC functionalizations were found in lymphocytes: no statistically significant differences were observed between the control and the T lymphocytes treated with NCs. On the other hand, the incubation with Chito-NCs induced cell apoptosis in T lymphocytes (P value < 0,05). A similar action of Chito-NCs was also assessed against monocytes. The apoptosis induction in

monocytes was more than three times higher compared to controls. Moreover, in this type of cells also pluro-NCs were responsible for a clear induction of apoptosis (P value < 0,01). Cell viability was not affected by PEG-NCs in both cell populations (**Figure 3B)**. These different actions exerted by Pluro and Chito-NCs were also confirmed by the proliferation assay on total PBMCs (**Figure 3C**).

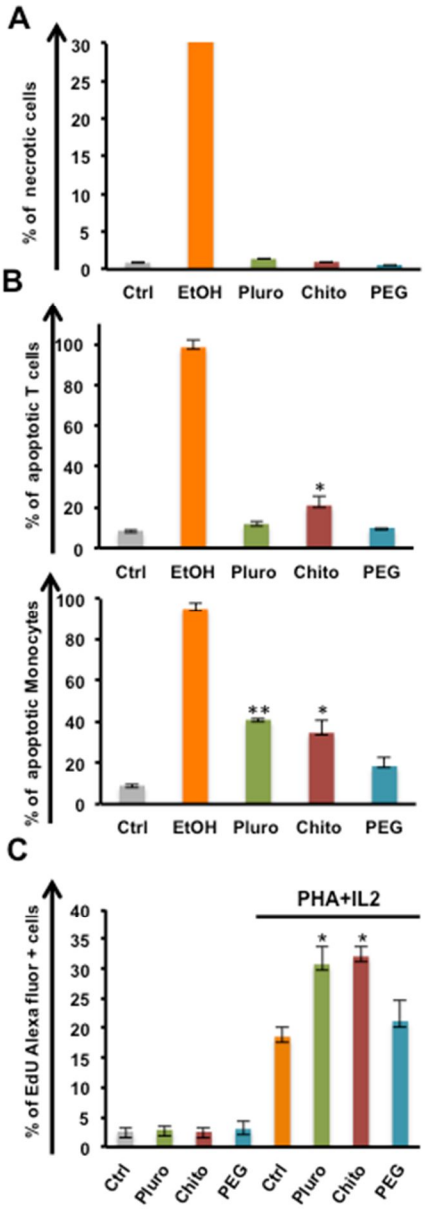

Figure 3 Viability and proliferation. PBMCs were incubated with Pluro, Chito and PEG NCs at the concentration of 1x1011 mL-1 or left untreated (Ctrl). A) Percentage of necrotic cells was assessed by a Live/Dead staining after 24 hours of incubation, ethanol (70%) was used as positive control. B) Apoptosis was assessed using Annexin V staining for Monocytes (CD14+ cells) and T cells (CD3+ cells), ethanol (70%) was used a positive control. Samples were analyzed by FACS Calibur (BD Biosciences). C) Proliferation assay was performed on stimulated cells with phytohemagglutinin 2% (PHA) and interleukin 2 (IL2) 30 u/mL for three days. 5-ethynyl-2´-deoxyuridine (Edu) is incorporated into DNA during active DNA synthesis; Percentage of Edu positive cells is reported. All experiments were performed at least in triplicate in independent assays (*= P value < 0,05, **= P value < 0,01).

Samples were treated with phytohemagglutinin at 2% and 30 μ/mL of IL2 for three days to boost the proliferation in presence of lipid nanocapsules. Control samples were left untreated. A staining with 5-ethynyl-2´-deoxyuridine (Edu) alexafluor conjugated was performed; Edu was incorporated into DNA during active DNA synthesis. Interestingly, Pluro and Chito NCs induced an enhancement of proliferation compared to controls ($P < 0,05$). PEG-NCs confirmed the viability data; in fact, PEG-NCs treated samples were perfectly comparable with controls, showing the total absence of cell induction.

Immune cells activation analysis

The different action of Pluro, Chito and PEG NCs on the immune cell functionality was analyzed by two activation assays (**Figure 4**). Firstly, cell morphological changes in terms of diameter after NC incubation were observed. In fact, when immune cells are under activation stimuli a change in diameter occurs by increasing the cellular volume. For instance, activated monocytes increase their diameter starting phagocytosis. In addition, the naïve T cells before the contact with the antigen have a resting diameter of 6-8 μm, in our case the same role can be played by NCs; on the other hand, activated T cells increase their diameter of 12 μm or more, thanks to the induction of the replication cycle [46]. This is the criterion used to deeply analyze the immune impact of NCs and to further validate data found with Flow Cytometry. The present study was carried out on PBMCs from healthy donors that included different cell populations, T cells, B cells, monocytes, dendritic cells and natural killer cells to better reflect the effects on the pool of cell populations relevant to *in vivo* immune responses.

PBMCs from healthy donors were treated with the three NCs at the intermediate concentration of $1x10^{11}$ mL^{-1}; experiments and data analysis were carried out with Scepter (Millipore). **Figure 4A** shows the cell diameter of monocytes (**Figure 4A ii**) after treatment with Pluro and Chito NCs, compared to controls; in particular, Chito NCs led to similar changes in monocyte diameter compared to lipopolysaccharide (LPS) treated samples. Thus, cells with a diameter of $2,52 \times 10^4$ larger than 11,75μm were found in Chito NCs compared to cells of $2,33 \times 10^4$ in LPS; the relative amount of cells in control samples was $1,35 \times 10^4$ (**Figure 4A iii**). Intriguingly, PEG-NCs samples were perfectly comparable with controls having $1,08 \times 10^4$ cells, without any activation stimuli (**Figure 4A iii**).

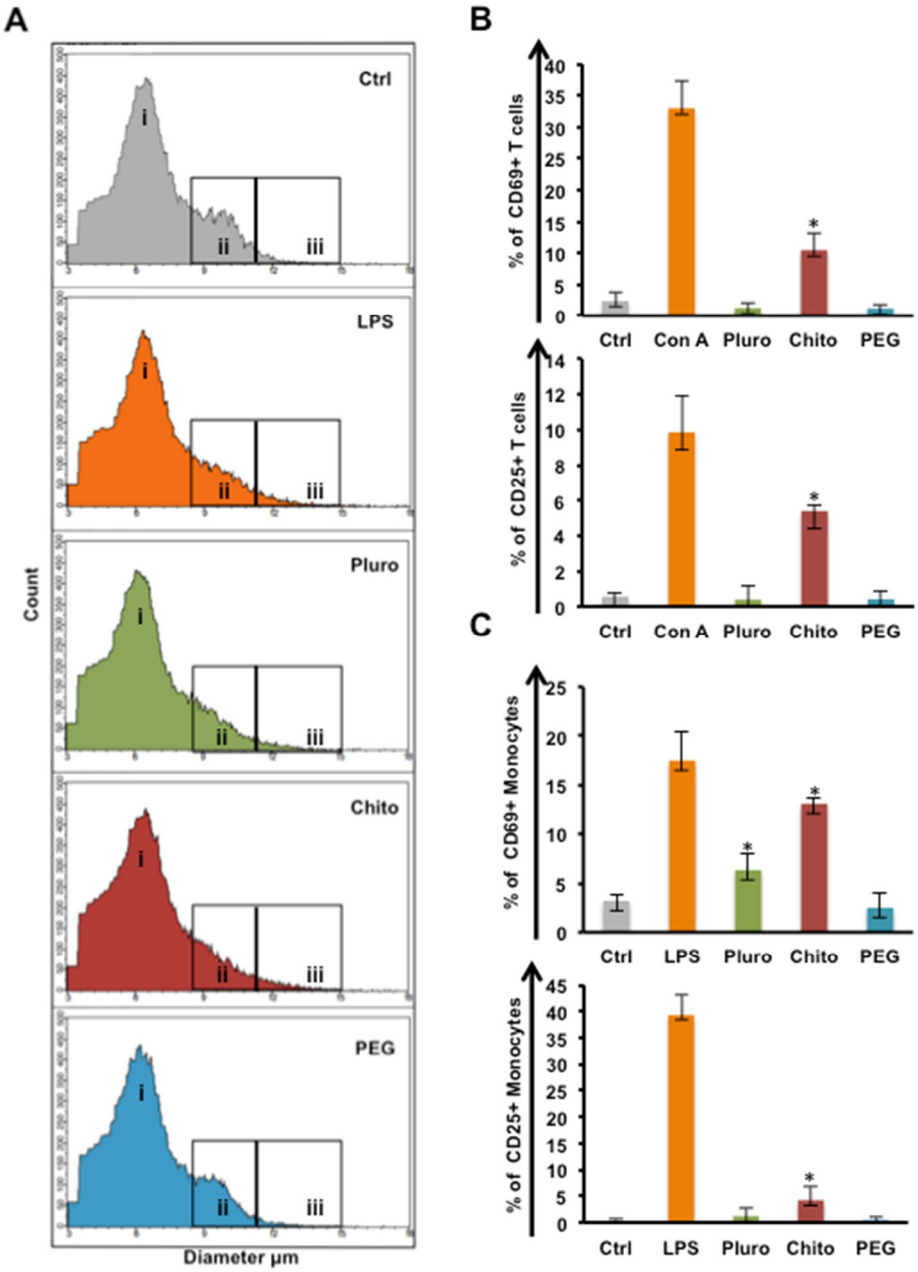

Figure 4 Activation assays. PBMCs were incubated with Pluro, Chito, PEG NCs at the concentration of $1x10^{11}$ mL^{-1} or left untreated (Ctrl) for 24h. Lipopolysaccharides (LPS 2µg/mL) or concanavalin A (ConA, 10 µg/mL) were used as positive controls. A) Morphological analysis (count and diameter) of PBMCs with Scepter 2.0 (Millipore) **i** highlights the lymphocytes peaks boxes, **ii** highlights monocyte peaks and **iii** highlights activated monocytes with a diameter higher than 11,25µm. Percentage of CD25 and CD69 cell surface activation marker expression on T cells (B) and monocytes (C) were analyzed by flow cytometry. Experiments were performed at least in triplicate (*p value < 0,05).

Afterwards, the different immune activation mediated by Pluro, Chito, PEG NCs was analyzed by observing the modulations of CD25 and CD69 cell surface activation markers on T cells and monocytes. CD25 and CD69 are critical markers for the immune response. CD25 (alpha chain of the IL-2 receptor) is a late activation antigen. Whereas, the CD69, a member of the C-type

lectin superfamily (Leu-23), is one of the earliest cell surface antigens expressed by immune cells following activation. PBMCs were treated with the three NCs at the intermediate concentration of $1x10^{11}$ mL^{-1}. Interestingly, CD25 and CD69 expression on T cells and monocytes was not modulated by PEG NCs (**Figure 4 B and C**), evidencing no induced activations on both analyzed cell types. Likewise, Pluro NCs did not boost the expression of activation markers on T cells (**Figure 4B**). However, Pluro NCs were found able to induce CD69 expression on monocytes (**Figure 4C**), highlighting the Pluro NCs specific action on this cell population. Notably, Chito NCs were able to strongly activate the immune cells, giving a powerful CD25 and CD69 modulation on both immune cell types (**Figure 4 B and C**).

Cytokine secretion

To further investigate the Pluro, Chito and PEG NC action on immune cells, the protein level was evaluated using ELISA multiplex technology to measure the secretion of a wide variety of cytokines: IL4, IL6, IL10, TNFα, IFNγ, IL13, IL12 and IL2 (**Figure 5**).

The different impact of the three functionalized NCs on immune cells was confirmed. Analytically, figure 5 shows that Pluro and Chito NCs have a higher effect compared to PEG NCs. Pluro NCs induced IL6, TNFα (P value < 0,01), IL12 and IL10 secretion (P value < 0,05). Moreover, Chito NCs gave a significant enhancement in IL6, IL10, TNFα, IFNγ, IL13 (P value < 0,01) IL4 and IL12 secretion (P value < 0,05). Intriguingly, PEG NCs confirmed to be perfectly inert for cells.

The cytokines found expressed such as IL6, TNFα and IL12 are normally secreted by monocytes/macrophages and their action is directed on the activation of the acute inflammation process [47]. IL12, for instance, activates NK cells and T Lymphocytes to produce IFN-γ (which we found modulated by Chito NCs) and specifically induce differentiation of T cells in T helper 1 (Th1) confirm a Th1-mediated protection enhancing also an increased cytotoxic activity [48-51]. IL10, which we found secreted in both Pluro NCs (P-Value <0.05) and Chito NCs (P-Value < 0.01), is a cytokine mainly secreted by activated macrophages that through a negative feedback directly control the immune response. IL10 plays a crucial role in the innate immunity in controlling the immune cell response, which is normally correlated with the inhibition of IL12 secretion.

Taken together these results show that Pluro and Chito NCs mediated the induction of both innate and adaptive immunity response. However, as showed in **figure 5** the action of Pluro

NCs was significantly lower than Chito NCs, taking in consideration the expression of IL10 and TNFα, 2 times and 4 times lower, respectively. This trend was also showed in the activation marker analysis on monocytes (**Figure 4B**). Furthermore, Chito NCs mediated also a production of IL13 and IL4 (P-Value < 0,05). Both cytokines are strictly correlated with the activation of the lymphocyte T helper 2 [52].

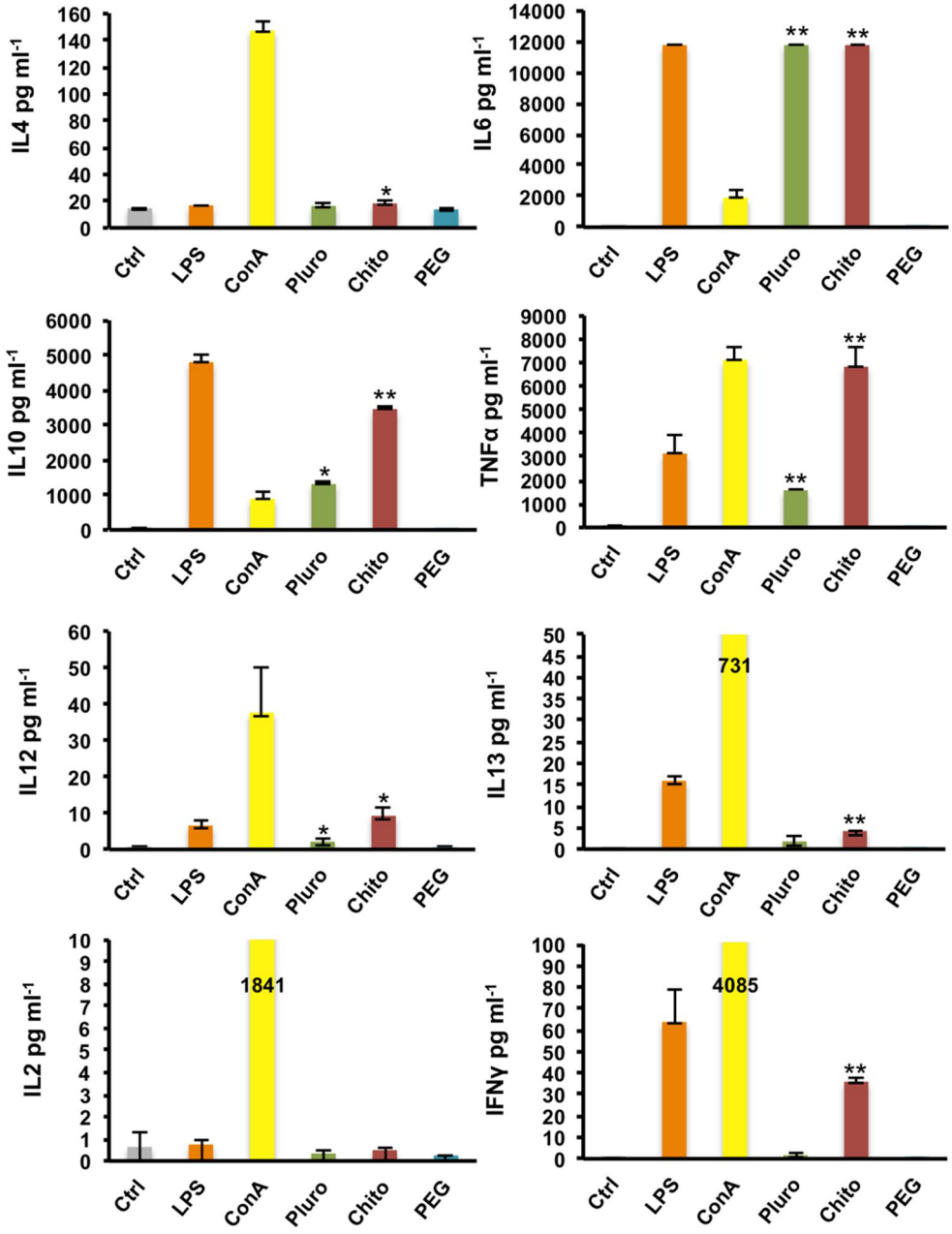

Figure 5. Cytokine secretion. Cytokine release was assessed by multiplex ELISA on PBMCs. Cells were incubated with nanocapsules: Pluro, Chito and PEG at dose of $1x10^{11}$ mL^{-1} or left untreated. Concanavalin A (ConA, 10 µg/mL) and lipopolysaccharides (LPS 2µg/mL) were used as positive controls. After 24 hour the supernatants were collected and analyzed. Supernatants were analyzed by MILLIPLEX® MAP Multiplex Assays Using Luminex xMAP® Technology. All the experiments were performed at least in triplicate (*= P value < 0,05, **= P value <0,01).

Discussion

Functionalized NCs have been developed for biomedical purposes due to many advantages: (i) improved biocompatibility and stability; (ii) extended circulation time; (iii) specific targeting function; (iv) enhanced drug encapsulation efficiency and reduced drug leakage; (v) great potential as multimodal therapeutics. All of these NC properties open new scenarios in medicine [53].

Particularly in the context of drug delivery, our data give many positive inputs for further translational medicine research regarding the ability of the three NCs studied to pass through the immune cell membrane and to passively target the immune cells. We have previously shown that cell internalization might be useful in the context of chemotherapy by using tumor-targeted molecules [6,42]. Indeed, targeting capacities of these systems can be implemented by surface modification with specific molecules (*e.g.* antibodies) [14,54-58]. However, here we have demonstrated that molecules used to functionalize NCs might have diverse impacts on immune cell viability and activation, evidencing the need to know well, before any medical application, the expected action of different functionalized particles on immune cells. Pluro Chito and PEG coatings have been well investigated and characterized by many reports [20,59-61]. However, this is to our knowledge the first study comparing the action on immune cells of three highly used nanocapsule coatings for biomedical applications as it is well known in nanoscience the extreme importance of evaluating the immune response to different nanoformulations [62]. As a matter of fact, the possible interactions between nanoparticles with different coatings and the immune system, could result into an immunostimulation or an immunosuppression, which might either be applied in immunotherapy or may promote inflammatory/autoimmune disorders [63,64]. The main function of the immune system is to protect the host from foreign substances; however, inadvertent recognition of nanoparticles as foreign by the immune cells may result in a multilevel immune response against nanoparticles [63]. Addressing the need to carry out additional evaluation and an overall comparison of the immune impact of different nanoparticles, we aimed here at provide a broad a complete picture on the impact of differently functionalized NCs on human primary immune cells. The surface modification of systemic drug carriers by PEG is one of the preferred ways to decrease opsonization by reducing interactions with blood [65]. Recent investigations regarding PEG showed a reduced uptake and clearance by immune cells when using PEG-coated nanoparticles [20,59,66,67]. Jang *et al.* investigated interactions of PEG-coated grafts with embryonic immune cell lines showing that they are able

to maintain stemness properties[59]. Yang *et al.* demonstrated the well-known stealth property of PEG; specifically, they showed a reduced uptake of polymeric nanoparticles by macrophages [20]. A recent report also indicate that repeated injections of PEGylated liposomes induce significant immune responses [68]. In this work the overall immune-compatibility of PEG NCs was highlighted, proving the absence of toxicity and activation stimuli. Our data may give new insights into the use of PEG coating for NCs and other nanomaterials to be used as highly safe and inert molecule [15,16,69,70]. A contribution was given to improve the knowledge on the absence of immune impact and toxicity of PEG in monocytes, as already reported in literature [18,19] and also in primary human immune cells, total PBMCs and specifically in T cell populations. Moreover, in the context of PEG nanoparticle uptake, our PEG-PLA coating was able to bypass the well know stealth property of PEG, showing a good internalization of NCs into immune cells [20]. As it was previously proved by Stefanick JF *et al.*, this can be explained through a modulation of many parameters such as the brush conformation of the particle surface mediated by the used PEG and through a control of PEG concentration compared to PLA [37,38], as it was shown by Saw P E *et al*. Notably, the length of the PEG used in this work is quite short and this may explain the higher uptake observed [33]. Moreover, Vonarbourg A *et al.* described that the stealth property of PEG NCs decreased with the increase of NC size, especially for macrophage uptake [71]. Pluro NCs showed its potential as safe coating without induced necrosis. However, data indicated an induction of apoptosis phenomena on monocytes exclusively in the 40% of cells. Our hypothesis is that Pluro NCs may have a specific action on monocytes; this is also emphasized by the membrane cell markers and cytokine analysis that showed CD69 up-modulation in monocytes and increased the release of IL6, IL10, IL12 and TNFα. The activation observed during our study might also be responsible for the apoptotic induction, a phenomenon that normally occurs during the activation process of immune cells [72,73]. Moreover, pluronic and chitosan were previously studied for vaccine formulations as adjuvants able to increase the immune response [74,75]. Our new Pluro NCs could be useful for better internalizing and delivering vaccines thanks also to their activation properties, through the specific activations of monocytes with a systemic immunization of the body enhancing the antigen presentation activity of monocytes to T Cells. The abilities of Pluro NCs on monocyte activations could be useful for drug delivery combined to immunotherapy for future new tools in cancer therapy [76]. Intriguingly, our data are not in agreement with the study of Kim HG and colleagues, as they declared that pluronic nanoparticles do not modulate immune responses

mounted by macrophages. However, for their experiment that research group used a murine macrophage cell line (RAW cells) that is a good system to collect preliminary data but is not perfectly comparable with the response of human primary immune cells. Moreover, the activation that was observed in our study and particularly on cytokine secretions could be a result of various cell interactions that are possible in a PBMCs system. For this reason, further studies with Pluro NCs for its application in immunotherapy will be carried out by our research group; in fact, this may be the new frontier to fight cancer based on specific activation stimuli of immune cells against cancer cells, *i.e.* to treat melanoma, avoiding at the same time the immunosuppression of the healthy immune system induced by tumor growth [77-79].

Moreover, data showed also an immune activation of cells treated with Chito NCs that is similar and even higher compared to those treated with Pluro NCs. Intriguingly, Chito NCs induced apoptosis in both populations, monocytes and T cells. The apoptotic induction of Chito NCs can be explained in the same way as for Pluro NCs; our data showed, indeed, the Chito NCs mediated induction of T cells and monocytes immune response and that action was followed by the activation of cell proliferation of both monocytes and T lymphocytes.

Cytokine analysis clarifies that after incubation with Chito and Pluro NCs, T cell activation occurred through the action of monocytes that induce the differentiation of naïve T cells in T helper cells. Thus, we observed an induced secretion of TNF and IL12 mediated by monocytes/macrophages that normally activate the T cells and NK cells to produce in the pro-inflammatory phase the same cytokine resulted increased in our experiments, such as the INF-γ which stimulates macrophages to produce TNFα. Moreover, IL12 promotes the differentiation of $CD4^+$ T cells in Th1 cells that continue to produce IFN-γ as a reinforcement of macrophage immune response [48,49]. These cytokines organize inflammatory centers and enhance cellular immune response. With the enhancing of cytotoxic activity many intracellular pathogens can be killed through the activation of antimicrobial defenses [80,81]. These data confirm and extend to a human *ex vivo* system the work of Shibata Y *et al.*, where authors showed in mice that phagocytosable small-sized chitin particles activated alveolar macrophages to express cytokines such as IL-12, TNFα, and IL-18, leading to INF-γ production mainly by NK cells [82]. These results are supported also by the work of Li X *et al.*, where the systemic administration of chitosan provides significant priming effects in alveolar macrophages and NK cells in mice [60]. Interestingly, an action of Chito NCs in the secretion of IL-4 and IL-13 cytokines was found during the present study. The effector T helper 2 cells (Th2) produce

normally a cytokine profile such as IL-4, IL-6, IL-10, IL-13, here were found up-regulated by Chito NCs, that together instruct B cells to proliferate and differentiate into antibody-secreting plasma cells. As such, Th2 cells play an important role providing protection against certain extracellular pathogens, such as bacteria and a variety of parasites, and are also involved in asthmatic reactions [80,81]. The possible activation of Th2 cells mediated by Chito NCs could be responsible for an induction of allergic response that must be well evaluated by further studies. However, the modulation of the Th response is one of the main purposes of immunotherapy and it can be useful for other therapy strategies *i.e.* in the context of vaccines [80]. As reported above for pluronic, also chitosan is currently used as an adjuvant for vaccines [60,83]. Nevertheless the evaluation of adjuvant properties is challenging since available data are insufficient to demonstrate immunogenicity of chitosan, its mechanism of action and to exclude impurities as the active substance [83]. Herein, we clearly reported Chito NCs mediated induction of monocytes, T cells and NK cells; specifically, we demonstrated an induction mediated by the innate immunity of Th1 able to provide a full enhancement of the immune response after treatment. All these actions occurred exclusively for Chito NCs that in our screening resulted as an excellent first step for further studies on vaccines delivery perspectives, immunotherapy and immunomodulation activities.

Conclusions

In summary, although lipid nanocapsules harbour interesting medical applications, the potential immune impact still needs to be carefully evaluated. To our knowledge, no comprehensive studies were carried out on human immune cell populations *ex vivo* using a wide variety of functionalized NCs. In the present work, the immune cell interactions of NCs coated with pluronic, chitosan and PEG in immune cell types from healthy donors were investigated. We observed that different types of NCs lead to different impacts on immune cells and subpopulations of T cells and monocytes: totally inert (PEG NCs) or immune inductive (Pluro NCs and Chito NCs). Thanks to our data we open new windows for applications of different coated NCs in future nanomedicine-based therapies. Specifically, the Pluro NCs targeted induction of monocytes could be extremely useful for macrophage-based immunological therapies, particularly against metastases formation. In addition, the Chito-NCs-mediated induction of monocytes that activate lymphocytes Th1 response and also a Chito NCs mediate Th2 response was evidenced, providing the whole enhancement of the immune response after

treatment. Based on these results, it will be useful to focus on Pluro and Chito NCs as future tools in vaccines delivery, immunotherapy and immunomodulation activities. In conclusion, our findings are of particular value towards a well-defined pre-selection of specific NC coatings based not only on their specific biomedical purposes but also in view of their immune-interaction and immuno-modulation.

Materials and Methods

Nanocapsule preparation

The nano-systems studied were prepared by a modified solvent displacement technique following the procedure of Calvo *et al.* [29]. Briefly, an organic phase composed of 40mg of Epikuron 145V and 125 µL of olive oil, dissolved in 0.5 mL of ethanol and 9.5 mL of acetone, was added to 20 mL of an aqueous phase under magnetic stirring containing 50mg of Pluronic F68 (Pluro NCs), 10mg of chitosan (Chito NCs) or 30mg of PEG-PLA (PEG NCs). Organic solvents (acetone and ethanol) plus a portion of the volume of water were evaporated in a rotary evaporator at 40°C, obtaining a final volume of 15 mL. Finally, nanoparticles were extensively cleaned by dialysis through ultrapure water for 24 hours to remove the unbound surfactant molecules.

Coumarin 6-loaded lipid nanocapsules were formulated by dissolving the dye in the olive oil phase at a concentration of 0.025% (w/w). The concentration of the different nanoemulsions was estimated by calculating the volume of a single particle with the equation of the volume of a sphere: $V=4/3.\pi.r^3$, using the hydrodynamic mean radius obtained from DLS measurements, and then the number of particles that were formed by the total volume of olive oil were used in the synthesis.

Size and electrophoretic mobility

A Zetasizer-nano Z (Malvern Instruments) was used to measure the hydrodynamic mean diameter and the electrophoretic mobility (µe) of the nanocapsules. The µe was measured as a function of pH while maintaining a constant low-ionic-strength value (0.002 M). The size and mobility data were recorded in triplicate.

Colloidal stability

Colloidal stability was spectrophotometrically studied monitoring the turbidity of the nanocarriers (Beckman DU 7400 spectrophotometer) working at 570nm in simple saline media (pH 7.4). The salts used were NaCl and $CaCl_2$. From the analysis of aggregation kinetics, we calculated two important parameters in colloidal-stability studies, the critical coagulation concentration (CCC), defined as the minimum salt concentration needed for the most rapid aggregation, and the critical stabilization concentration (CSC) defined as the minimum salt concentration at which the system begins to re-stabilize when salinity is progressively increased and related to the surface hydrophilicity [34].

Peripheral blood mononuclear cell preparation

For each experiment, human PBMCs were obtained from EDTA-venous blood samples from healthy male donors (25-50 years of age) using a standard Ficoll-Paque (GE Healtcare) separation and cultured in RPMI medium added with FBS 10% and 1% of Penicillin/Streptomycin solution. All donors provided a written informed consent. The study was reviewed and approved by the Ethics Committee of the University of Sassari. The studies were carried out in accordance with the approved guidelines.

Uptake analysis

Uptake of coumarin 6-loaded Pluro, Chito and PEG-Nanocapsules by immune cells was studied. Nanocapsules were incubated with PBMCs for 24 hours at different concentrations ($1x10^{10}mL^{-1}$, $1x10^{11}mL^{-1}$ and $1x10^{12}mL^{-1}$). Time points experiments were also conducted at 6, 12 and 24 hours with all three studied NCs, at the fixed concentration of $1x10^{11}mL^{-1}$. After incubation, cells were harvested, washed twice in cold phosphate buffered saline (PBS) and re-suspended for analysis. Cell fluorescence was measured after the cells were washed with a 0.4% (w/v) trypan blue solution in order to quench fluorescence from non-internalized NCs [17].

The gating of cell populations was performed with specific fluorescently-labeled monoclonal antibodies: fluorescein isothiocyanate (FITC), phycoerythrin (PE), peridinin chlorophyll protein (PerCP), or allophycocyanin (APC) conjugated with anti-CD3, anti-CD4, anti-CD8, anti-CD14, anti-CD56 and anti-CD20, antibodies that were purchased from BD Biosciences (Mountain View, CA, USA). Uptake analyses were performed with flow cytometry (FACS Calibur BD Bioscience) using CellQuest software (BD Biosciences). A total of 50,000 events

per sample were recorded. Data analyses and plots were performed with FlowJo software (MACS Miltenyi Biotec).

For the confocal microscopy imaging analysis, PBMCs were incubated with Courmarin 6-loaded nanocapsules as described above, washed twice with PBS and re-suspended at the concentration of 2 x 10^6 cells/0,5 mL; 30µL of the cell solution was put onto a slide, fixed with shellac and observed by confocal laser scanning microscopy (Leica TCS SP5, Leica Microsystems). Courmarin 6 was excited with an argon laser at 405 nm with 20x camera lens, the excitation filter bandwidth was: BP470/40 and the emission filter was: BP525/50. At least 20 pictures per sample for each experiments were captured.

Hemolysis, cell viability, apoptosis and necrosis assay

Hemolysis test was conducted following previously used protocols [84]. Fresh human whole blood was taken from volunteer healthy donors stabilized with ethylenediamine tetraacetic acid (EDTA). Serum was removed from blood samples by centrifugation at 200 g for 5 minutes. Resulting RBCs were washed five times with sterile isotonic PBS and then diluted 10 X with EDTA. To determine the hemolytic activity of different NCs, Pluro, Chito and PEG NCs at the concentration of 1x10^{11}NC mL^{-1} were added to dilute RBCs suspension (0.2 mL, 4 x 10^8 cells/mL) in a final volume of 1mL PBS. After vortexing, the mixtures where left at room temperature for 2 hours, NCs and intact RBCs were removed by centrifugation. A microplate reader (Sunrise, Tecan) measured the absorbance (A) of the hemoglobin in the supernatant at 570 nm, with the absorbance at 620 nm as a reference.

For viability assay, PBMCs were transferred to a 24-well plate and treated for 24 hours in triplicate with Pluro, Chito, PEG nanocapsules at the concentration of 1x10^{11}NC mL^{-1} or left untreated. Cells were treated with EtOH 70% as a positive control and then washed in cold PBS before the staining reaction. After incubation, cells were harvested, washed in cold PBS and re-suspended in 1mL of PBS at 1 x 10^6 cells mL^{-1}. Viability was assessed by the LIVE/DEAD® Fixable Dead Cell Stain Kit (Invitrogen) following the manufacturer instructions; the kit employs an amine-reactive fluorescent dye for cells with compromised membranes (late apoptotic and necrotic), the dye reacts with free amines both inside the cell and on the cell surface. In viable cells, the dye reactivity is restricted to the cell surface amines, resulting in less intense fluorescence. To detect cells undergoing apoptosis, Annexin-V FITC staining was employed (Invitrogen). Cells were analysed by flow cytometry (FACS Calibur BD-

Bioscience). Data analysis was performed by flow cytometry (FACS Calibur, BD Biosciences) using CellQuest® software (BD Biosciences) and with Flowjo software (MACS Miltenyi Biotec).

Proliferation assay

To perform the proliferation assay, the Click-iT® EdU Alexa Fluor® 488 Flow Cytometry Assay Kit (Life Technologies) was used. Experiments were performed according to the manufacturer's instructions. Cells were seeded at the concentration of 1 x 10^6 cells mL^{-1} in 96-multiwell rounded bottom plates. PBMCs were treated with Pluro, Chito, PEG NCs at the concentration of $1x10^{11}$NC mL^{-1} and Phytohemagglutinin 2% (PHA) and interleukin 2 (IL2) 30 μ/mL or left untreated. 5-ethynyl-2-deoxyuridine (EdU) were added in sterile conditions 16 hours before analysis. After 72 hours of incubation, cells were harvested, washed in PBS, fixed with 4% paraformaldehyde, washed in PBS plus 1% Bovine Serum Albumin (BSA), permeabilized with a saponin-based reagent and prepared for the Cu-assisted EdU-Azide Click-iT reaction. The reaction occurs after adding 500 μl of Click-iT reaction cocktail (PBS, $CuSO_4$, fluorescent dye azide and reaction buffer additive) to each sample. Analyses were performed by Flow cytometry (FACS Calibur BD Bioscience) using CellQuest software (BD Biosciences). A total of 50, 000 events per sample were recorded.

Activation analysis

To investigate the functional impact of Pluro, Chito, and PEG NCs on primary lymphomonocytes, considering their activation as a crucial endpoint, we previously consucted an immune cells diameter analysis. PBMCs were incubated with three NCs at the concentration of $1x10^{11}$ mL^{-1} for 24 hours. Lipopolysaccharides (2 μg/mL) were used as positive controls. After 24 hours of incubation, samples were harvested and cells were suspended in PBS. Analyses were carried out with Scepter (Millipore) using 40 μm sensor; plots and data analysis were done with Scepter Software Pro 2.1 (Millipore).

At a later stage we evaluated the expression of CD69 and CD25 activation markers by flow cytometry. Concanavalin A (4 μg/mL) or lipopolysaccharides (2 μg/mL) were used as positive controls. After 24 hours of incubation, PBMCs were stained to identify immune cell populations and analyze activation marker expression. Staining with anti-CD3, anti-CD14 anti-CD25 and anti-CD69 fluorochrome-conjugated monoclonal antibodies was performed in the dark for 20

minutes. After washing, cells were analyzed by flow cytometry (Accuri BD Biosciences). A total of 50,000 events per sample were recorded, data analysis was conducted with FlowJo software (MACS Miltenyi Biotec).

Multiplex cytokine analysis

Cell culture supernatants from PBMCs after treatment with nanocapsules were used to quantify the secretion of cytokines using a MILLIPLEX MAP 8-plex Cytokine Kit, according to manufacturer's protocol. Concanavalin A (ConA, 10 μg/mL) and lipopolysaccharides (LPS 2μg/mL) were used as positive controls. The following human cytokines were measured: IL4, IL6, IL10, TNFα, IFNγ, IL13, IL12 p70 and IL2. Briefly, supernatants were centrifuged for 10 minutes to remove debris and 25 mL were added to 25 mL of assay buffer. Then, 25 mL of magnetic beads coated with specific antibodies were added to this solution and incubated for 2 hours under shaking. At the end of the incubation, the plate was washed twice in buffer and incubated for 1 hour with 25 mL of a secondary biotinylated antibody at room temperature. The plate was incubated for 30 minutes with Streptavidine Phycoerythrin, washed twice, and incubated with 150 mL of sheath fluid for 5 minutes. The plate was observed immediately on a Luminex 100/200 platform (Luminex Corporation) with xPONENT 3.1 software. Standard curves for each cytokine (in duplicate) were generated using the supplied reference cytokine concentrations. Cytokine concentrations in the samples were determined with a 5-parameter logistic curve. Final concentrations were calculated from the mean fluorescence intensity and expressed in pg/mL. All incubation steps were performed at room temperature and in the dark.

Author contributions statement

CF, PSM, MO and RM performed experiments; LGD, PSM and CF wrote the manuscript; JMPG, JAM, RM and LGD supported and designed the project; FS and YA critically revised the manuscript. All authors reviewed the manuscript. ‡These authors contributed equally.

Additional informations

Competing financial interests:

The authors declare no competing financial interest.

Acknowledgement

This work was partly supported by the Fondazione Banco di Sardegna (grant N° 2013.1308, 2014.6035 to L.G.D.), the University of Sassari (Italy), the Sardinia Region (grant N° CRP-59720 to L.G.D.), the Gianfranco del Prete Association "The future: medicine, biology and nanotechnology Award" to L.G.D, the Instituto de Salud Carlos III (FEDER funds, grant N° PI10/02295 to J.A.M), the Consejería de Economía, Innovación y Ciencia (Junta de Andalucía, excellence grant N° (CTS-6568 to J.A.M) and by the grant N° (MAT2013-43922-R).

References

1 Godsey, M. E., Suryaprakash, S. & Leong, K. W. Materials innovation for co-delivery of diverse therapeutic cargos. *RSC advances* **3**, 24794-24811, doi:10.1039/C3RA43094D (2013).

2 Delogu, L. G. *et al.* Functionalized multiwalled carbon nanotubes as ultrasound contrast agents. *Proceedings of the National Academy of Sciences of the United States of America* **109**, 16612-16617, doi:10.1073/pnas.1208312109 (2012).

3 Huynh, N. T., Passirani, C., Saulnier, P. & Benoit, J. P. Lipid nanocapsules: a new platform for nanomedicine. *International journal of pharmaceutics* **379**, 201-209, doi:10.1016/j.ijpharm.2009.04.026 (2009).

4 Liu, Q. *et al.* A general strategy for biocompatible, high-effective upconversion nanocapsules based on triplet-triplet annihilation. *Journal of the American Chemical Society* **135**, 5029-5037, doi:10.1021/ja3104268 (2013).

5 Bulcao, R. P. *et al.* In vivo toxicological evaluation of polymeric nanocapsules after intradermal administration. *European journal of pharmaceutics and biopharmaceutics : official journal of Arbeitsgemeinschaft fur Pharmazeutische Verfahrenstechnik e.V* **86**, 167-177, doi:10.1016/j.ejpb.2013.04.001 (2014).

6 Sanchez-Moreno, P., Boulaiz, H., Ortega-Vinuesa, J. L., Peula-Garcia, J. M. & Aranega, A. Novel drug delivery system based on docetaxel-loaded nanocapsules as a therapeutic strategy against breast cancer cells. *International journal of molecular sciences* **13**, 4906-4919, doi:10.3390/ijms13044906 (2012).

7 DeMuth, P. C., Moon, J. J., Suh, H., Hammond, P. T. & Irvine, D. J. Releasable layer-by-layer assembly of stabilized lipid nanocapsules on microneedles for enhanced transcutaneous vaccine delivery. *ACS nano* **6**, 8041-8051, doi:10.1021/nn302639r (2012).

8 Sanchez-Moreno, P. *et al.* Characterization of different functionalized lipidic nanocapsules as potential drug carriers. *International journal of molecular sciences* **13**, 2405-2424, doi:10.3390/ijms13022405 (2012).

9 Liu, X., Wang, Z., Feng, R., Hu, Y. & Huang, G. A novel approach for systematic delivery of a hydrophobic anti-leukemia agent tamibarotene mediated by nanostructured lipid carrier. *Journal of biomedical nanotechnology* **9**, 1586-1593 (2013).

10 Wang, Z. & Ho, P. C. Self-assembled core-shell vascular-targeted nanocapsules for temporal antivasculature and anticancer activities. *Small* **6**, 2576-2583, doi:10.1002/smll.201001122 (2010).

11 Shuhendler, A. J. *et al.* A novel solid lipid nanoparticle formulation for active targeting to tumor alpha(v) beta(3) integrin receptors reveals cyclic RGD as a double-edged sword. *Advanced healthcare materials* **1**, 600-608, doi:10.1002/adhm.201200006 (2012).

12 Messaoudi, K., Saulnier, P., Boesen, K., Benoit, J. P. & Lagarce, F. Anti-epidermal growth factor receptor siRNA carried by chitosan-transacylated lipid nanocapsules increases sensitivity of glioblastoma cells to temozolomide. *International journal of nanomedicine* **9**, 1479-1490, doi:10.2147/IJN.S59134 (2014).

13 Caltagirone, C. *et al.* Cancer-cell-targeted theranostic cubosomes. *Langmuir : the ACS journal of surfaces and colloids* **30**, 6228-6236, doi:10.1021/la501332u (2014).

14 Hervella, P. *et al.* PEGylated lipid nanocapsules with improved drug encapsulation and controlled release properties. *Current topics in medicinal chemistry* **14**, 1115-1123 (2014).

15 Lee, P. *et al.* Enhancement of anticancer efficacy using modified lipophilic nanoparticle drug encapsulation. *International journal of nanomedicine* **7**, 731-737, doi:10.2147/IJN.S28783 (2012).

16 Fang, Y. P. *et al.* Modification of polyethylene glycol onto solid lipid nanoparticles encapsulating a novel chemotherapeutic agent (PK-L4) to enhance solubility for injection delivery. *International journal of nanomedicine* **7**, 4995-5005, doi:10.2147/IJN.S34301 (2012).

17 Delogu, L. G. *et al.* Conjugation of antisense oligonucleotides to PEGylated carbon nanotubes enables efficient knockdown of PTPN22 in T lymphocytes. *Bioconjugate chemistry* **20**, 427-431, doi:10.1021/bc800540j (2009).

18 Bahmani, B., Gupta, S., Upadhyayula, S., Vullev, V. I. & Anvari, B. Effect of polyethylene glycol coatings on uptake of indocyanine green loaded nanocapsules by human spleen macrophages in vitro. *Journal of biomedical optics* **16**, 051303, doi:10.1117/1.3574761 (2011).

19 Anvari, B. et al. Uptake of PEGylated indocyanine green loaded nanocapsules by cells of reticuloendothelial system. *Proc. SPIE* **7910**, doi:10.1117/12.875729 (2011).

20 Yang, Q. *et al.* Evading immune cell uptake and clearance requires PEG grafting at densities substantially exceeding the minimum for brush conformation. *Molecular pharmaceutics* **11**, 1250-1258, doi:10.1021/mp400703d (2014).

21 Danhier, F., Messaoudi, K., Lemaire, L., Benoit, J. P. & Lagarce, F. Combined anti-Galectin-1 and anti-EGFR siRNA-loaded chitosan-lipid nanocapsules decrease temozolomide resistance in glioblastoma: In vivo evaluation. *International journal of pharmaceutics* **481**, 154-161, doi:10.1016/j.ijpharm.2015.01.051 (2015).

22 Malmo, J., Sorgard, H., Varum, K. M. & Strand, S. P. siRNA delivery with chitosan nanoparticles: Molecular properties favoring efficient gene silencing. *Journal of controlled release : official journal of the Controlled Release Society* **158**, 261-268, doi:10.1016/j.jconrel.2011.11.012 (2012).

23 Dong, X. & Mumper, R. J. Nanomedicinal strategies to treat multidrug-resistant tumors: current progress. *Nanomedicine* **5**, 597-615, doi:10.2217/nnm.10.35 (2010).

24 Jones, M. C. *et al.* Quantitative assessment of nanoparticle surface hydrophobicity and its influence on pulmonary biocompatibility. *Journal of controlled release : official journal of the Controlled Release Society* **183**, 94-104, doi:10.1016/j.jconrel.2014.03.022 (2014).

25 Orecchioni, M. *et al.* Impact of carbon nanotubes and graphene on immune cells. *Journal of translational medicine* **12**, 138, doi:10.1186/1479-5876-12-138 (2014).

26 Delogu, L. G. *et al.* Ex vivo impact of functionalized carbon nanotubes on human immune cells. *Nanomedicine* **7**, 231-243, doi:10.2217/nnm.11.101 (2012).

27 Pescatori, M. *et al.* Functionalized carbon nanotubes as immunomodulator systems. *Biomaterials* **34**, 4395-4403, doi:10.1016/j.biomaterials.2013.02.052 (2013).

28 Crescio, C. *et al.* Immunomodulatory properties of carbon nanotubes are able to compensate immune function dysregulation caused by microgravity conditions. *Nanoscale* **6**, 9599-9603, doi:10.1039/c4nr02711f (2014).

29 Prego, C., Fabre, M., Torres, D. & Alonso, M. J. Efficacy and mechanism of action of chitosan nanocapsules for oral peptide delivery. *Pharmaceutical research* **23**, 549-556, doi:10.1007/s11095-006-9570-8 (2006).

30 Peula J.M. et al Study on the colloidal stability mechanisms of acetal-functionalized latexes. *Langmuir*, 6377-6384 (1998).

31 Gupta, A. K. & Curtis, A. S. Lactoferrin and ceruloplasmin derivatized superparamagnetic iron oxide nanoparticles for targeting cell surface receptors. *Biomaterials* **25**, 3029-3040, doi:10.1016/j.biomaterials.2003.09.095 (2004).

32 Santander-Ortega, M. J., Lozano-Lopez, M. V., Bastos-Gonzalez, D., Peula-Garcia, J. M. & Ortega-Vinuesa, J. L. Novel core-shell lipid-chitosan and lipid-poloxamer nanocapsules: stability by hydration forces. *Colloid Polym Sci* **288**, 159-172, doi:10.1007/s00396-009-2132-y (2010).

33 Sanchez-Moreno, P. *et al.* Balancing the effect of corona on therapeutic efficacy and macrophage uptake of lipid nanocapsules. *Biomaterials* **61**, 266-278, doi:10.1016/j.biomaterials.2015.04.049 (2015).

34 Molina-Bolivar JA, O.-V. J. How proteins stabilize colloidal particles by means of hydration forces. *Langmuir : the ACS journal of surfaces and colloids* **13**, 2644-2653 (1999).

35 Mosqueira, V. C. *et al.* Biodistribution of long-circulating PEG-grafted nanocapsules in mice: effects of PEG chain length and density. *Pharmaceutical research* **18**, 1411-1419 (2001).

36 Lesniak, A. *et al.* Nanoparticle adhesion to the cell membrane and its effect on nanoparticle uptake efficiency. *Journal of the American Chemical Society* **135**, 1438-1444, doi:10.1021/ja309812z (2013).

37 Stefanick, J. F., Ashley, J. D. & Bilgicer, B. Enhanced cellular uptake of peptide-targeted nanoparticles through increased peptide hydrophilicity and optimized ethylene glycol peptide-linker length. *ACS nano* **7**, 8115-8127, doi:10.1021/nn4033954 (2013).

38 Saw, P. E. *et al.* Effect of PEG pairing on the efficiency of cancer-targeting liposomes. *Theranostics* **5**, 746-754, doi:10.7150/thno.10732 (2015).

39 Dobrovolskaia, M. A. & McNeil, S. E. Immunological properties of engineered nanomaterials. *Nature nanotechnology* **2**, 469-478, doi:10.1038/nnano.2007.223 (2007).

40 Wilson, K. D. *et al.* Effects of intravenous and subcutaneous administration on the pharmacokinetics, biodistribution, cellular uptake and immunostimulatory activity of CpG

ODN encapsulated in liposomal nanoparticles. *International immunopharmacology* **7**, 1064-1075, doi:10.1016/j.intimp.2007.04.002 (2007).

41 Sheng, Y. *et al.* In vitro macrophage uptake and in vivo biodistribution of PLA-PEG nanoparticles loaded with hemoglobin as blood substitutes: effect of PEG content. *Journal of materials science. Materials in medicine* **20**, 1881-1891, doi:10.1007/s10856-009-3746-9 (2009).

42 Sanchez-Moreno, P., Ortega-Vinuesa, J. L., Boulaiz, H., Marchal, J. A. & Peula-Garcia, J. M. Synthesis and characterization of lipid immuno-nanocapsules for directed drug delivery: selective antitumor activity against HER2 positive breast-cancer cells. *Biomacromolecules* **14**, 4248-4259, doi:10.1021/bm401103t (2013).

43 Fang, C. L., Al-Suwayeh, S. A. & Fang, J. Y. Nanostructured lipid carriers (NLCs) for drug delivery and targeting. *Recent patents on nanotechnology* **7**, 41-55 (2013).

44 Qian, K., Wu, J., Zhang, E., Zhang, Y. & Fu, A. Biodegradable double nanocapsule as a novel multifunctional carrier for drug delivery and cell imaging. *International journal of nanomedicine* **10**, 4149-4157, doi:10.2147/IJN.S83731 (2015).

45 Nasr, M. & Abdel-Hamid, S. Lipid based nanocapsules: a multitude of biomedical applications. *Current pharmaceutical biotechnology* **16**, 322-332 (2015).

46 Abbas, A. K. L., Andrew H; Pillai, Shiv. *Cellular and molecular immunology / Abul K. Abbas, Andrew H. Lichtman, Shiv Pillai ; illustrations by David L. Baker, Alexandra Baker.* Eighth edition edn, (Philadelphia, PA : Elsevier/Saunders, [2015], 2015).

47 Tosato, G. & Jones, K. D. Interleukin-1 induces interleukin-6 production in peripheral blood monocytes. *Blood* **75**, 1305-1310 (1990).

48 Trinchieri, G. Interleukin-12: a proinflammatory cytokine with immunoregulatory functions that bridge innate resistance and antigen-specific adaptive immunity. *Annual review of immunology* **13**, 251-276, doi:10.1146/annurev.iy.13.040195.001343 (1995).

49 Okamura, H., Kashiwamura, S., Tsutsui, H., Yoshimoto, T. & Nakanishi, K. Regulation of interferon-gamma production by IL-12 and IL-18. *Current opinion in immunology* **10**, 259-264 (1998).

50 Asthana, S. *et al.* Immunoadjuvant chemotherapy of visceral leishmaniasis in hamsters using amphotericin B-encapsulated nanoemulsion template-based chitosan nanocapsules. *Antimicrobial agents and chemotherapy* **57**, 1714-1722, doi:10.1128/AAC.01984-12 (2013).

51 Aste-Amezaga, M., Ma, X., Sartori, A. & Trinchieri, G. Molecular mechanisms of the induction of IL-12 and its inhibition by IL-10. *Journal of immunology* **160**, 5936-5944 (1998).

52 Hershey, G. K. IL-13 receptors and signaling pathways: an evolving web. *The Journal of allergy and clinical immunology* **111**, 677-690; quiz 691 (2003).

53 Tan, S., Li, X., Guo, Y. & Zhang, Z. Lipid-enveloped hybrid nanoparticles for drug delivery. *Nanoscale* **5**, 860-872, doi:10.1039/c2nr32880a (2013).

54 Chana, J., Forbes, B. & Jones, S. A. Triggered-release nanocapsules for drug delivery to the lungs. *Nanomedicine* **11**, 89-97, doi:10.1016/j.nano.2014.07.012 (2015).

55 Wu, H., Zhu, L. & Torchilin, V. P. pH-sensitive poly(histidine)-PEG/DSPE-PEG co-polymer micelles for cytosolic drug delivery. *Biomaterials* **34**, 1213-1222, doi:10.1016/j.biomaterials.2012.08.072 (2013).

56 Lamprecht, A., Bouligand, Y. & Benoit, J. P. New lipid nanocapsules exhibit sustained release properties for amiodarone. *Journal of controlled release : official journal of the Controlled Release Society* **84**, 59-68 (2002).

57 Plaunt, A. J., Harmatys, K. M., Hendrie, K. A., Musso, A. J. & Smith, B. D. Chemically triggered release of 5-aminolevulinic acid from liposomes. *RSC advances* **4**, 57983-57990, doi:10.1039/C4RA10340H (2014).

58 Gustafson, T. P. *et al.* Blood Triggered Rapid Release Porous Nanocapsules. *RSC advances* **3**, 5547-5555, doi:10.1039/C3RA22693J (2013).

59 Jang, M. *et al.* A feeder-free, defined three-dimensional polyethylene glycol-based extracellular matrix niche for culture of human embryonic stem cells. *Biomaterials* **34**, 3571-3580, doi:10.1016/j.biomaterials.2013.01.073 (2013).

60 Li, X. *et al.* Chitin, chitosan, and glycated chitosan regulate immune responses: the novel adjuvants for cancer vaccine. *Clinical & developmental immunology* **2013**, 387023, doi:10.1155/2013/387023 (2013).

61 Yong, H. Pluronic nanoparticles do not modulate immune responses mounted by macrophages. *Macromolecular Research* **21**, 1355-1359 (2013).

62 Dobrovolskaia, M. A., Germolec, D. R. & Weaver, J. L. Evaluation of nanoparticle immunotoxicity. *Nature nanotechnology* **4**, 411-414, doi:10.1038/nnano.2009.175 (2009).

63 Zolnik, B. S., Gonzalez-Fernandez, A., Sadrieh, N. & Dobrovolskaia, M. A. Nanoparticles and the immune system. *Endocrinology* **151**, 458-465, doi:10.1210/en.2009-1082 (2010).

64 Goldberg, M. S. Immunoengineering: how nanotechnology can enhance cancer immunotherapy. *Cell* **161**, 201-204, doi:10.1016/j.cell.2015.03.037 (2015).

65 Danhier, F. *et al.* Paclitaxel-loaded PEGylated PLGA-based nanoparticles: in vitro and in vivo evaluation. *Journal of controlled release : official journal of the Controlled Release Society* **133**, 11-17, doi:10.1016/j.jconrel.2008.09.086 (2009).

66 Verhoef, J. J. & Anchordoquy, T. J. Questioning the Use of PEGylation for Drug Delivery. *Drug delivery and translational research* **3**, 499-503 (2013).

67 Knop, K., Hoogenboom, R., Fischer, D. & Schubert, U. S. Poly(ethylene glycol) in drug delivery: pros and cons as well as potential alternatives. *Angewandte Chemie* **49**, 6288-6308, doi:10.1002/anie.200902672 (2010).

68 Laverman, P. *et al.* Factors affecting the accelerated blood clearance of polyethylene glycol-liposomes upon repeated injection. *The Journal of pharmacology and experimental therapeutics* **298**, 607-612 (2001).

69 Ying, B. & Campbell, R. B. Delivery of kinesin spindle protein targeting siRNA in solid lipid nanoparticles to cellular models of tumor vasculature. *Biochemical and biophysical research communications* **446**, 441-447, doi:10.1016/j.bbrc.2014.02.120 (2014).

70 David, S. *et al.* Treatment efficacy of DNA lipid nanocapsules and DNA multimodular systems after systemic administration in a human glioma model. *The journal of gene medicine* **14**, 769-775, doi:10.1002/jgm.2683 (2012).

71 Vonarbourg, A. *et al.* Evaluation of pegylated lipid nanocapsules versus complement system activation and macrophage uptake. *Journal of biomedical materials research. Part A* **78**, 620-628, doi:10.1002/jbm.a.30711 (2006).

72 Opferman, J. T. *et al.* Development and maintenance of B and T lymphocytes requires antiapoptotic MCL-1. *Nature* **426**, 671-676, doi:10.1038/nature02067 (2003).

73 Curtale, G. *et al.* An emerging player in the adaptive immune response: microRNA-146a is a modulator of IL-2 expression and activation-induced cell death in T lymphocytes. *Blood* **115**, 265-273, doi:10.1182/blood-2009-06-225987 (2010).

74 Coeshott, C. M. *et al.* Pluronic F127-based systemic vaccine delivery systems. *Vaccine* **22**, 2396-2405, doi:10.1016/j.vaccine.2003.11.064 (2004).

75 Westerink, M. A. *et al.* ProJuvant (Pluronic F127/chitosan) enhances the immune response to intranasally administered tetanus toxoid. *Vaccine* **20**, 711-723 (2001).

76 Roy, A., Singh, M. S., Upadhyay, P. & Bhaskar, S. Combined chemo-immunotherapy as a prospective strategy to combat cancer: a nanoparticle based approach. *Molecular pharmaceutics* **7**, 1778-1788, doi:10.1021/mp100153r (2010).

77 Mao, Y., Poschke, I. & Kiessling, R. Tumour-induced immune suppression: role of inflammatory mediators released by myelomonocytic cells. *Journal of internal medicine* **276**, 154-170, doi:10.1111/joim.12229 (2014).

78 Tomei, S., Wang, E., Delogu, L. G., Marincola, F. M. & Bedognetti, D. Non-BRAF-targeted therapy, immunotherapy, and combination therapy for melanoma. *Expert opinion on biological therapy* **14**, 663-686, doi:10.1517/14712598.2014.890586 (2014).

79 Bedognetti, D. *et al.* SITC/iSBTc Cancer Immunotherapy Biomarkers Resource Document: online resources and useful tools - a compass in the land of biomarker discovery. *Journal of translational medicine* **9**, 155, doi:10.1186/1479-5876-9-155 (2011).

80 Knutson, K. L. & Disis, M. L. Tumor antigen-specific T helper cells in cancer immunity and immunotherapy. *Cancer immunology, immunotherapy : CII* **54**, 721-728, doi:10.1007/s00262-004-0653-2 (2005).

81 Dong, C. & Flavell, R. A. Cell fate decision: T-helper 1 and 2 subsets in immune responses. *Arthritis research* **2**, 179-188, doi:10.1186/ar85 (2000).

82 Shibata, Y., Metzger, W. J. & Myrvik, Q. N. Chitin particle-induced cell-mediated immunity is inhibited by soluble mannan: mannose receptor-mediated phagocytosis initiates IL-12 production. *Journal of immunology* **159**, 2462-2467 (1997).

83 Vasiliev, Y. M. Chitosan-based vaccine adjuvants: incomplete characterization complicates preclinical and clinical evaluation. *Expert review of vaccines* **14**, 37-53, doi:10.1586/14760584.2015.956729 (2015).

84 Li, H. C. *et al.* The hemocompatibility of oxidized diamond nanocrystals for biomedical applications. *Scientific reports* **3**, 3044, doi:10.1038/srep03044 (2013).

Supporting informations

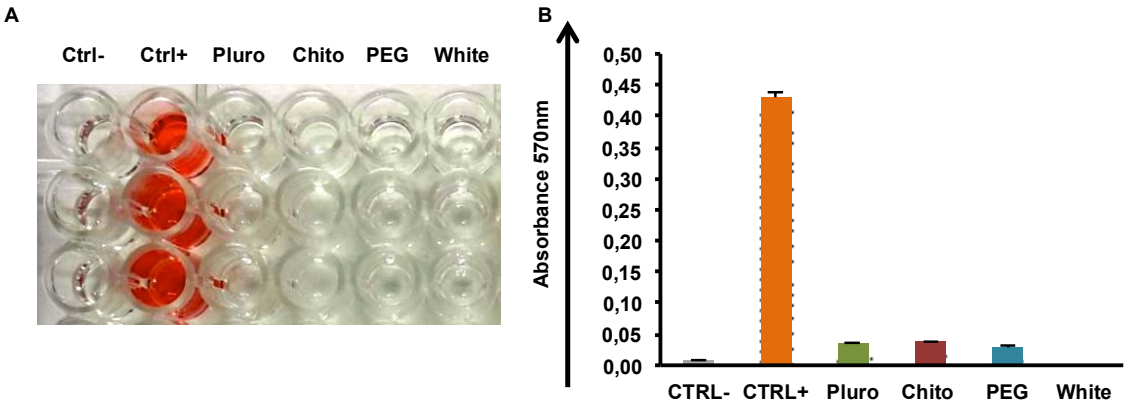

S. Figure 1. Hemolysis. Pluro, Chito, PEG-NCs ($1x10^{11}$ mL^{-1} concentration) were incubated with red blood cells (RBCs) at 25°C for 2 h. (A) Pictures of human RBCs treated with Pluro, Chito and PEG NCs. The red color of the solution is due to the release of hemoglobin from the damaged RBCs. PBS mixed with RBCs (Ctrl-) and ultrapure water mixed with RBCs (Ctrl+) served as negative and positive control respectively, PBS alone was used as additional control (white). (B) Sample Absorbance at the wavelength of 570nm-620nm. Experiments were performed in triplicate.

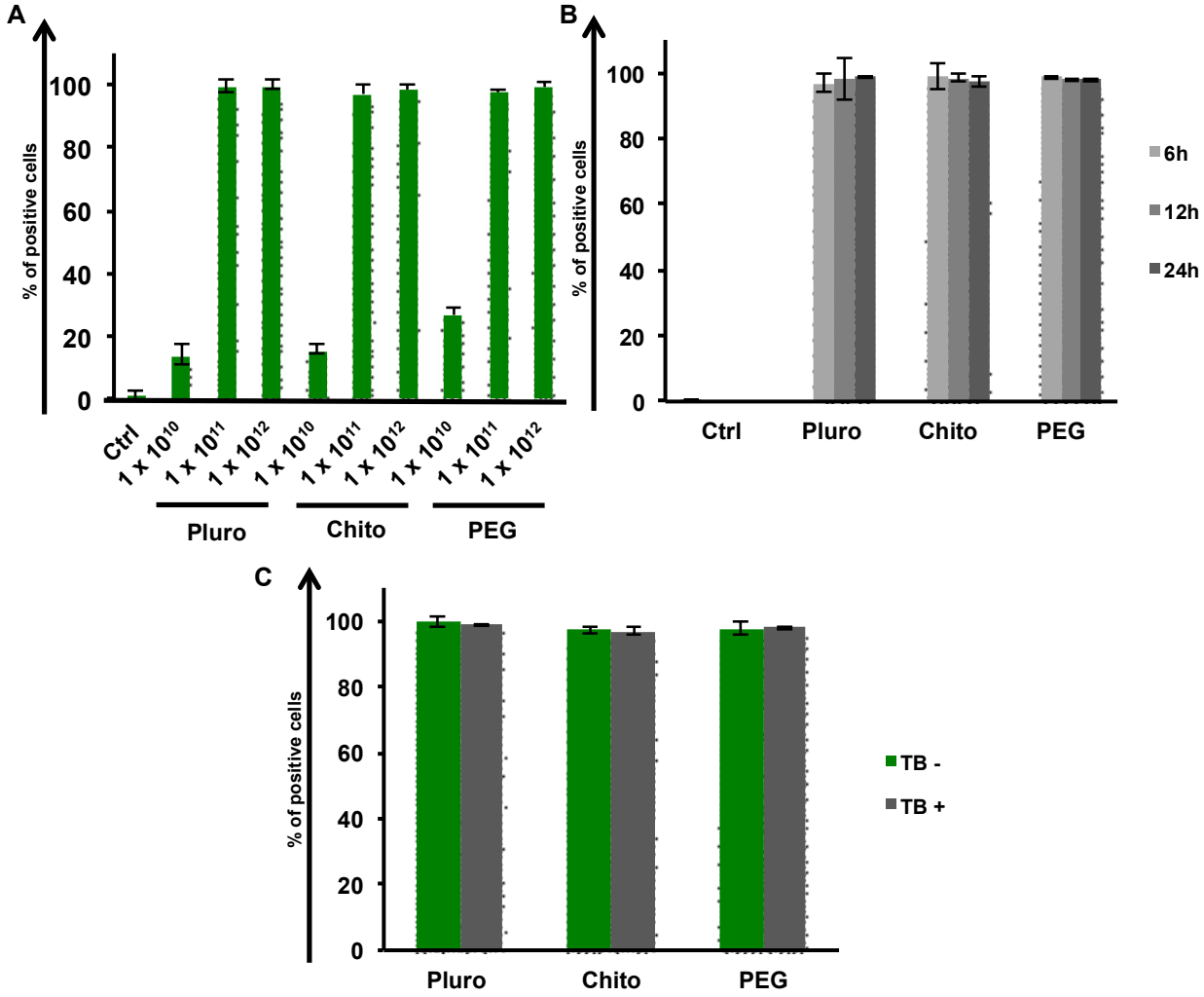

S. Figure 2. Uptake analysis. A) PBMCs were either left untreated or incubated for 24 h with $1x10^{10}$ mL^{-1} , $1X10^{11}$ mL^{-1}, $1X10^{12}$ mL^{-1} of three different functionalized nanocapsules (Pluro, Chito, Peg) with Courmarin 6. **B)** Uptake analysis at different time points 6h, 12h and 24h of three NCs at the concentration of $1X10^{11}$ mL^{-1} Trypan Blue (TB) was used as a quencher for non-internalized NCs. As a control we used the untreated cells. **C**) Uptake comparison between cells washed and unwashed with TB after 24h of incubation with the three NCs at the concentration of $1X10^{11}$ mL^{-1}. Experiments performed in triplicate were analyzed by Flow Cytometry and FlowJo software.

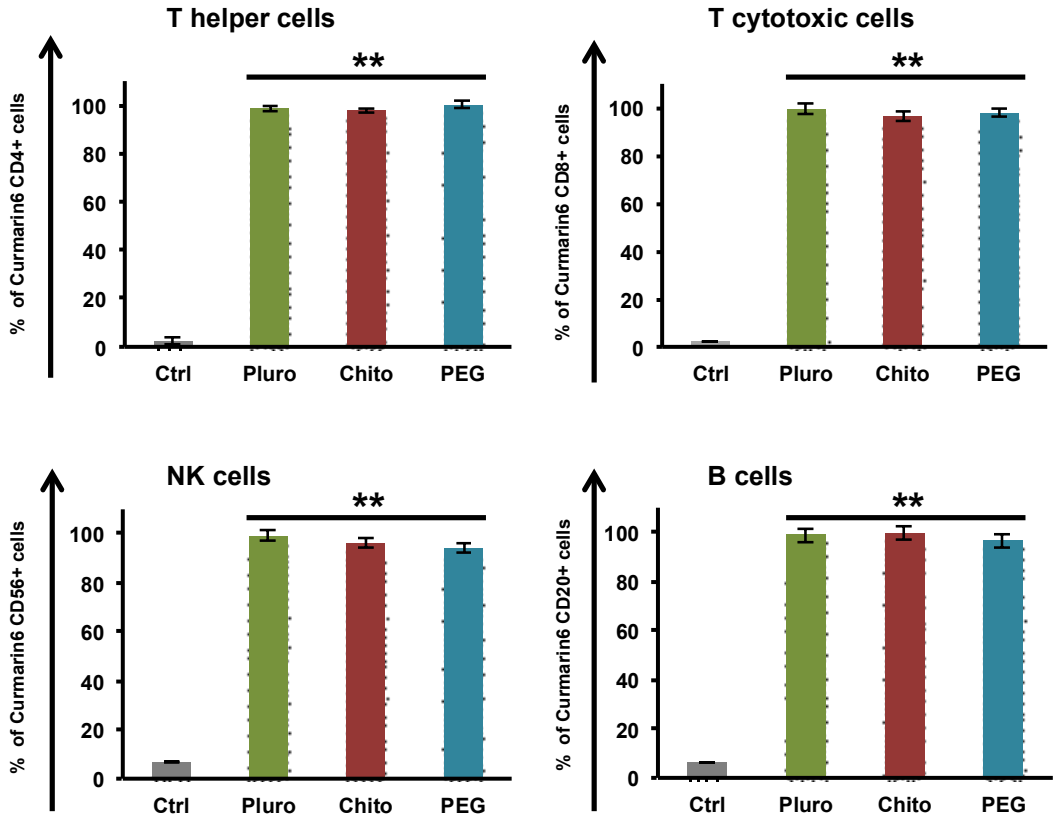

S. Figure 3. Uptake analysis on PBMC subpopulations. NCs uptake assessment on lymphocytes T helper (CD4+), lymphocytes T cytotoxic (CD8+), Natural killer (CD56+) and B cells (CD20+). Cells were incubated for 24 hour with Pluro, Chito and PEG NCs at the concentration of at $1x10^{11}$ mL^{-1} or left untreated, samples were analyzed by flow cytometry. Experiments were performed at least in triplicate. **= P value<0.01.

Paper VI: *Immune compatible cystine-functionalized superparamagnetic iron oxide nanoparticles as a new contrast agents in vascular ultrasonography*

Sara Dolci[1], Valentina Domenici[1], Gianpaolo Vidili[2], Marco Orecchioni[3], Pasquale Bandiera[4], Roberto Madeddu[4], Cristiano Farace[4], Massimiliano Peana[3], Maria Rosaria Tiné[1], Roberto Manetti[2], Francesco Sgarrella[3] and Lucia Gemma Delogu[3]*

[1] Department of Chemistry and Industrial Chemistry, University of Pisa, via Moruzzi 13, 56124 Pisa (Italy).

[2] Department of Clinical and Experimental Medicine, University of Sassari, Viale San Pietro 07100 Sassari, Italy.

[3] Department of Chemistry and Pharmacy, University of Sassari, via Muroni 23, 07100 Sassari, Italy.

[4] Department of Biomedical Sciences, University of Sassari, Viale San Pietro 43c, 07100 Sassari, Italy.

Keywords: Superparamagnetic iron oxide nanoparticles, immune system, MRI, ultrasounds, gene expression, cytokines

Published in:

RSC Adv., 2016, 6, 2712

Abstract

Superparamagnetic iron oxide nanoparticles (SPIONs) have been extensively investigated for many biomedical applications. A good quality functionalization that combines imaging goals with a high-level biocompatibility remains one of the challenges for particle translation into medical practice. Here, we focus on a new functionalization of SPIONs with cystine (Cy-SPIONs). Cystine is able to make SPIONs stable and dispersible in water and in culture cell media. New insights are provided into the biological and immune effects of Cy-SPIONs with a wide variety of standard and molecular assays to evaluate cytotoxicity, cell activation, cytokine release and the expression of 84 genes related to immune responses. A good immune biocompatibility of Cy-SPIONs on primary immune cells was found. The great potential of Cy-SPIONs for further *in vivo* studies and as contrast agents for magnetic resonance imaging (MRI) is highlighted. In addition, we also exploited ultrasonography, since it is a safer, less expensive and common imaging technology. The good echogenic properties of Cy-SPIONs in water and in whole blood are shown, both in a phantom vein and in a microfluidic device for bloodstream simulations. Our results open up a new scenario for future applications of cystine-functionalized SPIONs as immune-compatible ultrasound and MRI contrast agents.

Manuscript

Introduction

Magnetic nanoparticles have attracted much interest among scientists and the general public [1] as advanced nanomaterials for several types of applications, as well as for drug and gene delivery or/and imaging agents [2, 3]. Superparamagnetic iron oxide nanoparticles (SPIONs) have been investigated for biomedical applications such as tissue repair, immunoassays, detoxification of biological fluids, hyperthermia, drug delivery, probes, in vitro cell separation and to produce antibiotic-resistant biofilms. They are thus them important candidate materials for new perspectives in nanomedicine [4].

Since 2005 SPIONs were introduced as tracers for tomographic magnetic particle imaging modality [5]. One of the major aims of scientists in improving diagnostic technologies is to create better contrast agents and superior imaging systems, however every system has its weaknesses [6].

SPIONs are excellent materials for multimodal imaging [7]. One interesting modality is the use of MRI and ultrasonography (US) at the same time. US is fundamental in everyday clinical practice and many researchers are now using new nanomaterials to improve this imaging methodology which is very economical and safe [8-10]. Further innovations in the development of diagnostic tools that possess the advantages of MRI and US dual-modality properties are still needed, i.e. the US-triggered release of therapeutic agents to tumor cells for the battle against cancer [11-13].

In order to achieve efficient imaging applications and loading capacity of SPIONs, one of the main challenges is to obtain nanoparticles with good hydrophilic surface coating [14-15, 16]. To achieve this goal the functionalization is of fundamental importance for the good biocompatibility and safety of SPIONs. Thus, the first concern is to reduce both SPIONs' instability in biological media and the concentration necessary for efficient functionalization.

At the same time this would minimize toxic effects and costs, while maintaining a high-resolution contrast. In a previous work, we reported a new method to increase the stability of SPIONs in biological media through the surface coating of SPIONs with cystine [17]. Cystine acts as a precursor for proteins, antioxidant glutathione (GSH) biosynthesis, as well as maintaining physiological redox conditions inside/outside the cell [18]. We found that this new type of functionalization improved SPIONs' hydrophilicity and water stability [17, 19]. In this

Dr. Marco Orecchioni. Titolo "Biomedical applications of different nanomaterials: Characterization and interaction with the immune system"
Tesi di dottorato in Life Sciences and Biotechnologies, Università degli Studi di Sassari.

work the echogenic properties of Cy-SPIONs were assessed *in vitro* in degassed water and *ex vivo* in human blood and *in silico* in a synthetic microvasculature network chip. We show how Cy-SPIONs could be used in US as novel intravenous contrast agents. However, an extensive and molecular assessment of the potential impact of SPIONs on immune cells is still lacking. Toxicity and immune compatibility are still major blocks to the use of nanomaterials in medicine [20-24]. Thus, all the applications cited above normally require intravenous administration and the first cells that come in contact with foreign substances are blood immune cells. It is therefore necessary to analyze the possible impact of SPIONs on immune cells also using a molecular approach such as gene expression analysis. Jin R *et al.* [15] highlighted the importance of immunological studies especially for the potential use of SPIONs in future pre-clinical testing, considering also that any difference in nanoparticle-conjugated moiety can lead to a different toxicological and immune impact. Most studies that have analyzed the effect of SPIONs on immune cells, have only considered one type of immune cell population, such as monocytes or macrophages [27-31]. Instead in this study we used total PBMCs for our analysis, which include many different cell populations, such as T cells, B cells, monocytes, Nk cells and dendritic cells.

Our approach better simulates the normal bloodstream behavior with the interaction of different types of cells that can modulate each other's activations against foreign substances, such as nanoparticles. The *ex vivo* analysis also gives a better overview of the real action of Cy-SPIONs on immune cells, opening up the way for future pre-clinical application studies. To lay the foundation of our cystine functionalized SPIONs (Cy-SPIONs) in imaging, it is also critical to assess their contrast properties. We thus decided to start from the safest imaging modality: ultrasonography.

In this paper we focus on Cy-SPIONs, which are easily dispersible in biological media. We provide new insights into the biological and immune effects of Cy-SPIONs with a standard and molecular range of assays to evaluate the cytotoxicity, cell activation, cytokine release and the expression of 84 genes related to the immune response.

Experimental section

Materials

Iron pentacarbonyl ($Fe(CO)_5$), oleic acid ($C_{18}H_{34}O_2$), dioctyl ether ($C_{16}H_{34}O$), trimethylamine N-oxide (C_3H_9NO), ethanol, L-cysteine ($C_3H_7NO_2S$) and hexane were purchased from Sigma-Aldrich®. Toluene was distilled from the usual drying agents under nitrogen. All reactions were carried out under a nitrogen atmosphere using standard Schlenk techniques. The reaction vessels were oven-dried at 130°C prior to use, evacuated (10-2 mmHg) and then filled with nitrogen.

Synthesis and characterization of Cy-SPIO nanoparticles

To obtain monodisperse, highly crystalline and nanometer-size iron oxide nanoparticles, oleate-coated SPIONs (OA-SPIONs) were prepared by following a thermal decomposition method [32] and then functionalized with cystine using a ligand exchange reaction, as described in ref. [24]. $Fe(CO)_5$ (0,66 mL, 5 mmol) was added to a solution of oleic acid (1.59 mL, 5 mmol) in dyoctyl ether (50 mL) at 373 K, under nitrogen atmosphere. The mixture was heated to reflux (559 K) for 1 hour. After cooling to room temperature, anhydrous trimethylamine N-oxide (376 mg, 5 mmol) was added and the mixture heated again (to 413 K for 2 h and then to reflux for 1 h). Ethanol was used to precipitate the resultant OA-SPIONs, which were separated by centrifugation and dried *in vacuo* (1.0×10^{-3} Torr).

Cystine coated SPIONs (Cy-SPION) were prepared by dissolving OA-SPIONs (506.4 mg, iron content 30.3% (w/w)) in 80 mL of toluene and adding an excess of L-cysteine (1.485 g, 12.25 mmol) under nitrogen atmosphere. The resulting brown mixture was heated to reflux (383 K) for about 4 h, up to the precipitation of a brown solid to the bottom of the flask that produced a colorless solution. The solid was washed with hexane, collected by centrifugation and dried *in vacuo* (1.0×10^{-3} Torr). The solid was then washed with water to remove the free L-cysteine and dried with a vacuum pump. During the exchange reaction, the oxidation of cysteine to cystine takes place, promoted by Fe_2O_3 [17], until complete replacement of the oleic acid by the *in situ* generated cystine.

The iron content of SPIONs was determined by the spectrophotometric method [17] [19]. The SPION size and morphology were determined by analyzing TEM images obtained with a Philips CM 12 operating at 100 kV. Samples were prepared by placing one drop of a solution

Dr. Marco Orecchioni. Titolo "Biomedical applications of different nanomaterials: Characterization and interaction with the immune system"
Tesi di dottorato in Life Sciences and Biotechnologies, Università degli Studi di Sassari.

of Cy-SPION in water on the specimen grid and allowing the solvent to evaporate. The SPION dimensions were analysed with ImageJ. The surface functionalization of Cy-SPIONs was characterized by several complementary techniques [17],[19].

MRI phantom analysis of Cy-SPION dispersions

Additional experiments were carried out to investigate the stability of water Cy-SPION dispersions and their MRI potentialities . In particular, *in vitro* ^{1}H NMR relaxation rates measurements were performed on aqueous Cy-SPION dispersions containing increasing iron concentrations using the 7 Tesla 950-MR scanner GE Healthcare machine.

Approximately 13 mg of Cy-SPIONs were introduced in a vial and 1mL of deionized water were added. After 10 minutes of sonication with a BRANSONIC 220 water bath sonicator, the vial was centrifuged for 5 minutes at 3500 rpm to remove nanoparticles in the mixture. The solution was then diluted in various ratios in order to obtain Cy-SPION aqueous dispersions at various concentrations. NMR glass tubes containing Cy-SPION dispersions with [Fe] equal to 0.320, 0.213, 0.160 and 0.106 mM were placed in an agar phantom and the proton NMR relaxation times, T_1 and T_2*, were recorded using standard inversion recovery (IR) and spin echo (SE) sequences, respectively.

Cell culture maintenance

Jurkat cells (T cell line) and peripheral blood mononuclear cells (PBMCs) were cultured in RPMI 1640 medium containing 1% antibiotic-antimicotic mixture and 10% heat-inactivated fetal bovine serum (FBS) (Invitrogen) in an incubator at 37 °C in a 5 % CO_2. Human PBMCs were obtained from blood samples from healthy male donors (25-50 years old) using a standard Ficoll-Paque (GE Healthcare) separation. All the donors provided written informed consent. The study was reviewed and approved by the ethics committee of the University of Sassari (Italy).

Cy-SPION viability and activation on immune cells

For the viability assay, PBMCs were transferred to a 24-well plate and treated for 24 h in triplicate with 50, 100, 200 μg mL^{-1} of Cy-SPION or left untreated. Cells were treated with EtOH 70% as a positive control and then washed in cold PBS before the staining reaction. After incubation, cells were harvested, washed in cold PBS and re-suspended in 1mL of PBS at 1 x

10^6 cells mL^{-1}. Viability was assessed by the LIVE/DEAD® Fixable Dead Cell Stain Kit (Invitrogen), which uses an amine-reactive fluorescent dye, cells with compromised membranes (late apoptotic and necrotic). The dye reacts with free amines both inside the cell and on the cell surface, yielding intense fluorescent staining. In viable cells, the dye reactivity is restricted to the cell surface amines, resulting in less intense fluorescence.

To detect cells undergoing apoptosis and necrosis, Annexin-V FITC and propidium iodide staining were used (Invitrogen). Cells were analysed by flow cytometry (FACS Calibur BD-Bioscience). To identify T cells and specifically CD8+ and CD4+ T cell populations, the populations were isolated using specific antibodies: CD3 for the entire T cell gating, CD8 and CD4 for Cytotoxic T cells and T helper cells, respectively. To assess the cell activation, specific antibodies were used against CD25, CD69 and CD30 cell activation markers. Al the antibodies used were purchased from BD Biosciences. Data analysis was performed by flow cytometry (FACS Calibur, BD Biosciences) using CellQuest® software (BD Biosciences).

Proliferation assay

To perform the proliferation assay, the Click-iT EdU Alexa Fluor 488 Flow Cytometry Assay Kit (Life Technologies) was used. The experiments were performed according to the manufacturer's instructions. Cells were seeded at the concentration of 1 x 10^6 cells mL^{-1} in 96 multi-well rounded bottom plates. PBMCs were treated with Cy-SPIONs (50, 100, 200 μg mL^{-1}) and phytohemagglutinin 2% (PHA) and interleukin 2 (IL2) 30 u/mL or left untreated. 5-ethynyl-2-deoxyuridine (EdU) was added in sterile conditions 16 h before the analysis. After 72 h of incubation, cells were harvested, washed in PBS, fixed with 4% paraformaldehyde, washed in PBS + 1% BSA, permeabilized with a saponin-based reagent, and prepared for the Cu-assisted EdU-Azide Click-iT reaction. The reaction occurs after adding 500 μl of Click-iT reaction cocktail (PBS, CuSO4, fluorescent dye azide and reaction buffer additive) to each sample. Analyses were performed by flow cytometry (FACS Calibur BD Bioscience) using CellQuest® software (BD Biosciences). A total of 50,000–100,000 events were recorded.

Immune cell gene expression analysis

Total RNA was extracted from Jurkat cells after incubation with SPIONs 200 μg mL^{-1}. RNA purification was performed with TriZol Reagent (TriZol, Invitrogen, Carlsbad, CA, USA). After extraction, cDNA synthesis was performed using a SuperScript® II reverse transcriptase

(Invitrogen) following the manufacturer's instruction. Comparison of the relative expression levels of 84 immune response genes was performed with a RT2 Profiler PCR Array (PAHS-052ZD, Superarray Bioscience Corporation, Frederick, MD), (instrument CFX96 Bio-Rad). Data were analyzed by the comparative threshold cycle (CT) method. The relative quantification of the gene expression using the $2-\Delta\Delta Ct$ method correlated with the absolute gene quantification obtained using a standard curve. Data were analyzed with RT2 profiler PCR array data analysis software (http://www.superarray.com/pcrarraydataanalysis.php). Untreated cells were compared to Cy-SPIONs treated samples. Experiments were performed in triplicate.

Ultrasound Imaging

Technos MPX (Esoate) was used for all ultrasonography experiments. The analyses were recorded at 14-MHz; the instrument was set in conventional US modality (B mode), depth 31 mm, gain 170, −1.3 dB, and mechanical index=1. The US signal was calculated using Adobe Photoshop CS5 (Adobe Systems). US signal is reported in 8-bit gray scale intensity from 0 to 255 shades of gray. For US images on degassed water, the areas of interest were selected. A comparison of samples was performed on the same areas with 29205 analyzed pixels. Experiments were done in triplicate.

Idealized synthetic microvascular network (SMN) and related viability test

The Synthetic Microvascular Networks or SMNs were purchased from SYN VIVO CFDRC Huntsville, Alabama, USA. The SMN is able to perfectly reproduce a trait of the rat microvasculature (vessels depth of 100 μm). The chip was developed using a standard photolithography process [33]. The SMN was used in order to assess the potential impact of Cy-SPIONs on human primary immune cells in an *in vivo* like simulation under ultrasonography. Tygon tubing was inserted into the inlet/outlet ports of the device, a syringe was loaded onto a syringe pump and PBMCs with or without Cy-SPIONs (200 μg/mL) injected at rates flow of less than 1μl/min. After 24 h of incubation at 37° in 5% of CO_2, the device was covered with plastic paper and gel for ultrasonography, and sonication with an US probe was then performed for 10 minutes. PBMCs with or without Cy-SPIONs were immediately extracted and cell count performed with a trypan blue solution (4%, Sigma Aldrich) under inverted microscopy (Nikon Instruments Inc.).

Results and Discussion

Synthesis and characterization of Cy-SPIONs

In this work we studied the bio-immune impact and properties in ultrasound imaging of SPIONs with a new type of functionalization, using cystine. Cystine has a fundamental biological role as a component of antioxidant glutathione (GSH), and also for the maintenance of physiological redox conditions inside and outside the cell. The cystine receptor is also present in many cells of the body and is responsible for many biological processes [18].

Our previous studies [17, 19] showed that Cy-SPIONs are stable nanoparticles and very interesting for medical applications, since their dispersion in water is quite stable. The preparation of Cy-SPIONs involves the synthesis of oleate-coated SPIONs (OA-SPION) by a thermal decomposition method [34] and the subsequent functionalization by a ligand exchange reaction with L-cysteine.

Using X-ray diffraction, magnetic properties and microscopy analysis (i.e. TEM and AFM), it was possible to characterize the chemical structure of both the magnetic core and the surface coating of Cy-NPs, as previously reported [19]. In particular, the ligand exchange between oleate and cysteine was fully clarified, showing that the complete oxidation of cysteine to cystine produced an external cystine-shell, which is fundamental for biomedical applications. The water stability of Cy-NP dispersion is very important and the water dispersion was confirmed to be stable for more than 7-8 h [19]. Concerning the chemical-physical properties of these Cy-NPs, both spectroscopic (FT-IR) and microscopy (AFM and TEM) studies agree with the schematic picture reported in **Fig. 1A**. The average iron oxide core dimension of Cy-SPIONs ranges from 3.6 and 3.95 nm, as determined independently by three methods (namely AFM, TEM and magnetic curve analysis [17]).

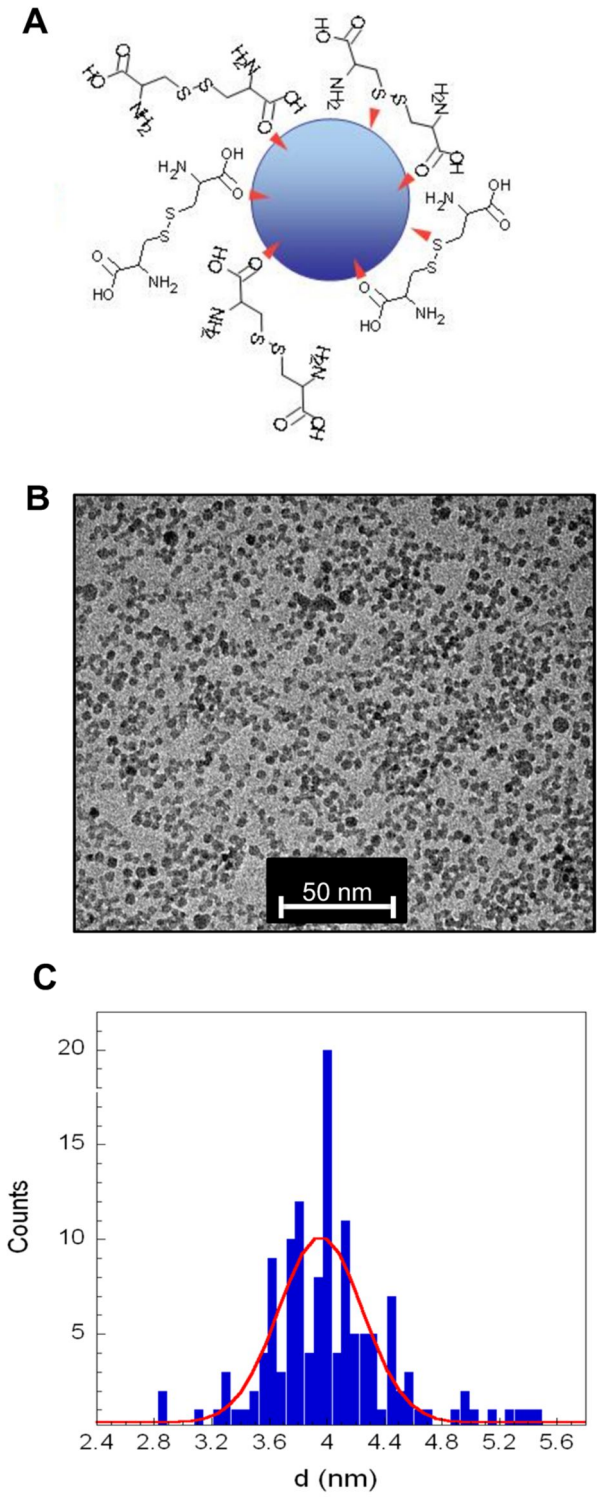

Fig. 1 Cy-SPION characterization. (A) Coating around the iron-oxide nanoparticle core. (B) TEM image of the nanoparticles showing high monodispersity and average dimension of 3.95 nm. (C) Distribution of diameters through analysis of TEM images.

As an example, a TEM image of Cy-SPIONs is shown in **Fig. 1B** and the corresponding dimension distribution is reported in **Fig. 1C.** According to the analyses of five new TEM

images obtained as reported in the previous section, the average diameter of these nanoparticles was 3.95 nm (with a standard deviation of 0.41 nm), in agreement with previous investigations [17], [19]. In our previous work [17], a preliminary study of the ^{1}H NMR relaxation properties at low and high magnetic fields indicated the potential of Cy-SPION water dispersions as MRI contrast agents. At concentrations lower than 0.5mM, we found that the spin-lattice relaxation rate R_1 ($=1/T_1$) decreases by increasing the value of the field, while the spin-spin relaxation rate R_2 ($=1/T_2$) has the opposite trend. This is interesting for MRI applications, since the efficiency of contrast agents for imaging applications is related to the ratio R_2/R_1. The possibility of changing this ratio by changing the magnetic field strength opens new possibilities of using our Cy-SPIONs as negative as well as positive contrast agents. To confirm such behavior [17], we report new data acquired at 7 Tesla (corresponding to a ^{1}H Larmor frequency of 300 MHz) by an MRI machine. By using a phantom, prepared as described in the previous section, we collected several MRI images and calculated the relaxation rates, R_1 and R_2, of four Cy-NP dispersions with different iron concentrations (indicated in **Fig. 2** as "region of interest", namely ROI) and one sample of pure water (ROI number 5), as a reference.

A

	[Fe] (mM)	R_2 (s^{-1})	R_1 (s^{-1})	EHC
ROI 1	0.320	20.33	0.42	-69.63
ROI 2	0.213	14.88	0.43	-59.60
ROI 3	0.160	11.81	0.40	-50.76
ROI 4	0.106	8.35	0.39	-35.78

B

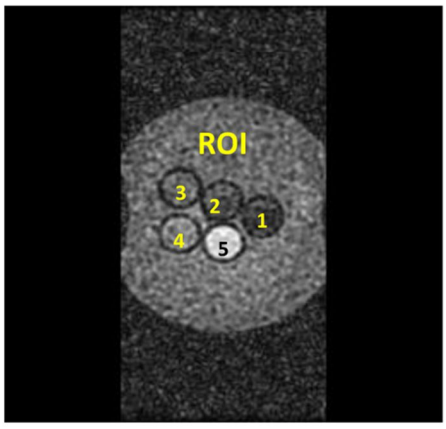

Fig. 2 Cy-SPION MRI properties. (A) In vitro relaxivity study at 7 Tesla of the four Cy-SPION dispersions. [Fe], relaxation rates R_1 and R_2, Enhancement contrast ratio (EHC) are reported. (B) Image of the phantom prepared with five NMR tubes with different iron contents. Roi number 5 corresponds to water, and is used in order to highlight the contrast effect of Cy-NPs. The MRI T2-weighted image was obtained with an echo time of 100 ms and a repetition time of 2500 ms.

The enhancement contrast ratio (EHC) was calculated by using the following equation, in order to evaluate the contrast power:

$$EHC(\%)=\left(\frac{(SI_{Cy-NP}-SI_{water})}{SI_{water}}\right)x100$$

where $SI_{cy\text{-}NP}$ and SI_{water} $SI_{Cy\text{-}NP}$correspond to the signal intensity evaluated on the MRI image for the Cy-SPION dispersions and water reference, respectively. EHC, R_1 and R_2 of the Cy-SPIONs water dispersions are reported in **Fig. 2A**, while a MRI T_2-weighted image is shown in **Fig. 2B**. From this investigation we can confirm that Cy-SPIONs are stable in water. In addition, the values of EHC and the fact that the ratio R_2/R_1 is in the range 20-50 for concentrations of Cy-SPIONs in the range 0.106-0.320 mM, indicate that these nanoparticles act as negative MRI contrast agents.

In the following sections, these nanoparticles are investigated in order to check, first, their biocompatibility and, second, their possible use as ultrasound contrast agents.

Cy-SPION potential in ultrasonography imaging

The classical application of SPIONs is as contrast agents in MRI. The recent interest in multimodal imaging has thus opened up new perspectives, indeed each imaging technique has advantages but also intrinsic limitations, in some cases low sensitivity, in others low spatial resolutions [35]. Many groups have reported the use of SPIONs encapsulated into other particles such as microbubbles, vesicles or liposome for a bimodal imaging using MRI and US [36-40]. Microbubbles are the most commonly used US contrast agents for medical applications, thanks to their highly echogenic *in vivo* properties [41]. The presence of SPIO nanoparticles in the bubble shell can alter the surface tension of bubbles, boosting the acoustic impedance and enhancing the detectable backscatter. Yang F *et al*., for example, used SPIONs conjugated microbubbles improving their capabilities in US imaging and also, thanks to SPIONs, producing a good MRI contrast [37]. The size of the most common microbubble-based US contrast agent (1–8 μm) renders them as merely intravascular flow tracers and the SPIONs encapsulated in microbubbles or vesicles reached these dimensions. In contrast, the chemico-physical characteristics of SPIONs (i.e., 4 nm in diameter in the present study) make them potentially capable of extravasating and reaching a tumor region, which can exhibit a vascular pore size up to 780 nm [42]. The small size of SPIONs means that they can cross endothelial barriers and, as targetable materials, can reach a tumor region, acting at the same time as vehicles for therapeutic agents [32].

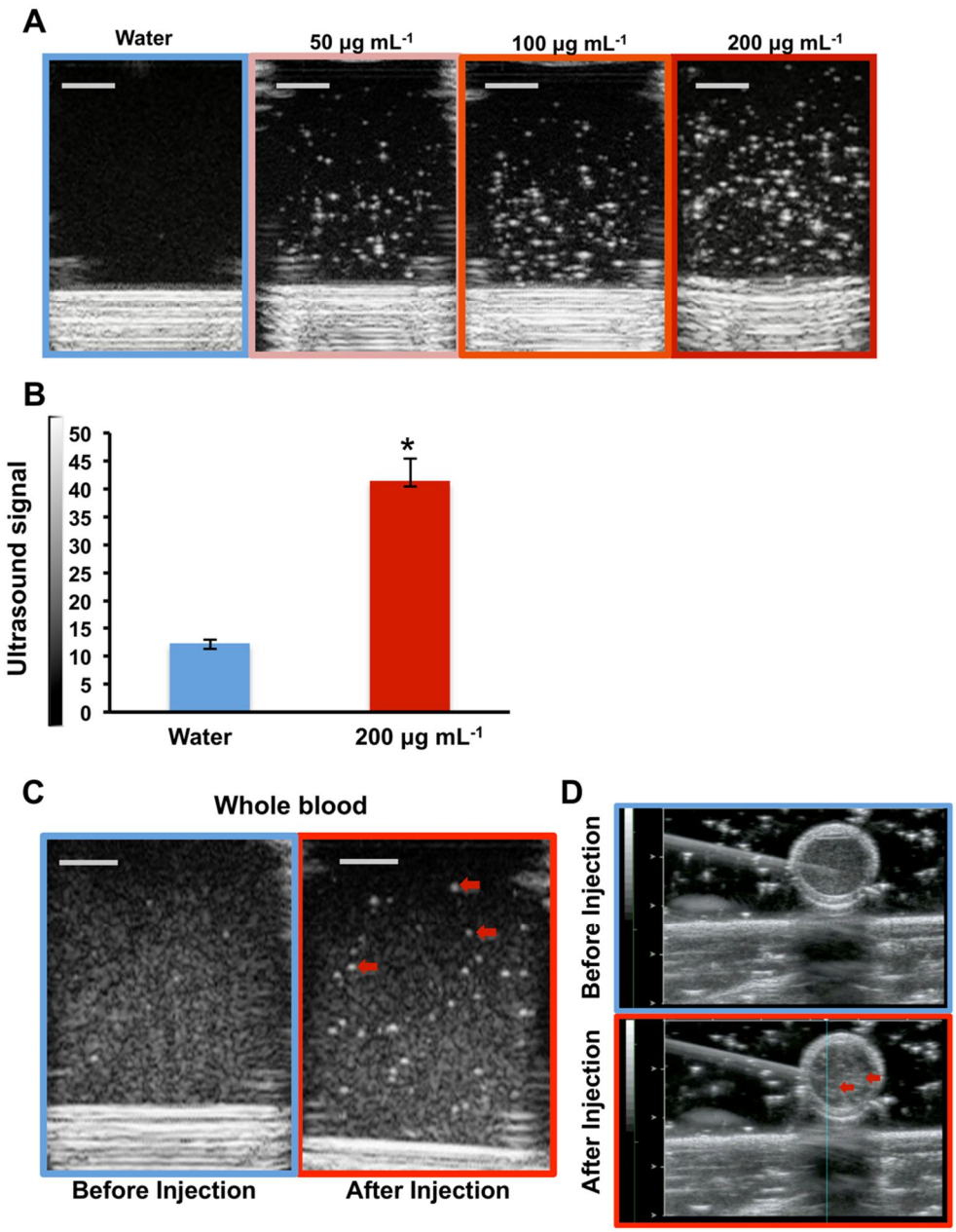

Fig. 3. Ultrasonography of Cy-SPION in water and whole blood.
(A) Degassed water alone (left side) or with Cy-SPION (50, 100 and 200 µg mL^{-1}) (right side) under ultrasound probe sonication in two plate wells (diameter 6.4 mm). (B) Calculation of the ultrasound signal of Fig. A (water and 200 µg mL^{-1}) (analyzed pixels= 29205). The ultrasound signal is reported in 8-bit gray scale intensity from 0 to 255 shades of gray. Signal intensity was calculated on measurements of three investigations. Degassed water was used as a negative control. *p values= 0,05. (C) Whole blood before and after injection with Cy-SPION (200 µg mL^{-1}) under ultrasonography (Scale bar 2.5mm). Red arrows highlight the particle signals. (D) Detection of Cy-SPION in a fresh whole blood filled vein phantom. A vein phantom was built specifically to assess the echogenic properties of Cy-SPION in whole blood from healthy donors. The phantom was constituted of non-toxic, non-hemolytic, and non-pyrogenic natural rubber medical tubing with no absorption/adesion properties. Vein phantom showed a diameter of 0,5 cm. The vein phantom was filled with fresh extracted human whole blood (37 °C in heparin). As visible at the lower picture, a solution of Cy-SPION (100 µl at 200 µg/mL) was injected with a syringe; particles are clearly visible in the blood showing hyperechogenic spots (Red arrow); ultrasound images were recorded at 14.0 MHz in tissue harmonic imaging (THI) modality.

To the best of our knowledge few studies have tested the US ability of SPIONs without any coating. For example, Mehrmohammadi M. *et al.* successfully used SPION (Feridex) for magneto-motive US imaging. However, they did not find a significant US signal from the free SPIONs in a tissue phantom, and they stated that SPIONs are not useful US contrast agents due to their weak reflectivity [43]. We are aware of the fact that the modification of SPIONs with other molecules or particles may change their contrast properties [40].

In order to investigate our uncoated Cy-SPIONs as potential ultrasound contrast agents, after having assessed the uptake and ruled out the possible cytotoxic of our nanoparticles at different concentrations, we assessed the echogenic property of Cy-SPIONs in dose responses at 50, 100 and 200 μg mL^{-1} in degassed water. To avoid the possible bubble-formation after injection of Cy-SPION solution we carefully suspend the Cy-SPIONs in degassed water for all the experiments. **Fig. 3A** shows visible and well-dispersed nanoparticles under ultrasonography. The white area visible in the US image suggests the high echogenicity of Cy-SPIONs. Interestingly, the US signal of dispersed Cy-SPIONs was three times more intense than same degassed plain water used as a negative control (11.0 vs. 43.0, respectively; $P < 0.05$) (**Fig. 3B**). In view of the results obtained from the experiments in water, we tested the echogenic propriety of Cy-SPIONs on whole blood. Intriguingly, the red arrows in the US image (**Fig. 3C**) indicate a visible and strong US signal of Cy-SPION nanoparticles well dispersed in whole blood.

To confirm these data, we performed an experiment with a phantom vein and human blood to simulate the bloodstream conditions (**Fig. 3D**). The brightness of Cy-SPIONs after injection in the phantom vein under ultrasonography was detected (**Fig. 3D**). These experiments proved that Cy-SPIONs were also perfectly visible in a complex fluid such as blood that *per se* has a high background signal compared to water. Our data are not in agreement with the weak reflectivity of SPIONs found by Mehrmohammadi M. *et al*. The higher US signal that we found with our uncoated Cy-SPIONs could be due to the different functionalization compared to Feridex used by Mehrmohammadi M et al [43]. Thanks to the high dispersbility in water of our CY-SPIONs, they are able to give a strong US signal.

Uptake and biocompatibility of Cy-SPIONs

SPIONs uptake has already been reported for different cell lines [44]. Here for the first time we assessed their ability to cross the membrane as cystine functionalized SPIONs in *ex vivo* human

PBMCs from healthy donors (**S. Fig. 1**). Cells were incubated for 24 h with Cy-SPIONs at high doses (200 μg mL^{-1}) and analyzed by TEM. **S. Fig. 1(A)** shows a representative image of the control samples, where all organelles are clearly visible and correspond to the normal functionality of cells. **S. Fig. 1(B)** shows the presence of a large number of Cy-SPION inside the cells in the treated samples. Due to their phagocytic properties, monocytes were the cell population with the highest capacity of uptake (>70% of visible Cy-SPION clusters) compared to the other cell types present in PBMC populations (T cells, B cells, natural killers).

Some toxicology studies with SPIONs lacking in bio-functionalization have highlighted the possible toxicity of these nanoparticles [45, 46].

To check the cell compatibility of Cy-SPIONs, we performed multiparametric flow cytometry assays looking at early and late apoptosis, necrosis, cell membrane status and proliferation on *ex vivo* immune cells (**Fig. 4**). First, we performed a live/dead staining and apoptosis and necrosis assay in dose response (50, 100, 200 μg mL^{-1} of Cy-SPIONs) on cells incubated for 24 h (**Fig. 4A and 4B**). Ethanol incubation was used as a positive control. We chose these concentrations following the work of Naqvi S *et al,* where the authors studied the effect of SPION concentration (from 25 to 500 μg mL^{-1}) on immune cells, specifically on macrophages [47]. Even at high concentrations of 200 μg mL^{-1}, Cy-SPIONs did not exert any toxicity.

Data in agreement with Yeh CH et al; the authors pointed out that the Resovist (FDA approved) do not give any toxicity in macrophage also at the higher concentration used (200μg/mL)[48]. Recent studies also displayed that there was no toxicity in murine macrophages after overnight labeling with Ferumoxides (Feridex, Advanced Magnetics, USA, Endorems, Guerbet, France; dextran-coated, hydrodynamic diameter of 120–180 nm) [49].

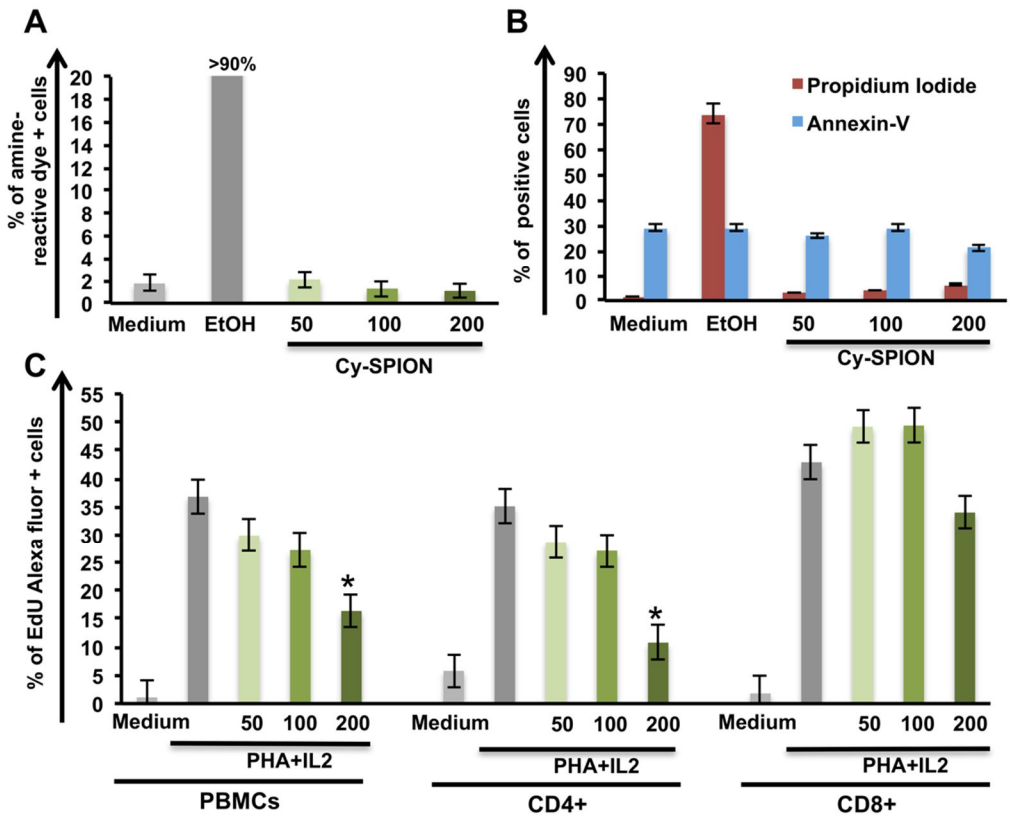

Fig. 4 Viability and proliferation assays on human primary immune cells. PBMCs were incubated with Cy-SPION at increasing doses (50µg/mL, 100µg/mL and 200µg/mL) or left untreated (medium). Data were analyzed with different stainings on flow cytometry. (A) Percentage of late apoptotic and dead cells was assessed by staining with an amine-reactive dye after 24 h of incubation; ethanol was used as a positive control. (B) Necrosis and apoptosis were assessed using propidium iodide and Annexin V staining; ethanol was used a positive control. (C) Proliferation assay was performed on stimulated cells with phytohemagglutinin 2‰ (PHA) and interleukin 2 (IL2) 30 u/mL for three days. 5-ethynyl-2′-deoxyuridine (Edu) is incorporated into DNA during active DNA synthesis. Edu positive cells are reported.

Differences from the control percentage were not statistically significant, including annexin-V staining (as shown in **Fig. 4A** and 4B). In addition, we assessed whether Cy-SPIONs impact cellular proliferation (**Fig. 4C**) of total PBMCs and through the specific gating of T cells CD4+ and CD8+. We focused on the T cell subpopulation since it is the most abundant on PBMCs (up to 40%) and is the easiest one to culture *ex vivo* for a long time, as required for proliferation assays.

Samples were treated with phytohemagglutinin at 2% and 30 µ/mL of interleukin 2 for three days to boost the proliferation in the presence of magnetic particles. Control samples were left untreated. A staining with 5-ethynyl-2′-deoxyuridine (Edu) Alexa-Fluor conjugated was performed, and Edu was incorporated into DNA during active DNA synthesis. No significant

difference in treated samples compared to controls was observed. However, at 200 µg mL^{-1} we found a decrease in proliferation for each cell population.

These results confirmed the lack of cytotoxicity of Cy-SPIONs. The bio-immune-compatibility of Cy-SPIONs found may be related to the physiological functions of cystine as a component of glutathione and therefore as protection for the cells from oxidation stress.

Biocompatibility of Cy-SPION under US into idealized synthetic microvascular network (SMN).

Additional biocompatibility experiments were performed using a microfluidic device (SynVivo technology), which simulates the micro-vascular system of mice (**Fig. 5**).

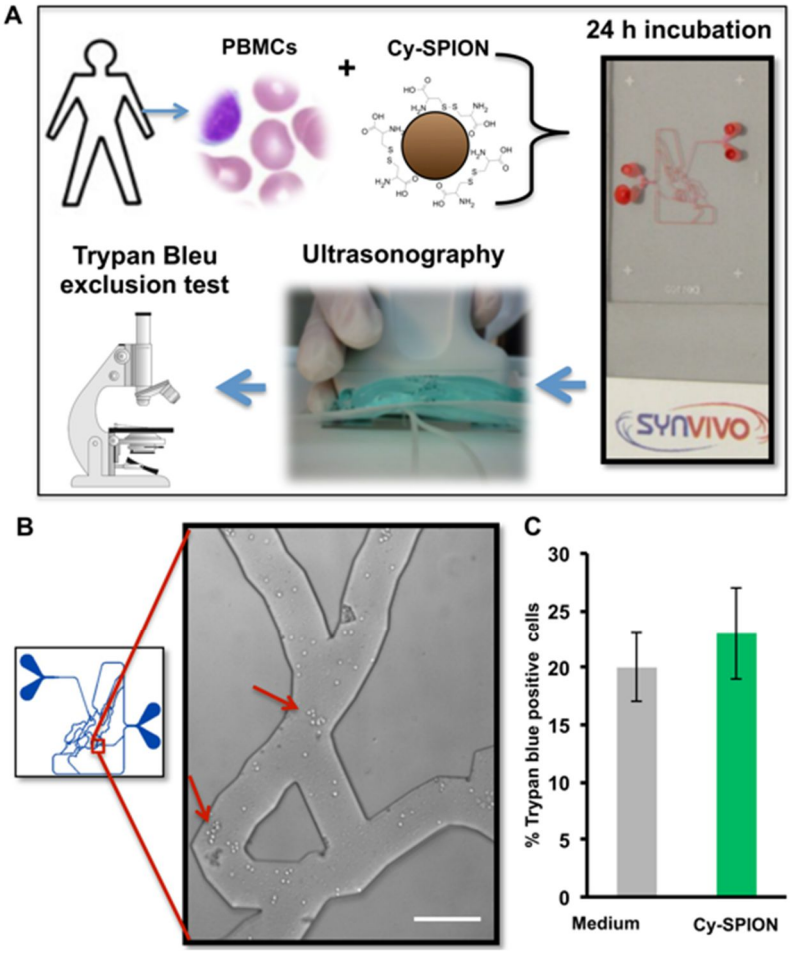

Fig. 5 In silico microvasculature assay and viability under ultrasonography. (A) PBMCs were extracted from healthy donors and treated with Cy-SPION 200 µg/mL or left untreated. Cells were incubated in the synthetic microvasculature network (SMN) chip for 24 h, ultrasonography was applied for 15 minutes and viability assay (trypan blue exclusion test) was performed. (B) Phase image of a 100X zoom in the SMN with Cy-SPION treated cell; arrows indicate some of the live primary cells in the flow. (C) Viability after ultrasonography on medium control and Cy-SPION treated primary cells (Scale bar 500 µm).

We used purified PBMCs treated with the higher concentration (200 μg mL^{-1}) of Cy- SPIONs; untreated PBMCs were used as a control. The cells were added to the microfluidic device and after 24 h of incubation with Cy-SPIONs were exposed to US for 15 minutes (the time necessary for US exams on humans) on top of the microfluidic channel, and then a viability assay with a Trypan Blue exclusion test was performed (**Fig. 5A**). Red arrows highlighted well-dispersed Cy-SPIONs inside the microchannel (**Fig. 5B).** No statistically significant difference in terms of percentage of dead cells between treated and control samples was found (**Fig. 5C**). We assume that our Cy-SPIONs are perfectly biocompatible also under US, improving their future application in *in vivo* applications.

Cy-SPION impact in human PBMCs

The preservation of normal immune functions is fundamental in the use of Cy-SPIONs for potential treatment or the future diagnosis of any disease. The analysis of activation reveals the functionality of immune cells. We thus investigated the expression of the activation-related surface molecules: i) CD69, a member of the C-type lectin superfamily (Leu-23), one of the earliest cell surface antigens expressed by immune cells following activation; ii) CD25 (alpha chain of the IL-2 receptor), a late activation antigen; and iii) CD30, a cell membrane protein of the tumor necrosis factor receptor family. Due to their well-known activation properties, concanavalin A (Con A) and lipopolysaccharide (LPS), were used as a positive control. **Fig. 6A** shows the percentage of CD25+ cells after incubation with different concentrations of Cy-SPIONs, highlighting the total comparability of treated samples with controls. We also found (**Fig. 6A**) the same results for the CD69 and CD30 expression markers. The total absence of activation after particle incubation is also reported. As stated by Mahmoudi M *et al.* there is little direct evidence on the induction of inflammatory pathways and cytokines by engineered SPIONs (both uncoated and coated*) in vivo* and *in vitro* [45].

To fill this gap in the literature we studied the secretion of a wide variety of cytokines after incubation with 200 μg mL^{-1} Cy-SPIONs in cells. In our analysis we examined four primary cytokines: TNFα, IL10, IL6 and IL1β (**Fig. 6B**) as they are among the most important cytokines secreted from PBMCs. Multiplex ELISA assay was used for the detection.

Interestingly, we found a Cy-SPION dose-dependent increase of TNFα, IL10 and IL6 (p-value < 0.05). The cytokines found expressed such as IL6 and TNFα are normally secreted by monocytes/macrophages and their action is normally directed on the activation of the acute inflammation process [50]. IL10 is a cytokine mainly secreted by activated macrophages that

through a negative feedback directly control and decrease the immune response [51]. This action, as previously proved by many research groups [52-55], could be the possible consequence of the uptake of Cy-SPIONs by monocytes shown in **S. Fig. 1.**

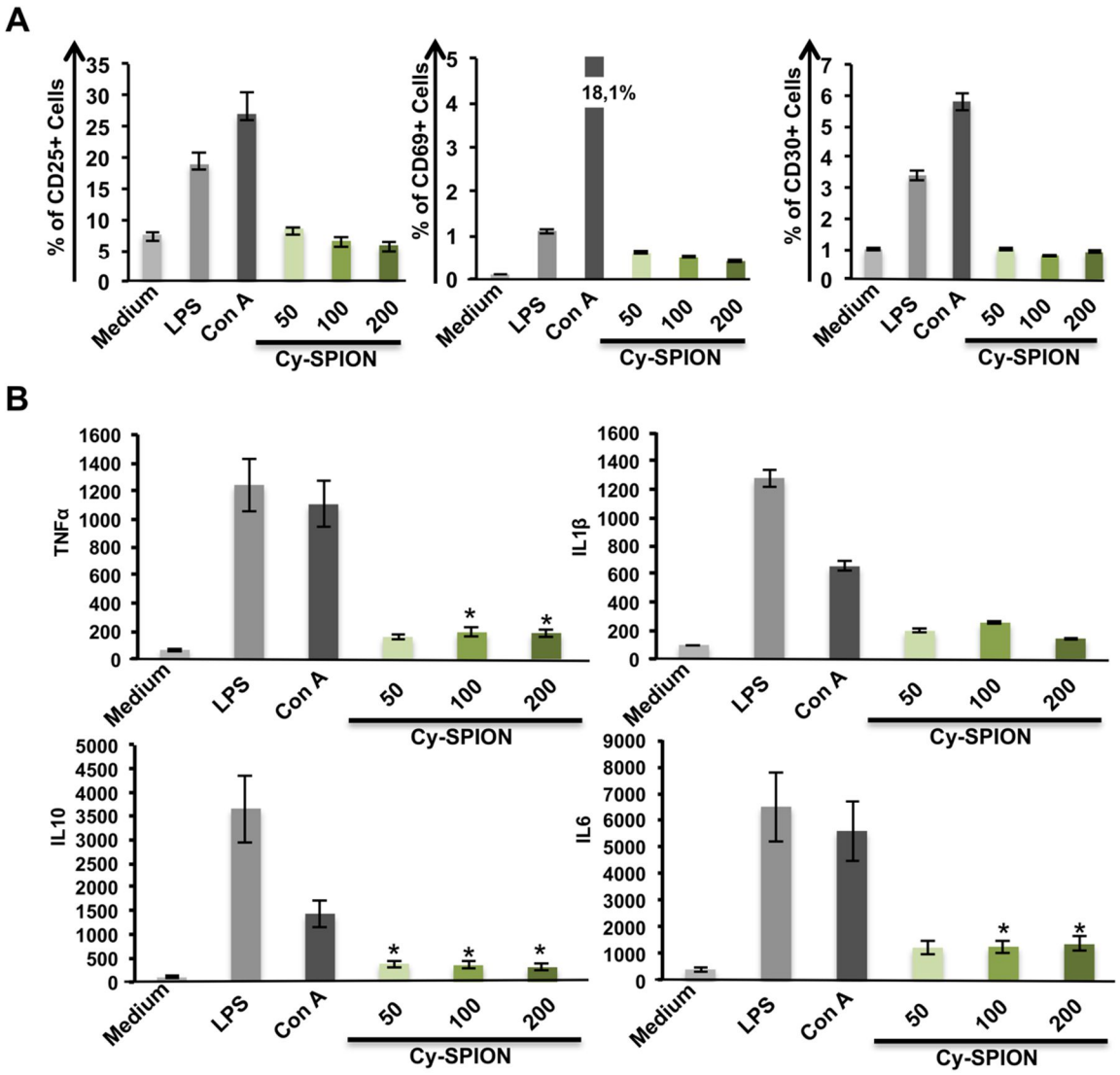

Fig. 6 Activation markers analysis and cytokines secretion assay. PBMCs were treated with Cy-SPION (50, 100 and 200 µg/mL) or left untreated (medium) for 24 h. Concanavalin A (ConA, 10 µg/mL) and lipopolysaccharides (LPS 2µg/mL) were used as positive controls. (A) CD25, CD69 and CD30 cell surface activation markers were analyzed by flow cytometry. (B) Cytokine secretion was assessed by multiplex ELISA, values are expressed in pg/mL (*pvalue <0,05).

Thus, studies conducted *in vitro* on the effect of SPIONs on macrophage functions have revealed modifications in cellular behaviors as well as in the modulated cytokine expressions [56, 57]. For instance, Hsiao JK *et al.* studied the response of clinically-used SPION ferucarbotran (Resovist) loading upon macrophage and found that high doses of SPIONs induced the

secretion of TNF-α and resulted in cellular activation through the production of nitric oxide [57]. Also in the study of Yeh CH et al. the cytokine secretion analysis indicated that Resovist could elicit the production of pro-inflammatory cytokines such as TNF-α, IL-1β and IL-6, but their levels were much lower than those with lipopolysaccharide (LPS) stimulation [48]. We found similar results with our Cy-SPION compared to other already approved SPIONs for MRI imaging evidencing no significant toxicity on immune cells [58, 59].

The uptake of SPIONs by phagocytic monocytes and macrophages provides a valuable *in-vivo* tool by which imaging techniques can be used to monitor the involvement of macrophages in inflammatory processes such as multiple sclerosis, traumatic nerve injury, stroke, brain tumors, and vulnerable plaques in carotid artery.

Our data are in accordance with findings on commercial clinically approved SPIONs to be used as SPION-based MRI contrast agents such as Resovist, Feridex and Combidex, which are coated with dextran, other carbohydrates or citrate-stabilized particles. SPIONs with other functionalizations (polymers, metals, silica) are in the development phase [52].

To better understand all aspects of Cy-SPIONs interaction with immune cells, an extensive genome study with an RT2 Profiler PCR Array testing was performed, studying the expression of 84 key genes on immune responses (**Fig. 7**). For a clear picture of gene expression, we focused on a well established T cell line (Jurkat) for two critical reasons: i) it is a good model particularly for the adaptive the immune-cell response; ii) T cells are the most abundant population in the blood flow, therefore their reactions can give a wide picture on SPIONs impact.

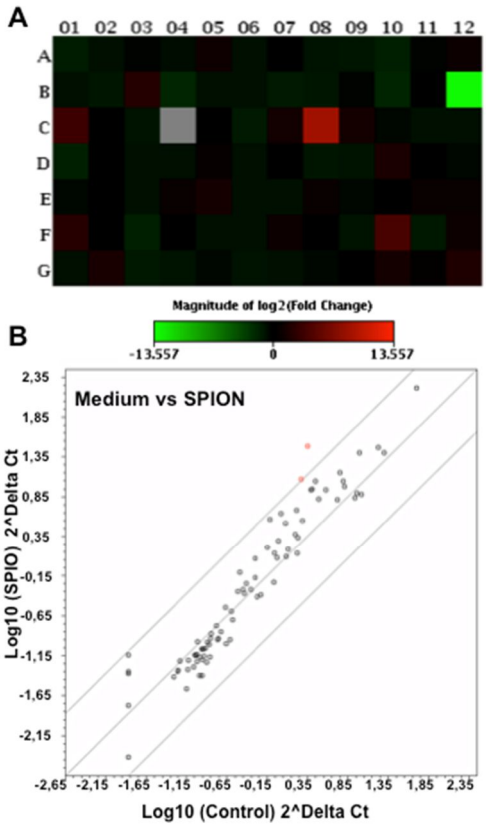

C

Genes	
B2M	2,2141
TNF	2,3302
MAPK1	2,3651
TLR2	2,6909
IRAK1	2,7644
TYK2	3,1924
NLRP3	4,2372
HLA-A	9,0533

Fig. 7 Immune gene expression array. T cells were incubated with Cy-SPION (200 μg/mL) for 24 h or left untreated. The expression of 84 immune response related genes was evaluated. A) Heatmap Cy-SPION treated sample versus control medium. Genes are displayed for fold change variations versus medium control and colored by their standardized expression value (red= high expression, green= low expression) (for gene names see S. Fig. 2). B) Scatter plot. Genes upregulated with fold regulation >4 are shown in red circles. Unaffected genes are in black. C) Modulated genes versus control with a fold change >2.

The heatmap (**Fig. 7A**) shows 84 genes displayed for fold change variations in comparison to the medium control and colored by their standardized expression value (red= high expression; green= low expression). The induction of TNF expression found was in perfect agreement with the cytokine data. The other genes modulated with a fold change higher than 2 were: B2M, MAPK1, TLR2, IRAK1, TYK2, NLRLP3 and HLA-A (**S. Fig. 2**). The up-regulation of the toll-like receptor 2 (TLR2) in T cells led us to hypothesize that Cy-SPIONs come in contact with immune cells through a toll-like receptor. This interaction may also be responsible for the up-regulation of genes such as MAPK1, TYK2 and IRAK1, which are normally implicated in

signal transduction. MAPK/ERK pathways are responsible for many functions such as cell growth and proliferations. TYK2 and IRAK1 also encode for kinases that are responsible for interferon and IL1 secretion. These data were confirmed in the Scatter Plot (**Fig. 7B**); all genes were shown in accordance to fold regulation. Only two, NLRP3 and HLA-A, were up-regulated with a fold regulation greater than 4. **Fig. 7C** reports the up-regulated genes. The modulated genes found are not implicated with a significant modification in cell functionality, indeed the few genes up-regulated and also the activation markers analysis did not show any cell-activation response.

Conclusions

To conclude, in this work we give new insight into the use of cystine functionalized SPIONs in imaging, not only for MRI but also for ultrasonography due to their echogenic properties in water and blood, as shown in the present study. Intriguingly the small size of our Cy-SPIONs make them able to cross endothelial barriers and, as targetable materials, to potentially reach a tumor region, acting at the same time as vehicles for therapeutic agents. The potentiality of our Cy-SPIONs to extravasate and localize in a tumoral region highlight that Cy-SPIONs could be successfully exploited for theranostic applications. Moreover our data clearly point out the good immune and biocompatibility of Cy-SPION, with absence of activation stimuli on treated PBMCs.

These findings make Cy-SPIONs perfect materials for new *in vivo* dual mode imaging studies where the preferential route of administration is by intravenous injections.

Acknowledgments

We thank the staff of CFD Research Corporation (Huntsville, Alabama, USA) for their technical help. The authors would also like to thank Prof. Maja Remskar for the TEM images, and Dr. Michela Tosetti for giving us access to the IMAGO 7 Foundation equipment for MRI preliminary investigations. V. Domenici and M.R. Tinè thank MIUR for the project entitled "Nanoscale functional organization of (bio)molecules and hybrids for targeted application in sensing, medicine and biotechnology", PRIN 2010-2011, No. 2010C4R8M8. This work was also partly supported by the Fondazione Banco di Sardegna (grant N° 2013.1308, 2014.6035 to

L.G.D.), the Sardinia Region (grant N° CRP-59720 to L.G.D.) and the Gianfranco del Prete Association “The future: medicine, biology and nanotechnology Award” to L.G.D.

References

1. G. Sechi, D. Bedognetti, F. Sgarrella, L. Van Eperen, F. M. Marincola, A. Bianco and L. G. Delogu, *Nanomedicine*, 2014, **9**, 1475-1486.
2. C. Wu, F. Gong, P. Pang, M. Shen, K. Zhu, D. Cheng, Z. Liu and H. Shan, *PloS one*, 2013, **8**, e66416.
3. P. Pang, C. Wu, M. Shen, F. Gong, K. Zhu, Z. Jiang, S. Guan, H. Shan and X. Shuai, *PloS one*, 2013, **8**, e76612.
4. A. K. Gupta and M. Gupta, *Biomaterials*, 2005, **26**, 3995-4021.
5. B. Gleich and J. Weizenecker, *Nature*, 2005, **435**, 1214-1217.
6. S. Lee and X. Chen, *Molecular imaging*, 2009, **8**, 87-100.
7. F. Liu, S. Laurent, H. Fattahi, L. Vander Elst and R. N. Muller, *Nanomedicine*, 2011, **6**, 519-528.
8. S. G. Zheng, H. X. Xu and H. R. Chen, *World journal of radiology*, 2013, **5**, 468-471.
9. M. Postema and O. H. Gilja, *World journal of gastroenterology : WJG*, 2011, **17**, 28-41.
10. L. G. Delogu, G. Vidili, E. Venturelli, C. Menard-Moyon, M. A. Zoroddu, G. Pilo, P. Nicolussi, C. Ligios, D. Bedognetti, F. Sgarrella, R. Manetti and A. Bianco, *Proceedings of the National Academy of Sciences of the United States of America*, 2012, **109**, 16612-16617.
11. F. M. Kievit, Z. R. Stephen, O. Veiseh, H. Arami, T. Wang, V. P. Lai, J. O. Park, R. G. Ellenbogen, M. L. Disis and M. Zhang, *ACS nano*, 2012, **6**, 2591-2601.
12. Y. Song, Z. Huang, J. Xu, D. Ren, Y. Wang, X. Zheng, Y. Shen, L. Wang, H. Gao, J. Hou, Z. Pang, J. Qian and J. Ge, *Biomaterials*, 2014, **35**, 2961-2970.
13. M. K. Yu, D. Kim, I. H. Lee, J. S. So, Y. Y. Jeong and S. Jon, *Small*, 2011, **7**, 2241-2249.
14. B. Basly, G. Popa, S. Fleutot, B. P. Pichon, A. Garofalo, C. Ghobril, C. Billotey, A. Berniard, P. Bonazza, H. Martinez, D. Felder-Flesch and S. Begin-Colin, *Dalton transactions*, 2013, **42**, 2146-2157.
15. R. Jin, B. Lin, D. Li and H. Ai, *Current opinion in pharmacology*, 2014, **18C**, 18-27.
16. X. Wang, X. Xing, B. Zhang, F. Liu, Y. Cheng and D. Shi, *International journal of nanomedicine*, 2014, **9**, 1601-1615.

17. S. Dolci, V. Ierardi, A. Gradisek, Z. Jaglicic, M. Remskar, T. Apih, M. Cifelli, G. Pampaloni, C. A. Veracini and V. Domenici, *Current Physical Chemistry*, 2013, **3**, 493-500.
18. H. Gmunder, H. P. Eck and W. Droge, *European journal of biochemistry / FEBS*, 1991, **201**, 113-117.
19. Dolci S, Remskar M, Jaglicic Z, Pineider F, Boni A, Pampaloni G, Veracini CA and Domenici V, *J Mater Sci* 2013, **48**, 1283–1291.
20. M. A. Dobrovolskaia and S. E. McNeil, *Nature nanotechnology*, 2007, **2**, 469-478.
21. L. G. Delogu, E. Venturelli, R. Manetti, G. A. Pinna, C. Carru, R. Madeddu, L. Murgia, F. Sgarrella, H. Dumortier and A. Bianco, *Nanomedicine (Lond)*, 2012, **7**, 231-243.
22. M. Pescatori, D. Bedognetti, E. Venturelli, C. Menard-Moyon, C. Bernardini, E. Muresu, A. Piana, G. Maida, R. Manetti, F. Sgarrella, A. Bianco and L. G. Delogu, *Biomaterials*, 2013, **34**, 4395-4403.
23. C. Crescio, M. Orecchioni, C. Menard-Moyon, F. Sgarrella, P. Pippia, R. Manetti, A. Bianco and L. G. Delogu, *Nanoscale*, 2014, **6**, 9599-9603.
24. M. Orecchioni, D. Bedognetti, F. Sgarrella, F. M. Marincola, A. Bianco and L. G. Delogu, *Journal of translational medicine*, 2014, **12**, 138.
25. X. Chen, R. Wong, I. Khalidov, A. Y. Wang, J. Leelawattanachai, Y. Wang and M. M. Jin, *Biomaterials*, 2011, **32**, 7651-7661.
26. E. A. Vermeij, M. I. Koenders, M. B. Bennink, L. A. Crowe, L. Maurizi, J. P. Vallee, H. Hofmann, W. B. van den Berg, P. L. van Lent and F. A. van de Loo, *PloS one*, 2015, **10**, e0126687.
27. R. D. Oude Engberink, E. L. Blezer, E. I. Hoff, S. M. van der Pol, A. van der Toorn, R. M. Dijkhuizen and H. E. de Vries, *Journal of cerebral blood flow and metabolism : official journal of the International Society of Cerebral Blood Flow and Metabolism*, 2008, **28**, 841-851.
28. J. Gunn, R. K. Paranji and M. Zhang, *Biophysical journal*, 2009, **97**, 2640-2647.
29. A. Beduneau, Z. Ma, C. B. Grotepas, A. Kabanov, B. E. Rabinow, N. Gong, R. L. Mosley, H. Dou, M. D. Boska and H. E. Gendelman, *PloS one*, 2009, **4**, e4343.
30. A. Gramoun, L. A. Crowe, L. Maurizi, W. Wirth, F. Tobalem, K. Grosdemange, G. Coullerez, F. Eckstein, M. I. Koenders, W. B. Van den Berg, H. Hofmann and J. P. Vallee, *Arthritis research & therapy*, 2014, **16**, R131.

31. A. Barrefelt, M. Saghafian, R. Kuiper, F. Ye, G. Egri, M. Klickermann, T. B. Brismar, P. Aspelin, M. Muhammed, L. Dahne and M. Hassan, *International journal of nanomedicine*, 2013, **8**, 3241-3254.
32. L. B. Thomsen, T. Linemann, K. M. Pondman, J. Lichota, K. S. Kim, R. J. Pieters, G. M. Visser and T. Moos, *ACS chemical neuroscience*, 2013, **4**, 1352-1360.
33. N. Doshi, B. Prabhakarpandian, A. Rea-Ramsey, K. Pant, S. Sundaram and S. Mitragotri, *Journal of controlled release : official journal of the Controlled Release Society*, 2010, **146**, 196-200.
34. T. Hyeon, S. S. Lee, J. Park, Y. Chung and H. B. Na, *Journal of the American Chemical Society*, 2001, **123**, 12798-12801.
35. D. E. Lee, H. Koo, I. C. Sun, J. H. Ryu, K. Kim and I. C. Kwon, *Chemical Society reviews*, 2012, **41**, 2656-2672.
36. C. Sciallero, D. Grishenkov, S. V. Kothapalli, L. Oddo and A. Trucco, *The Journal of the Acoustical Society of America*, 2013, **134**, 3918-3930.
37. F. Yang, L. Li, Y. Li, Z. Chen, J. Wu and N. Gu, *Physics in medicine and biology*, 2008, **53**, 6129-6141.
38. B. Xu, H. Dou, K. Tao, K. Sun, J. Ding, W. Shi, X. Guo, J. Li, D. Zhang and K. Sun, *Langmuir : the ACS journal of surfaces and colloids*, 2011, **27**, 12134-12142.
39. T. Y. Liu, H. H. Huang, Y. J. Chen and Y. J. Chen, *Acta biomaterialia*, 2011, **7**, 578-584.
40. Y. Sun, Y. Zheng, H. Ran, Y. Zhou, H. Shen, Y. Chen, H. Chen, T. M. Krupka, A. Li, P. Li, Z. Wang and Z. Wang, *Biomaterials*, 2012, **33**, 5854-5864.
41. S. T. Kang and C. K. Yeh, *Chang Gung medical journal*, 2012, **35**, 125-139.
42. S. K. Hobbs, W. L. Monsky, F. Yuan, W. G. Roberts, L. Griffith, V. P. Torchilin and R. K. Jain, *Proceedings of the National Academy of Sciences of the United States of America*, 1998, **95**, 4607-4612.
43. M. Mehrmohammadi, J. Oh, S. Mallidi and S. Y. Emelianov, *Molecular imaging*, 2011, **10**, 102-110.
44. N. Singh, G. J. Jenkins, R. Asadi and S. H. Doak, *Nano reviews*, 2010, **1**.
45. M. Mahmoudi, H. Hofmann, B. Rothen-Rutishauser and A. Petri-Fink, *Chemical reviews*, 2012, **112**, 2323-2338.
46. M. Radu, M. C. Munteanu, S. Petrache, A. I. Serban, D. Dinu, A. Hermenean, C. Sima and A. Dinischiotu, *Acta biochimica Polonica*, 2010, **57**, 355-360.

47. S. Naqvi, M. Samim, M. Abdin, F. J. Ahmed, A. Maitra, C. Prashant and A. K. Dinda, *International journal of nanomedicine*, 2010, **5**, 983-989.
48. C. H. Yeh, J. K. Hsiao, J. L. Wang and F. Sheu, *J Nanopart Res*, 2010, **12**, 151-160.
49. A. S. Arbab, G. T. Yocum, H. Kalish, E. K. Jordan, S. A. Anderson, A. Y. Khakoo, E. J. Read and J. A. Frank, *Blood*, 2004, **104**, 1217-1223.
50. G. Tosato and K. D. Jones, *Blood*, 1990, **75**, 1305-1310.
51. K. W. Moore, A. O'Garra, R. de Waal Malefyt, P. Vieira and T. R. Mosmann, *Annual review of immunology*, 1993, **11**, 165-190.
52. Y. X. Wang, *Quantitative imaging in medicine and surgery*, 2011, **1**, 35-40.
53. A. Saleh, M. Schroeter, C. Jonkmanns, H. P. Hartung, U. Modder and S. Jander, *Brain : a journal of neurology*, 2004, **127**, 1670-1677.
54. E. A. Neuwelt, P. Varallyay, A. G. Bago, L. L. Muldoon, G. Nesbit and R. Nixon, *Neuropathology and applied neurobiology*, 2004, **30**, 456-471.
55. C. von Zur Muhlen, D. von Elverfeldt, N. Bassler, I. Neudorfer, B. Steitz, A. Petri-Fink, H. Hofmann, C. Bode and K. Peter, *Atherosclerosis*, 2007, **193**, 102-111.
56. I. Siglienti, M. Bendszus, C. Kleinschnitz and G. Stoll, *Journal of neuroimmunology*, 2006, **173**, 166-173.
57. J. K. Hsiao, H. H. Chu, Y. H. Wang, C. W. Lai, P. T. Chou, S. T. Hsieh, J. L. Wang and H. M. Liu, *NMR in biomedicine*, 2008, **21**, 820-829.
58. I. Raynal, P. Prigent, S. Peyramaure, A. Najid, C. Rebuzzi and C. Corot, *Investigative radiology*, 2004, **39**, 56-63.
59. A. S. Arbab, L. A. Bashaw, B. R. Miller, E. K. Jordan, B. K. Lewis, H. Kalish and J. A. Frank, *Radiology*, 2003, **229**, 838-846.

Supporting informations

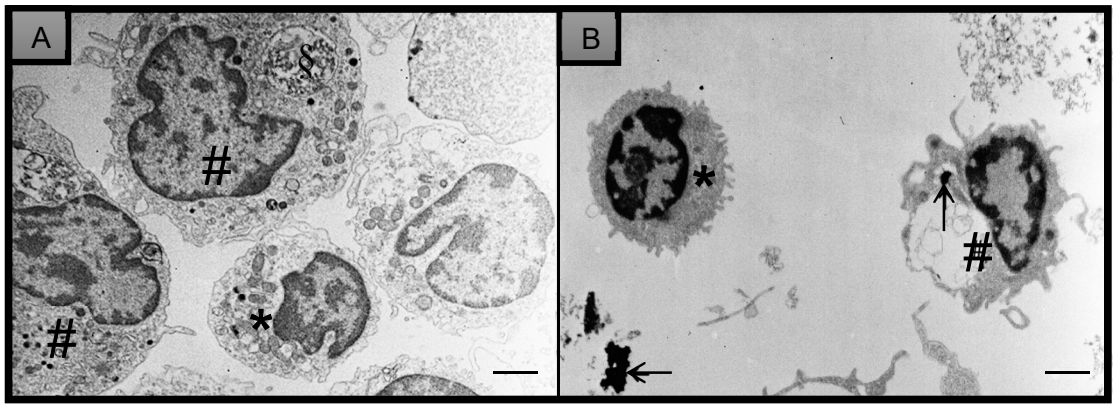

S. Fig. 1 TEM images of PBMCs Cy-SPIONs treated. (A) Untreated PBMCs. Transmission electronic microscope captured image of lymphocytes (*) and monocytes (#). Lymphocytes show a slightly indented nucleus, with plenty of heterochromatin, scant cytoplasm with few organelles (Golgi complex, mitochondria). The nucleus of monocytes, more voluminous than lymphocytes, has less *elettrondensa* chromatin; the abundant cytoplasm shows numerous organelles (Golgi complex, endoplasmic reticulum, mitochondria and numerous electron-granules). Vesicles are also visible in amorphous content (§). (B) Cy-SPIONs (200 µg/ml) treated PBMCs. Lymphocytes (*) and monocytes (#) are clearly visible. Monocytes present large cytoplasmic protrusions and large vacuoles of phagocytosis, containing small electron-clusters, corresponding to aggregates of particles (arrow) suggesting the nanoparticles uptake. Cy-SPIONs are also present in the extracellular medium (arrow). Bar scale correspond to 1 µm (3000 X).

Layout	01	02	03	04	05	06	07	08	09	10	11	12
A	APCS -2.99	C3 -1.91	CASP1 -1.21	CCL2 -1.62	CCL5 1.98	CCR4 -1.87	CCR5 -1.18	CCR6 -2.04	CCR8 -2.30	CD14 -3.22	CD4 -1.29	CD40 1.65
B	CD40LG -1.95	CD80 -2.28	CD86 3.65	CD8A -4.05	CRP -1.99	CSF2 -1.80	CXCL10 -2.62	CXCR3 -2.25	DDX58 -1.25	FASLG -3.86	FOXP3 -1.11	GATA3 -12049.55
C	HLA-A 9.05	HLA-E 1.18	ICAM1 -2.14	IFNA1 -5.22	IFNAR1 -1.00	IFNB1 -2.54	IFNG 2.11	IFNGR1 379.15	IL10 2.23	IL13 -1.38	IL17A -1.92	IL18 -1.85
D	IL1A -3.28	IL1B -1.01	IL1R1 -1.87	IL2 -1.81	IL23A 1.34	IL4 -1.81	IL5 -1.13	IL6 -2.29	IL8 -2.04	IRAK1 2.76	IRF3 1.19	IRF7 -1.37
E	ITGAM -1.45	JAK2 1.04	LY96 -1.95	LYZ 1.43	MAPK1 2.37	MAPK8 -1.74	MBL2 -1.91	MPO 1.57	MX1 -1.47	MYD88 1.02	NFKB1 1.52	NFKBIA 1.54
F	NLRP3 4.24	NOD1 -1.18	NOD2 -3.23	RAG1 -1.09	RORC -2.00	SLC11A1 -1.82	STAT1 1.71	STAT3 -1.18	STAT4 -2.06	STAT6 13.90	TBX21 -2.49	TICAM1 1.83
G	TLR1 -1.82	TLR2 2.69	TLR3 -2.36	TLR4 -2.05	TLR5 -1.47	TLR6 -2.16	TLR7 -1.93	TLR8 -1.47	TLR9 -1.02	TNF 2.33	TRAF6 1.23	TYK2 3.19

S. Fig. 2 Heat Map description table. Gene names and values as log2 fold change in comparison to the control are reported for all genes showed in the Heat Map (Figure 4A). Empty box in terms of values correspond to undetermined samples.

Chapter 5

Conclusions

Based on the experimental evidences herein provided, it is clear that generalization regarding the impact of different nanomaterials, especially CBMs, on the immune cells should be avoided considering that many parameters crucially involved in their biological behavior are not always addressed and fully described. Appropriate functionalization and controlled shape dimensions can change the interaction of nanomaterials with the immune system increasing also the biocompatibility. As illustrated before is proved that different nanomaterials, following their administration into the body, might cause a response mediated by the immune system. This response could be an immune activation as a result of the response of leukocytes or even immune suppression due to their ability to induce apoptosis or necrosis in these cells. The different studies here presented explicitly demonstrate that the interactions between nanomaterials and the immune cells depend on many factors correlated to their physicochemical characteristics. A positive impact of nanomaterials on the immune system, able to trigger immune suppression and/or immune activation, is a new concept helpful in the development of new nanoscale platforms in medicine as proved i.e. for f-CNTs applied to counteract the microgravity immune cell dysregulation. These new platforms indeed can be investigated as immunotherapy tools, vaccine carriers, adjuvants, and drug delivery systems to target pathology or inflammatory and inflammation-associated disorders. In this context, the results presented with the help also of high throughput technologies for a deep molecular characterization, evidenced how some CBMs and specific type of functionalized NCs could enter into these new platforms and revolutionize the current medicine thanks to their intrinsic properties. A specific use of a "bad" property was also herein provided. Thus, a specific type of graphene called FLG found able to induce specific toxicity on monocytes was applied in a "good" way to target and kill monocytoid cancer cells from acute myeloid leukemia and chronic myelomonocytic leukemia patients being extremely promising as a new cancer tool. In a similar way the application of a new functionalized Cy-SPIONs can give new insights into the use of this materials in imaging, not only for MRI but also for ultrasonography, due to their echogenic properties in water and blood. Moreover, our data pointed out the good immune-compatibility

of Cy-SPION, without no activation stimuli on treated PBMCs resolving the inflammatory reactions found with other SPIONs already present in the market such as Feridex and Resovist. To conclude, the different results presented in this thesis underline that changing the physicochemical characteristics of nanomaterials based on their interaction with the immune system is a crucial aspect that need to be always explored for a successful application of nanotechnology in medicine. The analyzed and immune characterized nanoplatforms presented in this thesis, indeed can be further investigated and applied in therapy or imaging applications helping to reach the hoped medical revolution of nanomedicine.

Chapter 6

Acknowledgements

Firstly, I would like to express my sincere gratitude to my advisor Dr. Lucia Gemma Delogu for the continuous support of my Ph.D study and research, for her patience, motivation, and knowledge. I could not have imagined having a better advisor and mentor for my Ph.D study.

A special thanks to Prof. Proto Pippia and Prof. Antonella Pantaleo, who gave me access to their laboratory and research facilities, and helped me during these years.

Thanks to Dr. Claudio Fozza and Dr. Patrizia Virdis for their precious support and help.

My sincere thanks also goes to Prof. Gianaurelio Cuniberti, Prof. Lorenz C. Hofbauer, and Dr. Martina Rauner, who provided me the opportunity to join their team at the Technische Universität Dresden, (Germany).

I thank my fellow labmates Valentina, Elisabetta and Giulia for the stimulating discussions, the time spent working together, and for all the fun we have had in the last years.

Thanks to all the national and international partners of my advisor that helped me during my Ph.D study, especially:

Thanks to Prof. Alberto Bianco, CNRS Strasbourg (France).

Thanks to Prof. Kostas Kostarelos, University of Manchester (UK).

Thanks to Dr. Davide Bedognetti and Prof. Francesco Marincola, of the Sidra Medical and Research Center, (Qatar).

Thanks to Prof. Gianni Cesareni and all his research group at the University of Roma Tor Vergata.

Thanks to Prof. Matteo Pasquali for the opportunity to visit his lab at the Rice University, Houston, USA.

Last but not the least, I would like to thank my family: my parents, my brothers, my fiancée Martina and all my friends for supporting me spiritually throughout writing this thesis, my Ph.D study and my life in general.